Cross Linked Sulphonated Poly(ether ether ketone) for the Development of Polymer Electrolyte Membrane Fuel Cell

Abdul Ghaffar Al Lafi, MSc.

A Thesis Submitted for the Degree of

Doctor of Philosophy

The School of Metallurgy and Materials, The College of Engineering and Physical Sciences, The University of Birmingham, Birmingham, UK.

September 2009

Synopsis

Ion irradiation has been investigated as a route for the preparation of mechanically stable and highly durable cross linked sulphonated PEEK for fuel cell application. Ion irradiation was carried out using the University of Birmingham's Scanditronix MC-40 Cyclotron operating at 11.7 MeV for H^+ and 30 MeV for He^{2+} and the irradiated materials were characterized focusing on structural, thermal, morphological as well as dielectrical properties.

Alterations produced in the molecular structure of amorphous PEEK by ion irradiation have been interpreted as due to chain scission and formation of cross links, as confirmed by sol-gel analysis in MSA using the well known Charlesby–Pinner equation.

The thermal decomposition of irradiated PEEK was similar to that of untreated PEEK in that it occurred by a random chain scission process. The thermal decomposition temperature and kinetic data for irradiated PEEK films quantitatively suggest that these films still have sufficient thermal stability for long term applications as fuel cell membranes.

The observed T_g increased linearly with cross link density in accordance with the DiBenedetto equation. The DSC results also indicated that the cross links which accompanied irradiation retard the crystallization, but no changes were observed in the mechanism of crystallization.

The apparent activation enthalpy of the glass forming process, determined from DRS, however, decreased and analysis of the dielectric response by Cole-Cole, Havrilak-Negami and Kohlrausch-Williams-Watts equations indicated that the dipole relaxation was broadened and becoming more asymmetric with cross link density. This was interpreted as the cross linked network progressively restricting the length of the chain segments involved in dipole relation process yet adding to the complexity of the modes of segmental motions.

The sulphonation of the cross linked PEEK was investigated in concentrated sulphuric acid following the kinetics of the reaction at room temperature. The rate of reaction decreased with the degree of cross linking and the progress with time was consistent with diffusion control of

the sulphuric acid into the cross linked matrix. The results were consistent with the efficiency of the ions in cross linking PEEK and in particular with the differences in their linear energy transfer (LET).

The materials properties of different cross linked SPEEK membranes have been investigated focusing on water uptake kinetics, stability tests and the performance in a single fuel cell. Increasing cross link density resulted in more bound water present in the equilibrated membranes and increasing the ion exchange capacity (IEC) gave rise to more free water. The results indicated that the cross linked membranes have lower methanol permeability and electro-osmotic drag as well as improved mechanical stability. The presence of a nano-structure in the cross linked membranes was confirmed and the sizes of pore present were comparable to those of Nafion. The effects of cross linking and IEC on the membranes stability in chemical, oxidative and thermal environments have also been considered. Cross linking had little effect in improving both thermal and oxidative stabilities but its effect in improving the chemical stability in particular in methanol solution was pronounced.

The polarisation curves indicated that film thickness, IEC, cross link density as well as temperature affect the performance of the PEM fuel cell, but that the IEC values had a greater effect than cross link density. The performance of the cross linked membranes was very similar to that of non cross linked PEM suggesting the same mechanism of proton transport was present in both systems. The cross linked membranes showed better performance (higher power output and current density) compared to those of the non cross linked solvent cast SPEEK membranes of similar IEC due to the solvent effect. The measurement of power output and energy efficiency suggested that the cross linked PEMs produced in this work are promising candidates to replace Nafion membranes but more information is required, in particular on their long term stability under fuel cell operating conditions, and also in understanding the relationship between material properties and cross linking density.

Acknowledgments

In the Name of Almighty ALLAH (GOD),
the Most Merciful, the Most Compassionate

To my parents…

To my wife and my kids…

Table of Contents

Chapter 1

Polymer Electrolyte Membrane Fuel Cells:

Systems and Applications

Chapter 2

Materials, Experimental Techniques

and Apparatus

Chapter 3

Structural and Thermal Properties
of Irradiated PEEK

Chapter 4

Melting and Isothermal Crystallization Studies
of Irradiated PEEK

Chapter 5

Dielectric Relaxation Spectroscopy

of Irradiated PEEK

Chapter 6

Synthesis and Characterization

of Sulphonated PEEK

Chapter 7

Water Uptake, State of the Water and
Thermoporometry of Cross Linked PEM

Chapter 8

Stability Testing of Cross Linked PEMs and
Their Performance in a Single PEM Fuel Cell

Chapter 9

Conclusions and Future Work

Abbreviations

AC   Alternative current

AFC   Alkaline fuel cell

DETA   Dielectric thermal analysis

DMAc   N,N-dimethyl acetamide

DMFC   Direct methanol fuel cell

DMSO   Dimethylsulphoxide

DRS   Dielectric relaxation spectroscopy

DS   Degree of sulphonation

DSC   Differential scanning calorimetry

DTG   Derivative thermogravimetry

EB   Electron beam

EI   Electrochemical interface

EIS   Electrochemical impedance spectroscopy

FRA   Frequency response analyzer

FEP   Poly(tetrafluoroethylene-hexafluoropropylene)

FTIR   Fourier transformation infra red spectroscopy

GDE   Gas diffusion electrode

GDL   Gas diffusion layer

HN   Havriliak–Negami

IAEA   International Atomic Energy Agency

IEC   Ion exchange capacity

KWW   Kohlrausch-Williams-Watts

LET   Linear energy transfer

LSV   Linear sweep voltammetry

MCFC	Molten carbonate fuel cell
MEA	Membrane electrode assembly
MSA	Methane sulphonic acid
NMP	N-methyl-2-pyrrolidone
NMR	Nuclear magnetic resonance spectroscopy
OCV	Open circuit voltage
PAFC	Phosphoric acid fuel cell
PBI	Poly(2,2`-m-(phenylene)-5,5`-bibenzimidazole), Polybenizimidazole
PEEK	Poly(ether-ether-ketone), Poly (oxy-1.4-phenyleneoxy-1.4-phenylenecarbonyl-1.4-phenylene)
PEI	Poly(ether imide)s
PEM	Proton exchange membrane or polymer electrolyte membrane
PEMFC	Proton exchange membrane fuel cell
PFSA, PSEPVE	Nafion, poly(perfluoro-sulphonylfluoride ethyl-propyl-vinyl ether)
PP	Polypropylene
PS	Polystyrene
PTA	Phosphotungstic acid
SOFC	Solid oxide fuel cell
SPEEK	Sulphonated poly(ether-ether-ketone)
SPSU	Ortho-sulphone-sulphonated poly(ethersulphone)
TG	Thermogravimetry
TMR	Time to reach the maximum rate of the crystallization
TRIM	Transport of ions in matter
TTS	Time-temperature superposition
WLF	Williams-Landel- Ferry

Symbols

a_x	Chemical activity of substance x
b_o	Separation between two adjacent fold planes
$\Delta C_p(T_g)$	Change in the specific heat at T_g
D	Radiation dose, also diffusion coefficient
D_g	Gel dose
E	Activation energy, also Energy of radiation
E^o	Standard theoretical potential
E_{input}	Input energy
E_{theo}	Theoretical cell voltage
E_{useful}	Useful energy
F	Faraday constant (96485 coulombs equivalent^{-1})
$G(S)$	Number of scission occurring per 100 eV (1.6×10^{-17} J) of absorbed energy
$G(X)$	Number of cross link occurring per 100 eV of absorbed energy
ΔG^o	Gibbs free energy
H_l	Heating value of hydrogen (10.8×10^6 J m^{-3})
ΔH_c	Heat of crystallization
ΔH_f	Heat of fusion per unit volume
ΔH_m	Heat of fusion
ΔH_m^0	Heat of fusion for totally crystalline PEEK
ΔH_{rc}	Heat of re-crystallization
ΔH_u	Heat of fusion per repeating unit

I	Current
i	Current density, current per unit area
i_o	Exchange current density
K_g	Nucleation constant
k	Boltzmann constant
l	thickness
M	Atomic or molecular mass of the product or reactant species
n	Reaction order, also Avrami exponent
R	Universal gas constant (8.314 J mole^{-1} K^{-1})
R_{ohm}	Ohmic resistance
p_o	Ratio of main chain breaks to chain units per unit irradiation dose
q_o	Proportion of cross linked units per unit irradiation dose
s	Soluble fraction
T	Absolute temperature
T_c	Crystallization temperature
T_d	Onset of degradation temperature
T_g	Glass transition temperature
T_g^0	Ideal or thermodynamic glass transition
T_m	Melting temperature
T_{max}	Temperature corresponding to maximum
T_m^o	Thermodynamic (equilibrium) melting temperature
T_{rc}	Re-crystallization temperature on cooling
ΔT	Degree of supercooling

t_f	Lifetime
$t_{1/2}$	Half life of the crystallization
$\tan \delta$	Loss tangent
u	Weight average of the initial degree of polymerization
X_c	Cross link density
$X_{c,w}$	Weight degree of crystallinity
X_t	Fractional crystallinity, which has developed at time t
Z	Composite rate constant, also pre-exponential factor
α	Fractional conversion, also Anodic transfer coefficient
Δ	Change in …
ε_o	Absolute permittivity of free space (8.85×10^{-12} F m^{-1})
ε'	Dielectric constant or permittivity
ε''	Loss factor
Φ	Track density (number of ions incident per unit area)
λ	Hydration number
η_{act}	Activation polarization
η_{conc}	Concentration polarization
η_{energy}	Energy efficiency
η_{id}	Ideal efficiency
η_{ohm}	Ohmic polarization
σ	Fold surface free energy, also Conductivity
w	Angular frequency

List of Figures

List of Scheme

List of Tables

Chapter 1

Polymer Electrolyte Membrane Fuel Cells:

Systems and Applications

1.1 Introduction

Polymer electrolyte membranes based fuel cells have reached a technological stage where they offer a real challenge to conventional power generating technologies, particularly for transportation. The first working fuel cell was invented by Sir William Grove in 1843 by reacting oxygen and hydrogen on separate platinum electrodes that were immersed in dilute sulphuric acid inside five cells of a gas voltaic battery and using the current produced to electrolyse water in another similar cell [1-3]. However, fuel cells found their first major application when NASA utilised hydrogen-powered fuel cells to produce electricity and water for the Gemini space missions. The high cost and short lifetimes of fuel cells prevent their use in mass markets.

Unlike internal combustion engines, ICE, fuel cells offer the potential to generate energy very efficiently, without any of the emissions usually associated with combustion. The comparison between fuel cells and batteries is obvious because they serve many of the same applications; however, fuel cells differ from batteries in two distinct characteristics. First, fuel cells are

considered to be energy conversion devices whereas batteries are both energy storage and energy devices. Fuel cells do not need to be recharged with an external source of power such as batteries, they simply need to be replenished or refilled with an appropriate fuel. This brings up the second major difference between batteries and fuel cells; the fuel in a battery is stored internally, whereas a fuel cell stores its fuel externally to its core components.

The hydrogen fuel cell is defined as an electrochemical energy conversion device that converts the chemical energy of burning hydrogen in oxygen into electricity and heat by electrochemical redox reactions at the anode and the cathode of the cell, respectively, and produces water as the only by-product.

The fuel cell has a high-energy conversion efficiency of more than 40–50%. This is more efficient than a coal fired power station or an internal combustion engine. It has no moving parts apart from the air and fuel blowers and is therefore more reliable and less noisy; it has lower maintenance costs and longer operating life compared to an equivalent coal-fired power station or internal combustion engine.

Its modular compact design enables the consumer to increase or decrease power by simply adding or removing modules without having to redesign and reconstruct the whole plant. It is a clean technology and therefore, has very low chemical pollution. It can use pure hydrogen or a variety of primary fuels such as natural gas or methanol that can be used directly or used to produce hydrogen fuel. In a high temperature fuel cell, combined heat and power generation increases efficiency.

There are six main types of fuel cell of commercial importance: the alkaline fuel cell, AFC, the phosphoric acid fuel cell, PAFC; the molten carbonate fuel cell, MCFC; solid oxide fuel cell, SOFC; the proton exchange membrane fuel cell, PEMFC; and the direct methanol fuel cell, DMFC. These major types of fuel cells, classified by the electrolyte, are outlined in Table 1.1[1, 4].

Table 1.1: Types of fuel cells [1, 4].

Fuel cell	Temperature (^{o}C)	Efficiency (%)	Electrolyte
AFC	50-90	50-70	Aqueous solution of potassium hydroxide soaked matrix
PAFC	175-220	40-45	Phosphoric acid soaked in a matrix
MCFC	600-650	50-60	Solution of lithium, sodium and/or potassium carbonates soaked in a matrix
SOFC	800-1000	50-60	Solid zirconium oxide with a small amount of yttrium as Y_2O_3
PEMFC*	60-100	40-50	Solid organic polymer
DMFC*	50-120	25-40	Solid organic polymer

 (*) Sometimes a DMFC is categorised as another type of fuel cell, despite it having the same electrolyte as PEMFC.

Fuel cell technology has drawn most attention because of its simplicity, viability, quick start-up, and the fact that it has been used in almost all conceivable applications.

Table 1.2 [1, 4] shows briefly some of these applications as well as the advantages and disadvantages associated with each.

Table 1.2: Fuel cells application [1, 4].

Fuel cell	Application	Advantages	Disadvantages
AFC	Space application	High efficiency	Intolerant to CO_2 in impure H_2 and air, corrosion and expensive.
PAFC	Stand-alone, combined heat and power	Tolerant to impure H_2, commercial	Low power density, corrosion and sulphur poisoning.
MCFC	Central, stand-alone, combined heat and power	High efficiency, near commercial	Electrolyte instability, corrosion and sulphur poisoning.
SOFC	Central, stand-alone, combined heat and power	High efficiency and direct fossil fuel	High temperature, thermal stress failure and sulphur poisoning.
PEMFC	Vehicle and portable	High power density, low temperature	Intolerant to CO in impure H_2 and expensive.
DMFC	Vehicle and small portable	No reforming, high power density and low temperature	Low efficiency, methanol crossover and poisonous by-product.

4

1.2 Proton Exchange Membrane Fuel Cells

Fuel cells based on the Proton Exchange Membrane, PEM, also known as the Polymer Electrolyte Membrane, are one of several types of fuel cell devices. Figure 1.1 shows the simplest hydrogen fuel cell, H_2-PEMFC, consisting of cathode, anode and PEM.
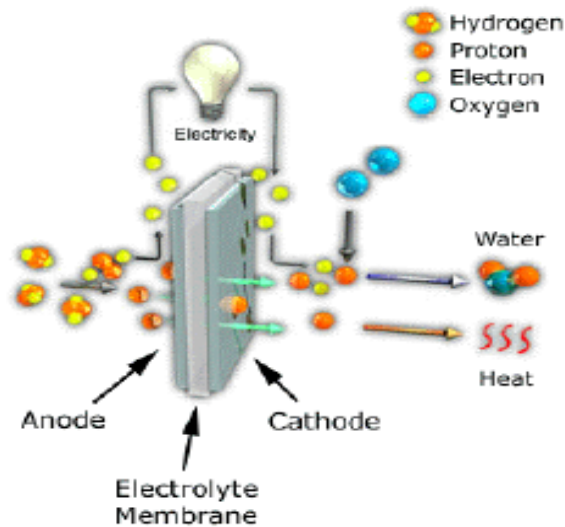
Figure 1.1: Basic description of a PEMFC [5].

The anode and cathode current collector conduct the electrical current and are designed to distribute the H_2 and O_2 evenly to the anode and cathode. These have a porous backing, typically made of carbon, which are electrically conducting and allow the gases to diffuse to the Membrane Electrode Assembly, MEA, which is the heart of the fuel cell [1].

The membrane electrode assembly consists of two electrically and ionically conducting electrodes containing the platinum catalyst bonded to the proton exchange membrane. A schematic of the MEA is shown in Figure 1.2.

The electrodes contain either unsupported as in methanol fuel cells, or supported catalysts as in hydrogen fuel cells and are usually composed of the same copolymer as the proton

5

exchange membrane. The precious metal loading determines the amount of catalyst per active area and can vary between 5-20% weight, depending on the application requirements.
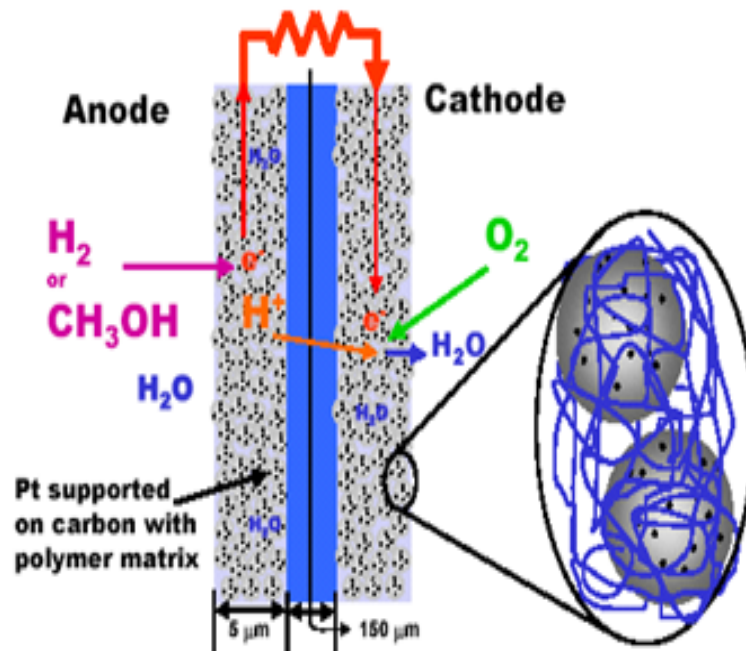
Figure 1.2: The membrane electrode assembly (MEA).

The PEM is coated with a thin catalyst layer, represented by the middle blue area, see Figure 1.2. This consists of nano-size platinum catalyst particles coated onto fine porous carbon particles, which are coated with a very thin layer of polymer electrolyte, typically Nafion a per-fluoro sulphuric acid ionomer.

There are several functions that the PEM must fulfil. These are conduction of protons from the anode to the cathode, act as a support for the catalyst and a barrier for the fuel gases preventing crossover and it must be a non-conductor for electrons, so separating the anode and cathode [1].

1.3 Review on the Nafion Based PEMFC Technology: Achievements and Challenges

For many years, the standard material used for PEM was the per-fluorinated copolymers containing sulphuric acid groups, PFSA. PFSA membranes are composed of carbon-fluorine backbone chains with per-fluoro side chains containing sulphonic acid groups [6]. The sulphonic acid groups are highly acidic due to the effect of the strongly electronegative fluorine atoms that are located next to it. This class of polymers has the trade name Nafion and is manufactured by several companies; but mostly by DuPont™. The chemical structure of PFSA is shown in Figure 1.3 along with the structure parameters which depend on the manufacturer [7].

$$-\left(CF_2 - CF_2\right)_x -\left(CF_2 - CF_2\right)_y -$$
$$\mid$$
$$\left(O - CF_2 - CF\right)_m - O - \left(CF_2\right)_n - SO_3H$$
$$\mid$$
$$CF_3$$
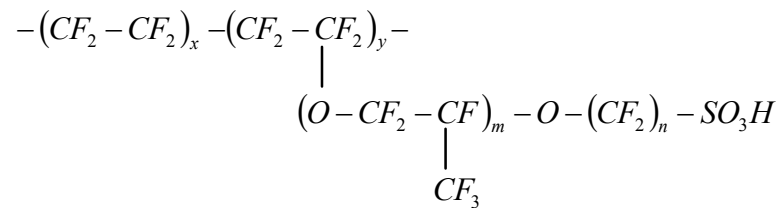
Figure 1.3: Molecular structure of PFSA polymer. The structure parameters are: (m=1; n=2; x=5-13.5, y=1) DuPont, Nafion, (m=0, n=1-5) Asashi Glass, Flemion, (m=0; n=2-5, x=1.5-14) Asashi Chemicals, Aciplex, and (m=0; n=2, x=3.6-10) Dow Chemical, Dow [7].

The side chain ends contain SO_3^- ion and H^+ ion, but because of ionic binding they are associated with SO_3H group. But in the presence of water dissociation occurs with migration of H_3O^+ ion. The group $-CF_2-SO_3H$ is a strong acid and in water is extensively ionized, e.g.,

$$-CF_2 - SO_3H \ \rightleftharpoons \ -CF_2 - SO_3^- + H^+$$
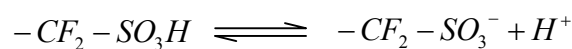
The polymer acts as an ionomer and the ionic nature makes the side chains tend to cluster within the overall structure of the membrane, resulting in two distinct regions. A hydrophobic

region contained the Teflon-like molecular backbone which gives these materials excellent long-term stability to both oxidative and reductive agents. A lifetime of over 60,000 hours has been reported with commercial Nafion membranes [7]. Hydrophilic regions are also created by clusters of the sulphonated side chains. These clusters allow the membranes to absorb relatively large amounts of water, up to 50% by weight and transport of the H^+ ions within the well-hydrated regions results in proton conductivity. These membranes exhibit a protonic conductivity as high as 0.10 $S.cm^{-1}$ under fully hydrated conditions but they dehydrate above 80^oC and cease to conduct protons [1, 2].

The membrane serves, at the same time, as a catalyst support and an effective gas separator. This is achieved by its excellent mechanical properties and low gas permeability [6] . On the other hand, these types of membranes suffer from high crossover rates for methanol as the fuel. In addition to the high price of Nafion (~800 \$ m^{-2}) and the environmental hazards associated with its synthesis and disposal [8, 9]. The following is a brief summary of the achievements and challenges for the PFSA-based PEMFC technologies.

1.3.1 Water Management

At room temperature, Nafion membranes equilibrated with 100% RH water vapour or with liquid water, the drag coefficient was reported to be in the range of 0.9 to 3.2 [6, 7]. Under fuel cell operating conditions, especially at higher temperatures and equilibrated with a water-methanol mixture, these values will be even higher [10, 11].

During operation of a PEMFC, the electro-osmotic drag causes dehydration of the membrane at the anode and leads to a dramatic decrease in conductivity. In addition, increase in the water content results in increased swelling. Conversely reduction in water content leads to shrinkage of the membranes, which in turn leads to deterioration of the membrane-catalyst interface or even a breaking up of the membrane. Therefore, an effective humidification

system of both the fuel and the oxidant is necessary. On the other hand, the presence of water limits the operational temperature to below 100 °C under atmospheric pressure and typically to around 80 °C. Operation of a PEMFC at such a temperature close to the boiling point of water involves a dual-phase water system. When the humidification is too high, water condenses and the gas diffusion electrodes are flooded. Careful management of the water balance is needed and is indeed one of the key issues in fuel cell system design and operation. For high-temperature operation, high water vapour pressures in the feed-gas stream are needed, which in turn require a high total pressure otherwise a low reactant-gas partial pressure results in increased concentration over-potentials. At a partial pressure of 0.5 atm for example, of reactant gases in a water-saturated feed stream, to maintain 90% of the relative humidity at 150 °C requires pressurization to at least 8 atm [7].

1.3.2 The CO Poisoning Effect

Another critical issue related to the low operational temperature is the reduced tolerance to fuel impurities, e.g., CO, in the hydrogen stream. At a typical operational temperature of 80 °C with a PFSA polymer membrane electrolyte fuel cell, a CO content as low as 20 ppm in the fuel stream will result in a significant loss in cell performance. As a consequence very pure hydrogen is needed for the operation of PEMFCs. This poisoning effect has been investigated and shown to be less pronounced at higher temperatures [12, 13].

1.3.3 Direct Hydrogen

When pure hydrogen is used as the fuel in the PEMFC, the cell performance is higher than 0.6 W cm^{-2} under atmospheric pressure or over 1.0 W cm^{-2} at higher pressures. The PEMFC stacks have achieved a power output higher than 1 kW kg^{-1} or 1 kW l^{-1} at a practical cell voltage, e.g., system efficiency above 40%. This technology has weight, volume, and other features which compete with those of the internal-combustion-engine propulsion systems.

However, the industry of new hydrogen infrastructure faces technological problems and economic uncertainties such as compact and lightweight hydrogen storage, hydrogen supply, distribution and refuelling systems [7].

1.3.4 Methanol Reformate

Methanol is an efficient and economical way to bring hydrogen into a fuel cell system because its storage and refuelling needs little infrastructure changes. Currently, methanol is used in an indirect way, e.g., via reforming. The reformate gas contains hydrogen, carbon dioxide, carbon monoxide, and residual water and methanol as well [14-16]. The three overall reactions which can be written for the given reactants and products are shown in Scheme 1.1.

$$CH_3OH + H_2O \underset{k_{-R}}{\overset{k_{+R}}{\rightleftharpoons}} CO_2 + 3H_2 \quad (a)$$

$$CO + H_2O \underset{k_{-W}}{\overset{k_{+W}}{\rightleftharpoons}} CO_2 + H_2 \quad (b)$$

$$CH_3OH \underset{k_{-D}}{\overset{k_{+D}}{\rightleftharpoons}} CO + 2H_2 \quad (c)$$
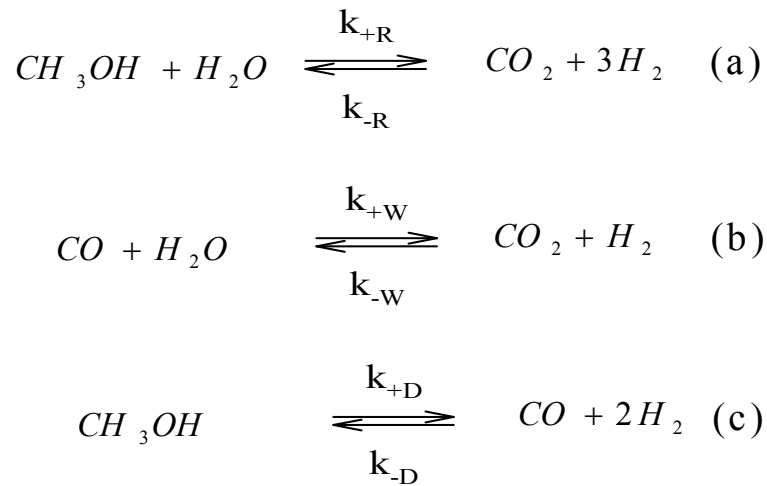
Scheme 1.1: The overall reactions in methanol-stream reforming [15].

where the subscript R refers to stream reforming, W the water-gas shift, WGS, reaction and D refers to decomposition.

As discussed above due to the CO poisoning effect, considerable efforts have been made to develop CO-tolerant catalysts. Among these the Pt-Ru alloys is considered to be the most promising candidates but a significant performance loss is still observed at CO concentration above 100 ppm at 80 °C [17]. Therefore, careful purification of the reformed hydrogen is of

prime importance to remove CO traces. This is carried out by different ways such as the water-gas shift reaction, preferential oxidation, membrane separation, or methanation. In the case of a small dynamic load as in a vehicle, the main challenge for an on-board fuel processing system is the complexity, which produces increased cost, weight, and volume. Such a fuel processing system generally covers 40-50% of the total cost of fuel cell power systems and the CO-cleanup unit accounts for the major increase in weight, volume, and cost of the fuel processing system. A CO-tolerant PEMFC would indeed simplify the power system [7].

1.3.5 Direct Methanol

Direct fuelling with methanol is a preferable option for propulsion of vehicles and other purposes. However, the direct methanol fuel cell (DMFC) technology suffers from two technical challenges [7, 18]. Firstly, the PFSA membranes have a large methanol crossover rate of about 10^{-6} mol cm^{-2} s^{-1}. This corresponds to a performance loss of current density of 50-100 mA cm^{-2}, which results in waste of fuel as well as decrease in energy efficiency and cell performance due to the mixed electrode potential [19].

Secondly, the anodic catalyst is not sufficiently active, leading to a high anodic over-potential loss of 350 mV, compared to 60 mV for hydrogen. The insufficient activity of the anode catalyst is due to the slow kinetics of the methanol oxidation and the strong poisoning effect of the intermediate species (CO) from methanol oxidation. If, however, the fuel processing system is eliminated, it is believed that a power density as low as 0.2 W cm^{-2} at a cell voltage above 0.5 V for a direct methanol fuel cell would be competitive with a power density of 0.5-0.6 W cm^{-2} from a direct hydrogen fuel cell. Such a power density target is difficult to achieve even at high operational pressures (3-5 atm) and high noble metal loadings (2-8 mg cm^{-2}) [7]. Both effects could be considerably improved by increasing the temperature of the DMFC.

1.3.6 Heat Recovery

The heat energy from a PEMFC stack operating at around 80 °C is too low to recover, either for stationary or for mobile applications. If the operational temperature is increased to, say, 200 °C, then steam would be produced at 15 atm from a fuel cell stack. This heat can be directly used for heating so that the overall efficiency would be improved for stationary purposes. It can also be used to operate the system at high pressures or to produce stream for fuel reforming. For stream reforming of both natural gas at 800 °C and methanol at 300 °C, preheating fuels and water up to 200 °C will significantly improve the overall efficiency [7].

1.4 The Need for Developing High Temperature PEM

It follows from the above discussion that most of the problems associated with the PFSA membranes operating at low temperature can be overcome or avoided by developing alternative membranes operational at temperatures higher than 100 °C. Operating the fuel cell at these temperatures results in [7, 20]:

1) The kinetics for both electrode reactions being enhanced. This is more advantageous for the direct oxidation of methanol in DMFC.

2) Operation of PEMFCs involves only a single water phase, e.g., vapour, and therefore the system is simplified.

3) The required cooling system will be simple and technically possible due to the increased temperature gradient between the fuel cell stack and the coolant.

4) The heat can be recovered as stream, which in turn can be used either for direct heating or steam reforming or for pressurized operation. In this way the overall system efficiency is significantly increased.

5) The CO tolerance is increased from 10-20 ppm of CO at 80 °C, to 1000 ppm at 130 °C, and up to 30000 ppm at 200 °C [21]. This makes it possible for a fuel cell system to be directly fuelled with hydrogen from a simple reformer, so that the water-gas-shift reactor, the selective oxidizer, and/ or the membrane separator for the CO cleanup can be eliminated from the fuel processing system.

6) Operating a fuel cell at a temperature around 200 °C allows for integration of the fuel cell with a methanol reformer or a high-capacity hydrogen storage tank as this temperature is close to temperatures for methanol reforming and for hydrogen desorption of the newly developed high capacity storage materials. The integration is expected to give the overall power system advantages including higher efficiency, smaller size, lighter weight, simple construction and operation, and efficient capital and operational cost [22]. High reliability, less maintenance, and better transient response capacities can also be expected as the potential features of the high-temperature PEMFC technology [7].

1.5 High Temperature Polymer Electrolyte Membranes

Generally, there are two directions in the development of PEMs. The first is to synthesize new membranes to substitute PFSA membranes for low-temperature operation due to the high cost and environmental hazards of PFSA. The second is to modify the PFSA or synthesize new classes of high temperature operating PEM. These approaches have generated new materials which have been studied extensively as PEMs for both low and high temperature fuel cell.

The resultant PEMs have been classified into three groups: (1) modified PFSA membranes, (2) alternative sulphonated polymers and their composite membranes, and (3) acid-base polymer membranes [7].

1.5.1 Modification of PFSA Membranes

One disadvantage of PFSA membranes is their low conductivity under low humidification and at elevated temperatures (above 90°C) because of water loss. Considerable efforts have been made to modify the PFSA membranes to achieve high temperature operation by replacing water with non-aqueous and low-volatile materials such as phosphoric acid, organic acids, and aprotic dipolar solvents [7, 20].

Savinell and co-workers [23] incorporated phosphoric acid in Nafion and achieved a conductivity of 0.05 S cm^{-1} at 150 °C. Another group [24] impregnated Nafion-117 membranes with a phosphotungstic acid, PTA, in acetic acid. A high temperature fuel cell performing at 110 °C has been compared to that with the non-impregnated Nafion. Above 110 °C, the acetic acid evaporates.

Improving water management is necessary to simplify the low-temperature operation and also to enable a high temperature operation. The water balance in a PEMFC involves the following mechanisms [7]: (1) water supplied from the fuel and oxidant (humidification); (2) water produced at the cathode (current density); (3) water drag from the anode to the cathode (current density, humidity, temperature); and (4) back-diffusion of water from the cathode to the anode (concentration gradient and capillary forces), see Figure 1.4.
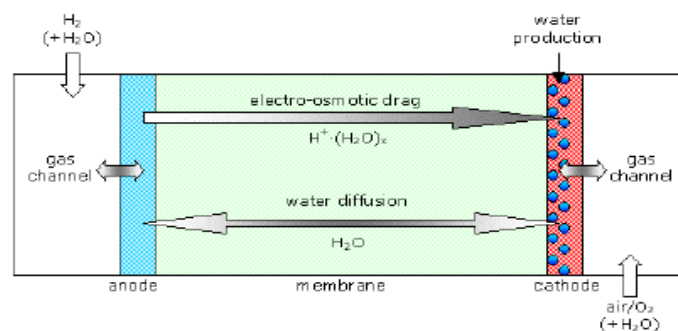
Figure 1.4: Water transport processes in a PEM fuel cell.

To achieve low humidification operation at both low (80 °C) and high (above 100 °C) temperatures, three approaches have been discussed [7].

The first approach is using thinner membranes which lowers the internal resistance, reduces material cost and improves water management during PEMFC operation [25]. On the other hand, increased water content reduces the mechanical strength, especially on swelling and at high temperatures. This can be overcome by the use of composite PFSA membranes with reinforcement such as a porous PTFE sheet or micro PTFE fibrils. By the use of reinforcement, PFSA membranes of 5-30 μm thickness, having good conduction and mechanical properties have been produced. The effective back-diffusion of water from the cathode to the anode side through such thin membranes improves water management and conductivity [7, 20].

The second approach has been to recast Nafion membranes with mixed hygroscopic oxides such as SiO_2 and TiO_2. This is an effective way to achieve low-humidity and high-temperature operation of the PFSA membranes. It has been shown that the water uptake by the oxide-containing membrane is higher than that of the pristine Nafion [26-28]. As a result of the water adsorption on the oxide surface, the back-diffusion of the cathode-produced water is enhanced and the water electro-osmotic drag from anode to cathode is reduced.

The third approach is to incorporate bi-functional particles such as hetero-poly-acids and zirconium phosphate, being both hydrophilic and proton conducting, into the PFSA membranes. This development was aimed at improving the hydration characteristics and raising the operational temperature. The presence of hydrophilic inorganic additives decreases the chemical potential of the water inside the membrane and therefore creates an additional

pathway for proton conduction. At the same time, they provide hydrogen-bonding sites for water in the membrane so that the hydration of the membrane is increased and the transport and evaporation of water will be reduced [27-29]. The enhanced water retention enables low humidification and high temperature operation of both DMFC and H_2/O_2 (air) fuel cells.

1.5.2 Alternative Sulphonated Polymer Membranes and Their Composites

A great number of polymer materials have been prepared and functionalized as membrane electrolytes principally for low temperature PEMFC. Some of these materials, especially the sulphonated hydrocarbons, show interesting features for possible high-temperature operation. The essential requirements for polymer membrane electrolyte materials of PEMFC include (1) proton conductivity; (2) thermal and chemical stability; (3) good mechanical properties (strength, flexibility, and processability); (4) low gas permeability and low water drag; (5) fast kinetics for electrode reactions; and (6) low cost and environmental friendly.

As a starting point these polymers should have high chemical and thermal stability. Two main groups of polymers have been widely investigated for this purpose. One group is polymers containing inorganic elements, e.g., fluorine in fluoro-polymers and silicon in polysiloxanes. The other group is aromatic polymers with phenylene backbones [7, 20, 26].

1.5.2.1 Fluoro-Polymers

An example of this group of polymer is poly (tetrafluoroethylene-hexafluoropropylene), FEP. The FEP film is first irradiated, and then styrene groups are grafted onto it with divinylbenzene, DVB, as a cross linker. The proton conductivity is introduced by sulphonating the aryl groups. Recent work reported a fuel cell lifetime over 5000 hours at 85 °C based on this type of membrane [20].

1.5.2.2 Polysiloxanes

An example of high temperature-resistant polymers is the silicone polymers, such as poly(dimethyl siloxanes). Attempts have been made to develop proton-conducting membranes for fuel cell applications by using arylsulphonic anions or alkylsulphonic anions grafted onto the benzyl group. The poly(benzylsulphonic acid siloxane), structure (1) in Figure 1.5. Membranes can also be cross linked by hydrosilylation, and they have been reported to exhibit a proton conductivity of 10^{-2} S cm^{-1} at room temperature and a thermal stability of the amorphous network up to 200 °C with optical transparency and chemical stability [7, 20].
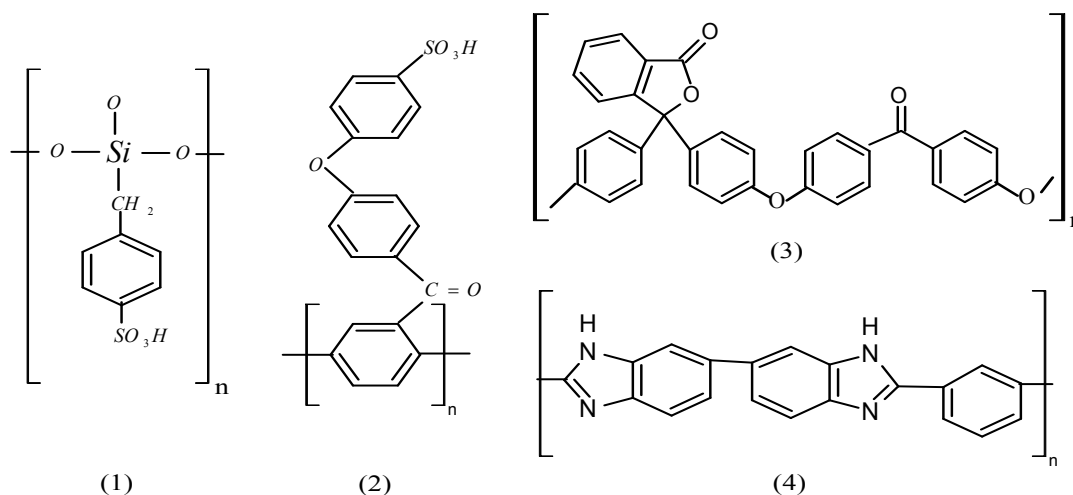
Figure 1.5: The molecular structures of (1) poly(benzylsulphonic acid siloxane), (2) SPPBP, (3) PEEK-WC and (4) PBI.

1.5.2.3 Aromatic Hydrocarbons

Aromatic hydrocarbons represent a large group of polymers which although expensive are available commercially. Here are a few examples including the most widely investigated systems for developing polymer electrolytes membranes for fuel cells.

The poly(aryl ether ketones) are a class of polymers consisting of sequences of ether and carbonyl linkages between phenyl rings, see Figure 1.6.
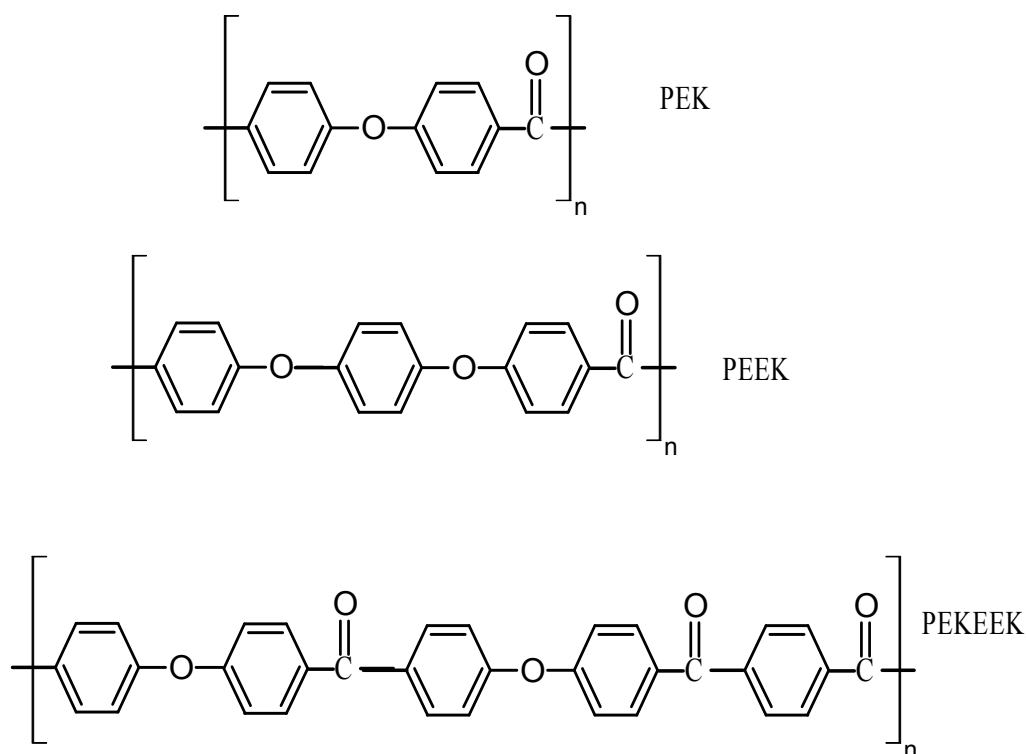
Figure 1.6: The molecular structures of some poly(arylether ketones).

A series of sulphonated poly(arylether ketones) have been developed. The level of sulphonation in this class of materials is dependant on the number of aromatic rings bridged by oxygen atoms as only O-phenyl- O units are sulphonated, while O-phenyl-CO groups remain un-sulphonated. Hence, increasing the proportion of ether groups relative to carbonyl groups leads to an increase in the number of sites available for sulphonation on the poly(aryl ether ketone) backbone.

A sulphonation level of around 60% has been found to be a good compromise between high conductivity and good mechanical properties. The conductivity of this material was found to be high at room temperature (~0.06 S cm^{-1}, compared with 0.1S cm^{-1} for fully hydrated Nafion-117). Durability of at least 4000 hours in a direct hydrogen fuel cell at 50°C has also been demonstrated [7, 20].

A variation on PEEK structure has been achieved by the condensation of phenolphthaleine with 4,4`-dichlorobenzophenone [30, 31] to produce poly(oxa-*p*-phenylene-3,3-phthalido- *p*-phenylene-oxa-*p*-phenylene-oxy-phenylene), PEEK-WC, as shown in Figure 1.5, structure (3). This amorphous polymer has been sulphonated with chlorosulphuric acid ,and sulphuric acid and has been demonstrated to be a good candidate to prepare PEM for fuel cell [32, 33].

Another material is a poly(p-phenylene) derivative, see Figure 1.5, structure (2), and by a direct sulphonation it is reported that a good proton conducting polymer is produced [34]. This material is reported to have higher water uptake and proton conductivity than sulphonated PEEK at an equivalent sulphonation level. The higher water uptake of these materials may be due to the flexible pendant side chains of it. These may also allow the membrane to maintain a more hydrated state above 100°C, giving this material a distinct advantage over Nafion and sulphonated PEEK, whose conductivities drop sharply due to dehydration.

1.5.2.4 Irradiation Application to PEM Synthesis

A relatively low-cost mode of production of proton-exchange membranes involves grafting of ionogenic groups onto a fluorinated polymer matrix. Radiation grafted membranes are produced from commercial films, such as poly(vinylidene fluoride), by irradiation with electron beams or γ rays to generate free radicals in the polymer material. By irradiation in the presence of styrene, grafting side chains of mostly polystyrene, are produced which can be sulphonated.

 It has been reported that the production of such membranes is economically more feasible than that of Nafion. This technique allows modification of fluorinated polymers, but the

resulting products have not been used to make PEMs. Variation in degree of grafting and sulphonation produced quite variable results.

$$-(CH-CH_2)_n-$$

SO$_3$H
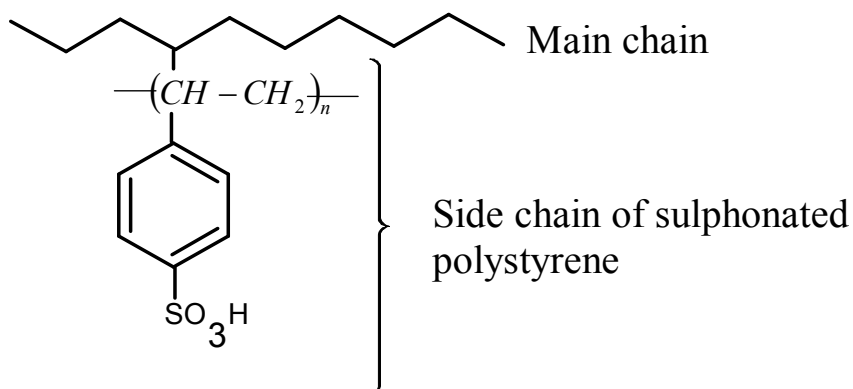
Figure 1.7: Irradiation grafted PEM [35].

Other polymer backbones include PEEK, copolymer of vinylidene fluoride and hexafluoropropylene with different co-monomer content but copolymers of tetrafluoroethylene and hexafluoropropylene have also been used. The proton conductivities of the membranes with a high degree of grafting compare well with those of Nafion membranes (up to 0.11 S cm^{-1} at 100% humidity and room temperature). One disadvantage of such membranes is their greater tendency to swell than that of Nafion membranes [36, 37].

However, because of the degradation of sulphonated polystyrene when used as membranes in fuel cells due to the attack of peroxides formed at the cathode these copolymers show little promise but other graft species have been investigated. Radiation induced grafting of acrylic acid onto poly(tetraflroroethylne-co-hexafluropropylene), FEP, followed by sulphonation produces a membrane having appreciable ionic conductance, acceptable mechanical properties and a stable performance in a fuel cell test up to 100 hr [38].

1.5.3 Acid-Base Polymer Membranes

Acid-base complexation represents an effective approach to the development of proton-conducting membranes. Polymers with basic sites such as ether, alcohol, imine, amide, or imide groups react with strong acids such as phosphoric acid and sulphuric acid. The basicity of the polymers produces hydrogen bonds with acids. In other words, the basic polymers act as a solvent in which the acid undergoes some further dissociation. Because of their unique proton conduction mechanism by self-ionization and self-dehydration, H_3PO_4 and H_2SO_4 exhibit effective proton conductivity even in an anhydrous form. When a basic polymer is present, the interaction between these acids and the polymer through hydrogen bonding or protonation increases the acid dissociation, compared to that of anhydrous acids. A number of basic polymers have been investigated for preparing acid-base electrolytes and the H_3PO_4-doped PBI is one example [39].

Another type of acid-base polymer membranes involves the use of acid-base blends. These blends constitute a new class of proton-conducting membranes with high conductivity, thermal stability, and mechanical flexibility and strength [40].

1.5.3.1 Acid-Doped PBI Membranes

Polybenizimidazole, PBI, structure (4) in Figure 1.5, is an amorphous thermoplastic polymer with a glass transition temperature of 425-436 °C. It has good chemical resistance and excellent textile fibre properties. When doped with acids as well as strong bases a PBI polymeric electrolyte is formed and it has been used as a PEM in a fuel cell membrane electrolytes at temperatures above 100 °C [7, 41].

PBI was cast from N,N-dimethyl acetamide, DMAc, and the film doped with phosphoric acid by immersing in 11 M phosphoric acid at room temperature. The equilibrium uptake is about

21

5 molecules of H$_3$PO$_4$ per repeat unit of PBI; about 2 molecules of phosphoric acid are bonded to each repeat unit of PBI, consistent with the fact that there are two nitrogen sites for the hydrogen bonding to the PBI monomer unit. The rest of the acid is un-bonded "free acid", which can be easily washed out of the system. The conductivity of acid-doped PBI electrolyte was found to be strongly dependent on the acid-doping level, temperature, and atmospheric humidity. An electro-osmotic drag due to the proton transport was observed. It was defined as the number of water molecules which moved with each proton in the absence of a concentration gradient. For PBI membranes, however, the water drag coefficient was found to be close to zero indicating that the conductivity of the acid doped PBI membranes is less demanding on the fuel humidification during the fuel cell operation [7, 20].

1.5.3.2 Acid-Base Polymer Blends

New ionomer blend membranes have been synthesised by ionic cross linking of polymeric nitrogen-containing bases (N-bases) with polymeric sulphonic acids. The sulphonic acid groups interact with the N-bases either to form hydrogen bonds or by protonation of the basic N-sites as shown in Figure 1.8 [40].

$$P-SO_3....H....N-P' \qquad\qquad \cdots\cdots \text{ Hydrogen bonding}$$

$$P-SO_3H+N-P' \rightarrow \left[P-SO_3\right]^- +^+\left[H-N-P'\right] \qquad \text{Protonation}$$
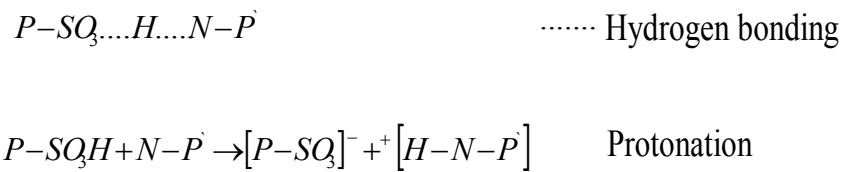
Figure 1.8: Specific interaction in the acid base blends [40].

Examples of this type of membrane blends are those based on sulphonated poly(ether ether ketone), S-PEEK, or *ortho*-sulphone-sulphonated poly(ethersulphone), SPSU, as the acidic component, and polybenzimidazole, PBI, as the basic component.

These membranes show excellent thermal stabilities (decomposition temperatures ranging between 270 and 350°C) and good proton conductivities. Their performance in direct

hydrogen fuel cells at 70°C is similar to that of Nafion-112 membrane. However, only limited durability of around 300h has been demonstrated. In addition to direct hydrogen testing, preliminary studies in DMFCs has shown their suitability for this application and it is reported that their methanol permeability is significantly lower than that of Nafion [42].

1.6 Scope of Research

Among the various polymers, which have been investigated over the past few years, are those based on polyaryls, in particular poly (ether ether ketone). These have shown considerable promise. Attempts to develop these instead of perfluorinated polymers were based mainly on cost and stability of the polymers [8, 9, 34, 43].

Sulphonated PEEK, SPEEK, membranes have been found to be thermally and chemically stable, and to possess high proton conductivity depending on the degree of sulphonation [44-46]. However, there are two problems that appear when operating these fuel cells: there is excessive osmotic swelling which results in low mechanical strength [9, 43]. This mechanical weakness of sulphonated polymers has initiated a number of attempts to develop more stable cross linked materials.

Sulphonated PEEK can be cross linked by using multi-functional cross linking agents, which react with the sulphonic acid groups on the polymer chains [47-51]. In spite of the improvement in mechanical and other properties, there is still a problem associated with the decrease in proton conductivity of the cross linked materials. Some researchers have impregnated the membranes with low molecular weight strong acids, i.e. H_3PO_4, to improve the conductivity [52]. However, these low molecular weight acids are leached out of the membranes over time [51].

Cross linking of PEEK has been reported to occur by thermal, chemical and irradiation methods [53-58]. However, the cross linked materials have not been given full consideration in PEM synthesis due to the fact that cross links limit the degree of sulphonation.

1.6.1 Objectives

The main focus of the present study includes:

- The identification of cross linking methods to modify PEEK and sulphonated PEEK.

- The synthesis of cross linked proton exchange membranes for PEMFC applications, which possess high proton conductivity (of the order of 0.1 S cm^{-1}), high thermal and oxidative stabilities, and mechanically strong and stable in water and methanol.

- Characterisation of the membranes prepared using various characterisation techniques.

- Single fuel cell fabrication from available materials and subsequent testing.

1.6.2 Research Structure

- The cross linking will be carried out using ion irradiation due to availability and effectiveness in altering the properties of PEEK.

- The characterization of irradiated PEEK was carried out to evaluate the effect of cross linking on structural and thermal properties.

- The sulphonation of cross linked PEEK was studied to investigate the effect of cross links in limiting the degree of sulphonation as well as to ascertain the ideal degree of sulphonation required for high conductivity and stability.

- The characterisation of the resultant materials as a candidate proton exchange membrane, PEM, for low temperature fuel cells (FC) will be addressed.

- The cross linking of sulphonated poly(ether ether ketone), SPEEK, using chemical methods based on the reduction of the carbonyl groups will also be addressed.

Chapter 2

Materials, Experimental Techniques and Apparatus

2.1 Materials and Reagents

2.1.1 Poly (perfluoro-sulphonylfluoride ethyl-propyl-vinyl ether), PSEPVE, Nafion^{TM}

Nafion^{TM} membranes are manufactured by several companies; the most well known is DuPont™. They are labeled with a letter N, followed by a 3-or 4- digit number, where the first two numbers indicate equivalent weight divided by 100, and the last digit or two represents the membrane thickness in mills (1mill = 10^{-3} inch = 25.4μm). The material properties of Nafion are summarized in Table 2.1[59].

In the present research, Nafion-112 (51μm) was obtained from Sigma-Aldrich Co., while Nafion-115 (127 μm) was supplied with the PEM cell hardware and purchased from H-Tec UK. Nafion-117 (178μm) was supplied by DuPont.

Table 2.1: Properties of Nafion membranes (from manufacturer data sheet) [59].

Properties	Typical value
Conductivity (S cm^{-1})	0.10*
Available Acid Capacity (meq g^{-1})	0.90*
Total Acid Capacity (meq g^{-1})	0.95 to 1.01
Density (g cm^{-3})	1.98
Water Uptake (%)	38
Tensile Modulus (MPa)	249[a], 114[b], 64[c]
Tensile Strength (MPa)	43[a], 34[b], 25[c]
Elongation at Break (%)	225[a], 200[b], 180[c]

[a]50% RH, 23 °C [b]water soaked, 23 °C [c]water soaked, 100 °C, * minimum value

2.1.2 Poly (oxy-1.4-phenyleneoxy-1.4- phenylenecarbonyl-1.4-phenylene), PEEK

Poly (ether ether ketone), PEEK is a semi-crystalline engineering polymer with outstanding properties. These include good processability, high thermal stability, high mechanical strength, excellent resistance to irradiation and to a wide range of chemical reagents. PEEK is commercially available under two trade names; PEEK Gatone from Garda Chemical Limited, and Victrex PEEK^{TM}. The later was used in this research and was obtained from Goodfellow Ltd. UK. PEEK™ polymer was used in the form of film, powder and granules. A summary of the key physical properties of PEEK used in this research e.g., PEEK 100 μm film, PEEK granules grade G450 and PEEK powder grade P150, is listed in Table 2.2 [60].

Table 2.2: Properties of PEEK materials (from manufacturer data sheet) [60].

Property	Typical value
Density (g cm^{-3}) (amorphous)	1.26
(crystalline)	1.32
Glass Transition Temperature (^{o}C)	143
Melting Temperature (^{o}C)	343
Melt Viscosity(kN s m^{-2}) (P150)	0.135
(G450)	0.468
Tensile Modulus (GPa)	3.5
Tensile Strength (MPa)	97 at 23 ^{o}C
Elongation at Break (%)	Up to 60%
Dielectric Strength (kV cm^{-1})	190 (film of 0.002 in)
Dielectric Constant (50 Hz, 0-150 ^{o}C)	3.2
(50 Hz, 200 ^{o}C)	4.5
Loss Factor	0.003
Volume Resistivity (10^{16} Ω cm)	4.9

2.1.3 Solvents

Methane sulphonic acid, MSA, was used as a solvent for PEEK and a swelling agent for cross linked PEEK. Dimethylformamide (DMF, b.p. 153 ^{o}C), dimethylacetamide (DMAc, b.p. 165 ^{o}C) were used to cast films of sulphonated PEEK for PEM preparation. Methanol was also used as solvent for highly sulphonated PEEK and as a rinsing agent. They were obtained as a reagent grade from Sigma-Aldrich Co. and used without further purification.

2.1.4 Reagents

Concentrated sulphuric acid (H_2SO_4), Sigma-Aldrich 97.5%, was used as a solvent and sulphonating agent for PEEK and a swelling agent for cross linked PEEK.

Aqueous solution of hydrogen peroxide H_2O_2 (3-30%) and ferrous sulphate $FeSO_4.7H_2O$ (4-30 ppm) obtained from Sigma-Aldrich, is well known as Fenton's reagent. It was used to determine the stability of the membranes to oxidation.

Sodium hydroxide, hydrochloric acid (35.5%) and phenolphthalein indicator were used to determine the ion exchange capacity of sulphonated PEEK.

Sodium borohydride $NaBH_4$, used as cross linking agent for sulphonated PEEK, was obtained from Sigma-Aldrich Co. and used as received.

2.2 Experimental Procedures and Apparatus

2.2.1 Cross Linking of PEEK

2.2.1.1 Ion irradiation

Irradiation was carried out using the University of Birmingham's Scanditronix MC40 Cyclotron. For this work, either a 11.7 or 12.5 MeV proton beam and 30.0 or 33.0 MeV helium ions were used. In each case, the beam passed through a 30 micron Havar window, then about 40 mm of air, followed by a stack of PEEK foils which was mounted in air in a water-cooled holder. The beam was defocused on to a spot size of approximately 10 mm in diameter and scanned over an area of up to 32×32 mm^2 by applying saw-tooth wave forms to the inputs of a pair of steering magnets. This experimental setup is shown in Figure 2.1.
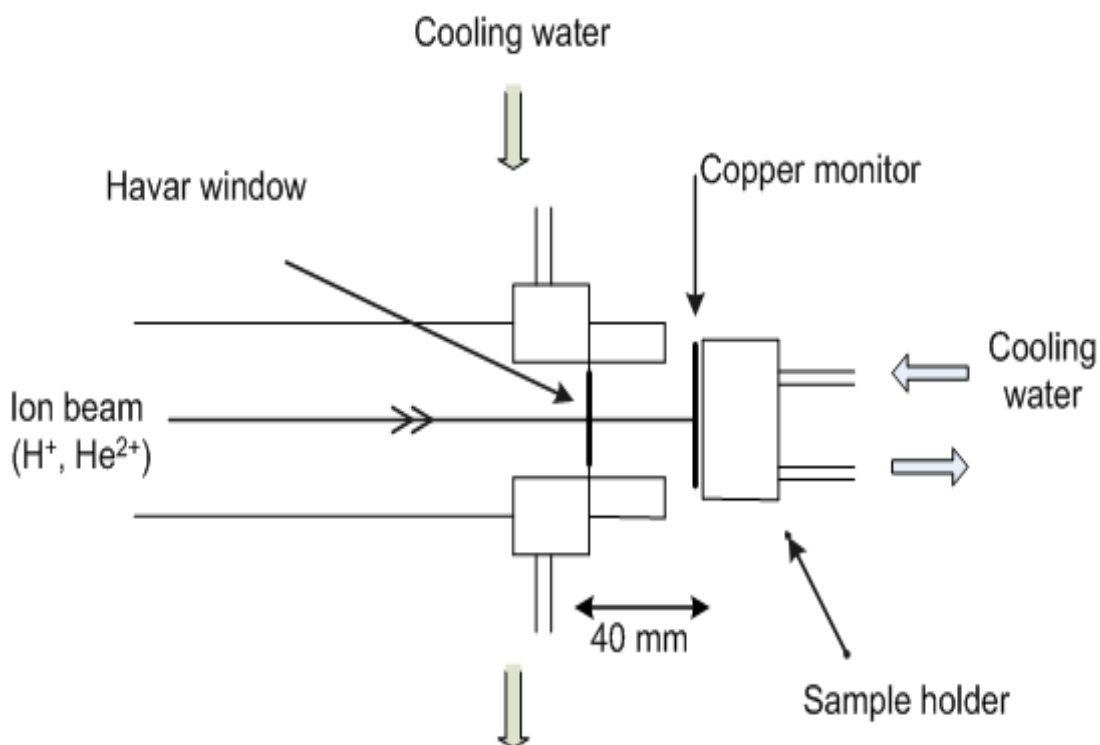
Figure 2.1: Schematic diagram of the ion irradiation equipment.

After allowing for the energy lost in the Havar window and the air gap, the energy of the protons incident on the first foil was calculated to be 11.0 or 11.2 MeV. The flux of helium ion irradiation was 200 nA and the incident energy on the first PEEK foil was 25.6 MeV. Generally, ion irradiation times varied from 10 to 130 minutes depending on the required dose.

The penetration ranges of 11.0 MeV protons and 25.6 MeV He^{2+} ions in amorphous PEEK were approximately 1.2 and 0.45 mm respectively, so a stack of 10 and 4 foils, each 100μm thick, covers almost the entire energy range for 11.0 MeV H^+ and 25.6 MeV He^{2+} respectively. The stopping power and projected range of PEEK for H^+ and He^{2+} ions were calculated using the TRIM89 code (version 92.12). Table 2.3 shows the ion energy on entry to each foil, and the stopping power in that foil.

2.2.1.2 Dosimetry

The absorbed dose, D (MGy), was calculated using the following equation [61]:

$$D = S \times \frac{Q}{Z_{inc}}$$ (2.1)

where S is the mass stopping power of the material (MeV m^2 kg^{-1}), Q is the fluence (C m^{-2}) and Z_{inc} is the charge number of the incident ion. The absorbed dose of the first PEEK layer was calculated based on the incident energy and those of the other PEEK layers were calculated based on the inlet energy after the ions had passed through the previous layer.

In some of the irradiation experiments, the total fluence was measured from the integrated charge entering the foil holder. The size of the irradiated area was determined by inspection of the irradiated foils, which are discoloured by the beam, and hence the flux (ions per unit area) was determined, assuming that the discoloured area was uniformly irradiated.

Table 2.3: Stopping power and projected range

(a) He^{2+} ions.

Layer No.	Energy at surface (MeV)	Stopping power (MeV m^2 kg^{-1})	Projected range (×10^{-3} m)
1	25.6	25.2	0.455
2	22.4	28.0	0.355
3	18.9	32.0	0.255
4	14.9	38.6	0.155

(b) H^+ ions.

Layer No.	Energy at surface (MeV)	Stopping power (MeV m^2 kg^{-1})	Projected range (×10^{-3} m)
1	11.0	4.10	1.200
2	10.5	4.24	1.100
3	10.0	4.42	1.010
4	9.4	4.63	0.905
5	8.8	4.87	0.809
6	8.2	5.16	0.710
7	7.6	5.51	0.620
8	6.9	5.96	0.522
9	6.1	6.54	0.420
10	5.3	7.34	0.327

This approach provides no indication of the uniformity of irradiation and suffers from errors in absolute charge collection due to escape of secondary electrons. Therefore, a 25 μm copper monitor was used; see Figure 2.1. In this case the Zn-65 activity produced in the copper monitor foil was used to determine the fluence. The Zn-65 yield was evaluated by detecting the characteristic 1115 keV gamma rays using an HPGe detector whose efficiency had previously been determined. The yield Y (atoms) in mass M of copper was converted to a fluence of incident ions using the relation

$$Y = \frac{Q.M}{e.m} \times \sigma \qquad\qquad (2.2)$$

where m is the mass of each copper atom, e is the charge carried by each ion, and σ is the cross section of the nuclear reaction. Based on the evaluated cross sections published by the

IAEA [62], values of $\sigma = 200$ mb (2.0×10^{-29} m^2) for the H$^+$ reaction and 650 mb (6.5×10^{-29} m^2) for the He^{2+} reaction were used.

Initially, the average flux over the whole area (32mm x 32mm) was determined, then the sample was cut into sixteen separate squares, each approximately 8mm x 8mm, and the flux was also determined in each. Any differences in area were allowed for by weighing the individual copper squares to determine their masses M. Table 2.4 summarizes the results obtained using this procedure.

2.2.1.3 Irradiation Cost

The operating cost for the MC-40 was estimated by Prof. D. J. Parker, a member of the School of Physics and Astronomy, The University of Birmingham, to be 200 £ h^{-1}. This charge included irradiation type, energy and any other additional experimental conditions such as cooling. It must be mentioned that irradiation experiments in this research were carried out free of charge.

Table 2.4: Irradiation dose evaluation.

Irradiation	Proton	Helium
Individual fluence range, (C m^{-2})	7.8 – 10.9	2.6-4.6
Average fluence over the whole irradiated area,(C m^{-2})	9.4	3.4
Standard deviation	0.9	0.7
Dose at first PEEK layer, (MGy)	37.9 ± 3.6	42.9 ± 8.8

2.2.2 Gel Content Measurement

The gel content of the irradiated films was determined by immersing samples (~10 mg) in 10 cm^3 of MSA at room temperature for 24 h. At the end of this period, the solvent was

decanted; the remaining gel was thoroughly washed in distilled water and methanol, and left to dry in air for 24 h and in a vacuum oven for at least 12 h at 60 $^{\text{o}}$C before finally being weighed. Gel percentages were calculated using the following equation:

$$\% \, Gel = \frac{m}{m_0} \times 100 \qquad\qquad (2.3)$$

where m_0 and m are the masses of samples before and after extraction, respectively.

2.2.3 Sulphonation Reaction

The sulphonation of PEEK, G450, was carried out using a three necked round bottom flask in air using two procedures: samples of PEEK were dried in a vacuum oven at 130°C for 48 h and other samples were used as received. Both were reacted at a concentration of 2.4 w/v % of polymer in concentrated H_2SO_4 at 20°C. The desired amount of PEEK was added to 700 cm^3 of concentrated H_2SO_4 and the solution stirred mechanically. In order to study the effect of time on the extent of sulphonation samples of 100 cm^3 of this solution were precipitated after 24, 48, 72, 96, 120, 144 and 168 h by drop-wise addition of the solution to 500 cm^3 of ice cooled distilled water. The samples were washed until the excess acid was removed, dried in air for 48 h and finally in an oven at 40°C for 24 h.

Similar experiments were carried out on other PEEK samples namely P150 and PEEK film. PEEK is soluble in concentrated sulphuric acid [63], and also sulphuric acid acted as a swelling and sulphonating agent for cross linked PEEK. Sulphonation of the cross linked PEEK was carried out using 100 μm films (about 7mg). The film was removed after various reaction times, washed with water and weighted. The change in weight, %Δ, was measured from the following equation:

$$\%\Delta = \frac{w_{sul} - w_{init}}{w_{init}} \times 100\% \qquad (2.4)$$

where w_{sul} and w_{init} are the dried weight of the sulphonated and initial samples [64]. The

conditions for each PEEK sample and sulphonation experiment are summarized in Figure 2.2.
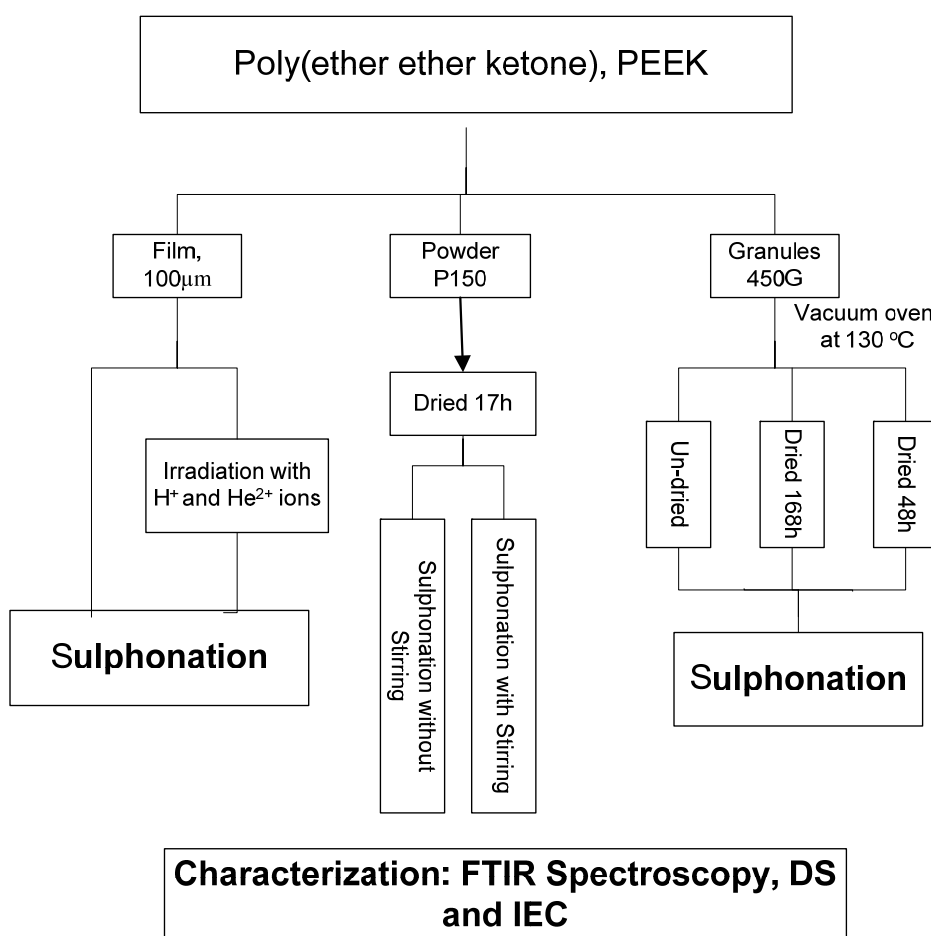
Figure 2.2: Schematic diagram of the preparation of sulphonated PEEK.

2.2.4 Sulphonated PEEK; Membranes Casting and Cross Linking

In the present work, films were obtained by casting a 2.4 % SPEEK solution in DMAc on

glass Petri dishes followed by drying at room temperature in a fume cupboard for several days

and finally in vacuum oven at 120° C for 24 h. The membranes were removed by submerging

in distilled water, and carefully peeled from the dishes using tweezers. They were then washed with distilled water before drying again in vacuum oven at 120° C for another 24 h. The thickness of the membranes was in the range 30 to 80 μm.

The choice of the solvent DMAc was based on the film properties since the use of DMF lead to opaque films and films obtained from methanol solution were mechanically weak.

Two different methods for cross linking SPEEK were investigated. First the films were thermally treated at 120 $^{\circ}$C in a vacuum oven for various periods. The second approach involved the use of different amounts of sodium borohydride as a reducing agent followed by thermal treatment.

2.2.5 Ion Exchange Capacity, IEC and Degree of Sulphonation, DS

A weighed amount of the SPEEK polymer was dissolved in 10 cm^3 of DMF and the solution titrated against standard 0.1N NaOH using phenolphthalein as an indicator. The volume of alkali required to change the indicator to red using 10 cm^3 of DMF was subtracted from all results (V_R = 0.1 cm^3). This procedure was used rather than soaking the polymer in excess sodium hydroxide solution overnight and titrating against HCl. This method proved to be irreproducible.

The ion exchange capacity, IEC, of SPEEK expressed in meq g^{-1} is given by the equation:

$$IEC = \frac{N(V_S - V_R)}{W} \tag{2.5}$$

where V_S, V_R are the NaOH volume in cm^3 taken in the titration of the sample and reference respectively and W is the weight of dry polymer in g.

The sulphonation degree, DS, is defined as the ratio of the moles of sulphonated PEEK units, N $_{SPEEK}$, to that of the total moles of sulphonated PEEK and un-sulphonated units of PEEK, N $_{PEEK}$, such that,

$$DS\% = \frac{N_{SPEEK}}{N_{SPEEK} + N_{PEEK}} \times 100 \qquad (2.6)$$

N $_{SPEEK}$ was obtained from the IEC, such that

$$N_{SPEEK} = 10^{-3} \times W \times IEC \qquad (2.7)$$

and N $_{PEEK}$ from the expression,

$$N_{PEEK} = \frac{W - (M_{SPEEK} \times N_{SPEEK})}{M_{PEEK}} \qquad (2.8)$$

where W was the polymer dried weight in g, M $_{SPEEK}$ and M $_{PEEK}$ were the molecular weights of the repeat units of sulphonated PEEK and PEEK, (368 and 288 g respectively). For SPEEK samples that did not dissolve in DMF as well as for the cross linked SPEEK samples, the IEC was determined by FTIR spectroscopy, discussed later.

2.2.6 Water Uptake, Hydration Number and Swelling Ratio

SPEEK film samples were dried at 120° C for 24 h, and the dried polymer films immersed in water at three different temperatures, namely 23, 50 and 70±2 ^{o}C. The water uptake was determined by removing samples after various times ranging from 0 to 900 hrs, drying off the surface water using a filter paper and weighting. The water uptake was calculated from the following equation,

$$WaterUptake\% = \frac{W_2 - W_1}{W_1} \times 100 \qquad (2.9)$$

where, W_2 and W_1 were the masses of the sample in water and the initial dried sample respectively.

The hydration number, λ, e.g., the number of water molecules absorbed per sulphonic acid unit present was calculated from the mass of water absorbed and the ion content of the dry copolymer, such that

$$\lambda = \frac{(W_2 - W_1)/M_{H_2O}}{IEC \times W_1}$$
(2.10)

where M_{H_2O} is the molecular weight of water (18.01 g mol^{-1}), W_2 and W_1 are as above and

IEC is the ion exchange capacity of the dry copolymer in equivalents per gram [65].

The swelling ratio was calculated from films 5 cm long and 1cm in width from the equation:

$$Swelling\ Ratio\ \% = \frac{L_{wet} - L_{dry}}{L_{dry}} \times 100$$
(2.11)

where L_{dry} and L_{wet} are the lengths of dry and wet films, respectively [66].

2.2.7 Oxidative Stability of PEM; Fenton Test

Currently the stability of fuel cell membranes to oxidation is assessed approximately using the Fenton test: the membrane is soaked in an aqueous solution of H_2O_2 (3-30%) and $FeSO_4$ (4-30 ppm), and membrane stability measured in terms of weight loss as a function of immersion time and time required for the membrane to break up or to begin to dissolve. In the present work, the oxidative stability was determined at 25 $^{\circ}$C using a solution of 30% H_2O_2 and 4ppm $FeSO_4$.

2.2.8 FT-IR Spectroscopy

2.2.8.1 Theory

Infrared spectroscopy is one of the most important and widespread structural characterisation methods used in polymer science. Infra-red absorbance is due to the interaction of the electric field vector with the molecule dipole transition moments due to molecular vibrations and the absorption of quanta of light.

Individual bonds may absorb at more than one frequency due to the fact that each covalent bond may vibrate in several modes, such as stretching or bending. Although, bending absorption is very weak it is useful in differentiating similar type of bonds in particular substituents on aromatic rings. It is also important to note that symmetrical vibrations do not absorb in the IR region. In general, bond order and the type of atoms joined by the bond are the most important factors in determining the frequency at which a chemical bond will absorb. Conjugation and nearby atoms also change the frequency that a specific bond absorbs. Therefore, the same or similar functional group in different molecules will typically absorb within the same and specific frequency range [67-69].

Hooke's law states that the IR frequency at which a chemical bond absorbs is inversely proportional to the square root of the reduced mass of the bonded atoms, such that

$$v = \frac{1}{2\pi} \sqrt{\frac{k}{\mu}} \tag{2.12}$$

where v is the wave number in cm^{-1}, μ is the reduced mass, $\dfrac{m_1 m_2}{m_1 + m_2}$, in which m_1 and m_2 are the atomic masses of two elements which makes the bond and k is the force constant.

The complex lower region below 1000 cm^{-1} is known as the fingerprint region because almost every organic compound produces a unique pattern in this area, therefore identity can often be confirmed by comparison of this region to a known spectrum [68, 69].

The % transmission is simply the intensity of sample beam (I_t) divided by the intensity of reference beam, I_0, e.g.

$$\%T = \frac{I_t}{I_0} \times 100 \tag{2.13}$$

A more useful parameter for quantitative work is the absorbance, A, or optical density, O.D., of a band,

$$A = \log \frac{I_0}{I_t} = \log \frac{1}{T} = 2 - \log \%T \qquad (2.14)$$

The transmission data (percent) is converted to absorbance data using eq. (2.14).

2.2.8.2 Experimental Procedure

The equipment employed for infrared spectroscopy experiments was a Nicolet Magna-IR 860 ESP spectrophotometer. An attenuated total reflectance, ATR, attachment was used with a Golden Gate Accessory and a DTGS detector. All spectra were recorded from 600-3800 cm^{-1} at a resolution of 2cm^{-1} and total of 200 scans accumulated for each. A background absorption spectrum was taken after each run and subtracted from the sample spectrum.

2.2.9 Differential Scanning Calorimetry, DSC

2.2.9.1 Theory

Differential scanning calorimetry, DSC, is one of the most widely used thermal analysis techniques to determine the thermodynamic properties of polymers. DSC measures the temperatures and heat flow associated with transitions in materials as a function of time and temperature. The technique provides qualitative and quantitative information about physical and chemical changes that involve endothermic or exothermic processes or changes in heat capacity using minimal amounts of sample. It has many advantages including fast analysis time, easy sample preparation, applicability to liquids and solids, a wide range of temperature and excellent quantitative capability [70].

DSC can be used to determine the glass transitions, melting point, degree of crystallinity, heats of fusion and reactions and specific heat and heat capacity. It is also used to study crystallization and reaction kinetics, as well as oxidative and thermal stabilities.
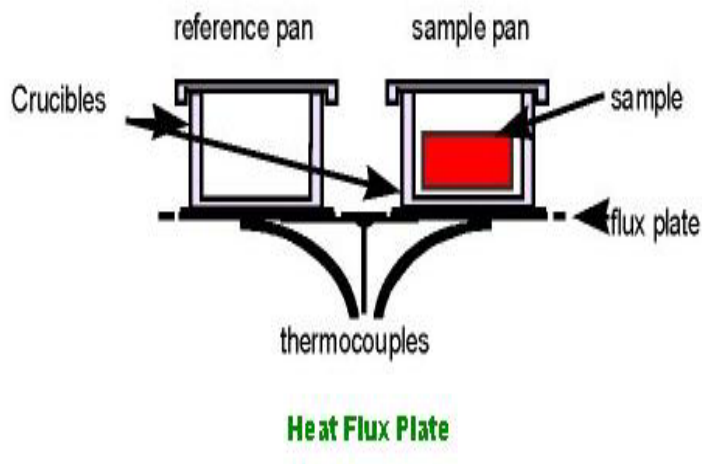
Figure 2.3: The DSC head.

2.2.9.2 Experimental Procedure

2.2.9.2.1 Characterization of Cross Linked PEEK

The thermal properties of the PEEK samples (7 ± 1 mg) were measured using a Perkin-Elmer differential scanning calorimeter, DSC-7. Measurements were carried out in argon at a flow rate of 20 cm^3 min^{-1} and heating and cooling rates of 20°C min^{-1}. The first heating scan was performed from 50 to 360°C by which temperature PEEK had completely melted. A cooling scan was subsequently performed from 360°C to the start temperature followed by a second heating run to 360 $^{\circ}$C.

The glass transition temperature, T_g, was determined from the midpoint of the inflection of the specific heat plot with temperature, using PYRIS software.

A baseline was established for the instrument using two empty aluminium DSC pans. This baseline allowed for the correction of heat flow variation due to the equipment by subtracting the baseline heat flow from the sample heat flow. Temperature and enthalpy calibrations were

carried out using ultra pure metal standards: indium (m.pt: 429.78 K, ΔH_f = 29.2 J g^{-1}), tin (m.pt: 505.06 K) and lead (m.pt: 600.65 K).

A DSC-2 equipped with a water-cooled jacket was used to study isothermal crystallization adopting procedures developed previously for the study of the crystallization and melting of PEEK [71]. Isothermal crystallization was performed at a sensitivity of 8.3mW under Argon flow of 20 cm^3 min^{-1}. Initially the samples were heated to 650 K at 320 K min^{-1} and held at this temperature for 5 min to ensure complete melting. The samples were then cooled to the crystallization temperate at 160 K min^{-1} and the rate of crystallization followed with time isothermally until the calorimeter response returned to the baseline. The melting endotherm was then determined from the heating run after each complete crystallization.

2.2.9.2.2 State of Water in PEMs

A Perkin-Elmer differential scanning calorimeter, DSC-7, was used to determine the amount of freezing and non freezing waters present in the polymer samples. Measurements were carried out at heating and cooling rates of 5 ^{o}C min^{-1} in the temperature range from -35 to 15°C. Temperature and enthalpy calibrations were carried out using ultra pure metal standard: indium (m.pt: 429.78 K, ΔH_f = 29.2 J g^{-1}).

The weight of freezable water was calculated assuming that the heat of fusion of free water in the PEMs was the same as that of the ice (322 J g^{-1}), e.g.

$$w_b = w_t - \left(w_f + w_{fb}\right) = w_t - \frac{\Delta H_f}{\Delta H_{ice}}$$

(2.15)

where W_t is the total water content in g; W_b is the amount of bound water in g; W_f and W_{fb} are the amounts of free water and bound water in g, respectively. ΔH_f and ΔH_{ice} are the heat of fusion, J g^{-1}, of free water in sample and that of ice respectively [72].

41

2.2.10 Thermogravimetric Analysis, TGA

2.2.10.1 Theory

This technique measures the weight of a sample as a function of temperature (or time) under a controlled atmosphere. The mass is recorded using a highly sensitive electronic microbalance. TGA is commonly used to determine polymer degradation temperatures, residual solvent levels, absorbed moisture content, and the amount of inorganic (non-combustible) filler in polymer or composite material.

TGA tests can be carried out in a dynamic mode at some controlled heating rate, or isothermally, in a flowing inert or oxidative gas atmosphere. Typical weight loss profiles are analyzed for the fractional or percent weight loss at any temperature, the fractional or percent of non-combusted residue at some final temperature, and the temperatures of sample degradation processes. It is also possible to evaluate the thermal degradation kinetics and predict materials life time [73].

2.2.10.2 Experimental Procedure

2.2.10.2.1 Thermal Degradation Kinetics of Cross Linked PEEK

Thermal degradation measurements were carried out using a Netzsch Jupiter STA 449C. This consisted of a thermobalance, temperature control unit and PC which was used to store and analyze the weight loss-temperature data. Samples of 5.0±0.5 mg were used and the thermal decomposition was carried out in an inert atmosphere of argon at a flow rate of 100 cm^3 min^{-1} over a temperature range of 75 to 850 ^{o}C at a constant heating rate of 10 ^{o}C min^{-1}. A baseline correction was made before each experiment by operating the TG analyzer using two empty ceramic crucibles and scanning over the same temperature range. In polymer degradation kinetics, the weight fraction conversion, α, was defined as,

$$\alpha = \frac{W_0 - W_t}{W_0 - W_\infty} \tag{2.16}$$

where W_0, W_t and W_∞ are the initial weight of the sample, at a given temperature or time t and the final weight in mg.

2.2.10.2.2 Thermal Stability of PEMs

Dry samples of the sulphonated polymer (5±0.5mg) were analyzed in flowing argon or air atmospheres at rate of 100 or 75 cm^3 min^{-1}, and over a temperature range 30 to 850 ^oC, at a heating rate of 10^oC min^{-1}.

2.2.11 Fuel Cell Systems and Testing

2.2.11.1 Junior Basic Fuel Cell System

The working fuel cell, shown in Figure 2.4, and attachments were obtained from H-tec with a range of accessories which included decade resistors, 2 multimeters and a lamp to activate the solar module. The PEMFC could be dismantled and used to test different membranes for comparison purposes, see Figure 2.5.
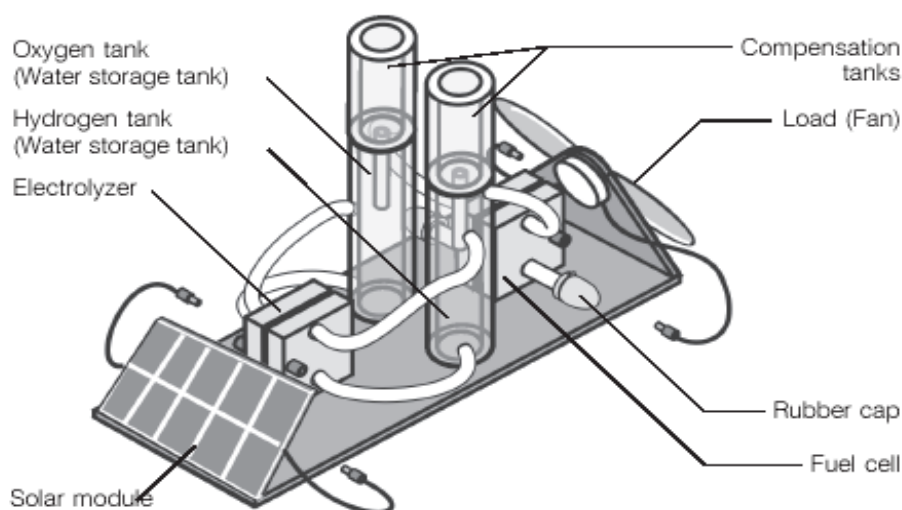
Figure 2.4: View of Junior Basic fuel cell system (H-tec)[74].

43
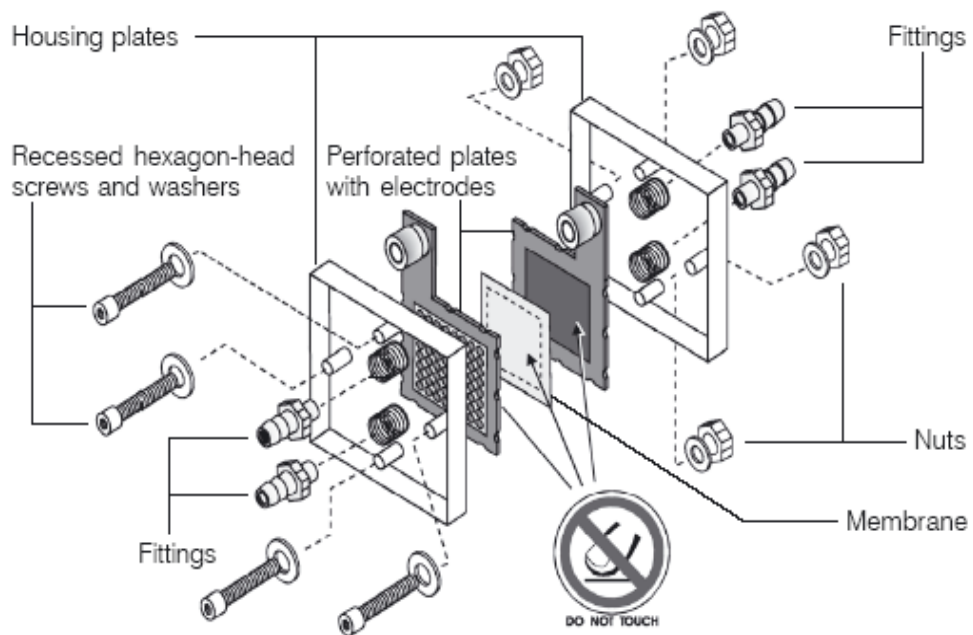
Figure 2.5: View of PEMFC Kit (H-tec)[74].

2.2.11.2 Testing of PEM in Fuel Cell

All measurements were carried out using the fuel cell connected in the circuit as shown in Figure 2.6.
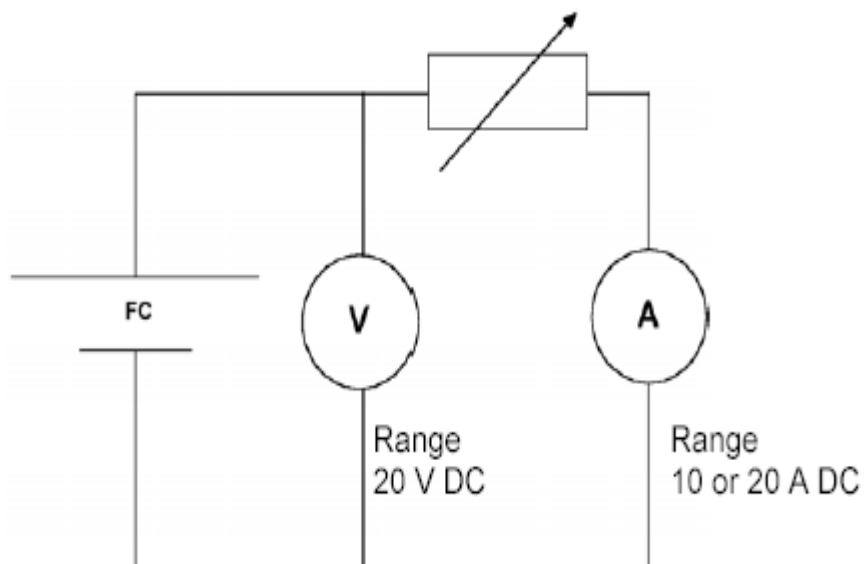
Figure 2.6: Setup for fuel cell testing (FC=fuel cell) [74].

The performance of a PEM fuel cell was characterized by the following measurements:

2.2.11.2.1 Voltage-Current Density Relationship

The output of the fuel cell depends on the external load resistance of the circuit and this was determined by changing the resistance and measuring the current at optimum power yield. The current-voltage characteristics were recorded with open circuit voltage and then by decreasing the resistance to smaller values. Approximately 20 s was allowed to elapse between each reading and each experiment was repeated three times. The mean values were taken with standard deviation.

2.2.11.2.2 Efficiency

The efficiency of the fuel cell in the circuit was measured with the apparatus set to produce the optimum power yield. The hydrogen consumption was recorded with time along with the current and voltage values.

The effect of temperature on the PEM fuel cell performance was carried out with a homemade cell placed in a furnace where temperature could be varied in the range 30 to 120 $^{\circ}$C.

2.2.11.3 Building the K18 Hard Graphite Fuel Cell

The individual components of a single-cell are shown in Figure 2.7.
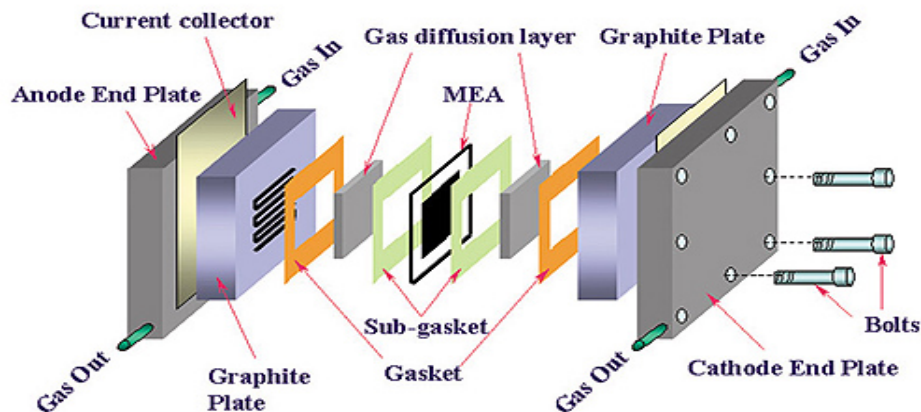
Figure 2.7: Components of a single fuel cell [75].

The Membrane Electrode Assembly, MEA, consists of a polymer electrolyte membrane, the anode and cathode catalyst layers and the anode and cathode gas diffusion layer, GDL. When the electrocatalyst is directly applied to the GDL as opposed to the membrane, the resulting electrode is often referred to as a gas diffusion electrode, GDE. The electrodes contain either an unsupported e.g. the methanol fuel cell or a supported, e.g. a hydrogen fuel cell catalysts and are usually composed of the same copolymer as the proton exchange membrane. The precious metal loading is determined by the amount of catalyst per active area and the ionomer content of the electrode can vary between 5-20 weight percent, depending on the application's requirements.

A 5 layers MEA was purchased from Fuel Cell Store for the incorporation in the cell, consisting of Nafion-112 and catalyst loading of 0.5 mg cm^{-2} on the cathode side and 0.2 mg cm^{-2} on the anode.

Edge gaskets on either side of the MEA provide a gas-tight seal between the flow channel and the membrane upon compression. The seal prevents reactant gases from leaking from the cell or crossing over from one electrode to the other. Gaskets are often made from polytetrafluoroethylene, PTFE, sheets or PTFE-filled fibre glass fabric. Silicon rubber gaskets were used. This was obtained as a sheet of 0.5 cm thick and was used up to temperatures as high as 120 $^{\circ}$C.

The flow channels deliver reactant gases to the GDL, and because they have to be good thermal and electrical conductors, they are made of graphite. Hard graphite was obtained as a sheet of 0.5 cm thickness. The flow channels were drilled in the School of Metallurgy and Materials workshop, Figure 2.8.

Figure 2.8: Hard graphite flow channels [76].

Current collector plates, Figure 2.9, made from copper, gold coated to prevent corrosion, were located on the backside of the graphite flow channels; the cell leads and voltammeter leads were connected to these plates [76].
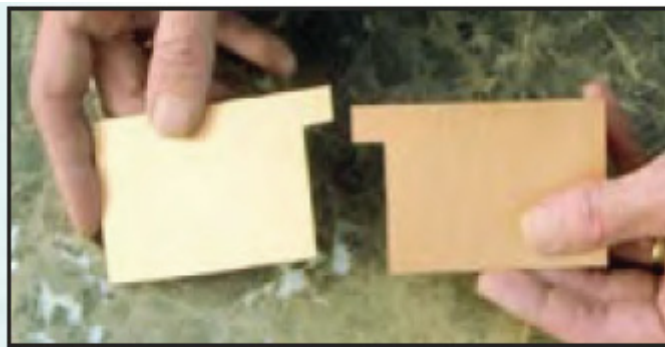
Figure 2.9: Current collector Gold coated Copper plates [76].

Finally, the end plates were torqued together to provide mechanical compression and connection of the fuel cell components, to seal the cell to inhibit gas leaks, and to reduce contact resistances. The end plates were fabricated in the School workshop from 1.5 cm thick aluminum. The gas inlet and outlet were drilled into both sides of the end plate and the screws used to hold all components together.

Figure 2.10 shows the end product; the K18 hard graphite fuel cell.
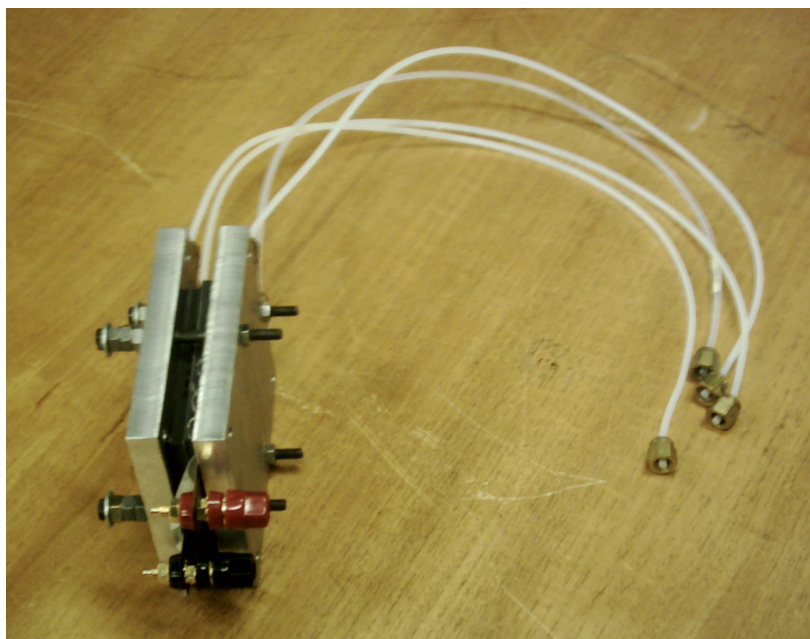
Figure 2.10: The K18 hard graphite fuel cell.

2.2.11.4 The K18 Fuel Cell; Testing and Further Developments

The home made fuel cell was initially tested using the 5 layers MEA and the H-tec solar system using the same setup as outlined in Figure 2.6. The performance deteriorated after a few minutes due to gas leakage. This was overcome by adding another gasket between the end plates and the graphite layers. However, the performance was not as good as the H-tec cell due to the poor contact between the various components and the soft rubbery gasket employed in the H-tec model. The components obviously play an important part in determining the performance of the fuel cells.

Further development of the K18 hard graphite fuel cell was carried out by exchanging the graphite flow channels and the copper electrodes with the H-tec nickel alloy electrodes. The later was designed to be a current collector as well as flow channels. Moreover, this allowed more control of the cell hardware to achieve the maximum contact between all components.

Measurements were carried out at elevated temperature, the electrodes and SPEEK / Nafion membranes were sandwiched between isolated end plates and the whole system was isolated

by wrapping in glass wool. These cells were studied over a range of temperature from 35 to 100 °C. The temperature was controlled using a Stuart CB162 heater and a Digitron T228 thermometer.

2.2.12 Dielectric Relaxation Spectroscopy, DRS

2.2.12.1 Theory

Dielectric measurements rely on the application of a sinusoidal voltage to the sample and measuring the current [77-80]. This current can be resolved into two fundamental dielectric characteristics: capacitance and conductance see Figure 2.11.
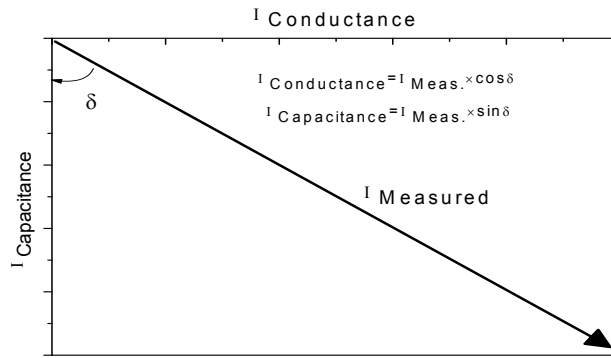
Figure 2.11: Schematic representation of current in the DETA.

The materials capacitance, C, and conductance, λ, are then calculated using the following equations:

$$C = \frac{I_C}{wV} \qquad (2.17)$$

$$\lambda = \frac{1}{R} = V \times I_c \qquad (2.18)$$

where $w = 2\pi \times f$ is the angular frequency, f is the frequency in Hz and V is the applied voltage in V.

In practice, the capacitance and conductivity responses of the material are expressed as the dimensionless quantities ε' and ε''.

ε' is the dielectric constant or permittivity. It represents the amount of alignment of the dipoles in the electric field. It is low for hydrocarbon polymers at low temperature, below thermal transitions, because the molecules are frozen in place and the dipoles cannot move to align themselves with the electrical field. Likewise, it is low for highly cross linked thermosetting resins.

ε'' is the loss factor and it measures the amount of energy needed to align the dipoles and move ions. Ionic conduction is not significant until the polymer becomes fluid (e.g. above T_g or T_m).

(a)   **(b)**
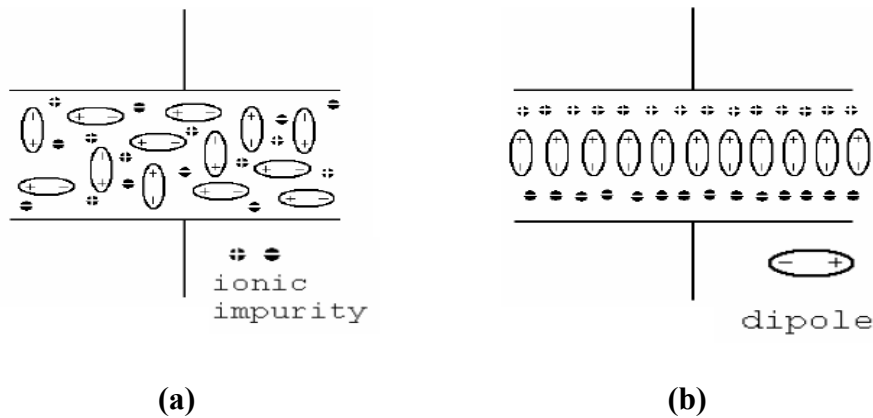
Figure 2.12: Response of polymeric material to an electric field (a) ionic conductivity and (b) dipole alignments [80].

The loss tangent, $\tan \delta$, is also defined as:

$$\tan \delta = \frac{\varepsilon''}{\varepsilon'} \qquad (2.19)$$

For parallel plate electrodes, ε' and ε'' can be calculated from the measurements of capacitance and conductance respectively, for a homogenous sample, as follows:

50

$$\varepsilon' = \frac{Cd}{\varepsilon_o A} \qquad (2.20)$$

$$\varepsilon'' = \frac{d}{RAw\varepsilon_o} \qquad (2.21)$$

where C is the capacitance, R is the resistance, A is the electrode plate area, D is the plate spacing between the electrodes or sample thickness and ε_o is the absolute permittivity of free space (8.85×10^{-12} F m^{-1}).

2.2.12.2 Experimental Procedures

A dielectric thermal analyzer, DETA, manufactured by Polymer Laboratories Ltd was used to follow the change in dielectric constant, $\varepsilon`$, dielectric loss, $\varepsilon``$ and tan δ with applied frequency and temperature. The DETA equipment consisted of a measuring cell, temperature controller and analyzer. The measuring cell consisted of circular parallel plate electrodes, 20 mm in diameter, placed in a thermostated furnace with a temperature range from −150 to 300°C. A fixed AC voltage, 1V, was used at various frequencies in the range of 50 to 10^5 Hz.

Dynamic experiments were carried out using five different frequencies namely 0.1, 1.0, 5.0, 10.0 and 50.0 kHz in the temperature range -140 to 240 ^{o}C at a heating rate of 1 ^{o}C min^{-1}. Step isothermal experiments were also carried out and the loss and dielectric constant were determined at twenty frequencies and recorded at isothermal temperatures from 120 to 240 ^{o}C in steps of 5 ^{o}C and soaking time of 10 minutes between each step.

In order to ensure a good level of conduction between the surfaces of the sample and the electrodes, the samples were coated with gold using a Polaron E5000 sputter coating unit.

2.2.13 Electrochemical Impedance Spectroscopy, EIS

2.2.13.1 Theory

In this technique, a small sinusoidal AC voltage or current signal of known amplitude and frequency (typically from 1Hz to 1 kHz) are imposed on an electrochemical cell and the AC amplitude and phase response of the cell monitored. Properties of the electrochemical system commonly evaluated using impedance spectroscopy include ohmic resistance, electrode properties such as charge transfer resistance and double layer capacitance, and transport effects.

A sinusoidal current signal, $I(w)$, is defined from its amplitude, I_{AC}, and angular frequency, w, as follow:

$$I(w) = I_{AC}.\sin(wt) \tag{2.22}$$

where t is time in second. The output AC voltage signal from the electrochemical cell is defined as,

$$V(w) = V_{AC}.\sin(wt - \theta) \tag{2.23}$$

where V_{AC} is the amplitude of the output voltage signal in volts and θ is the phase angle in radians which represents the difference in the phase of the sinusoidal voltage and current signals. In the case of an AC signal, the resistance of an electrochemical device which is not purely resistive is a function of the frequency of oscillation of the input signal. It follows from Ohm's Law for the AC case that,

$$Z(iw) = \frac{V(iw)}{I(iw)} \tag{2.24}$$

where $Z(iw)$ is the complex impedance in ohm, and $i \equiv \sqrt{-1}$ is the imaginary operator. Equation 2.24 indicates that impedance depends on the frequency at which it is measured. It can be written as:

$$Z = Z' + Z''$$ (2.25)

where $Z' = |Z|\cos\theta$ is the real, in phase, component of the impedance, $Z'' = |Z|\sin\theta$ is the imaginary, out of phase, component of the impedance, $|Z| = \sqrt{(Z')^2 + (Z'')^2}$ is the magnitude of the impedance and $\theta = \tan^{-1}(Z''/Z')$ is the phase angle.

It should be noted that the original time-variance of V and I, the input/ response signal defined by Eq. 2.22 and 2.23, have disappeared in Eq. 2.24 and 2.25 and the impedance at a fixed frequency itself is a time-invariant as long as the system itself is time invariant [4, 81].

2.2.13.2 Experimental Procedures

A Solartron 1250 Frequency Response Analyzer, FRA, coupled with a Solartron 1286 Electrochemical Interface, EI, was used. Measurements were carried out at a fixed AC potential of 10 to 100 mV over the frequency range from 10^{-3} to 6.5×10^4 Hz and at different temperatures. Calibration of the EIS apparatus was carried out using a home-made "Dummy Cell" with two types of connection, with four and two terminals, as well as a Randels circuit with three terminals, see Figure 2.13.

In testing fuel cell, connections were made with four terminals. The equivalent circuit analyses were consistent with the theoretical values of R and C. The equivalent circuit fit is a useful way to establish the electrical properties of the different component in the fuel cell.
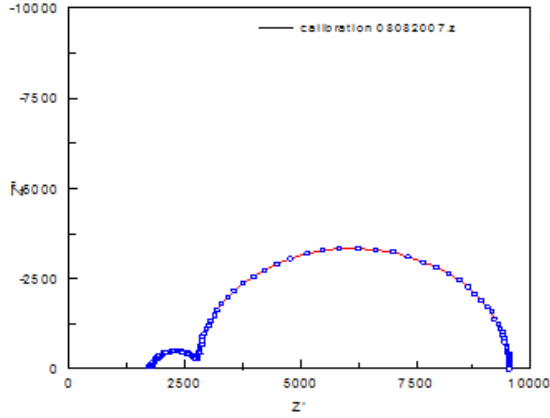
The Nyquist Plots for the Dummy Cell   The Bode Plots for the Dummy Cell
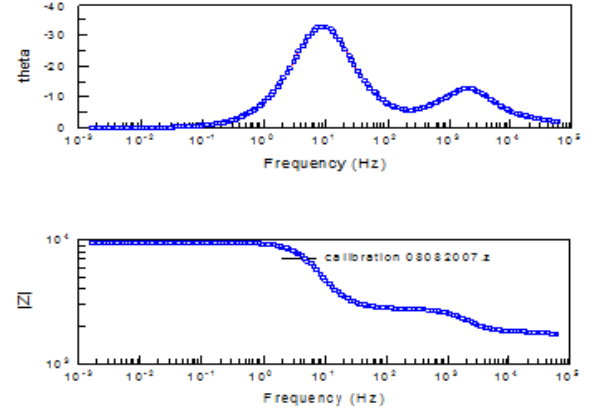
R_s, R_1 and R_2 =1.8, 1.0 and 6.8 kΩ, C_1 and C_2 =0.1 and 4.6 µF
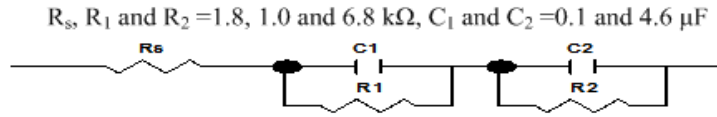
The Dummy Cell

Element	Freedom	Value	Error	Error %
Rs	Free(+)	1786	1.9417	0.10872
C1	Free(+)	9.3916E-08	6.6169E-10	0.70456
R1	Free(+)	1001	2.9781	0.29751
C2	Free(+)	4.7952E-06	1.1394E-08	0.23761
R2	Free(+)	6730	6.5071	0.096688

Chi-Squared: 0.00062189
Weighted Sum of Squares: 0.18594

Equivalent Circuit Model Fit Results

Figure 2.13: Impendence plots for the Dummy cell.

The EIS is used to carry out the following measurements:

2.2.13.2.1 Conductivity Measurement

The conductivity of the membranes was calculated using [82]:

$$\sigma = \frac{l}{RS} \tag{2.26}$$

where σ is the ionic conductivity in S cm^{-1}, l is thickness of the membrane, R membrane resistance, taken as the resistance corresponding to the phase angle closest to zero in the Bode diagram, and S the cross sectional area of the membrane, respectively.

2.2.13.2.2 Impedance Spectroscopy of PEM Fuel Cell

To carry out fuel cell testing we used the simple experimental set-up shown in Figure 2.14. The impedance spectroscopy was carried out on the working PEM fuel cell to monitor the different types of losses such as ohmic resistance, fuel crossover and transport limitations.
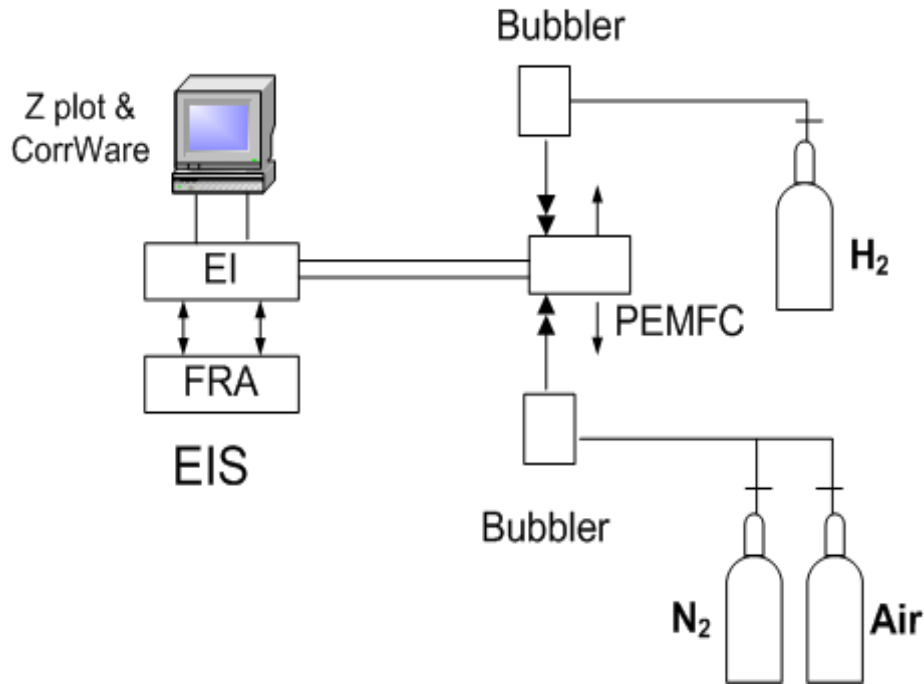
Figure 2.14: Experimental set-up for fuel cell test station.

The Nyquist plot for the Randels circuit representation of an electrochemical half-cell with finite ohmic resistance is shown schematically in Figure 2.15. Depending on the operational conditions used with the PEM fuel cell, similar plots are obtained, with one or two loops. The smaller the diameter of the loop the lower is the charge transfer resistance and the better is the electrochemical performance of the cell.

Moreover, by fitting the results to equivalent circuit such as Randels circuit, the values of R_{ohm}, R_{ct}, C_{dl} and C_{ct} can be calculated and different PEM / MEA or different operating conditions can be compared to optimize the performance of a fuel cell.
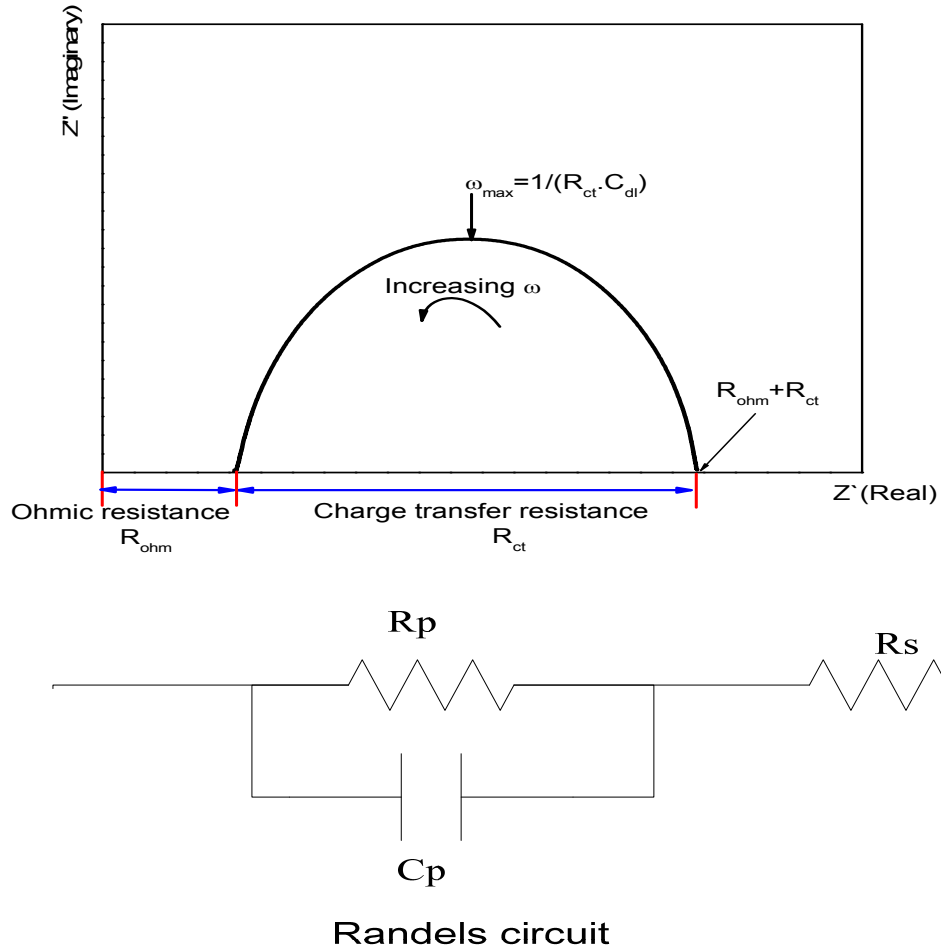
Figure 2.15: Complex plane representation of impedance data for an equivalent circuit analogue of an electrochemical half-cell consisting of an ideal parallel resistor-capacitor (R_{ct}-C_{dl}) network in series with a finite ohmic resistance (R_{ohm}) [4].

2.2.13.2.3 Linear Sweep Voltammetry, LSV, and Cyclic Voltammetry, CV

This experiment was used to evaluate two key properties of the hydrogen PEM fuel cell namely, hydrogen fuel crossover through the membrane and electrochemically active area of the electrode. The experiment was carried out using the Electrochemical Interface alone, e.g., the Solartron 1286 EI.

Crossover of hydrogen occurs from one electrode to the other by permeation through the membrane and this degrades the performance of the cell by reducing the open circuit voltage of the cell through induced mixed potentials and by decreasing fuel efficiency. Oxidant crossover can also occur through a similar mechanism.

Another source of loss within a fuel cell is that when direct conduction of electrons occurs between the electrodes through the membrane. This is the case if small portions of the individual electrode make contact with one another due to membrane thinning. This is known as internal short circuiting and degrades the performance of the cell.

A fuel crossover (or internal short circuits) current of 1 to 2 mA cm^{-2} may be acceptable if the operating current density of the system is around 400 mA cm^{-2}. This equates to a loss in efficiency of 0.25-0.5%.

Experimentally, the fuel crossover is determined by linear sweep Voltammetry, LSV. An inert gas is used to purge the fuel cell cathode while hydrogen is passed through the anode. The potential of the fuel cell cathode (the working electrode) is swept by means of a linear scan until a potential is reached at which any hydrogen present is instantaneously oxidized. The plot of working electrode current against working electrode potential is used to derive the hydrogen crossover flux from Faraday's law. The presence of significant internal shorting within a fuel cell is manifested as a positive slope in the current against potential plot.

Chapter 3

Structural and Thermal Properties of Irradiated PEEK

3.1 Introduction

Irradiation is a versatile route for polymer modifications. When irradiated with gamma rays, electron beam, EB, or X-rays the radiation passing throughout matter, such as polymers loses energy by interacting with the electrons of the polymer and produces free electrons, ionized atoms or molecules in excited states. The incident radiation and some of the electrons produced have high enough energy to cause chemical bond cleavage in the irradiated polymer. As a result, active species such as radicals, ions and excited states are formed, which in turn react in different ways leading to chain scission, cross linking, and formation of low molar mass volatiles and unsaturation. If irradiation is carried out in air, reactions of the active species with oxygen results in the formation of oxy radicals, peroxy radicals and hydro peroxides. These undergo further reaction and lead to the formation of functional groups such as carbonyl and hydroxy groups [83-87].

Different polymers have different responses to radiation. A parameter called the "G value" is used to quantify the chemical yield resulting from the radiation and is defined as the absolute chemical yield expressed as the number of individual chemical events occurring per 100 eV (1.6×10^{-17} J) of absorbed energy. Therefore the G values for cross linking, G(X), and for chain

scission G(S), is a measure of the number of cross links and chain scissions produced per 100 eV respectively [83, 84, 86].

Cross linking and degradation (through chain scission) are two competing processes that always co-exist under radiation. The ratio G(S)/G(X) can be used to indicate which process is dominant, such that, when G(S)/G(X) > 1 materials tend to undergo degradation and when G(S)/G(X) <1 materials tend to cross linking.

However, the overall effect depends on which of the two is predominant under the experimental conditions adopted. It should also be emphasized that for a given polymer G(X) and G(S) both change with radiation type and experimental conditions such as temperature, atmosphere and absorbed dose. The amount of energy absorbed per unit mass is measured in Gray (Gy) units =1 J kg^{-1}.

For some polymers, elevated temperature increases the mobility of the polymer chains and makes them more favourable to cross linking. Oxygen in the air usually assists degradation through the production of peroxides and this lead to a radical mechanism. In an oxygen-free atmosphere cross linking is more favourable. Both G(X) and G(S) increase with the dose, but, G(S) for a polymer generally increases more than G(X). The G values for a polymer are also affected by the radiation type. The so-called linear energy transfer, LET, is used to quantify the effect of different radiation types on a material. LET is defined as the energy deposition rate per track length (-dE/dx) of the radiation source and generally G(X) values increased with increasing LET values [83-89].

3.2 Irradiation of PEEK

The irradiation of PEEK with ions [56, 57, 61, 90], electron beams, EB, [61, 91-97] and gamma rays [55, 98] has been extensively studied, the effects of irradiation evaluated using

both thermal and mechanical techniques and less frequently by solvent extraction techniques. It has been found that crystalline PEEK has excellent resistance to irradiation over 50 MGy under non-oxidative conditions and that the main mechanism which accounts for the change in mechanical and physical properties in amorphous PEEK is due to the formation of cross links. Irradiation with EB results in the formation of gel when the absorbed dose exceeds 6 MGy, and the percentage of gel was noted to increase with absorbed dose [93].

The mechanical properties of the polymer have been reported to deteriorate with increasing irradiation dose, such that the elongation to break is reduced. The presence of cross links in the polymer reduces the rate of crystallization and the final degree of crystallinity achieved on crystallizing from the melt. It also depresses the observed melting points and at a sufficiently high degree of cross linking no crystallization or melting was observed [55-57, 61, 90-98].

3.3 Results and Discussions

3.3.1 Ion Irradiation and Dose Evaluation

The size of the irradiated area was determined by inspection of the irradiated foils, which were discoloured by the beam, and the flux (ions per unit area) determined, assuming that the discoloured area was uniformly irradiated. The principal uncertainty in the determination of dose arises from uncertainty in measurement of the integrated charge. This may be as large as 20%. The dose delivered is concentrated into narrow parallel tracks passing through the foil. Table 3-1 lists the track density Φ (number of ions incident on unit area) for each type of radiation, from which an estimate of the average tracks spacing, can be obtained as $(0.87 \times \Phi)^{-0.5}$. As can be seen from Table 3.1 in the present study the damage tracks effectively overlap and so cover the entire irradiated area.

Table 3.1: Irradiation conditions and dose evaluation for H^+ and He^{2+} ions.

Irradiation ions	Total charge ($\times 10^{-4}$ C)	Area ($\times 10^{-4}$ m^2)	Fluence (C m^{-2})	Ions per unit area ($\times 10^{18}$ m^{-2})	Average track spacing ($\times 10^{-10}$ m)	Dose[a] (MGy)
H^+	2.4	4.2	0.57	3.60	5.70	2.3
	1.5	0.8	1.90	12.00	3.10	7.8
	10.1	4.2	2.40	15.00	2.80	9.9
	12.0	2.3	5.20	32.50	1.76	21.3
	21.0	2.3	9.09	56.70	1.33	37.3
He^{2+}	1.2	2.3	0.52	1.62	0.84	6.6
	2.4	2.3	1.04	3.25	0.60	13.1
	4.8	2.3	2.08	6.50	0.42	26.2

[a] at the first layer.

3.3.2 Structural Characterization of Irradiated PEEK

3.3.2.1 Gel Contents

The gel content of the irradiated films was determined by swelling in the solvent, MSA, which has been reported as a non-sulphonating solvent for PEEK, even after one week in contact with it [45, 63]. Figure 3.1 shows the relationship between gel content and dose on irradiating amorphous PEEK with proton H^+ and helium He^{2+} ions. Similar dependence was observed for both ions namely an increase in the percentage of gel formed with increasing irradiation dose. This behaviour indicates that the effect of irradiating amorphous PEEK by ion occurs predominantly by a cross linking process. Although there is a similar dependence of gel content with dose, the He^{2+} ions were more effective in producing gel at a lower dose

than the H^+ ions. The maxima in gel content observed were $85 \pm 5\%$ and $75 \pm 5\%$ at a dose of 30 and 45 MGy on irradiation with He^{2+} and H^+ ions respectively. Similar results have been reported by Vaughan and Stevens [93] on the effect of electron irradiation on the percentage gelation in amorphous PEEK. The gel content was observed to level off at about 75% with increasing dose up to 100 MGy.
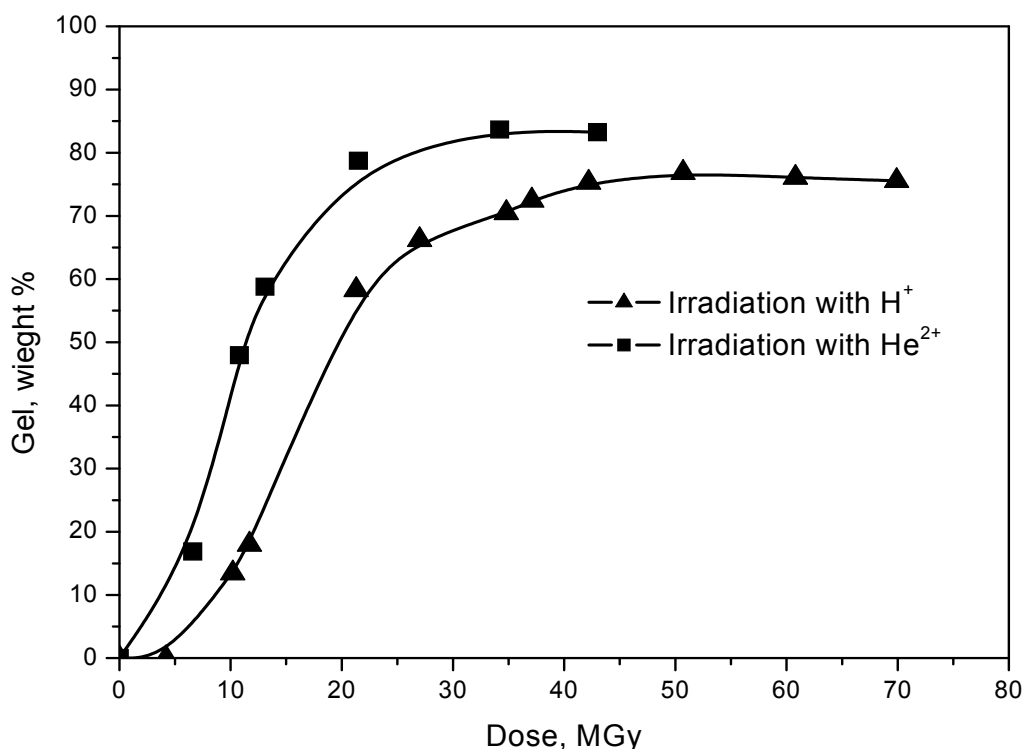
Figure 3.1: Gel content of irradiated PEEK samples obtained by solvent extraction with

MSA.

3.3.2.2 Gel-Sol Fraction Analysis

Gelation in polymers occurs on the formation of cross linking between the chains in a macromolecule, usually by the formation of covalent bonds. If these covalent bonds are formed from two tri-functional units the resultant is referred to as cross link or H-link. If, on

the other hand, one tri-functional unit is involved in the formation of a network the resultants is referred to as end-link or Y-link, see Figure 3.2 [83].
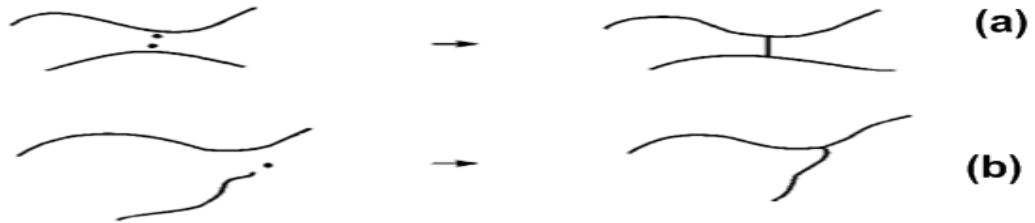
Figure 3.2: Cross linking of polymers, (a) H-link and (b) Y-link [83].

In order to determine quantitatively the cross link and chain scission reaction yields occurring during irradiation of PEEK, the well known Charlesby–Pinner equation [83] was used, such that,

$$s + \sqrt{s} = \frac{p_0}{q_0} + \frac{2}{q_0.u.D}$$

(3.1)

where S is the soluble fraction of polymer ($S = 1 - Gel$), D is the radiation dose in Mrad (1 rad = 100 ergs g^{-1}= 0.01 Gy), q_0 is the proportion of cross linked units per unit irradiation dose, p_0 is the ratio of main chain breaks to chain units per unit irradiation dose, and u ($u = \frac{M_w}{w}$ with M_w the weight average molecular weight and w the repeat unit molecular weight) is the weight average of the initial degree of polymerization. This equation applies only for polymers having a random initial molecular weight distribution, and predicts a linear relationship between ($s + \sqrt{s}$) and 1/D.

The G values can also be obtained from the following equations:

$$(a) \qquad G(X)_H = \frac{0.48 \times 10^6 q_0}{w}$$

(3.2)

$$\text{(b)} \qquad G(S)_H = \frac{0.96 \times 10^6 \, p_0}{w}$$

where w is the repeating unit molecular weight (288 g mol^{-1}) and the subscript H refers to the cross linking mechanism.

Figure 3.3 shows the Charlesby–Pinner plots for both sets of ions and it can be seen that $s + \sqrt{s}$ is a linear function of 1/D with regression coefficients of 0.997 and 0.996 for H$^+$ and He^{2+} respectively.
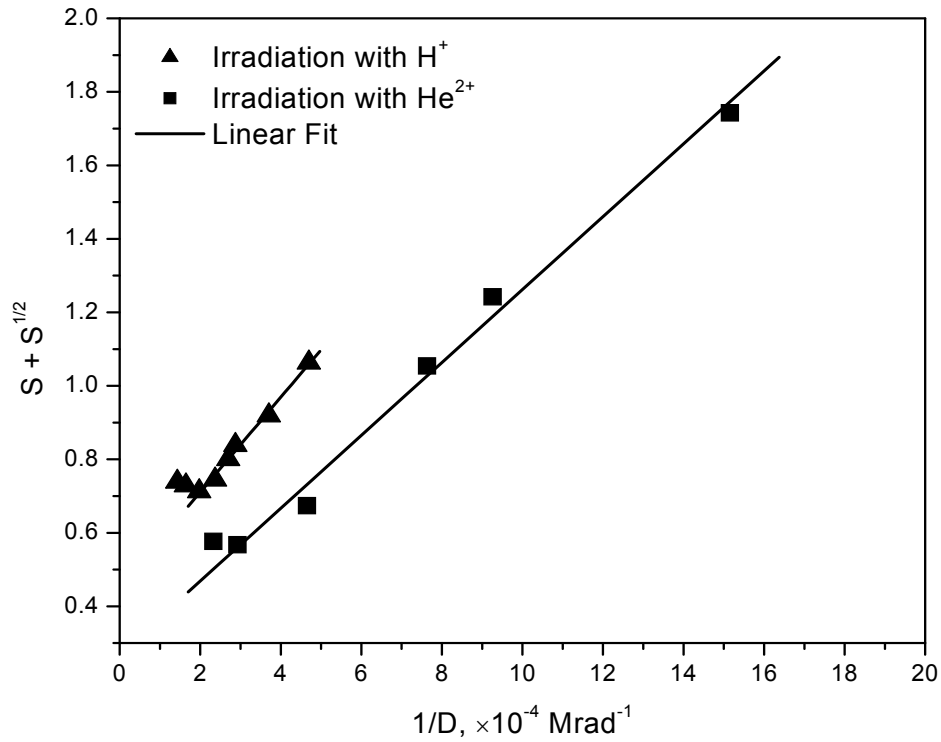
Figure 3.3: The variation in solubility with inverse dose, according to the Charlesby–Pinner equation, for ion irradiated amorphous PEEK films.

The p_0/q_0 values were calculated from the intercept of the lines and were found to be 0.45 $\pm$ 0.02 and 0.27 $\pm$ 0.05 for irradiation with H$^+$ and He^{2+} ions respectively. The gel dose, D$_g$, was determined by interpolating the lines to a value of $s + \sqrt{s} = 2$ and the G values were

calculated from equation (3.2) a and b. These are listed in Table 3.2 from which it is evident that PEEK tends to undergo more cross linking on He^{2+} irradiation at lower doses than protons. The ratios $G(X)_H / G(S)_H$, see Table 3.2, were greater than 1.0 for both ions suggesting that cross linking is more favourable in irradiating PEEK with ions.

Table 3.2: Gelation dose and G values of amorphous PEEK determined from the Charlesby–Pinner equation.

Ions	q_o (% MGy^{-1})	G(X)	G(S)	$\dfrac{G(X)}{G(S)}$	Gel dose, D_g (MGy)
		Event per 100 eV			
H^+	0.343	0.057	0.052	1.11	8.3
He^{2+}	0.447	0.075	0.040	1.83	5.7

Saito [99] has shown that for the Y-linking mechanism the soluble fraction, S, dependence on the dose, D in kGy, can be defined by the following equation[100]:

$$1 + 3\sqrt{s} = \frac{2G(S)_Y}{G(X)_Y} + \frac{1.930 \times 10^7}{G(X)_Y . M_{n,0} . D} \tag{3.3}$$

where $G(S)_Y$, $G(X)_Y$ and $M_{n,0}$ are the main chain scission yield, the yield of end-linking and the initial number average molecular weight respectively.

Figure 3.4 shows the Saito plots for both sets of ions. As can be seen the soluble fraction varied linearly with dose (r = 0.996 and 0.990 for H^+ and He^{2+} irradiation respectively) and the gel dose, D_g, was determined by interpolating the lines to a value of $1 + 3\sqrt{s} = 4$. The G values were calculated from the slopes and the intercepts of the lines. The cross linking and fracture density were calculated from equations (3.2) and are listed in Table 3.3.
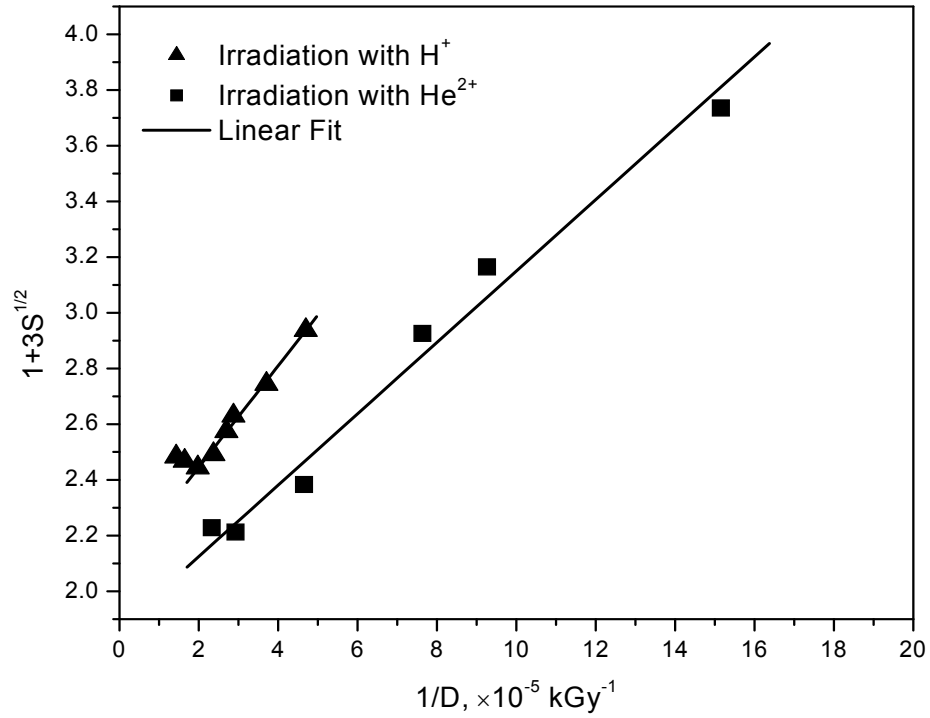
Figure 3.4: The variation of solubility with inverse dose according to the Saito equation, for ion irradiated amorphous PEEK films.

Table 3.3: Gelation dose and G values of amorphous PEEK determined from the Saito equation.

Ions	q_o (% MGy^{-1})	G(X)	G(S)	$\dfrac{G(X)}{G(S)}$	Gel dose, D_g (MGy)
		Event per 100 eV			
H$^+$	0.489	0.082	0.085	0.96	9.5
He^{2+}	0.695	0.116	0.108	1.00	6.1

As can be seen from Tables 3.3, the ratios $G(X)_Y/G(S)_Y$ for both ions were identical and equal to about 1.0, consistent with only one of the two new chain ends formed by chain

scission of the polymer is active and can form a cross link. The other chain end may degrade by an alternative reaction, such as abstraction of hydrogen atom, to form a stable end group.

The issue of whether Y-linking or H-linking plays the dominant role in the radiation chemistry of PEEK could not be resolved from the gel-sole fraction analysis. It has been reported [100, 101] that the calculation of G values from measurements of the molecular weight of the irradiated materials could provide evidence for cross link mechanism, if the agreement with the analysis of sol-gele fraction is achieved. Due to the high doses used in this research to irradiate PEEK with both ions this could not be carried out, but instead the FTIR spectroscopy was used for the investigation of any structural evidence of the cross linked formation on irradiation as discussed below.

3.3.2.3 Analyses by FTIR Spectroscopy

The FTIR spectra of amorphous and crystalline PEEK films are shown in Figure 3.5 from which the following peak assignments was made,

PEEK Absorbance (cm^{-1})	Assignment
3100-3200	Aromatic C-H stretching vibration
1650	Carbonyl stretching
1600, 1490, 1414	Aromatic ring vibration
1300-1000	Various C-O- , C-C and C-H vibration modes (stretching & bending)
860-840	A single broad peak characteristic of the out-of-plane C-H bending of two hydrogens of 1,4- disubstituted

The carbonyl stretching band and the shoulder at 1252 cm^{-1} have been reported to be sensitive to crystallization [102] such that the carbonyl stretching vibrations are at 1655 and 1648 cm^{-1} for amorphous and crystallize PEEK respectively, see Figure 3.5. This shift in the carbonyl stretching to lower frequency was attributed to the increased conjugation as a consequence of the co-planarity of the phenyl groups on crystallization in the diphenyl ketone moiety. In addition, the shoulder at 1252 cm^{-1} is weaker in absorbance on crystallization.
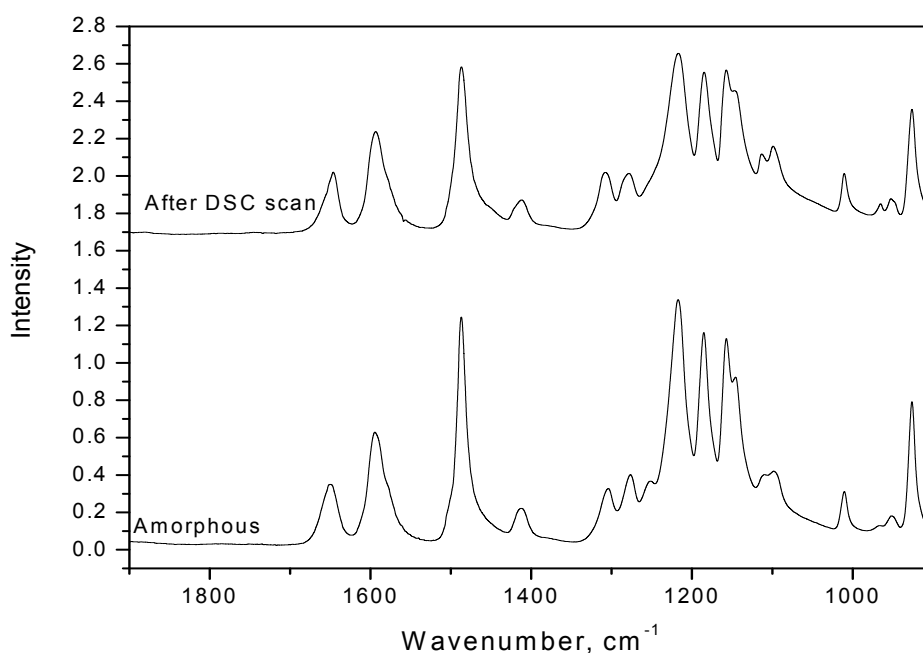
Figure 3.5: The FTIR spectra of amorphous and crystalline PEEK.

Figure 3.6 shows the FTIR spectra of ion irradiated PEEK. On irradiation, new bands developed at 1725, 1775 and 3300 cm^{-1} and these were accompanied by the progressive yellowing of the polymer film with dose. These are, however, minor bands of low intensity. The bands were attributed to the production of carbonyl and hydroxyl groups [67-69] produced by the reaction of chain scission radicals with molecular oxygen and subsequent decomposition of the peroxy radicals. No differences from the FTIR spectra could be revealed on irradiation with H^+ and He^{2+} except that the changes occurred at lower doses with He^{2+}.
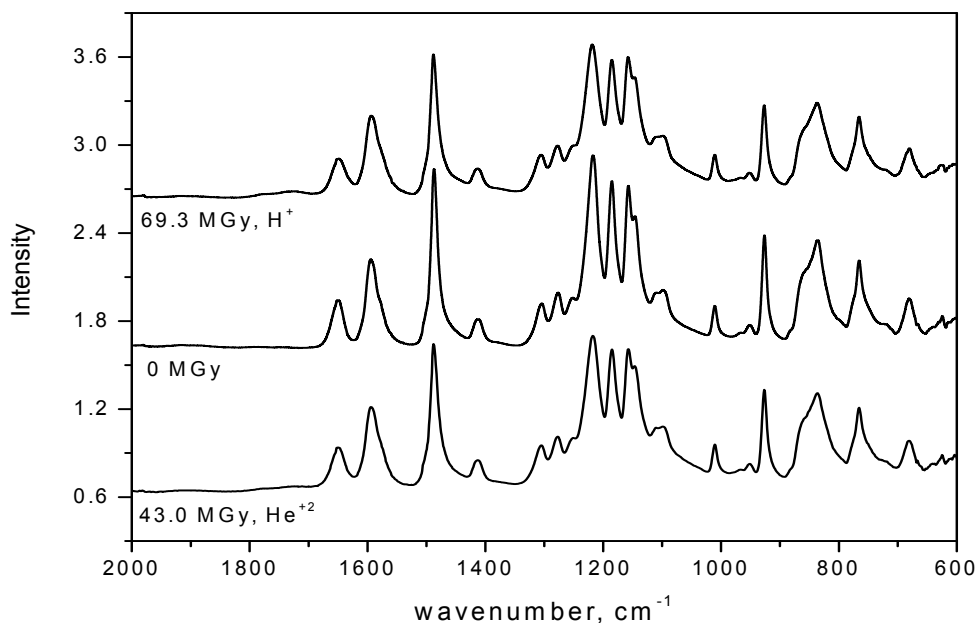
Figure 3.6: The FTIR spectra of different PEEK and irradiated PEEK samples in the region 600 to 2000 cm^{-1}.

To gain further information on the cross links structure, FTIR spectroscopic analysis was carried out on the insoluble gel after washing and drying, see Figure 3.7. This treatment significantly reduced the absorbances of the two bands at 1725 and 1775 cm^{-1} and indicated that these bands were present primarily in the soluble residue produced as a result of chain scission, in line with the primary radicals reacting with molecular oxygen.

FTIR spectra were also recorded on materials obtained after melting and re-crystallizing during DSC analysis, see Figure 3.8. No changes in the spectra were observed on irradiation with H$^+$, below a dose of 50 MGy, or He^{2+} below 23 MGy, and the FTIR spectra were similar to that of crystalline PEEK. At the higher doses used in this study, however, the irradiated samples showed a spectra characteristic of amorphous PEEK indicating that irradiation had stopped the crystallization from developing. Bands were also present at 1725 and 1775 cm^{-1} but greatly reduced by the heating and cooling treatment.
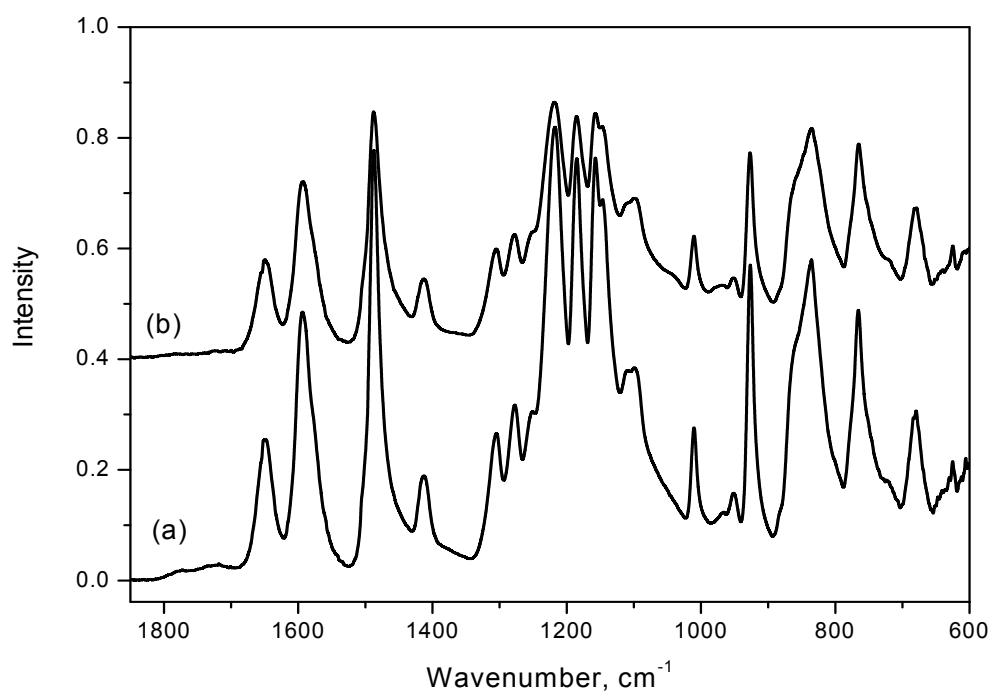
Figure 3.7: The FTIR spectra of (a) proton irradiated PEEK with dose of 38.1 MGy and (b) the dried gel of the same sample.
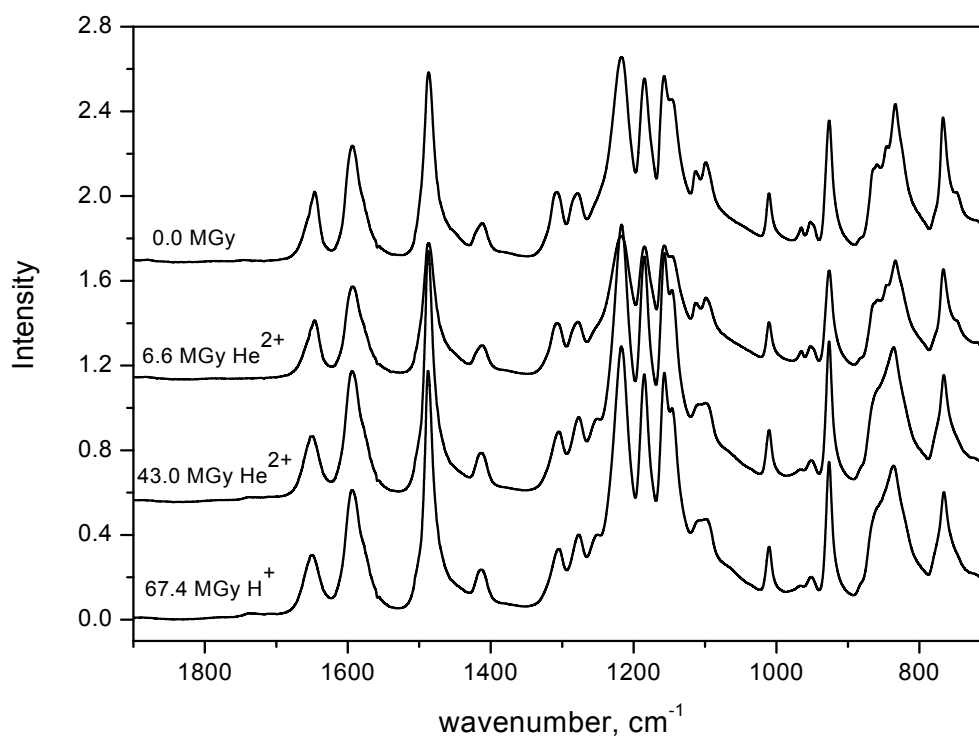
Figure 3.8: The FTIR spectra of irradiated PEEK samples after DSC scan.

3.3.3 Thermal Characterization of Irradiated PEEK

3.3.3.1 DSC Analysis

3.3.3.1.1 General Irradiation Effects

PEEK is readily characterized by its DSC response and Figure 3.9 showed that on heating an amorphous sample a glass transition occurs at about 145°C, as shown by a step change in the specific heat at T_g, $\Delta C_p(T_g)$. This is followed by a sharp crystallization exotherm at 180° C and a broad melting endotherm with a peak at about 335°C.
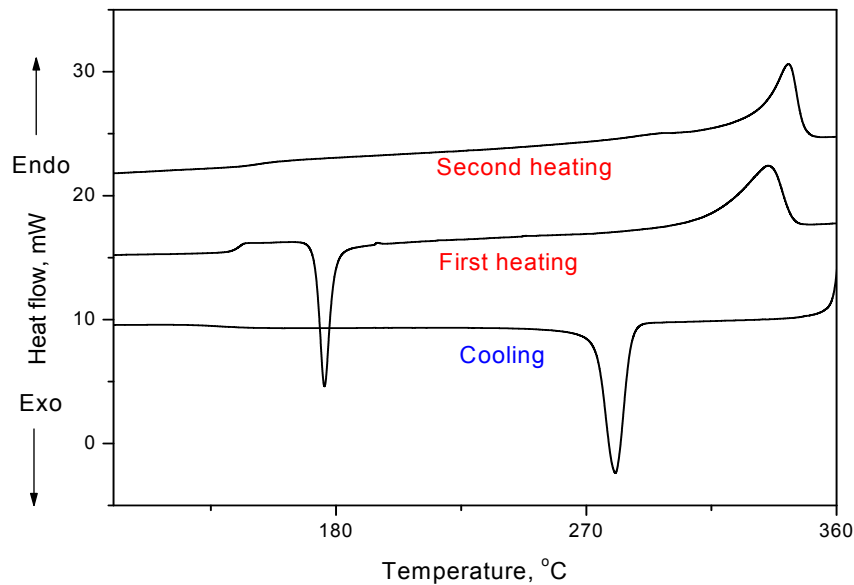
Figure 3.9: DSC profiles of amorphous PEEK as indicated; heating and cooling scans are 20 ^{o}C min^{-1}.

On cooling to room temperature at 20°C min^{-1}, PEEK re-crystallizes at about 280 ^{o}C and on reheating the T_g was raised to 152 ^{o}C with a greatly reduced value of $\Delta C_p(T_g)$ as well as a higher melting temperature, T_m, 342 ^{o}C, in line with its higher crystallization temperature on cooling from the melt [103].

71
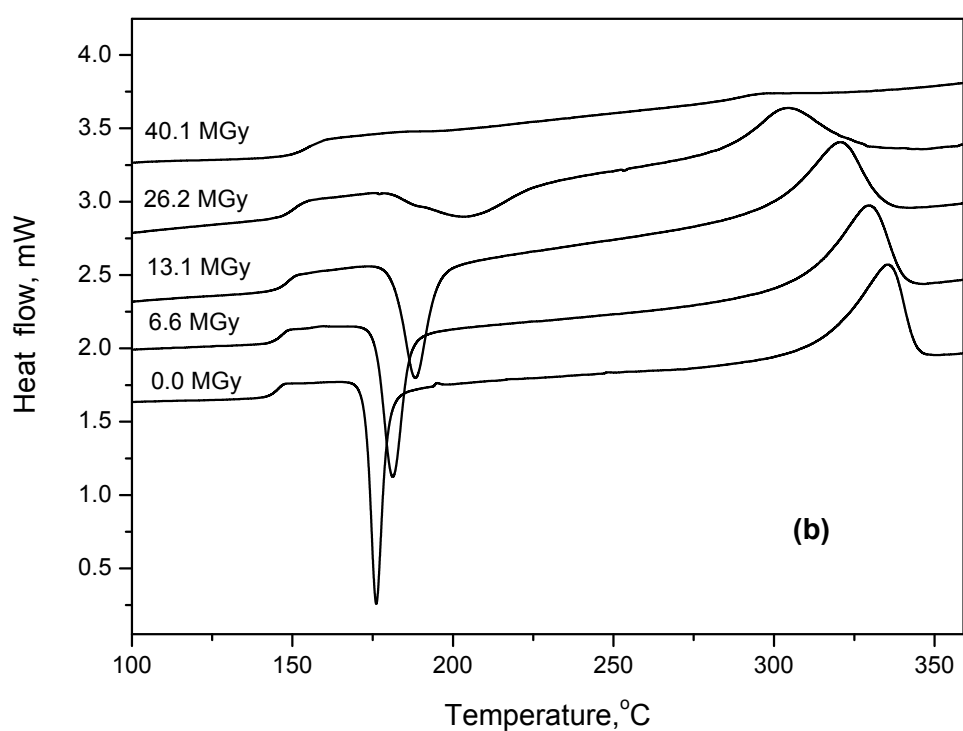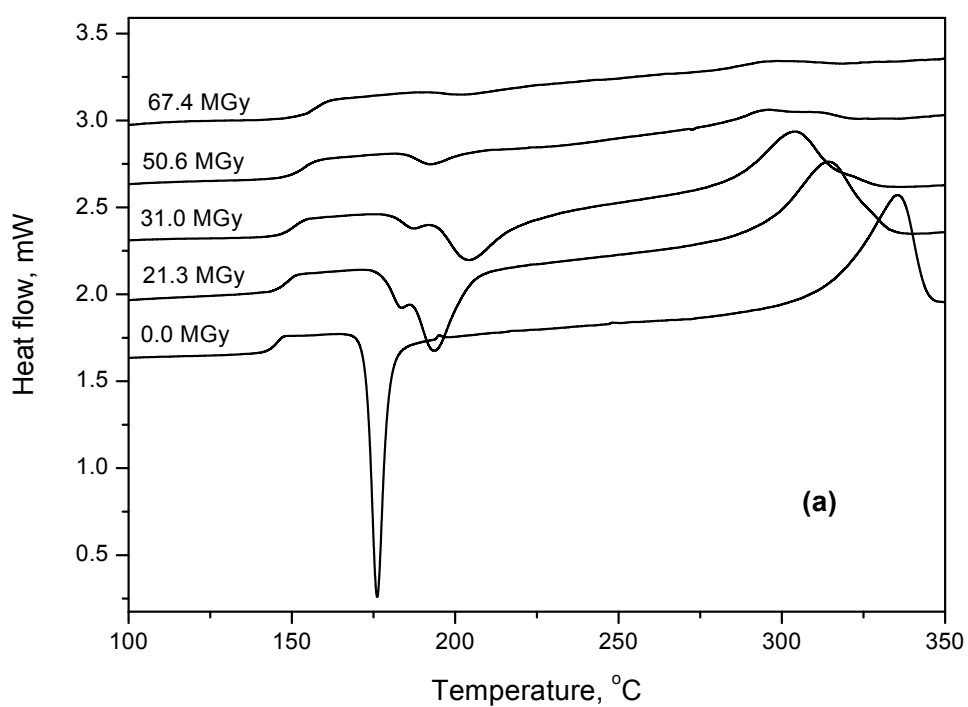
Figure 3.10: DSC thermal response of PEEK samples (first scan) after irradiation with (a) H^+ and (b) He^{2+} ions.

On ion irradiation and as the dose increases, a number of changes become apparent in the thermal properties of amorphous PEEK, see Figure 3.10. There was a progressive increase in the observed T_g with dose as measured during the first heating scan, see Figure 3.11, and with a reduction in the value of $\Delta C_p(T_g)$. This was followed by an increase in the crystallization temperature, T_c, taken as the temperature corresponding to the maximum in rate, a broadening of the temperature range over which crystallization occurred and a decrease in the exotherm. At a high dose no crystallization was observed and the polymer remained amorphous.

Although the irradiated samples crystallized at a higher temperature the observed melting point, T_m, decreased as well as the subsequent re-crystallization temperature, T_{rc}, on cooling with radiation dose. There was a decrease in heats of crystallization, ΔH_c, of fusion, ΔH_m, and re-crystallization, ΔH_{rc}, on subsequent cooling, consistent with the weight degree of crystallinity, $X_{c,w}$ (expressed as $X_{c,w} = \dfrac{\Delta H_m}{\Delta H_m^0}$, where ΔH_m^0 is the heat of fusion for totally crystalline PEEK) decreasing. ΔH_m^o was taken to be 122.5 J g^{-1} [103]. The effect of irradiation on melting and crystallization processes of PEEK will be discussed in details in Chapter 4.

3.3.3.1.2 Cross Link Density, T_g and The DiBenedetto Equation

Figure 3.11 shows the progressive increase in T_g with ions irradiation dose. As can be seen, the observed T_g on the first heating scan increases linearly with absorbed dose at a rate of 0.14 and 0.21 ± 0.01 °C MGy^{-1} on irradiation with H$^+$ and He^{2+} respectively (regression coefficient were 0.982 and 0.991).

The value of T_g is affected by many factors such as the chemical structure of repeating units of the polymer, crystallinity, interaction of chains and presence or absence of cross links [104].

In the present case, it is reasonable to attribute the rise in T_g by irradiation to restriction of chain mobility caused by the cross linking network developed in the amorphous regions of the polymer with increasing irradiation dose. This increase in T_g is clear evidence that cross linking is the more important mechanism on irradiation of amorphous PEEK. By comparison, chain scission would be expected to produce a decrease in T_g, with the reciprocal number average degree of polymerization. No reduction was observed on irradiation, even at low doses.
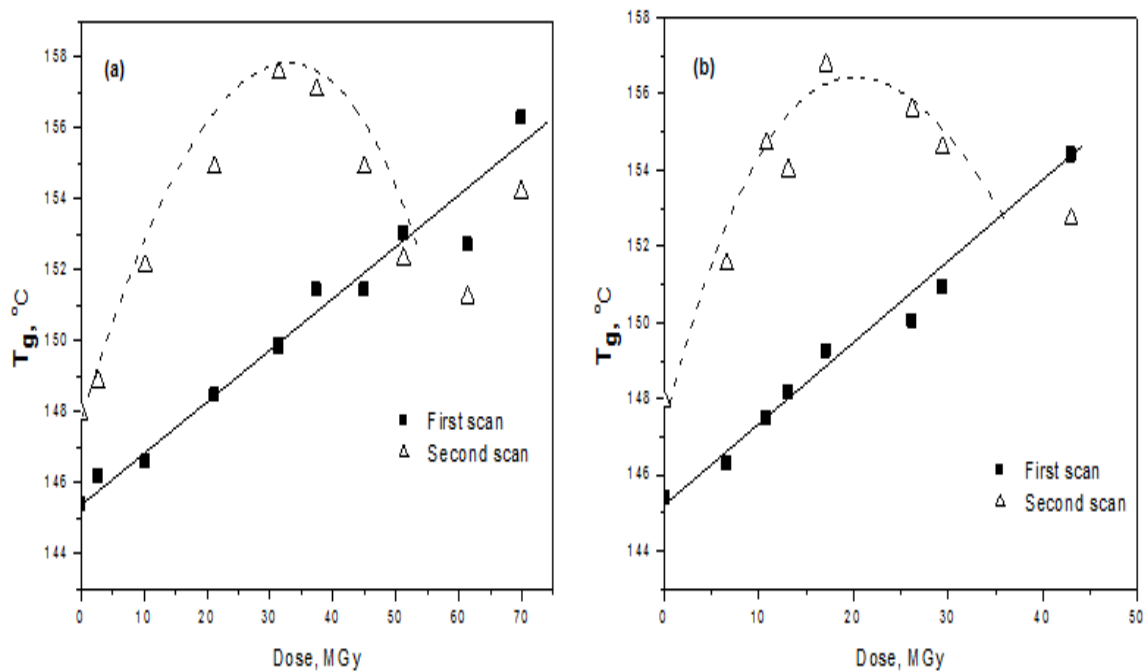
Figure 3.11: The dependence of the glass transition temperature of PEEK on the irradiated dose in the first and second heating scan, (a) H$^+$ and (b) He^{2+} ion.

At a given dose, the T_g was observed to shift to higher temperatures on the second heating scan compared to the first. This increase in T_g values is due to the effect of crystallization, since the second heating run was made on samples which had been cooled from the molten state at a relatively slow cooling rate of 20°C min $^{-1}$.

The extent of this increase is dependent of the degree of crystallinity achieved. As the dose increased the degree of crystallinity reduced and the increase in value of T_g on the second heating scan was reduced until at a certain dose (above 50 and 35 MGy for H^+ and He^{2+} respectively) it became similar to the value of T_g on the first heating scan. A full description of the dependence of T_g on dose can be found in Vaughan and Stevens works [96], who developed a model based on both the overall crystallinity and lamella thickness to quantitatively account for the observed dependence of T_g on the second heating run on the irradiation dose with EB. Similar dependence is presented in Figure 3.11 (a) and (b).

To analyze the influence of cross links on the glass transition temperature, as measured from the first heating scan, the DiBenedetto equation was used. This equation has been successfully applied to study curing reaction of polymer [105], and it relates the observed glass transition, T_g, to cross link density, X_c, since

$$\frac{T_g - T_g^0}{T_g^0} = \frac{\left[\dfrac{E_x}{E_m} - \dfrac{F_x}{F_m}\right]X_c}{1 - \left[1 - \dfrac{F_x}{F_m}\right]X_c} \qquad (3.4)$$

where T_g^0 is the glass transition of the uncross linked polymer and E_x/E_m is the ratio of the lattice energies of cross linked and uncross linked repeating units. F_x/F_m is the mobility ratio

at the glass transition temperatures. It is expected that the mobility of a cross linked unit at the glass transition temperature is essentially zero, thus eq. (3.4) simplifies to,

$$\frac{T_g - T_g^0}{T_g^0} = K \frac{X_c}{1 - X_c}$$

(3.5)

where K is a constant and X_c is the cross links density expressed as the mole fraction of repeat units present as cross links corresponding to the T_g. The cross link density was defined as the proportion of units cross linked and taken as the product ($q_0 \times D$) where q_0 is evaluated from Charlesby-Pinner equation and listed in Table 3.2 and D is the absorbed dose in MGy.

Figure 3.12 shows the results obtained by applying eq. (3.5) to the present T_g data. The cross links constants were found to be 0.081 ± 0.004 and 0.088 ± 0.005 for samples irradiated with proton and helium ions respectively (regression coefficient were 0.994 and 0.992). As can be seen the values are identical, within experimental error, and this indicates that the cross link constant is independent of the ion used.

The implication of this is that the same cross link structure is being produced by both type of ions, and also that the proposed equation is applicable to describe the relationship between T_g and cross linking introduced by ion irradiation.
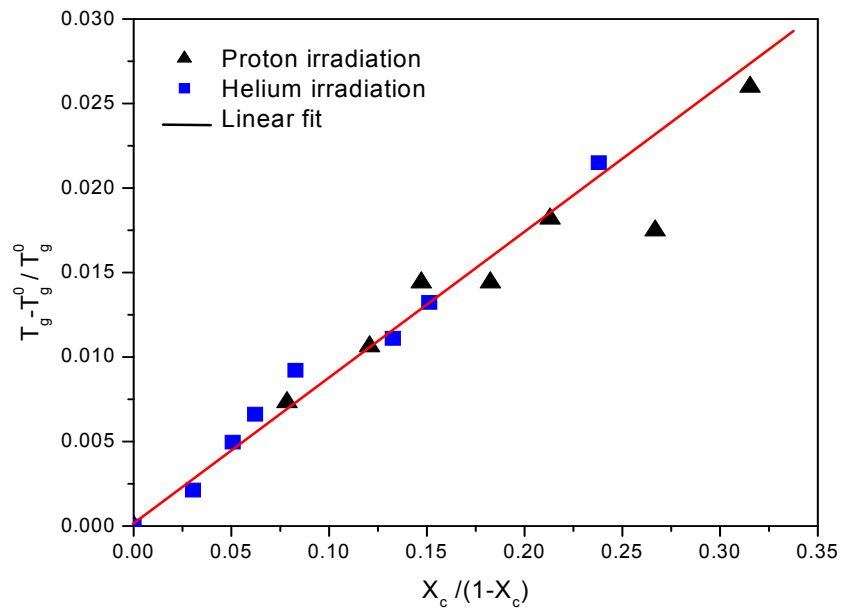
Figure 3.12: The dependence of glass transition temperature on the cross link Density according to DiBenedetto equation.

3.3.3.2 Thermogravimetric Analysis

3.3.3.2.1 General Irradiation Effects

The thermal decomposition of PEEK has been extensively studied by thermogravimetry, from 450-600 ^{o}C, and the mechanism of decomposition attributed to random scission reactions involving the cleavage of the ether and carbonyl bonds to produce volatile products such as phenol, benzophenone and low molecular weight chain fragments [106].

Figure 3.13 shows the fractional conversion α, rate of conversion, e.g., the first derivative of conversion against time (dα/dt) and second derivative (d^{2}α/dt^2) plotted against temperature at a heating rate of 10 K min^{-1} for un-irradiated PEEK (a) compared to that of various samples irradiated with both ions to different doses (b and c). Table 3.4 lists the onset degradation

temperature, T_d, the temperature corresponding to maximum in $d\alpha / dt$, T_{max}, and the yield of char at 850 °C.
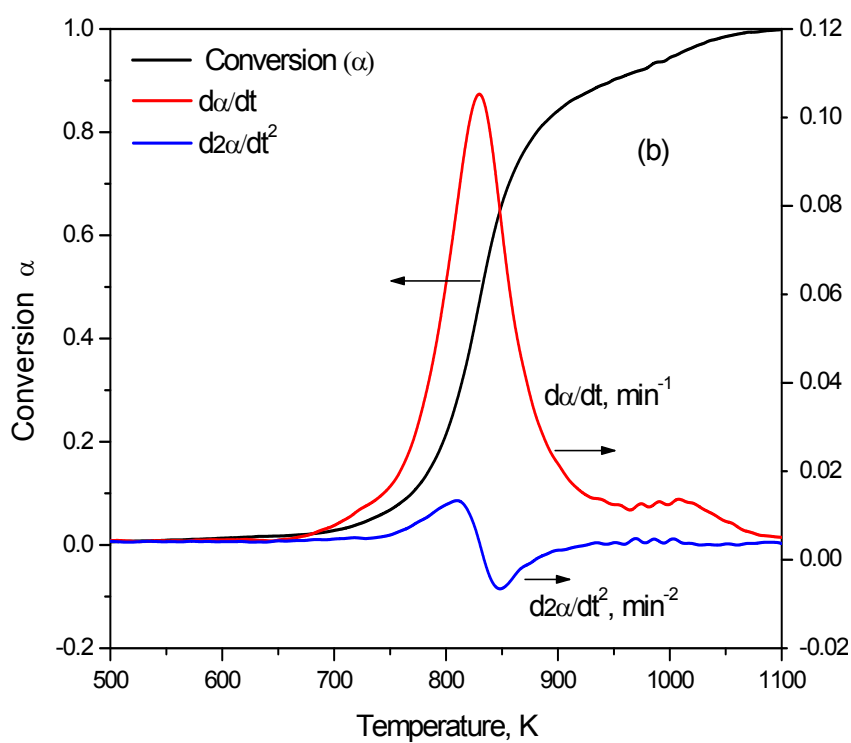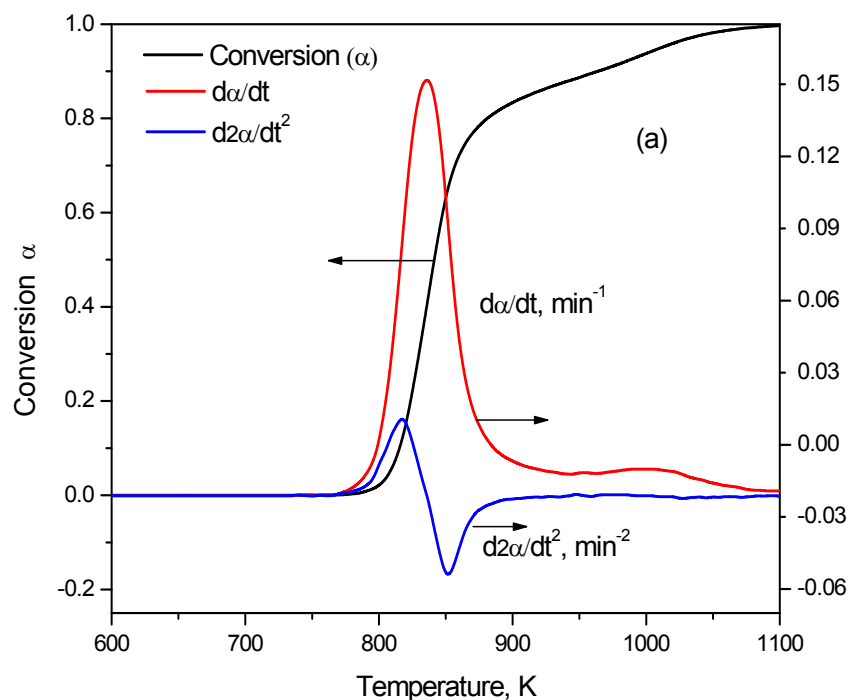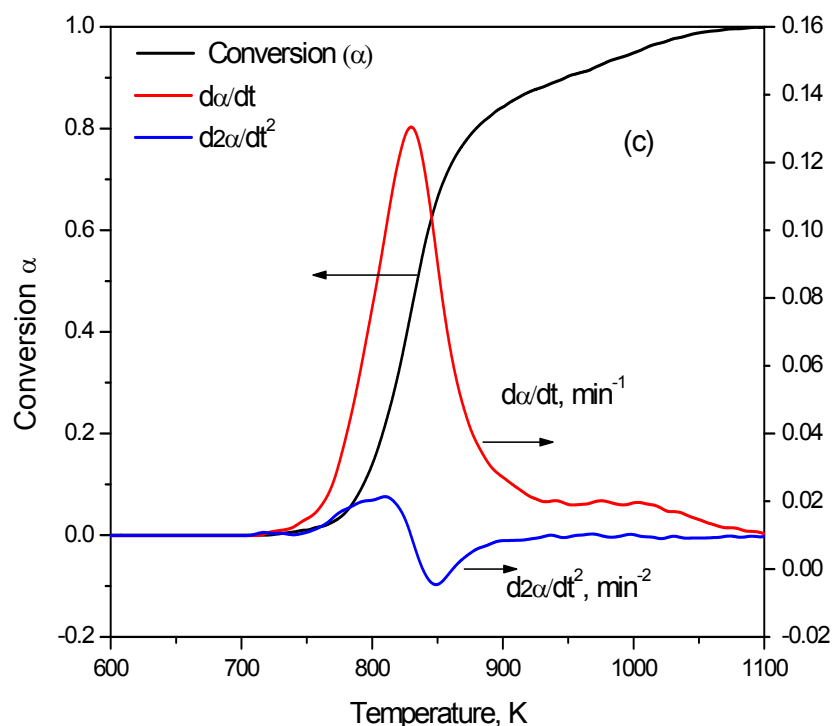
Figure 3.13: The fractional conversion, α, rate ($d\alpha/dt$) and second derivative ($d^2\alpha/dt^2$) plotted as a function of temperature for (a) unirradiated PEEK, (b) irradiated with 40.2 MGy protons and (c) irradiated with 13.1 MGy helium ions.

Un-irradiated PEEK did not lose weight before 500°C but above this temperature there was a single step loss due to the production of volatiles, e.g., phenol, and benzophenone [106]. A similar trend was observed with all the irradiated samples but the temperature of onset decreased progressively with radiation dose. However, loss of volatiles was not observed below 360°C and the irradiated material was considered to have sufficient thermal stability for many commercial purposes.

In the initial stages of thermal decomposition volatile production is accompanied by cross link formation [54, 106] and this leads to the production of a char, which is stable up to 850°C. Cross linking followed by aromatisation leads to stabilisation of the structure and char formation. Irradiation with ions, however, had no effect on the final yield of char and this

remained at about 50±5% weight for all the samples studied. Chain scission during irradiation creates more chain ends and this could account for the decrease in thermal stability, as measured by decrease in the onset of temperature for volatile production with dose.

Table 3.4: The effect of irradiation on the thermal stability of PEEK films.

Radiation method	Dose (MGy)	T_d (± 10 °C)	T_{max} (± 2 °C)	% Char residue (± 5)
Un-irradiated	0	510	563	53
H^+	2.3	490	560	53
	9.3	470	568	50
	10.5	500	568	50
	21.3	430	563	50
	40.2	410	557	50
	66.7	380	553	53
He^{2+}	7.3	480	563	50
	13.1	470	558	50
	40.1	400	554	51

3.3.3.2.2 Thermal Degradation Kinetics

Several analytical equations have been derived to evaluate the thermal degradation kinetics of polymer from its TG dynamic response at constant heating rate. These make use of the relationship between the conversion rate of the reaction, α, and absolute temperature T to determine the kinetic parameters, e.g. activation energy E, reaction order n, and pre-exponential factor Z.

The value of n was obtained directly from the symmetrical index of a derivative thermogravimetry (2DTG), from the second Kissinger method [107]:

$$n = 1.88 \times \frac{\left| d^2\alpha / dt^2 \right|_L}{\left| d^2\alpha / dt^2 \right|_R}$$

(3.6)

where L and R correspond to the maximum and minimum $d^2\alpha / dt^2$ values on the second derivative thermogravimetry (2DTG) curves, see Figure 3.13 as an example.

The n values for PEEK and irradiated samples are listed in Table 3.5. They were found to be fractional at 1.5 ± 0.3 indicating a complex series of reactions involved in the thermal decomposition, such as initiation, propagation and bimolecular termination of radicals.

The activation energy E and the frequency factor Z values were obtained using Chang equation [108], such that

$$\ln\left[\frac{d\alpha / dt}{(1-\alpha)^n} \right] = \ln Z - \frac{E}{RT}$$

(3.7)

The dependence of the left hand term on 1/T was linear in the range of α from 0.1 to 0.5, see Figure 3.14. E values and $\ln Z$ were obtained from the slope and intercept of the lines respectively (regression coefficients were larger than 0.980) and these are listed in Table 3.5. The activation energy of PEEK thermal decomposition is within the range of reported values of 223.5 and 219.7 kJ mol^{-1}, as determined from dynamic and isothermal procedures respectively [109] , and as can be seen from Table 3.5 this value decreased with dose due to the production of thermally less-stable products on irradiation. The same trend was found with the frequency factor which can be used as a measure of the lifetime of the materials. The reaction order was consistent with the same degradation kinetics involved on all samples studied, although it is a complex mechanism.

Table 3.5: Thermal degradation kinetic parameters for different PEEK samples using the Chang and second Kissinger techniques at $10^{\circ}C$ min^{-1} in Argon.

irradiation	Dose (MGy)	Activation energy, E (kJ mol^{-1})	Frequency factor, ln Z (min^{-1})	Reaction order 2nd Kissinger n ± 0.3
Un-irradiated	0	265 ± 10	37 ± 2	1.6
H$^+$	2.3	260 ± 5	36 ± 2	1.4
	9.3	245 ± 15	34 ± 2	1.2
	10.2	250 ± 20	35 ± 3	1.2
	21.3	225 ± 10	31 ± 2	1.5
	44.3	200 ± 5	28 ± 1	1.4
	66.7	170 ± 5	24 ± 1	1.5
He^{2+}	7.3	240 ± 5	34 ± 1	0.9
	13.1	230 ± 5	32 ± 1	1.4
	40.1	165 ± 15	23 ± 2	1.7

3.3.3.2.3 Lifetime Estimation

The kinetics parameters of the thermal degradation were used to estimate the lifetime t_f of PEEK samples to failure at different temperatures. This was calculated at a weight loss of 5 wt%, by the following equation [110]:

$$t_f = \frac{1-0.95^{1-n}}{Z(1-n)}.\exp\frac{E}{RT} \qquad (n \neq 1) \qquad (3.8)$$
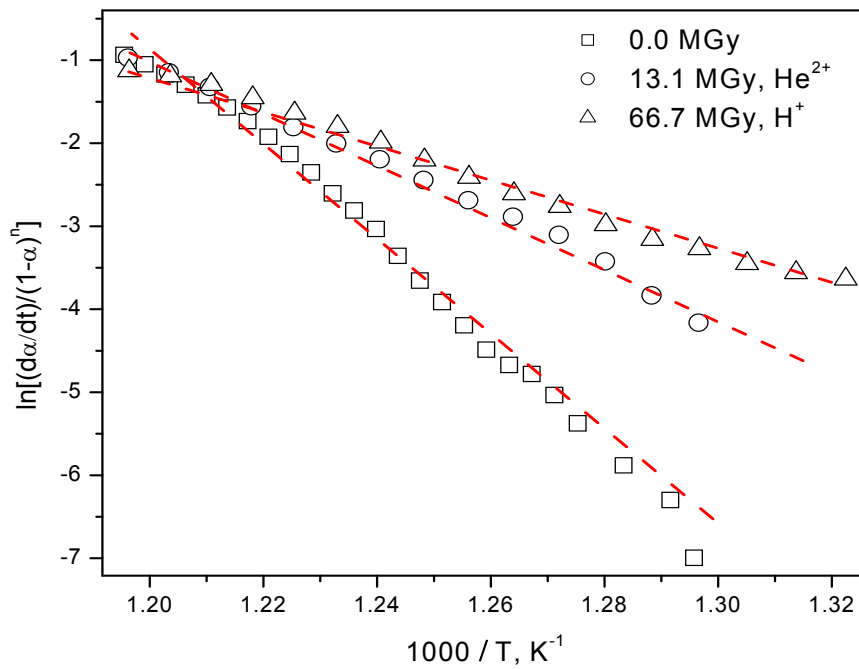
Figure 3.14: Application of Chang method to the thermal degradation kinetics of different PEEK samples.

Figure 3.15 represents the estimated lifetime as a function of temperature at constant irradiation dose. The analyses of PEEK degradation by this mean predict a lifetime of 10 years at 300°C.

A value that is consistent with the previous work [109] and well represents the high thermal stability of PEEK in inert atmosphere. On irradiation the lifetime decreased significantly but the irradiated materials was still considered to have good thermal stability for many industrial applications. The effect of irradiation dose on the estimated lifetime is presented in Figure 3.16 at three temperatures. It is clear that helium ions had a more marked effect in decreasing the lifetime and in general changing the materials properties of PEEK.
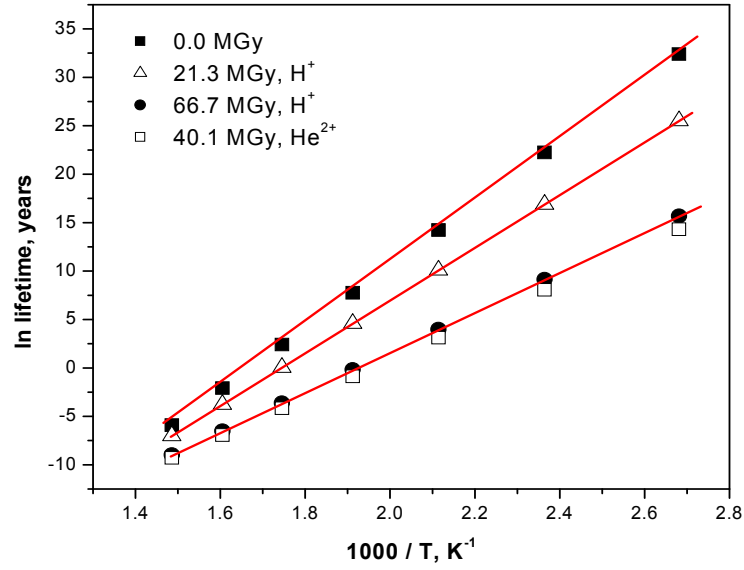
Figure 3.15: Estimated lifetime curves for PEEK samples.
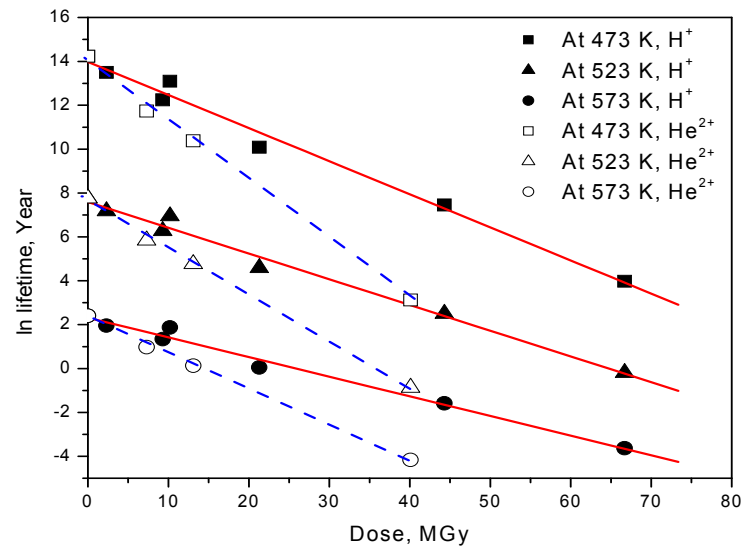
Figure 3.16: Estimation of lifetime at three different temperatures and the effect of dose.

3.3.4 Discussions

Irradiation effects on organic materials depend upon many factors such as the temperature, the atmospheric composition and dose. However, when the effects of different radiation sources are investigated another factor must be considered, that is the so-called linear energy transfer,

LET, [83, 85] which is defined as the energy deposition rate per track length (-dE/dx). The LET depends on the kinetic energy of the particles traversing the polymer, and on irradiating amorphous PEEK with protons and helium ions this dependence is shown in Figure 3.17. The LET for both ions increases with increasing energy, E, and reaches a maximum corresponding to relatively low values of E; 0.1 and 0.6 MeV for 40 MeV protons and 40 MeV helium respectively. Figure 3.17 also indicates that the LET is not constant nor a linear function of the energy, but for the energies used for the two ions, the LET of the helium ions was approximately five times higher than that of the protons.
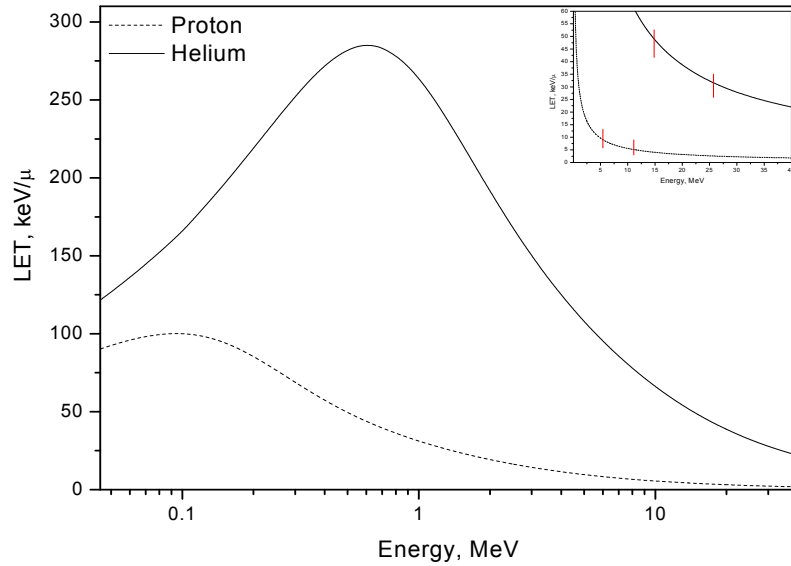
Figure 3.17: Linear energy transfer, LET, for helium and proton ions in amorphous PEEK; plotted as a function of ion energy.

This explains why the effect of irradiation with helium at low dose is more pronounced than with protons. Similar observation have been reported by Sasuga and Kudoh [61], who studied the effect of different radiation sources including electron, proton and helium on the thermal and mechanical properties of PEEK. It has also been reported, in the case of polystyrene [111, 112] and poly (methyl methacrylate) [113] that G(X) increases and G(S) decreases on

irradiation with ions of high LET. This phenomenon is explained in terms of the high density of excitation and a higher probability of recombination of active species [61, 111-113].

3.4 Conclusions

Alterations produced in the molecular structure of amorphous PEEK by irradiation with 11.7 MeV H^+ and 25.6 MeV He^{2+} ions have been interpreted as due to chain scission and formation of cross links. The efficiency of the ions in inducing these changes is dependent on their relative LET effects, but both ions altered the polymer's physical and thermal properties to a similar extent.

The detailed structure of the cross link units could not be established from the FT-IR spectra due to their relatively low concentration. However, there were little or no changes in the observed spectra on irradiation indicating that the molecular structure of PEEK is resistant to irradiation. The observed T_g increases linearly with cross link density in accordance with the DiBenedetto equation from which the cross linking constants were determined. Since these two constants were very similar the cross link structure produced by both ions must be very similar. The only difference between the two ions is their efficiency in cross linking in line with their LET effect.

The thermal decomposition of irradiated PEEK was similar to that of untreated PEEK and seems to be a random chain scission process. The thermal decomposition temperature and kinetic data for irradiated PEEK films quantitatively suggest that these films still have sufficient thermal stability for many long term applications.

Chapter 4

Melting and Isothermal Crystallization Studies of

Irradiated PEEK

4.1 Introduction

The study of the melting process of polymers provides useful information into the nature of crystals being destroyed and the thermal history of the sample, as well as determining the upper service temperature. The melting point determines the processing temperature of a polymer and also the onset of high temperature crystallization. The rate of crystallization at a given temperature depends upon the degree of supercooling of the melt. Therefore if the melting temperature is altered in any way, the crystallization behaviour will change accordingly.

It is well known that the properties of semi-crystalline polymers such as PEEK depend on the crystallization behaviour. Therefore, a study of the morphology and kinetics of crystallization is of prime importance in understanding the role of irradiation in suppressing the development of crystallinity and changing the nucleation character as well as gaining further information in to the use of irradiated PEEK, in the field of aerospace systems, fusion reactors [55, 61] and as a membrane for fuel cells [58].

4.2 Melting Point Theory

The melting point T_m is defined as the temperature at which an equilibrium between the liquid and crystalline phases in the materials is established, e.g., when the chemical potentials of the polymer repeating unit in the two phases are equal, such that $\mu_l^o = \mu_c^o$ [114].

High molecular weight crystalline materials do not have a single, well-defined melting temperature but they melt over a broad temperature interval as measured by DSC. This behaviour suggests that a range of crystal stabilities exists within the structure, each melts at a different temperature, and that the broad melting peak observed represents a distribution of different crystal stabilities.

4.2.1 The Thermodynamic Melting Point, T_m^o

The thermodynamic (equilibrium) melting temperature, T_m^o, is defined as that for an infinitely thick crystal. The observed melting temperature, T_m, as measured by DSC is well below this equilibrium value due to the thickness [115-118] of the lamellae produced at each crystallization temperature, T_c. Hoffman and Weeks [116] have derived a relationship between melting point, T_m, and crystallization temperature, T_c, which enables T_m^o to be determined, namely

$$T_m = T_m^o \left(1 - \frac{1}{2\beta}\right) + \frac{1}{2\beta} T_c \qquad (4.1)$$

where $\beta = \dfrac{\sigma_e l}{\sigma l_e}$, σ is the fold surface free energy, l is the lamellae thickness and the subscript e refers to equilibrium conditions. A plot of T_m against T_c is linear with slope $1/2\beta$ and $\beta = 1.0$ in the absence of re-crystallization or annealing [117, 119] during melting. This line interpolates to the equilibrium condition of $T_m = T_c$ at T_m^o, but its slope must be 0.5.

4.2.2 Melting Point Depression

The melting point, T_m, depends on the composition of the liquid phase. If a diluent is present in the liquid phase, T_m may be regarded alternately as the temperature at which the specified composition is that of a saturated solution. If the liquid polymer is pure, $\mu_u \equiv \mu_u^o$, where μ_u^o represents the chemical potential in the standard state, which in accordance with the custom in the treatment of solution we take to be the pure liquid at the same temperature and pressure. At the melting point of the pure polymer T_m^o, therefore, $\mu_u^o = \mu_u^c$. To the extent that the polymer contains impurities (solvent or copolymerized units) μ_u will be less than μ_u^o. Hence μ_u after the addition of a diluent to the polymer at the temperature T_m^o will be less than μ_u^c, and in order to re-establish the condition of equilibrium a lower temperature T_m is required.

The quantitative relationship between the equilibrium temperature and the composition of the liquid phase can be derived using this thermodynamic approach [114]. The condition of equilibrium can be expressed as follow:

The difference between the chemical potential of the crystalline repeating unit and the unit in the standard state (the pure liquid polymer at the same temperature and pressure), must be equal to the decrease in chemical potential of the polymer unit in the solution relative to the same standard state.

$$\mu_u^c - \mu_u^o = \mu_u - \mu_u^o \tag{4.2}$$

The former difference in the left hand side of eq. (4.2) is simply the negative of the free energy of fusion ΔG_u. Hence it may be written as

$$\mu_u^c - \mu_u^o = -\Delta G_u = -\left(\Delta H_u - T\Delta S_u\right) \tag{4.3}$$

Where ΔH_u and ΔS_u are the heat and entropy of fusion per repeating unit. At $T = T_m^o$ the difference in chemical potential is zero and the ratio $\Delta H_u^o \big/ \Delta S_u^o$ can be assumed to be constant in the temperature range T_m^o to T and equal to T_m^o. Eq. (4.3) is then expressed as follows:

$$\mu_u^c - \mu_u^o = -\Delta H_u \left(1 - T\big/T_m^o\right) \tag{4.4}$$

An expression for $\mu_u - \mu_u^o$ is also required as this represents the lowering of the chemical potential of the unit in the liquid phase due to the presence of diluent. In the case of an ideal solution, $\mu_2 - \mu_2^o = -RT \ln N_2$, where N_2 is the mole fraction of the crystallizing component (which is the solvent if melting point depressions are considered and the solute if the results are tabulated as solubilities). By combining this relation with eq. (4.4) we arrive at the solubility relationship for an ideal solution

$$\frac{1}{T_m} - \frac{1}{T_m^o} = -\frac{R}{\Delta H_2} \ln N_2 \tag{4.5}$$

where ΔH_2 is the heat of fusion of the major component, 2.

Similarly, in a copolymer system consist of monomer units which crystallize and structurally different units which did not and these are placed randomly along the chain, Flory [114] showed that:

$$\frac{1}{T_m} - \frac{1}{T_m^o} = -\frac{R}{\Delta H_u} \ln N_A \tag{4.6}$$

where N_A is the mole fraction of monomer units, R is the gas constant and ΔH_u is the heat of fusion per repeat unit.

4.3 Crystallization Kinetics

Crystallization is the transformation of a liquid into a crystalline phase and involves two basic processes, e.g., nucleation, initiation of the new phase from the parent phase and growth of the new phase [120].

4.3.1 Nucleation

In cooling a molten polymer there is a tendency for the randomly organized molecules in the melt to become aligned and form small ordered regions, which are called nuclei. This process is called nucleation. There are two types of nucleation, e.g., homogeneous and heterogeneous. The homogeneous process has a higher energy than the liquid and requires the polymer to be supercooled for a crystal to be created spontaneously in the interior of a uniform substance. On the other hand, nucleation can also occur heterogeneously on a foreign substrate such as bubbles, dust particles and surfaces. Heterogeneous nucleation always occurs at lower supercooling, since nucleation on an existing surface area has a lower free energy barrier.

Homogeneous nucleation can be subdivided according to the mode of formation, e.g., primary, secondary and tertiary nucleation. The formation of a polymer crystal from the liquid state starts with primary nucleation in which a few molecules pack parallel to one another and form small embryos of the crystalline state. After that the additions are accompanied by chain folding. In this step a crystal surface is created which has an excess of surface energy proportional to the surface area. Incorporating more molecules to the crystal leads to a decrease in the free energy by a factor which is proportional to the crystal volume. The surface-to-volume ratio gives an indication of the free energy of nucleus formation, ΔG_n, such that when the ratio is high $\Delta G_n > 0$ due to excess of surface energy over bulk. ΔG_n increases and reach a maximum corresponding to the critical size of the nucleus, after which

ΔG_n decreases. Finally the free energy will be less than that of the melt. These competing effects are shown graphically in Figure 4.1[120].

The secondary nucleation is the process by which a new layer grows on a pre-existing surface. It is similar to primary nucleation but with a lower free enthalpy barrier since the surface area newly created is smaller. On the other hand, the rate of crystal growth is nucleation controlled at low super cooling.

Tertiary nucleation only involves the formation of new layers between two pre-existing surfaces and determines the rate of covering a nucleated crystal surface. It has the lowest surface-to-bulk free energy ratio compared to primary and secondary nucleation.
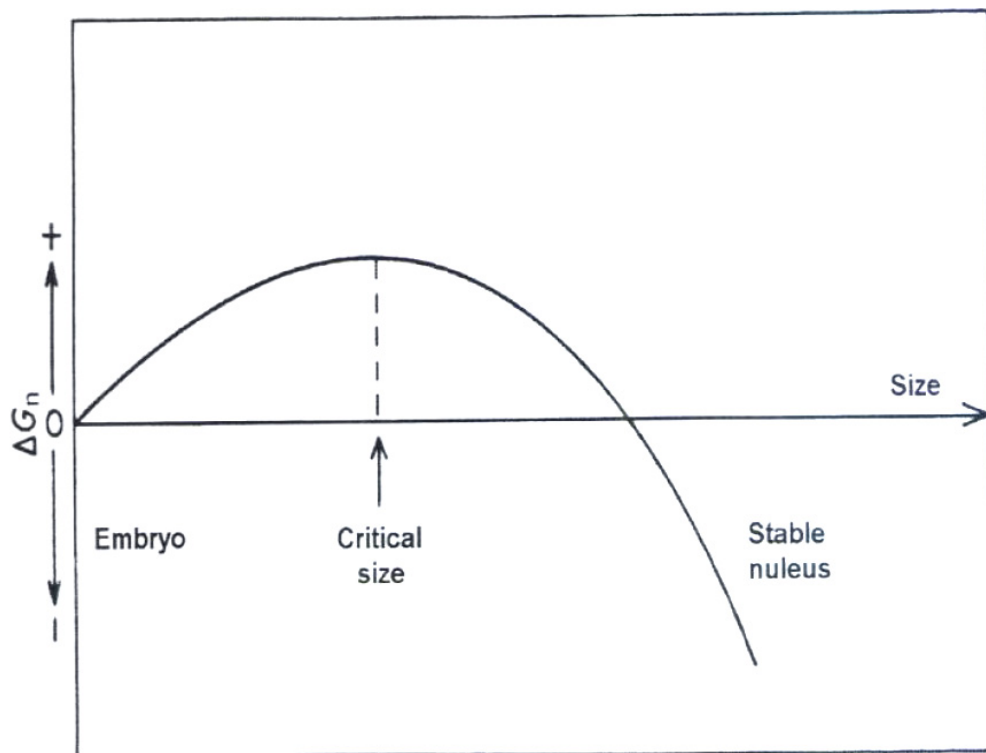
Figure 4.1: Schematic representation of the variation of free energy with nucleus size for the formation of a stable polymer crystal nucleus [120].

4.3.2 Crystal Growth

Crystals begin to grow on the surfaces once the critical size nucleus is formed. This process is called secondary nucleation. If the cross sectional area of the polymer chain is denoted as ($a \times b$), where a and b are the breadth and width of the crystallographic unit cell respectively, then the chain spreads gradually across the crystal face. After this initial chain attachment, molecular strands lay down gradually on a smooth crystal surface followed by additional chains adhering once more to this interface by a chain folding process. These chains then fold across the surface, thereby extending the growth front and crystal dimensions at a rate that depends on the under cooling [120].

4.3.3 The Temperature Dependence of Growth Rate

The overall temperature dependence of rate of growth, g, of a crystal is bell shaped and has been accounted for by the Gibbs-Thomson equation [121]. This has been modified by Hoffman and Lauritzen [119, 120, 122, 123] specifically for polymer crystallization, such that,

$$g = g_o \exp\left(-\frac{E/R}{T - T_\infty}\right) \exp\left(\frac{K_g}{T\Delta Tf}\right) \tag{4.7}$$

with g_o a constant and,

$$K_g = \frac{nb_o \sigma \sigma_e T_m^o}{\Delta H_f k} \tag{4.8}$$

The first exponential term of eq.(4.7) describes the effect of the temperature dependence of melt viscosity and accounts for the reduced molecular mobility as the temperature approaches the glass transition temperature, and in particular the thermodynamic glass transition

temperature $T_\infty = T_g - 30$. Hoffman has assigned a value of 6300 J mol^{-1} for E which represents the activation energy for chain transport and also viscous flow.

The second exponential term accounts for the rate determining effect of primary nucleation on the crystallization at low degrees of supercooling. The parameter $f = \dfrac{2T}{\left(T + T_m^o\right)}$ is a correction factor which accounts for the change in the latent heat of fusion that occurs with temperature.

The nucleation constant K_g contains the surface free energy product, $\sigma\sigma_e$, where σ is the lateral surface energy and σ_e fold surface free energy of the critical size nucleus, the heat of fusion ΔH_f per unit volume, the unit cell dimension, b_0, the separation between two adjacent fold planes, which in the case of PEEK is 0.592 nm [124], and k the Boltzmann constant.

The nucleation constant, K_g, depends on the nucleation regime for which Lauritzen and Hoffman defined three regimes predominating at different temperatures. These are termed as regime I, II and III and in eq. (4.8) n = 4 for regimes I and III and 2 for regime II.

In regime I, each nucleation on the growing crystal surface leads to rapid completion of the growth strip by chain folding prior to the next nucleation event, this occurs at temperatures approaching the melting point. At much lower temperatures there is prolific multiple nucleation on the growth surface and this is referred to as regime III. Regime II occurs between these two limits where there is competition between chain folding and nucleation.

4.3.4 The Avrami Equation

The kinetics of phase change on crystallization has been described by Avrami. This approach has been highly successful in describing crystallization in polymers [71]. The Avrami equation relates the extent of crystallinity to time [125-127], such that

$$1 - \frac{X_t}{X_\infty} = \exp(-Zt^n) \tag{4.9}$$

in which X_t, is the fractional crystallinity, which has developed at time t, Z is a composite rate constant incorporating nucleation and growth rate constants and n is an integer constant whose value depends on the crystallization mechanism. The corresponding expressions for n and Z are listed in Table 4.1.

In addition to assuming random nucleation in a supercooled melt, the Avrami equation was derived making the following assumption [120]:

1. The rates of nucleation and growth increase are constant with time.

2. Only primarily crystallization process and no secondary crystallization occur.

3. The volume remains constant during crystallization.

4. When one crystallite impinges upon another growth ceases.

5. The crystal keeps its original shape in one, two or three dimension (rods, discs or spheres, respectively) until impingement take place.

6. There is no induction time before crystallization.

Table 4.1: Avrami parameters for different types of crystallization mechanism[120].

Crystallization mechanism		n	Z *	Geometric restriction
Spheres	Sporadic	4	$2/3\,\pi g^3 l$	3 dimensions
	predetermined	3	$4/3\,\pi g^3 L$	3 dimensions
Discs	Sporadic	3	$1/3\,\pi g^2 l d$	2 dimensions
	predetermined	2	$\pi g^2 L\, d$	2 dimensions
Rods	Sporadic	2	$1/4\,\pi g l\, r^2$	1 dimension
	predetermined	1	$1/2\,\pi g L\, r^2$	1 dimension

* where g is crystal growth rate; l is nucleation rate; L is density of nuclei; d is constant thickness of discs and r is constant radius of rods.

4.4 Results and Discussions

4.4.1 Proton Irradiation

The details of ion irradiation were discussed in chapter 3; see Table 3.1 and paragraph 3.2. For the isothermal crystallization kinetics study only the PEEK samples irradiated with protons, using the same stopping power (the same layer number), with doses ranging from 0-10 MGy were considered. This clarified the effect of dose on the crystallization process and eliminated any changes that may arise from the particle track structure in amorphous PEEK and the LET effect [61, 83].

4.4.2 General Irradiation Effects on Melting and Crystallization Processes

Figures 4.2 and 4.3 show the changes in the crystallization characteristics of PEEK on ion irradiation. In the case of un-irradiated amorphous PEEK, crystallization occurs rapidly on heating above T_g, to give a narrow exotherm and an enthalpy of 22.0 J g^{-1}. As the absorbed dose increased, both the temperature of crystallization and the peak width increased, but the enthalpy of crystallization decreased.

On the other hand, the recrystallization temperature T_{rc} and the enthalpy of recrystallization, ΔH_{rc}, on cooling from the molten state decreased as the dose increased. This behaviour of T_c and T_{rc} with dose was consistent with the occurrence of cross linking as the later reduced the extent of crystallization of the polymer [55, 61, 91, 93, 96, 97]. The degree of cross linking increased with increasing dose [57, 83] in both irradiations, consequently the restriction of the re-crystallization process in amorphous PEEK was more apparent at higher doses and was of sufficient severity to prohibit crystallization of the material above 50 and 23 MGy on irradiation with H$^+$ and He^{2+}, respectively.

The melting point T_m of the un-irradiated PEEK shifted to higher values on second heating due to the change in chain conformation of the polymer after re-crystallizing on cooling from the molten state. As the dose increased, both T_m on the first and second heating runs decreased. This effect was a direct result of crystallization retardation above T_g and as a result of the development of cross links.

The enthalpy of fusion, ΔH_m, was observed to decrease with increasing irradiation dose indicating that molecular changes prevented crystallization from developing. This decrease

also indicated a lower weight degree of crystallinity, $X_{c,w}$, ($X_{c,w}$ was measured as $\Delta H_m \big/ \Delta H_m^0$

[104], where ΔH_m^0 is the heat of fusion for completely crystalline PEEK and was taken as

122.5 J g^{-1} [103]) due to the development of cross links on irradiation.
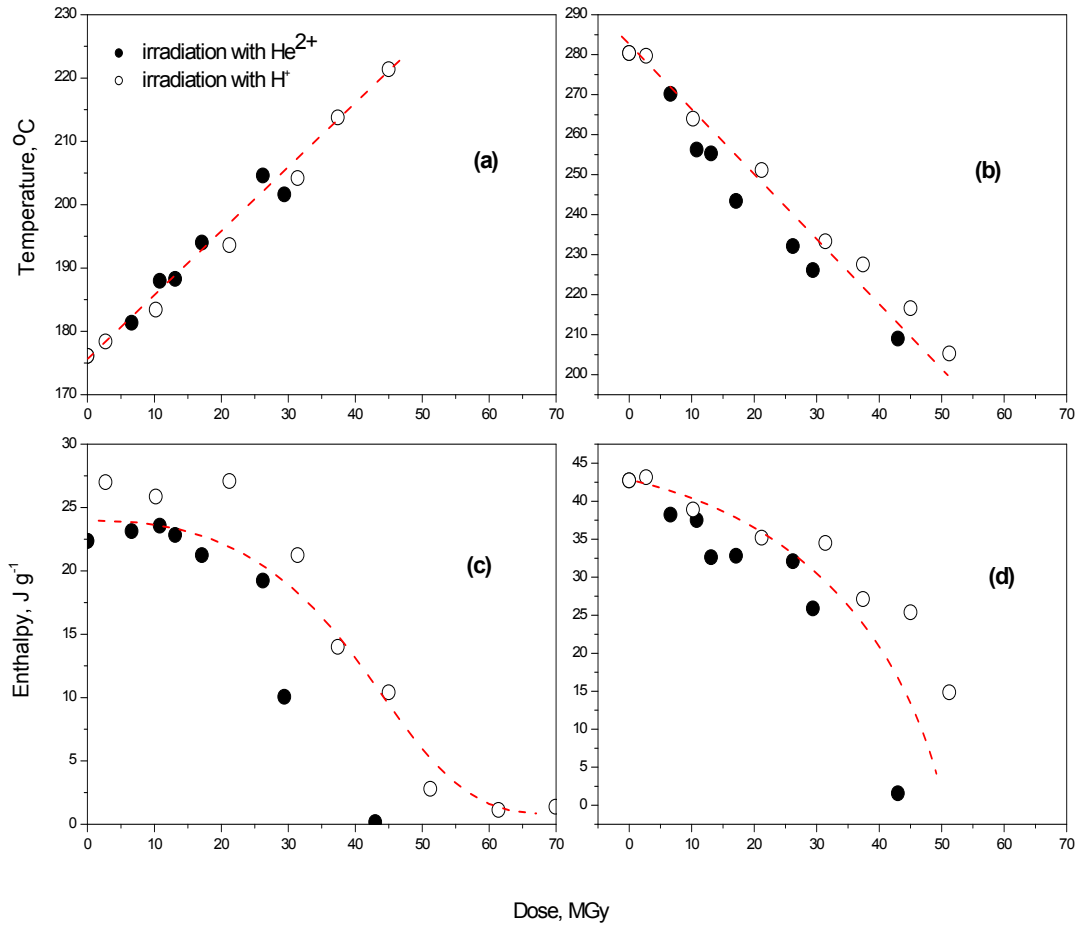
Figure 4.2: The dependence of T_c, ΔH_c , T_{rc} and ΔH_{rc} for irradiated PEEK samples on

dose; (a) crystallization temperature, (b) recrystallization temperature, (c) the enthalpy of

crystallization, and (d) the enthalpy of recrystallization.
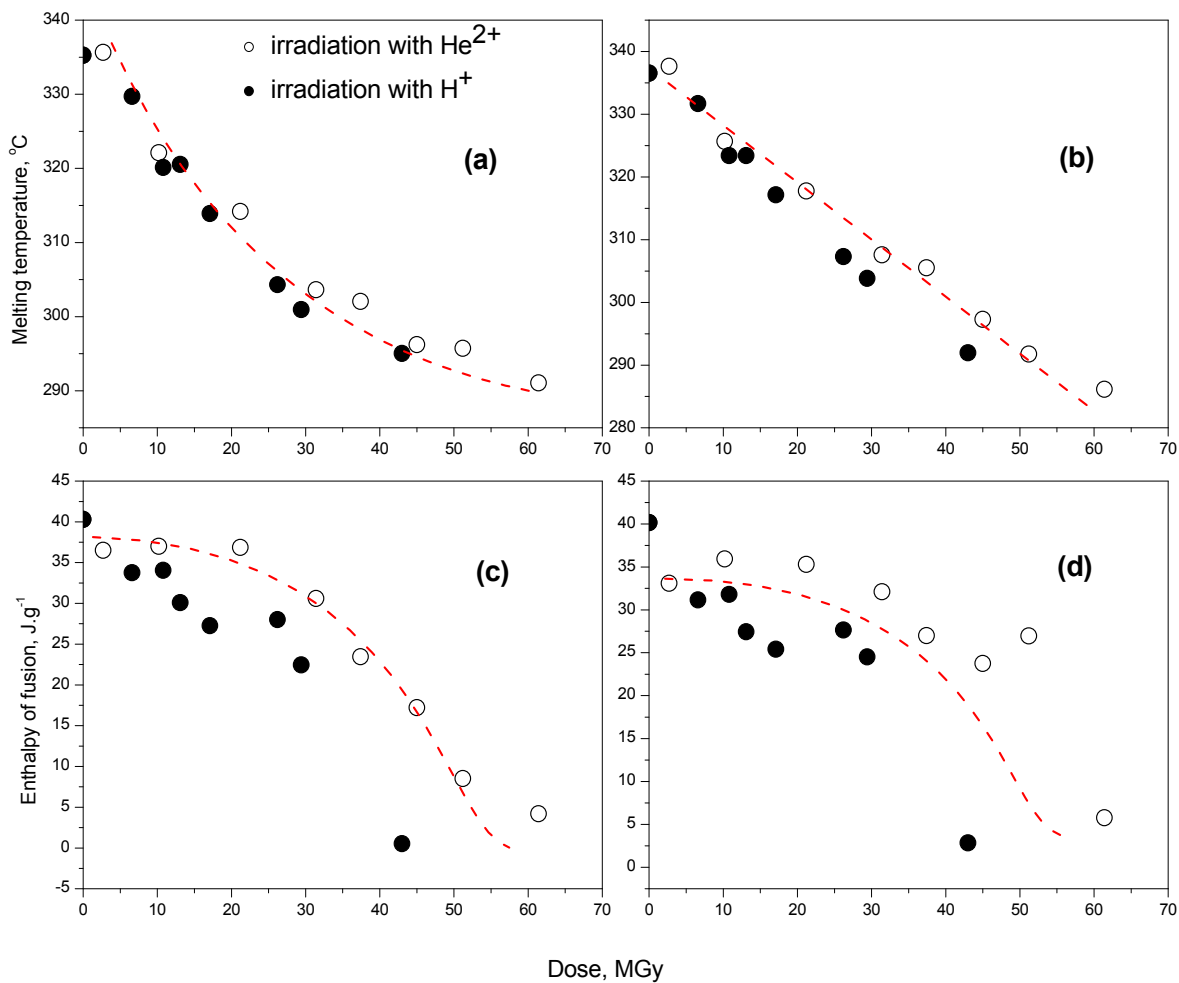
Figure 4.3: The dependence of T_m and ΔH_m for irradiated PEEK samples on dose. (a), (b) the melting point in first and second scan and (c), (d) the enthalpy of fusion in first and second scan respectively.

4.4.3 Melting Point Study

Figure 4.4 shows the Hoffman & Weeks plots for various PEEK samples. The linear fit of melting point against crystallization temperature gave slopes of 0.50 ± 0.05 consistent with equilibrium conditions, and on interpolation to $T_m = T_c$ gave the T_m^o values listed in Table 4.2.
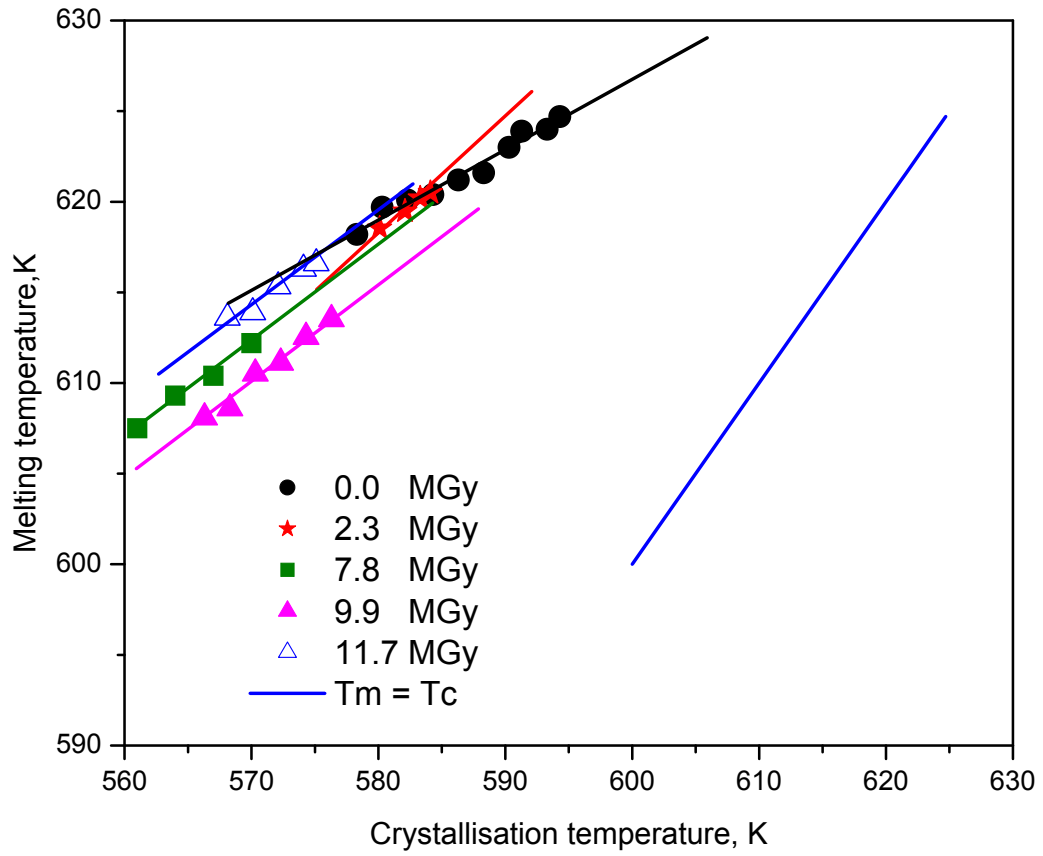
Figure 4.4: Hoffman & Weeks plots for amorphous and irradiated PEEK samples.

Table 4.2: The thermodynamic melting points of the PEEK samples.

Dose (MGy)	$\beta \pm 0.05$	$T_m^o \pm 2.0$ (K)	$1-N_A \pm 0.002$ (mole fraction)
0	1.02	662.6	0.000
2.3	1.00	661.1	0.015
7.8	0.98	659.8	0.027
9.9	0.96	657.2	0.055
11.7	1.06	653.2	0.078

The value of T_m^o obtained for PEEK compared favorably with values reported by Blundell [115, 128] and Proter [129] respectively namely 668.0, 670.1 and 663.0 K but there was a progressive decrease in T_m^o value with increasing irradiation dose, see Figure 4.5.
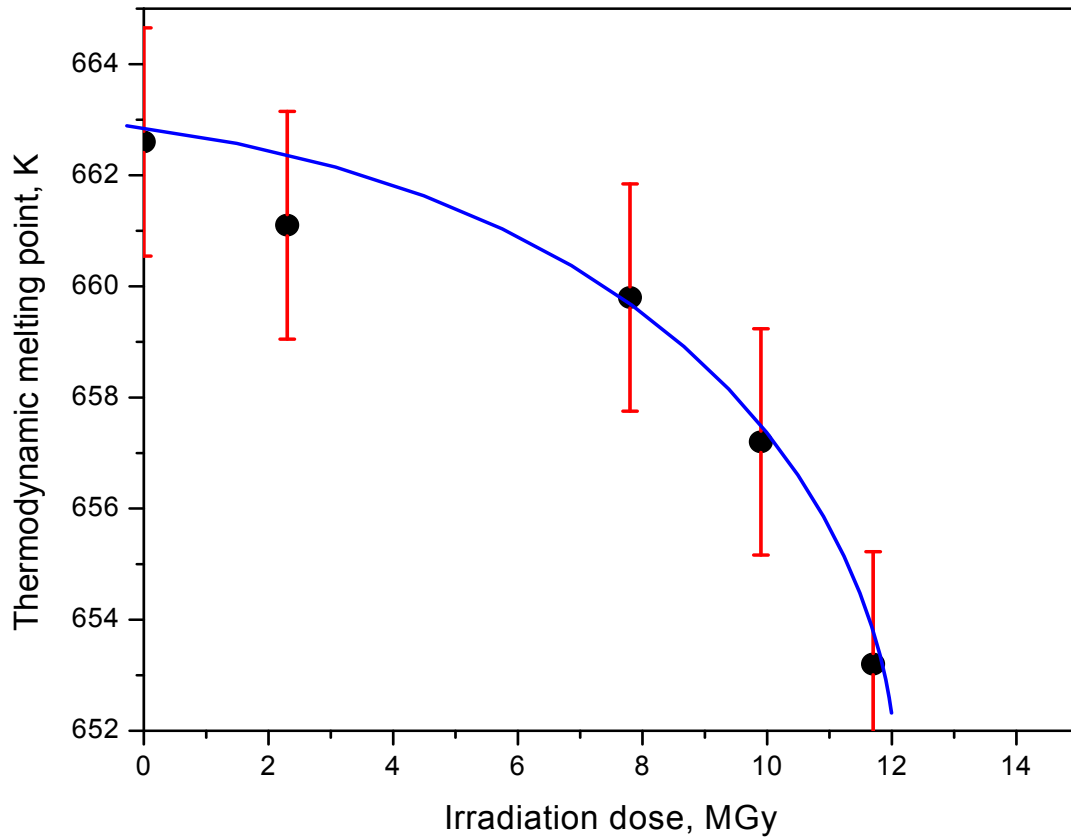
Figure 4.5: The thermodynamic melting point as a function of irradiated dose.

It is known that the thermodynamic T_m^o of crystalline polymers decreases with the number of impurity defects in the chain [130] if these are non-crystallizable since these defects restrict the length of the segments between adjacent defects along the chain which can crystallize, and so reduce the average length of the crystallizable units.

The depression of the thermodynamic melting point was analyzed by eq. (4.6) derived by Flory [114], using the analogy that the irradiated polymer consist of repeating units which crystallize and structurally different units which did not and these are placed randomly along

the chain. The effect of irradiation dose on the depression of the equilibrium melting point of PEEK is shown in Figure 4.5. The heat of fusion of PEEK [103] was taken to be 122.5 J g^{-1} and the mole fraction of non-crystallizable units produced on irradiation calculated from eq. (4.6), shown in Table 4.2. As can be seen, the fraction of non-crystallizable units increased progressively with dose.

The glass transition temperature also increases linearly with the concentration of impurity groups as determined by the depression of the equilibrium melting point, see Figure 4.6. It would appear that these structural irregularities are cross links as they alone would increase the glass transition temperature and increase with irradiation dose.
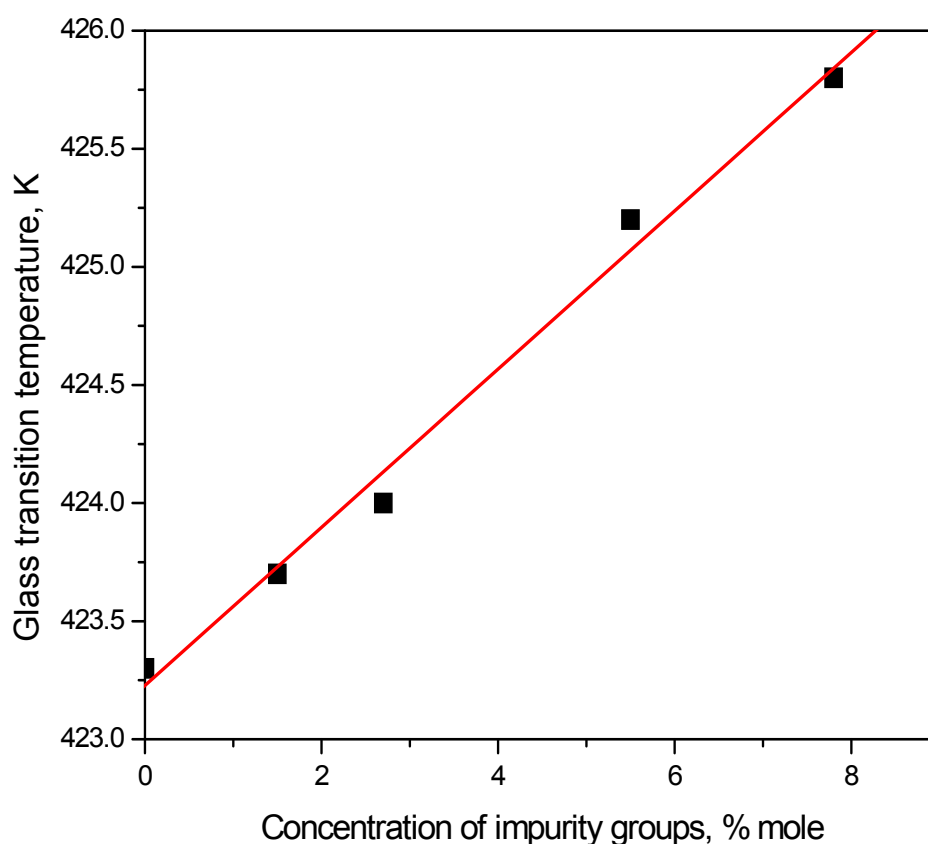
Figure 4.6: The increase in glass transition temperature with impurity concentration.

4.4.4 Isothermal Crystallization Study

4.4.4.1 Analysis of Crystallization Data; TMR Model

Figure 4.7 shows typical crystallization curves for amorphous PEEK at different isothermal temperatures as measured by rapid cooling to the crystallization temperature and after correcting for the cooling curve. The heat flow response was measured for sufficient time to enable the calorimeter response to return to the baseline when crystallization was considered to be complete. This procedure was repeated with the series of samples listed in Table 4.3 in order to determine the effect of the low irradiation dose on the overall crystallization rates characteristics.
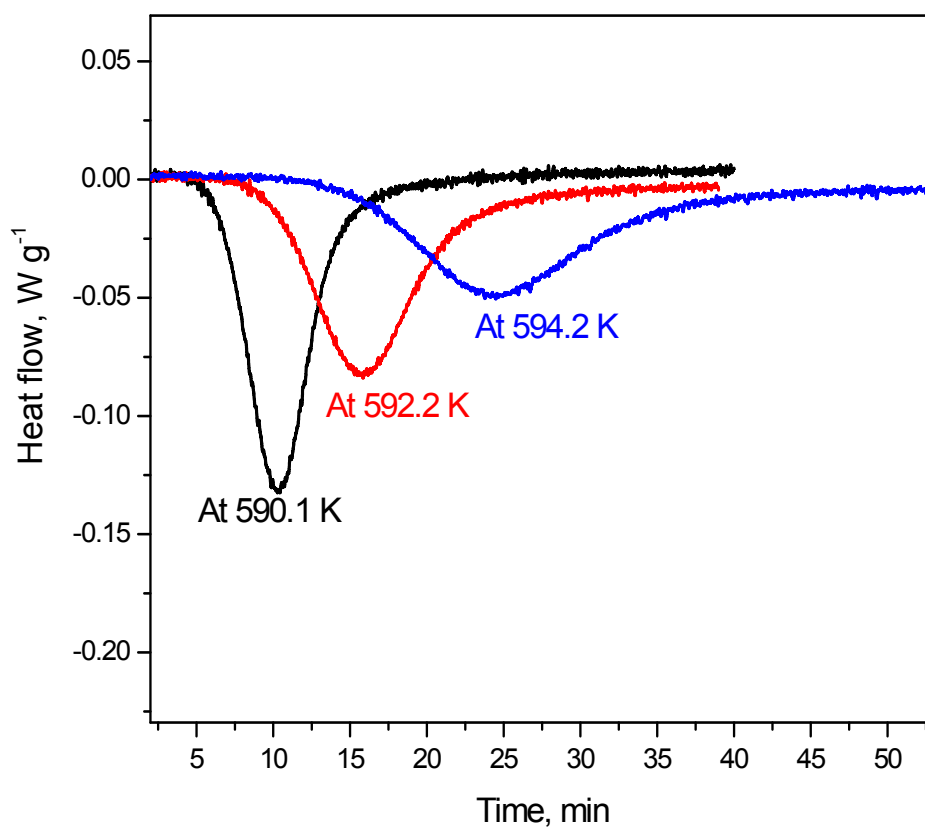
Figure 4.7: Isothermal crystallization of amorphous PEEK.

The half life of the crystallization, $t_{1/2}$, as measured from the time to reach the maximum rate of the crystallization [131], TMR, was used as a relative measure of the rate of crystallization since it was directly measured from the calorimeter response and did not require any assumptions about mechanism of crystal growth and suitable rate equations. It varied, see Figure 4.8, markedly with crystallization temperature, T_c, and showed a clear displacement of the half lives to lower temperature, by as much as 10-15 K, with radiation dose. Below 560 K the half lives of crystallization were too short for a clear separation of this trend. In the temperature range studied, the unirradiated PEEK samples crystallized fastest with shortest TMR and the rate decreased with increasing crystallization temperature.
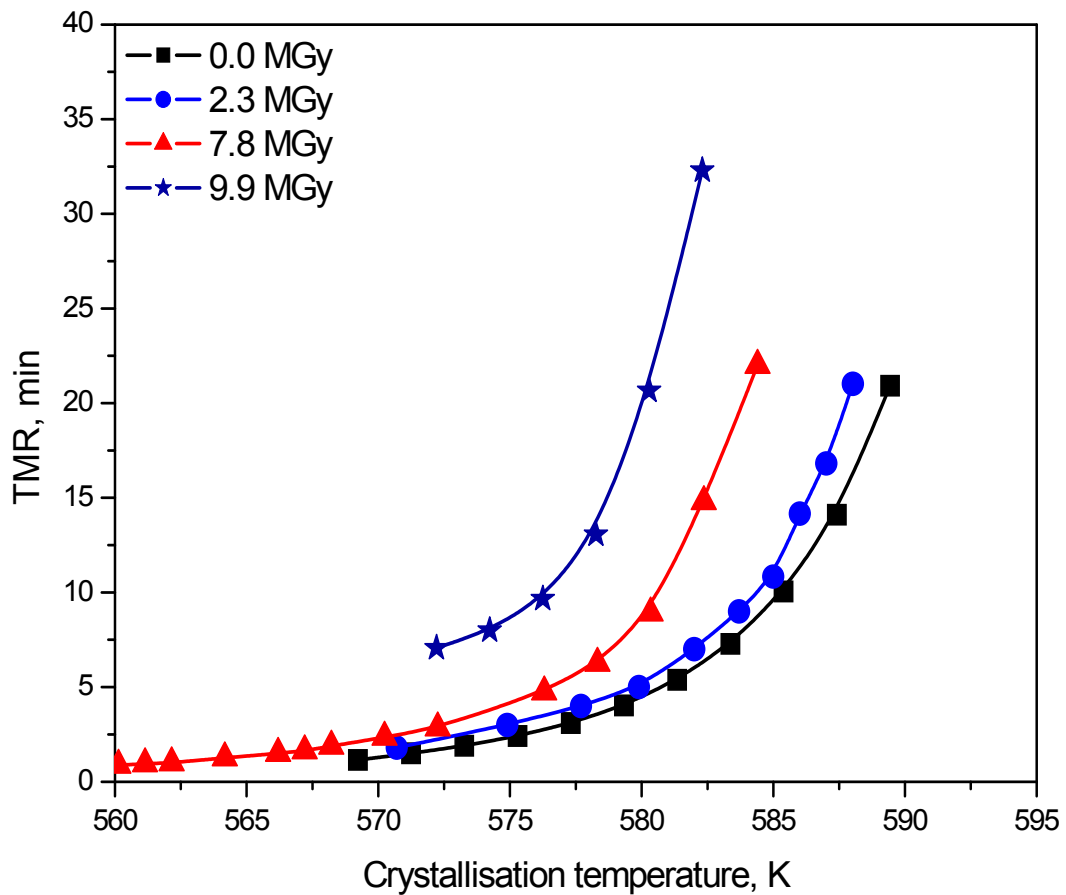
Figure 4.8: Variation of the TMR between the irradiated samples.

4.4.4.2 Crystallization Kinetics; Avrami Equation

A more detailed investigation on the effect of irradiation was carried out by an analysis of the crystallization kinetics using eq. (4.9). X_t was measured from the ratio of the two areas between the heat flow-time curve and baseline [131, 132], from t = 0 to t = t and from t = 0 to t = ∞, such that,

$$\frac{X_t}{X_\infty} = \frac{\int_0^t \left(\frac{dH_t}{dt}\right) dt}{\int_0^\infty \left(\frac{dH_t}{dt}\right) dt} \tag{4.10}$$

Rearranging the Avrami equation gave,

$$\log\left[-\ln\left(1 - \frac{X_t}{X_\infty}\right)\right] = n\log t + \log Z \tag{4.11}$$

The average value for the rate constant, Z, was calculated from the half-life, $t_{1/2}$, and the Avrami exponent n obtained from the slope of the plot of $\log(-\ln(1 - X_t))$ against log t, since,

$$Z = \frac{\ln 2}{(t_{1/2})^n} \tag{4.12}$$

Figure 4.9 shows plots of $\log(-\ln(1 - X_t))$ against log t for un-irradiated PEEK. These plots were linear up to 75-85 % conversion where the slope changes to 1.0. This was interpreted as due to a change in mechanism from primary to secondary crystallization.

The rate constants and n values along with $t_{1/2}$ are listed in Table 4.3 as a function of crystallization temperature for PEEK and the irradiated samples. The n values were essentially constant within experimental error at 3.0 ± 0.2, consistent with the growth of

predetermined spherulites. For each sample, $t_{1/2}$ increased and Z decreased, with increasing

crystallization temperature, see Table 4.3, but in every case PEEK crystallized at a faster rate

than the irradiated samples at the same temperature.
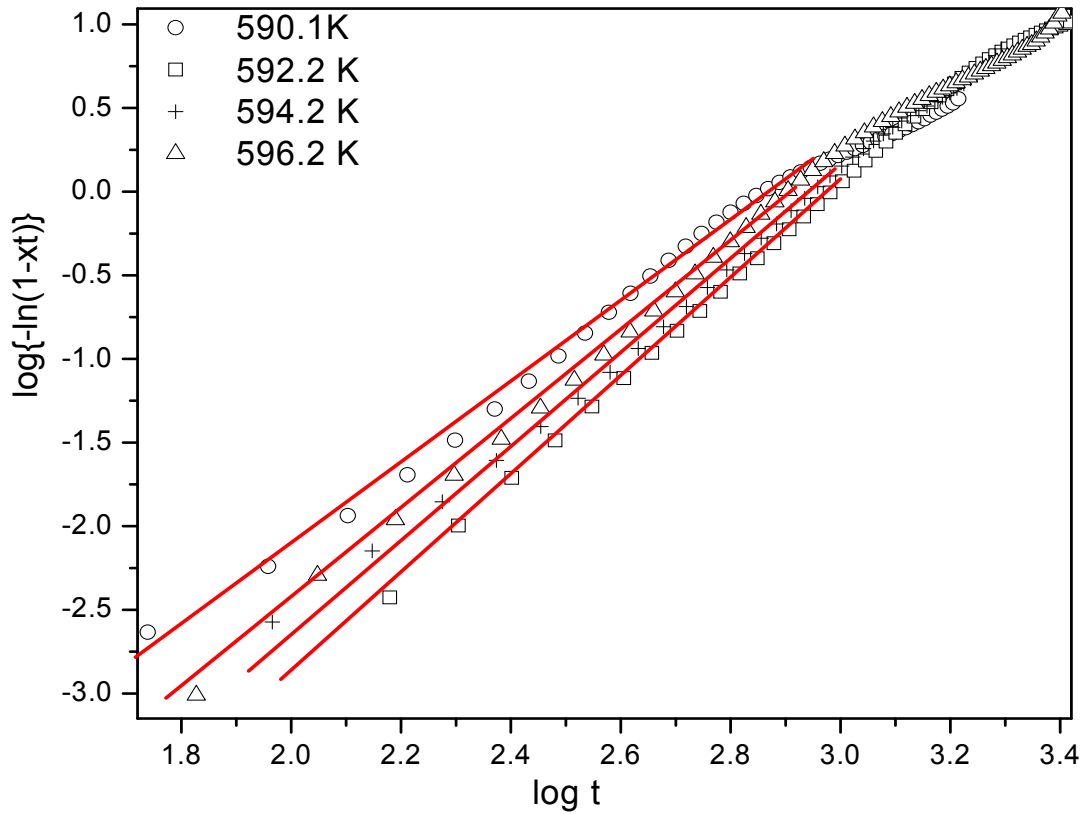
Figure 4.9: An Avrami plot for the isothermal crystallization of PEEK.

Similar conclusions were reached from the logarithmic plots of the half-lives, ln $(t_{1/2})$ against

crystallization temperature, T_c, in that the half lives progressively increased with irradiation

and the crystallization rates were displaced to lower crystallization temperatures with dose,

see Figure 4.10.

Irradiated samples were observed to crystallize at the same rate as PEEK at 6 to 10 K lower

than PEEK. This could be due to changes in the equilibrium melting point, T_m^o, or to changes

in the critical size nucleus.
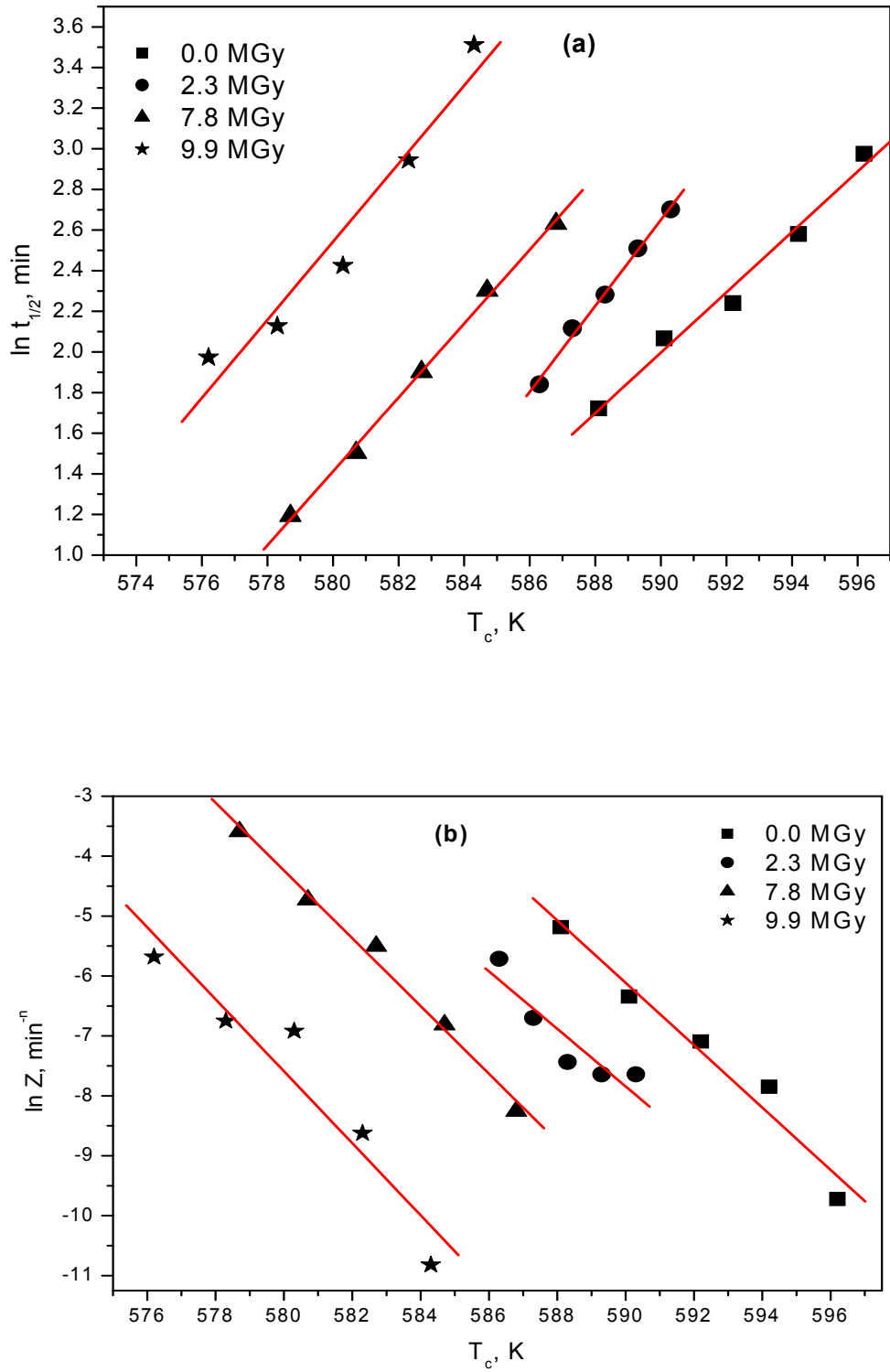
Figure 4.10: The effect of dose on the crystallization of PEEK. (a). Logarithmic plots of the half-life, $\ln t_{1/2}$, vs. crystallization temperature T_c and (b). Logarithmic plots of the rate constant, $\ln Z$, vs. crystallization temperature T_c.

Table 4.3: The Avrami parameters for PEEK samples.

Dose (MGy)	Crystallization Temperature (K)	Half-life $t_{1/2}$ (min)	$n \pm 0.2$	$Z \times 10^{-4}$ min^{-n}
0	588.1	5.6	2.8	56.0
	590.1	7.9	2.9	17.3
	592.2	9.4	3.0	8.3
	594.2	13.2	2.9	3.9
	596.2	19.6	3.0	0.9
2.3	586.3	6.3	2.9	33.3
	587.3	8.3	3.0	12.1
	588.3	9.8	3.1	5.9
	589.3	12.3	2.9	4.8
	590.3	14.9	2.7	4.7
7.8	578.7	3.3	2.7	276
	580.7	4.5	2.9	88.4
	582.7	6.7	2.7	40.8
	584.7	10.0	2.8	11.0
	586.8	13.9	3.0	2.6
9.9	576.2	7.2	2.7	33.6
	578.3	8.4	3.0	11.7
	580.3	11.3	2.7	9.9
	582.3	19.0	2.8	1.8
	584.3	33.5	3.0	0.2

Close to the melting point of a polymer the rate of crystallization is controlled by the critical size of the nucleus and there is a dependence of the rate on the degree of supercooling, $\Delta T = T_m^o - T_c$. Since, however, the maximum depression of the equilibrium melting point is about 5 K this alone is not sufficient to account for the total retardation in crystallization rate.

As can be seen from Figure 4.11 the dependence of the half-life on degree of super cooling was still displaced by as much as 9 K and so other criterion must have a more marked effect on the retardation of the crystallization than the depression of the melting point alone.
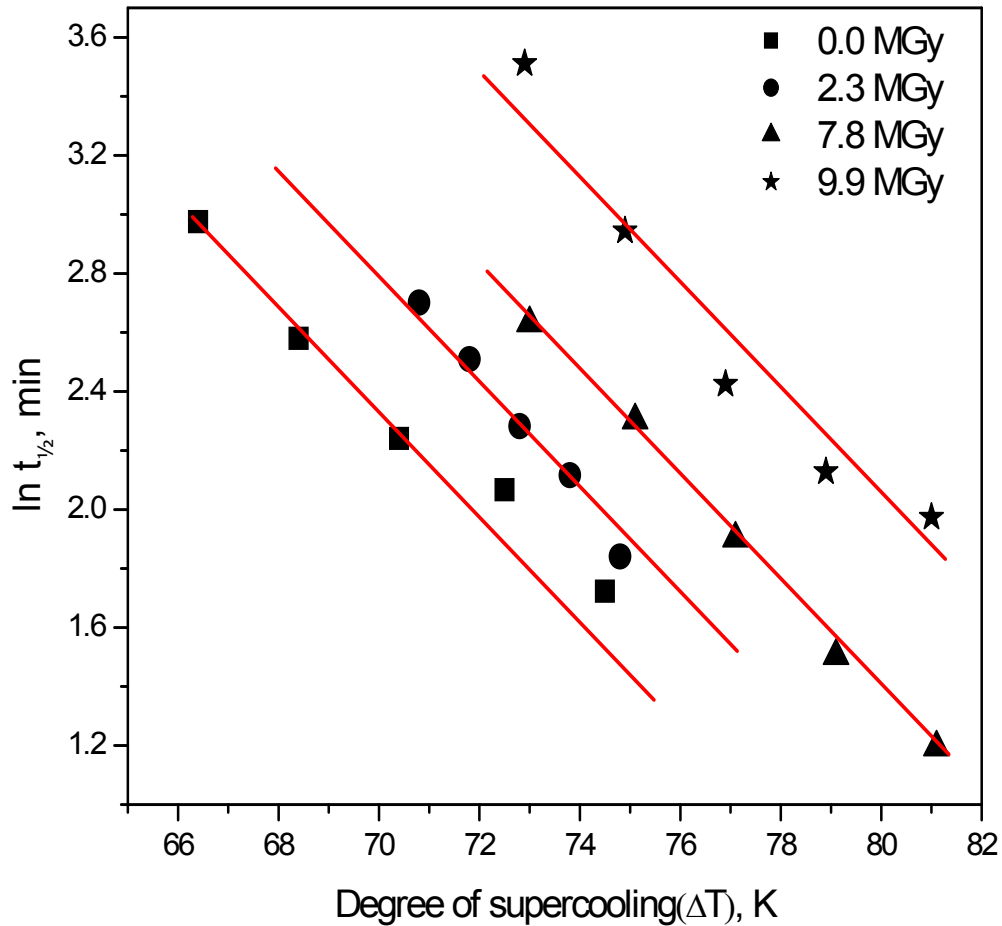
Figure 4.11: The effect of the degree of supercooling on the crystallization half-lives of PEEK samples.

4.4.5 Nucleation Control and Surface Free Energy

The primary nucleation was observed to be heterogeneous, e.g., $n = 3.0$, and the nucleation density was assumed to be constant and independent of temperature over the narrow crystallization temperature range studied, the linear growth rate g is then related to the Avrami composite rate constant Z, since

$$g = AZ^{1/n} \qquad (4.13)$$

with A is constant and n the Avrami exponent [122]. Considering eq. (4.15), it can be written that, $g \propto \ln\left(\frac{1}{t_{1/2}}\right)$ and the nucleation constant, K_g, can be determined from the slope of the linear plots, see Figure 4.12(a), of $\left\{ \ln\left(\frac{1}{t_{1/2}}\right) + \frac{E}{R(T - T_g + 30)} \right\}$ against $\left\{ \frac{1}{Tf(T_m^o - T)} \right\}$ and the values are listed in Table 4.4. The nucleation constant K_g was observed to change on irradiation and this in turn was attributed to a change in the surface free energy product, $\sigma\sigma_e$, listed in Table 4.4.

Table 4.4: Analysis of PEEK samples.

Dose (MGy)	Hoffman and Lauritzen model		Mandelkern Model	
	$-K_g \times 10^5$ (K^2)	$\sigma\sigma_e \times 10^{-3}$ ($J^2\,m^{-4}$)	$-Slope \times 10^3$ (K)	$\sigma_e \times 10^{-3}$ (*) ($J\,m^{-2}$)
0	6.45 ± 0.14	0.88 ± 0.02	0.871 ± 0.055	51.3 ± 1.4
2.3	8.37 ± 0.38	1.14 ± 0.05	$1.136 \pm 0.0\,23$	66.9 ± 3.2
7.8	8.23 ± 0.26	1.12 ± 0.04	1.095 ± 0.037	64.5 ± 2.2
9.9	10.04 ± 0.70	1.37 ± 0.10	1.370 ± 0.108	80.7 ± 6.4

(*) calculation based on the cell parameters of the PEEK crystal (a=7.781, b=5.922 and c=10.056 A^o [124]).

The effect of changes in the glass transition temperature on the temperature dependence of the half life of crystallization can be determined by comparing the above approach with a procedure outlined by Mandelkern et al. [133]. They simplified eq. (4.7) by rewriting it as

$$\ln\left(1/t_{1/2}\right) = A - \left(\frac{4\sigma\sigma_e}{R\Delta H_v}\right)\cdot\left(\frac{T_m^o}{T_c\left(T_m^o - T_c\right)}\right) \tag{4.14}$$

where A is a constant, ΔH_v is the heat of fusion per unit volume and R is the gas constant. This ignores any changes in T_g. The surface free energy product is then obtained from the slope of the linear plot of $\{-\ln (t_{1/2})\}$ against $\{\frac{T_m^o}{T_c\left(T_m^o - T_c\right)}\}$, see Figure 4.12(b). The results of this analysis are summarized in Table 4.4.

The free energy of the lateral surface, σ, arises from the parallel packing of the molecular chain in the crystal. It should not change with the presence of impurity groups and so it was assumed to be constant at $\sigma = 0.1 \times \Delta H_v$ [134]. The free energy of the chain fold surface, σ_e, is a measure of the relative packing of the chains emerging from the crystal. It has been observed to be sensitive to the composition of the melt and molecular irregularities, such as cross links and branches [135] which are rejected from the crystalline regions. Variations in the product $\sigma\sigma_e$ are thus attributed to changes in σ_e only. The product, $\sigma\sigma_e$, for PEEK is slightly lower than that reported in the literature, ($\sigma = 38\times10^{-3}$ J m^{-2} and $\sigma_e = 49\times10^{-3}$ J m^{-2}) [122, 136] but σ_e changes markedly on irradiation, from 51.3 to 80.7 $\times10^{-3}$ J m^{-2}.

The large increase in σ_e must represent an increase in steric hindrance near the fold surface from the accumulation of bulky cross links which cannot be accommodated within the crystal.
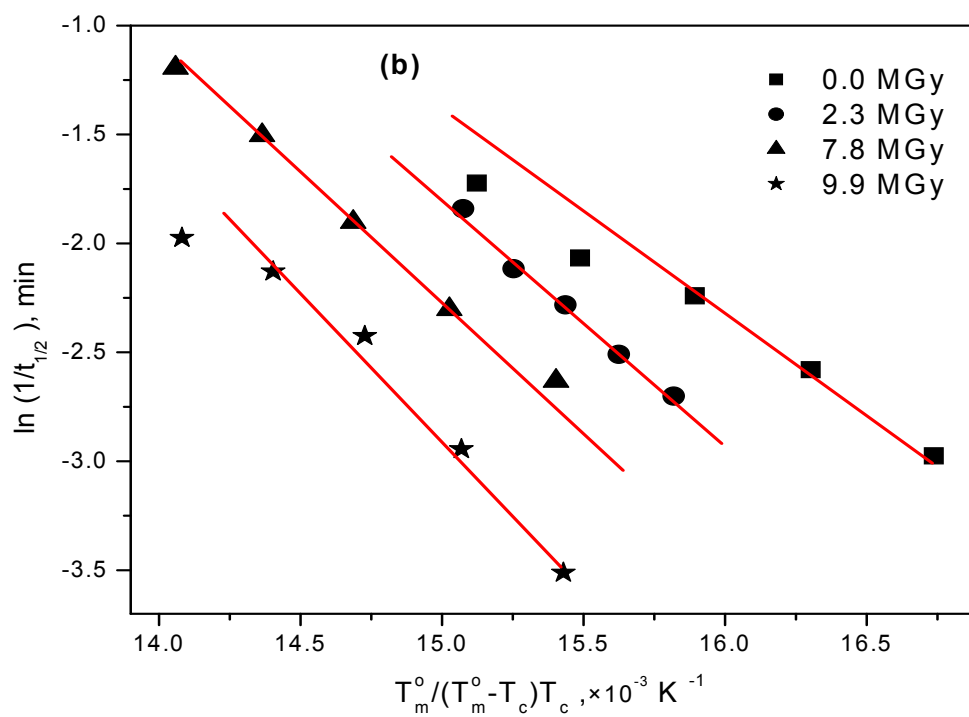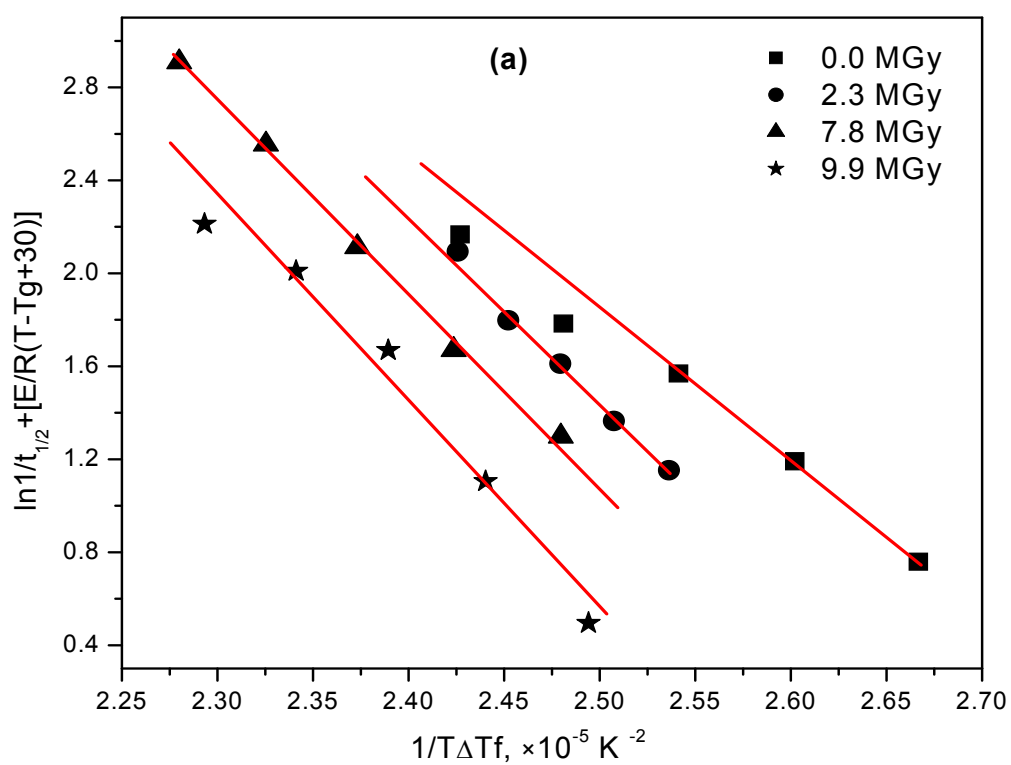
Figure 4.12: Analysis of crystallization half-lives, (a) according to Hoffman and Lauritzen

and (b) Mandelkern.

4.5 Conclusions

Proton irradiation has a significant effect on the melting and crystallization behaviour of amorphous PEEK. The DSC results indicate that the cross links which accompanied irradiation retard the crystallization, but no changes were observed in the mechanism of crystallization.

The equilibrium melting point, T_m^o, decreased with increasing irradiation dose and this depression was analyzed using the Flory equation [114] to calculate the concentration of non-crystallizable units in the molecular structure of irradiated PEEK. There was also a linear correlation between the amounts of these units and the increase in T_g which implies that these units are cross links.

The depression in T_m^o alone was not sufficient to account for the overall retardation of the crystallization. In addition, the fold surface energy, σ_e, increased on irradiation. This increase resulted from the increasing amount of cross linking within the amorphous regions, which also depressed the melting points and reduced the rate of crystallization. The average length of the repeating unit sequence between adjacent cross links determines the size of the lamellar thickness and since this decreases with increasing cross link density, it directly accounts for the inhibition of crystallization and its eventual cessation at high radiation dose.

Chapter 5

Dielectric Relaxation Spectroscopy of Irradiated PEEK

5.1 Introduction

Dielectric relaxation spectroscopy, DRS, measures changes in dielectric response of materials, such as polarization, permittivity, and conductivity, with temperature, applied voltage and frequency. This technique has been successfully applied to study molecular transitions and dielectric relaxations in polymers over a broad frequency range (from 10^{-3} to 10^{9} Hz) and a wide temperature range, and has been used to model molecular motions in dynamic systems [77, 78, 137].

Studying the dielectric behaviour of polymers provides direct practical information concerning electric insulation properties as well as microwave adsorption characteristics of polymers. This is important for amorphous polymers which are used traditionally for cable insulation as well as for passivation layers in modern electronic devices like microchips. Microwave adsorption characteristics of polymers that are necessary in relation to microwave transmission and reflection through or from materials used in telecomunication techniques or in radar applications. This is also directly related to the microwave heating characteristic of a polymer used in a microwave cooker [137].

5.1.1 Theory of Dielectric Analysis

The complex dielectric constant of a material, $\varepsilon*$, can be separated into real, ε' (permittivity) and imaginary, ε'' (loss factor) components. Both are related to the permittivity of free space, ε_o, (equal to 8.85×10^{-12} F m^{-1}), and are dependent on frequency.

$$\varepsilon* = \varepsilon' - i\varepsilon'' \tag{5.1}$$

When a sample is subjected to an applied electric field the dipoles in the material will orient in the direction of the electric field. The orientation process requires a characteristic time, called the dipole relaxation time, τ. The simplest model to describe the orientation mechanism was developed by Debye, who assumed a single relaxation time, τ, for all molecules and expressed the relative permittivity and loss factor as [77, 78, 137],

$$\varepsilon' = \varepsilon_o + \frac{\varepsilon_\infty - \varepsilon_o}{1 + (w\tau)^2} \tag{5.2}$$

$$\varepsilon'' = \frac{(\varepsilon_\infty - \varepsilon_o)w\tau}{1 + (w\tau)^2} + \frac{\sigma}{w\varepsilon_o} \tag{5.3}$$

Direct current, DC, conductivity contributes only to the imaginary part of permittivity, where σ is the specific DC conductivity of the material. The difference in the frequency dependence of the dipolar and the DC conductivity terms allows their experimental separation, as will be discussed later.

The Debye model was sufficient to analyze relaxation processes in gases and some liquids but failed to account for the majority of experimental results in complex systems, such as polymers, which were characterized by broader and usually asymmetric dielectric loss peaks. The dielectric response of such systems have been described quite well by fitting permittivity plots by a number of empirical expressions in the frequency or time domain [77].

To study the mechanism of the $\alpha-$relaxation process in polymer materials, the complex dielectric constant, $\varepsilon*$, is given by the general equation,

$$\varepsilon^* = \varepsilon' - i\varepsilon'' = \varepsilon_\infty + \frac{\varepsilon_0 - \varepsilon_\infty}{\left(1 + (iw\tau)^\beta\right)^\alpha} \tag{5.4}$$

with $0 \le \beta < 1$ and $0 < \alpha \le 1$.

where w is the angular frequency ($w = 2\pi f$) and τ is the relaxation time. ε_0 and ε_∞ are the low and high frequency limiting values of the dielectric constant respectively. The dielectric strength is defined by the following relationship,

$$\Delta\varepsilon(T) = \varepsilon_o(T) - \varepsilon_\infty(T) \tag{5.5}$$

and is proportional to the number of dipoles per unit volume which are capable of absorbing energy from the applied field at a given temperature.

Two cases of eq. (5.4) were considered for this study: the first case is according to Havriliak–Negami (HN) [138, 139], in which the parameters β_{hn} and α_{hn} are characteristic of the symmetric and asymmetric broadening of the relaxation time distribution. They are unique and they represent the distribution of relaxation times. The parameters $0 < \beta_{hn} < 1$ and $0 < \alpha_{hn} < 1$ represent the breadth and the skewness of the distribution of relaxation times but lack physical meaning.

The second case is according to Cole and Cole [140, 141], in which the parameter $\alpha = 1$, and $0 < \beta_{cc} < 1$, where β_{cc} represents the symmetrical distribution of the relaxation times τ.

The data were also analyzed in term of the Kohlrausch-Williams-Watts (KWW) model [142, 143]. In this model the relaxation function, $\phi(t)$ exhibits a stretched exponential dependence on time, t, according to the equation,

$$\frac{\varepsilon_o - \varepsilon^*}{\varepsilon_o - \varepsilon_\infty} \propto \phi(t) = \exp\left[-\left(t/\tau\right)^{\beta_{KWW}}\right] \tag{5.6}$$

where $1.0 > \beta_{KWW} > 0.0$, and ε_o, ε^* and ε_∞ have their usual meaning. τ is an average relaxation time and β_{KWW} is a measure of the breadth of the relaxation times of the processes involved in the dielectric relaxation and is inversely proportional to the extent of peak broadness.

5.1.2 The Dielectric Relaxation Time

The average relaxation time, τ, describes the transition probabilities between consecutive minimum energy configurations of the dipoles [77]. The rotational motion of each dipole presents a characteristic relaxation time and hindered dipoles will show higher, τ, and therefore their motion will be observed only at higher temperatures and low frequencies.

The relaxation time is temperature dependent, and different functional forms of this dependence have been described. The simplest case is of dipoles floating in a viscous fluid, the relaxation time at a particular temperature is the same for each unit and dependent upon the viscosity of the system. This is known as Debye model and an Arrhenius equation has been accepted to represent the relaxation time-temperature dependence, such that,

$$\tau(T) = \tau_0 \exp\left(\frac{\Delta H}{kT}\right) \tag{5.7}$$

where τ_0 is the pre-exponential factor and k is Boltzman constant.

Eq. (5.7) has been shown to be applicable for $\beta-$ and $\gamma-$ relaxation mechanisms in amorphous polymers, when uncorrelated rotations of side groups or local motions of short segments are involved [77]. The apparent activation enthalpy of the relaxation process, ΔH, depends on both the internal rotation barriers and the environment of the rotating unit. For truly local processes due to isolated polar units, τ_0 should be of the order of 1 ns. Values lower than 10^{-16} s imply an activation entropy, ΔS^*, as defined in eq. (5.8), greater than zero, which in turn indicates more complex molecular motions, e.g., cooperativity. In the latter case, ΔH has

been reported in the range 100-200 kJ mol^{-1}, as frequently observed for the highly restricted conformational main chain motions [77].

$$\Delta S^* = k \ln\left(\frac{kT}{h}\right) - k \ln \tau \tag{5.8}$$

where h is Planck's constant and k is Boltzmann constant.

Relaxation mechanisms of dipoles located in dissimilar environments, or originating from complex forms of molecular or ionic motion, usually exhibit a non-Arrhenius dependence. This curvature is usually interpreted in terms of the semi-empirical Williams–Landel–Ferry, WLF, equation [144], such that,

$$\log a_T = \log\left(\frac{\tau}{\tau_R}\right) = \frac{-C_1(T-T_R)}{C_2 + T - T_R} \tag{5.9}$$

where a_T is a shift factor, τ and τ_R are the relaxation times at temperatures T and T_R, respectively, and C_1 and C_2 are the WLF constants. The WLF equation is a consequence of a general principle, known as the time-temperature superposition principle, TTS, and describes, for a wide range of materials, the effect of the free volume on the relaxation behaviour of polymers in the temperature range between the glass transition temperature T_g and $T_g + 100^o$.

For segmental α–relaxations and similarly complex relaxation signals, the Vogel-Tammann–Fulcher–Hesse, VTFH, equation [145-147] has been widely used in dielectric literature to describe the frequency dependence of the relaxation times in the α–relaxation region and over a wide frequency range , such that,

$$\log f_{\max} = \log f_o - \frac{\Delta E_f}{2.303R(T - T_o)} \tag{5.10}$$

Here, $f_{\max}$ is the frequency corresponding to the maximum in dielectric loss at the isothermal temperature, T and $f_{\max} = 1/2\pi\tau$ with τ the average relaxation time associated with the transition; f_o is the frequency at T_o; R is the gas constant and ΔE_f is an energy term related

to bond rotational energies which we will relate to the activation energy. T_o is the Vogel reference temperature or the thermodynamic glass transition temperature, located 30-70 degrees below T_g.

5.2 Results and Discussions

5.2.1 Ion Irradiation

Irradiation was carried out using the new procedure described in Chapter 2 to cover larger surface areas, as well as to investigate the homogeniousity of irradiation. Table 5.1 summarizes the irradiation setup for this study. The analysis of the irradiated materials was carried out by mean of DSC and the results were consistent with those reported in Chapter 3. The only differences were the higher irradiation doses used here. The cross link densities were calculated using the previous G values (see Chapter 3) and they are quoted in Table 5.2 along with the glass transition temperatures for the samples used in this study.

Table 5.1: Irradiation setup and dose evaluation for H^+ and He^{2+} ions.

Irradiation ions	Total charge ($\times 10^{-4}$ C)	Fluence[a] (C m^{-2})	Ions per unit area ($\times 10^{18}$ m^{-2})	Average track spacing ($\times 10^{-10}$ m)	Dose[b] (MGy)
H^+	96.3	9.4	58.65	1.40	37.9
He^{2+}	34.8	3.4	21.20	2.33	42.9

[a] The irradiated area was the same for all samples at 10.24 cm^2

[b] at the first layer.

Table 5.2: Dose, glass transition temperature, T_g, and cross link density of PEEK samples.

Irradiation	Dose (MGy)	Tg ($\pm 1.0\,^{\circ}$C)	% unit cross linked (± 0.5)
As Received	0	145.4	0.0
Proton, H$^+$	39.3	152.7	16.8
	50.5	154.2	21.6
	59.1	156.0	25.3
	74.9	158.2	32.0
Helium, He^{2+}	42.9	155.4	22.0
	54.4	158.1	28.0

5.2.2 Dielectric Spectrum of Amorphous PEEK

The dynamic dielectric behaviour of amorphous PEEK was investigated at a heating rate of 1.0 K min^{-1} over the temperature range from -130 to 240 $^{\circ}$C. Figure 5.1(a) shows the variation in both the dielectric constant, ε', and dielectric loss, ε'', of amorphous PEEK with temperature, and highlights the presence of two relaxations at -50 and 150 $^{\circ}$C. These are accompanied by an increase in dielectric constant and a peak in dielectric loss and were assigned to the $\beta-$ and $\alpha-$ relaxations respectively. Above the $\alpha-$ transition, the dielectric constant decreases sharply corresponding to the onset of crystallization, and then recovers at higher temperatures. The relaxation of the newly formed crystal portion was evident as a broad but distinct shoulder in dielectric loss located on the high-temperature side of the glass transition loss peak [148]. Finally, there was a large increase in the dielectric loss, ε'', due to increasing ionic conductivity with temperature. The overlap of the temperature response of

the dielectric loss in the region 130 to 240 ^{o}C was resolved using appropriate relationships for the temperature dependence [149], e.g., assuming a Gaussian shape for the $\alpha-$relaxation. As can be seen from Figure 5.1 (b), the three distinct regions associated with the mobility of the molecular chains are clearly present in the change in the dielectric loss of amorphous PEEK with temperature.
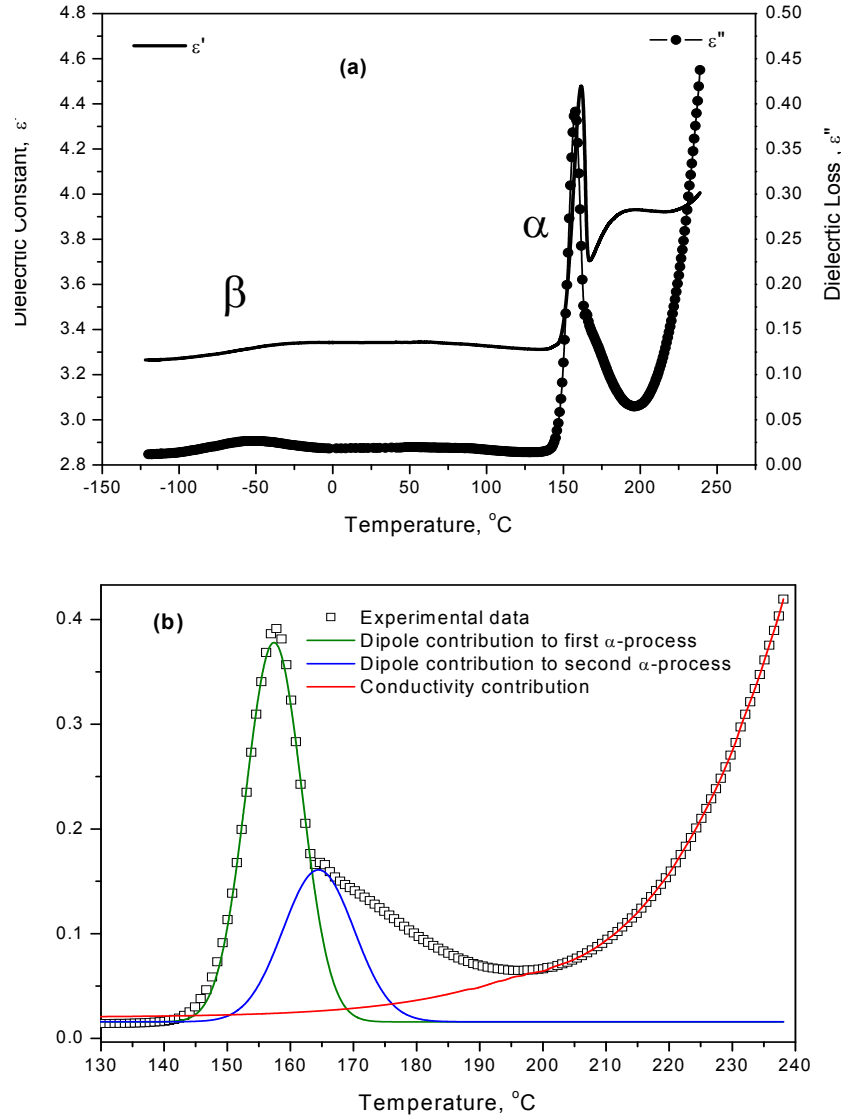
Figure 5.1: (a) Temperature dependence of the dielectric loss, ε'', and dielectric constant ε' at 1kHz for amorphous PEEK, (b) dielectric loss, ε'', as a function of temperature at 1.0 kHz for amorphous PEEK; showing the dipole and conductivity contributions.

5.2.3 Dielectric Spectrum of Ion Irradiated PEEK

The dynamic dielectric behaviour of ion irradiated PEEK was also investigated at heating rates of 1.0 K min^{-1} over the temperature range from -130 to 240 ^{o}C. The results of this analysis are shown in Figure 5.2.

On irradiation, similar behaviour was observed with the two transitions ($\alpha-$ and $\beta-$) but they occurred at slightly higher temperatures depending on radiation dose. Differences also existed above the $\alpha-$transition in that there was a single peak in ε'' followed by a rapid increase with temperature. As previously observed [56, 57] crystallization of amorphous PEEK is progressively suppressed by irradiation and, at a sufficiently high degree of cross linking, is completely inhibited. This appears to be the case with the irradiated sample shown in Figure 5.2.
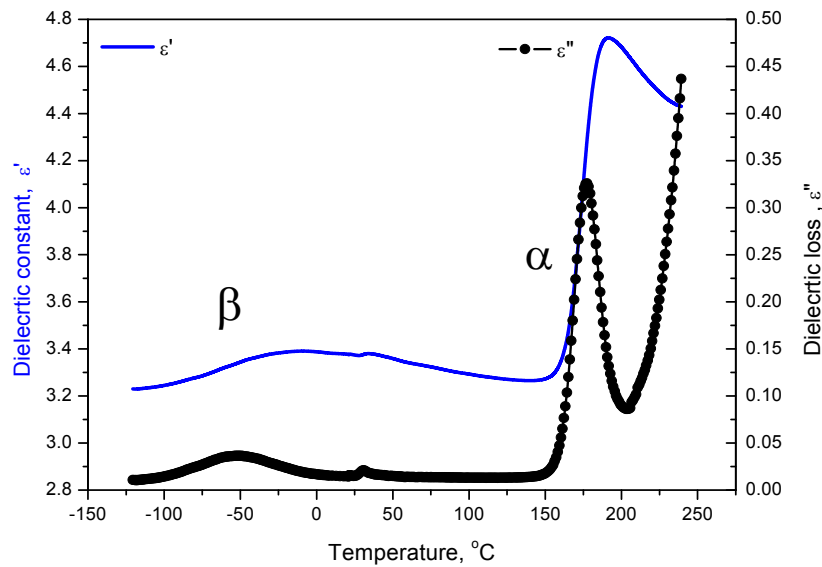
Figure 5.2: Temperature dependence of the dielectric loss, ε'', and dielectric constant ε' at 1kHz for irradiated PEEK samples with 56.1 MGy He^{2+}.

122

5.2.4 The Effects of Irradiation on the Relaxation Processes

The dielectric relaxations of irradiated PEEK have not been given full attention, and only few studies have been published on the effect of γ − rays and electron beam irradiation [150-152]. It has been reported that the glass transition temperature taken as the peak corresponding to the maximum in the dielectric loss increased with radiation dose indicating cross link formation. The results of the frequency dependency of the dielectric loss and constant have been analyzed by the Cole-Cole empirical function from which it was concluded that the magnitude of the induced dipoles and ions as well as the relaxation intensity increased with increasing radiation doses.

5.2.4.1 The β − Relaxation

The temperature dependence of the dielectric loss of amorphous and irradiated PEEK in the temperature range -120 to 20 $^{\mathrm{o}}$C is shown in Figure 3 (a), corresponding to the region of the sub-ambient β − relaxation of PEEK. The dielectric loss increased with radiation dose but no change in the temperature corresponding to the maximum in ε'' was observed for samples that were allowed to equilibrate with water vapour in the laboratory.

Equilibration with water was necessary as the amount present in the PEEK sample had a marked effect on the intensity and temperature of the sub-ambient β − transition, as defined by the maximum in ε''. Amorphous PEEK samples scanned immediately after drying in vacuum at 80 °C for 48 h, equilibrating in the laboratory for 24 h and after soaking in water at 50 °C for 24 h exhibited very different responses, as shown in Figure 3 (b). There was an increase in dielectric loss and the peak maximum temperature decreased with increasing moisture content, from -57 °C for the water equilibrated sample to -42 °C for the vacuum dried sample. These results have been explained by water acting as a plasticizer for the sub-ambient β − relaxation in PEEK[153].

The activation enthalpies, ΔH_β, for the sub-ambient β – transition was determined from the frequency dependence of the transition temperature, T_β, assuming an Arrhenius dependence, such that,

$$f = A\exp\left(-\Delta H_\beta / RT_\beta\right) \tag{5.11}$$

The values of ΔH_β were very similar at 45 ± 5 kJ mol^{-1} and were not markedly dependent on irradiation dose.

The sub-ambient β – relaxation is associated with phenyl ring motions, and while it is influenced by a number of factors such as water content, ageing history and morphology [153], it is reasonable to attribute the increase in intensity with irradiation to the introducing polar groups via oxidation as previously observed on the irradiation of polyethylene [154-156]. This is also consistent with the increase in sulphonation degree with irradiation observed in a previous article [157].

Moreover, it has been reported from a dielectric study of model aromatic compounds and related polymers by Schartel and Wendorff [158] that the sub-ambient β – relaxations in aromatic polymers are associated with inter and intra-molecular motions on a length scale equivalent to a single repeat unit, and accordingly cross linking does not have a marked effect on the mobility of such a small localised group.
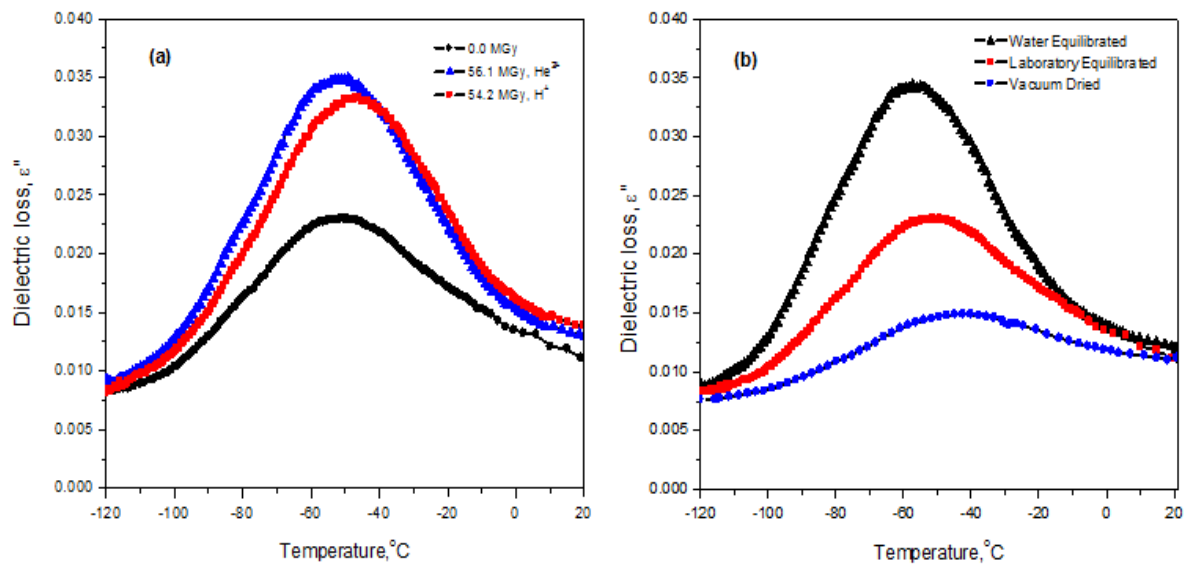
Figure 5.3: (a) The effect of irradiation dose on the $\beta-$relaxation of laboratory equilibrated

PEEK samples and (b) The effect of moisture content on the $\beta-$relaxation of PEEK.

5.2.4.2 The $\alpha-$Relaxation

The glass transition temperatures of the irradiated samples, as measured by the temperature

corresponding to the maximum in ε'', were greater than that of the amorphous PEEK sample,

shifting to higher temperature with increasing irradiation dose, see Figure 5.4. This is in

agreement with the calorimetric results reported earlier [56, 57] and indicated that the main

mechanism of ion irradiation effects in PEEK is that of cross linking.
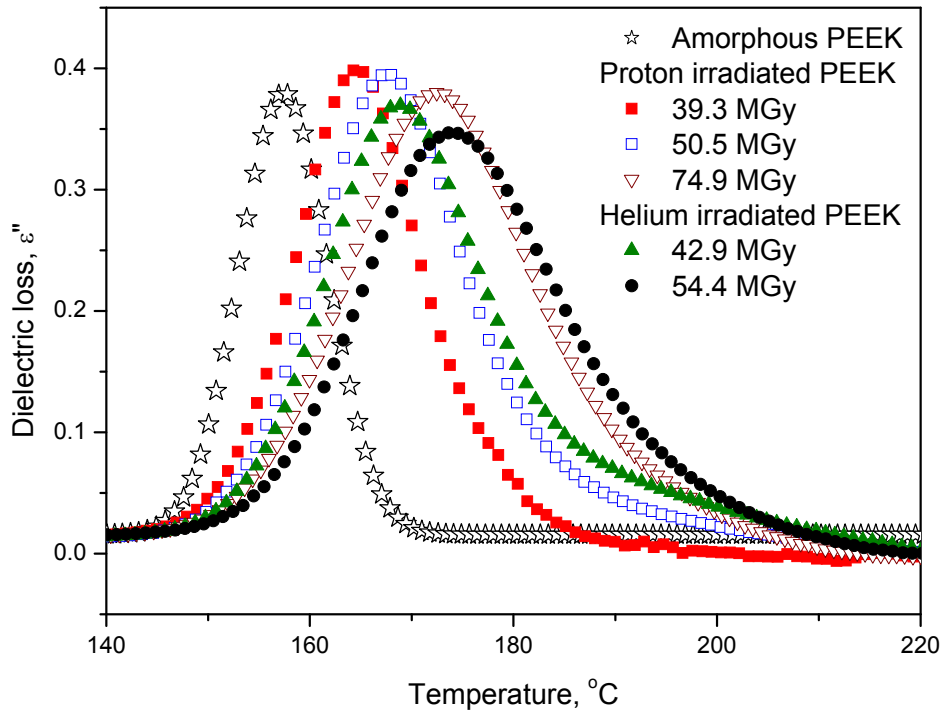
Figure 5.4: The dipole dielectric loss, ε'' of irradiated PEEK samples as a function of temperature. Heated at 2 K min^{-1} at fixed frequency of 1.0 kHz.

Because of the complex behaviour observed in the dielectric response of PEEK and irradiated PEEK, stepwise isothermal scans were carried out over a wide frequency range from 0.05 to 100 kHz at 5K intervals. These results are presented in Figure 5.5 showing the changes in $\tan \delta$, and dielectric constant, ε', with temperature, where $\tan \delta = \varepsilon''/\varepsilon'$.

Both ε'' and $\tan \delta$ appeared to change with increasing temperature in a similar way, and corresponded to the presence of a glass transition, second glass transition due to crystallization and ionic conduction in amorphous PEEK. In the irradiated specimens crystallization was absent. The glass transition temperature of the un-irradiated samples were less frequency dependent, shifting from 250 to 257 ^{o}C, than the irradiated specimens, 167 to 195 ^{o}C while the overall relaxation processes have also broadened.

126
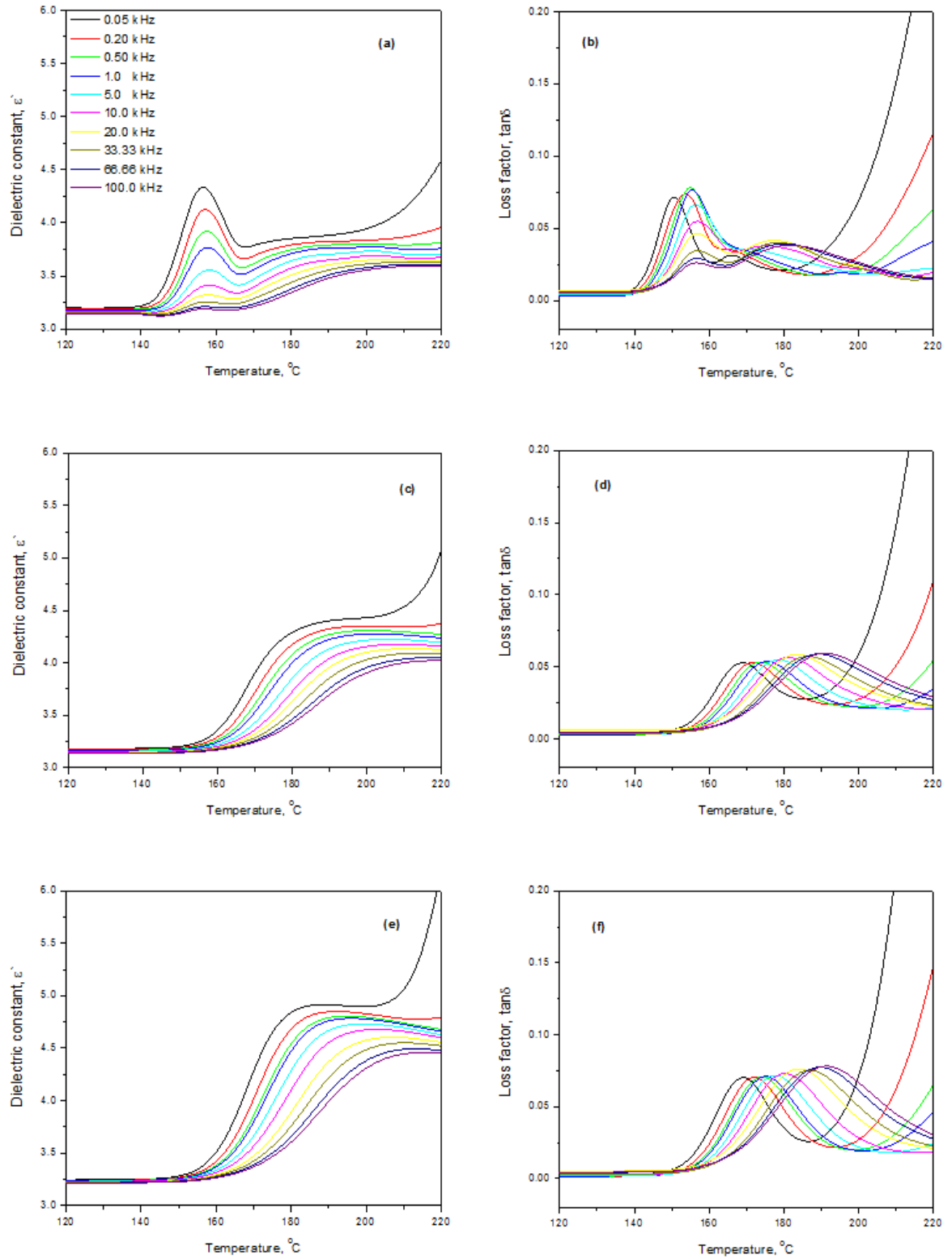
Figure 5.5: Change in dielectric constant and $\tan \delta$ with temperature at different frequencies for PEEK (a), (b) helium irradiated PEEK with 42.9 MGy (c), (d) and proton irradiated PEEK with 74.9 MGy (e), (f).

The conventional step-change in ε' of the irradiated samples were observed and this is associated with a change from the un-relaxed to relaxed values of ε', e.g., from ε_0 to ε_∞. It was observed that the value of the dielectric strength, $\varepsilon_\infty - \varepsilon_0$ decreases with frequency and increases on irradiation.

The dielectric loss and the dielectric constant dependencies on the applied frequency at different temperatures above the α – transition are presented in Figure 5.6 for amorphous and irradiated PEEK. As can be seen, the distribution of both $\varepsilon`$ and $\varepsilon``$ follow the usual trend.

It can be seen from Figure 5.6 that the frequency corresponding to the maximum in dielectric loss increases with increasing temperature and this was used to estimate the activation enthalpy of the α – process, ΔH_α, using the Arrhenius relationship, such that,

$$f_{max} = A \exp\left(- \Delta H_\alpha / RT \right) \qquad (5.12)$$

where R is the gas constant, and A is a pre-exponential factor. The frequency, f_{max}, corresponding to the maximum in dielectric loss ε'' was taken to be a measure of the relaxation time, τ, since $f_{max} = 1/2\pi\tau$, at the isothermal temperature T [159].

Although the temperature dependence of the frequency exhibited considerable curvature, see Figure 5.7 (a) Arrhenius plots were used for comparison and for determining the effect of cross linking on the dynamics of the glass transition, see Table 5.3. The value of 950 ± 100 kJ mol^{-1} obtained for amorphous PEEK compares favourably with the values quoted in the literature [160], but there was a marked decrease in activation enthalpy with irradiation dose.
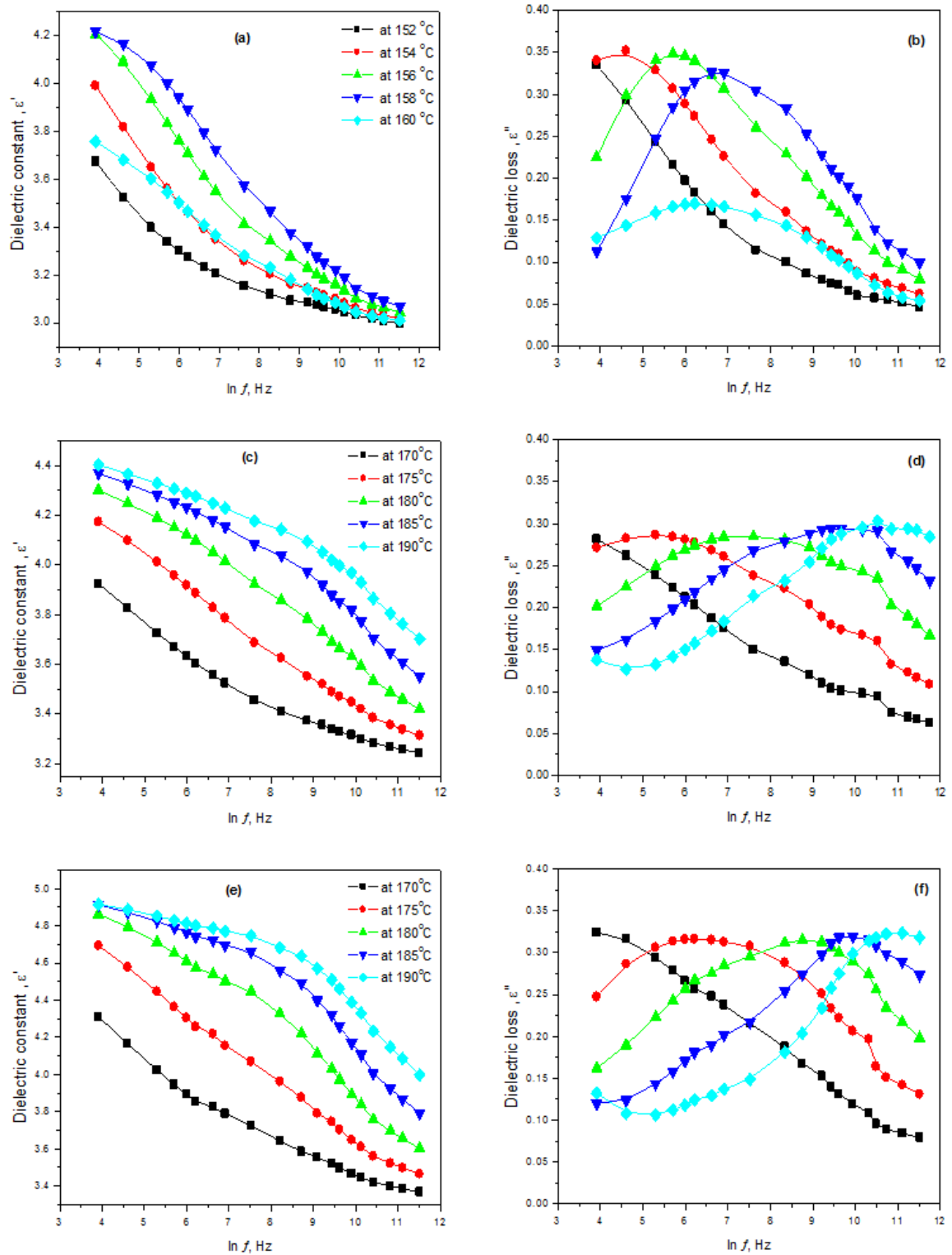
Figure 5.6: Dielectric dispersion curves (ε' *vs* $\ln f$) and dielectric loss curves (ε'' *vs.* $\ln f$) for PEEK (a), (b) irradiated PEEK with 42.9 MGy He2+ (c), (d) and irradiated PEEK with 74.9 MGy (e), (f) in the region of the glass transition.

129

The Vogel-Fulcher equation eq. (5.10) is considered to be a better empirical expression to describe the frequency dependence of the α – relaxation temperature over a wider frequency range.

Equation (5.10) was a better fit of the data over the full frequency range than the Arrhenius relationship, see Figure 5.7 (b), and the results of these analyses are presented in Table 5.3.

Table 5.3: The Vogel-Fulcher parameters of the PEEK samples.

Irradiation	Dose (MGy)	ΔE_f (kJ mol^{-1})	$\log f_o$ (Hz)	$T_0 \pm 10.0$ (K)	Activation enthalpy [*] ΔH_α (kJ mol^{-1})
As received	0	9.6 ± 0.3	14.7 ± 0.5	388.0	950 ± 100
Proton, H$^+$	50.5	9.4 ± 0.3	11.9 ± 0.3	395.0	480 ± 80
	59.1	7.7 ± 0.3	11.3 ± 0.2	398.0	470 ± 80
	74.9	8.3 ± 0.5	11.8 ± 0.5	400.0	550 ± 75
Helium, He^{2+}	42.9	6.9 ± 0.1	10.2 ± 0.1	396.0	620 ± 50
	54.4	8.0 ± 0.2	11.2 ± 0.2	400.0	630 ± 130

[*] calculated using eq. (5.12)

The same trend was observed in that the activation energy term in the VFT analysis decreased with increasing irradiation dose, but the Vogel reference temperature was observed to increase with dose.

The WLF constants for the calorimetric T_g are [161],

$$C_1 = \frac{C_{1g} C_{2g}}{C_{2g} + T_R - T_g} \qquad (5.13)$$

$$C_2 = C_{2g} + T_R - T_g \qquad (5.14)$$

C_{1g} and C_{2g} are the WLF constants at T_g.

The apparent activation energy at T_g, $E_a\left(T_g\right)$, follows a temperature dependence such that [161],

$$E_a\left(T_g\right)=\frac{2.303RC_{1g}\left(Tg\right)^2}{C_{2g}}\qquad(5.15)$$

At high temperatures the intra-molecular, or primitive, activation energy, which is associated with local barriers opposing rotation, is calculated from [161],

$$E = 2.303RC_{1g}C_{2g}\qquad(5.16)$$

The calculated values of the parameters C_{1g}, C_{2g} and E are listed in Table 5.4 along with the Vogel temperature T_o given by [161],

$$T_o = T_g - C_{2g}\qquad(5.17)$$

The values of $E_a\left(T_g\right)$ increased with irradiation dose which implies a reduction in segmental mobility with cross link density.
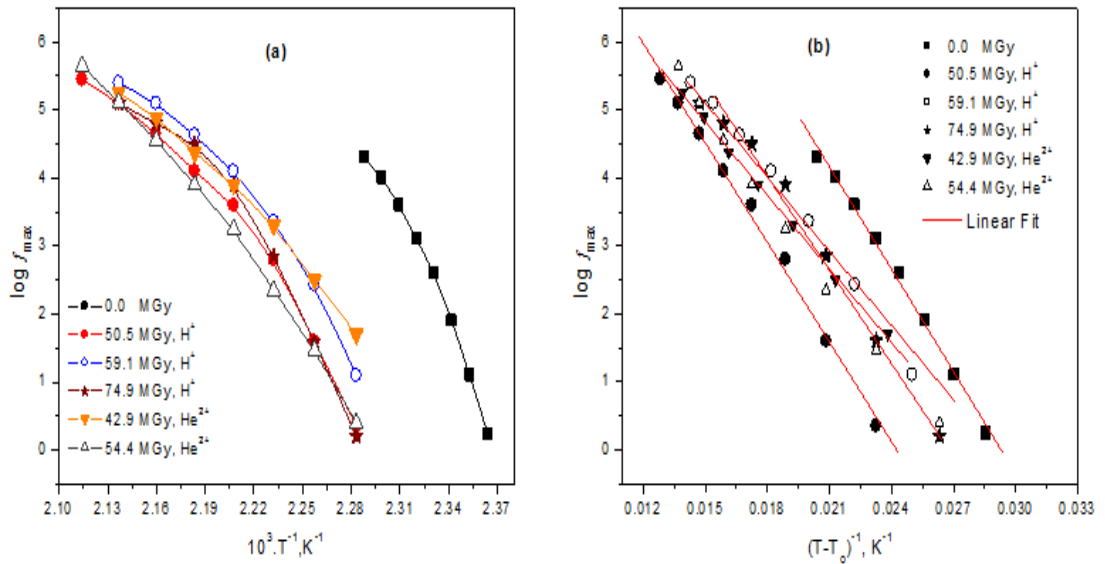
Figure 5.7: Effect of irradiation dose on transition temperature (a) Arrhenius dependence and (b) Vogel-Fulcher plots.

Table 5.4: The WLF parameters at T_g of different PEEK samples.

Irradiation	Dose (MGy)	T_R (°C)	C_{1g}	C_{2g} (K)	T_o (K)	$E_a\left(T_g\right)$ (kJ mol^{-1})	E (kJ mol^{-1})
As Received	0	156	13.7	51.0	367.4	900	13.3
Proton, H^{+}	50.5	170	17.6	58.8	368.4	1050	19.9
	59.1	165	13.6	45.9	383.1	1040	12.0
	74.9	170	13.3	43.7	387.5	1100	11.2
Helium, He^{2+}	42.9	170	14.9	50.9	377.5	1030	14.6
	54.4	170	14.6	45.0	386.1	1150	12.5

5.2.4.3 The DC Conductivity

The extent of conduction at high temperature above T_g was observed to vary with the reciprocal frequency, f, and ε'' are related to the ionic conductance, σ, by

$$\varepsilon`` = \sigma \Big/ \left(\omega\varepsilon_0 \frac{A}{D}\right)$$
(5.18)

where ε_0 is the permittivity of free space (8.86×10^{-12} F m^{-1}), A/D is the ratio of the electrode area (A) to the plate separation or sample thickness, D, and $\omega = 2\pi.f$ is the angular frequency. The ionic conductances, σ, were determined from linear plots of dielectric loss against reciprocal frequency at constant temperature, see Figure 5.8. The conductivity increased with irradiation dose suggesting insertion of ionic species on irradiation.
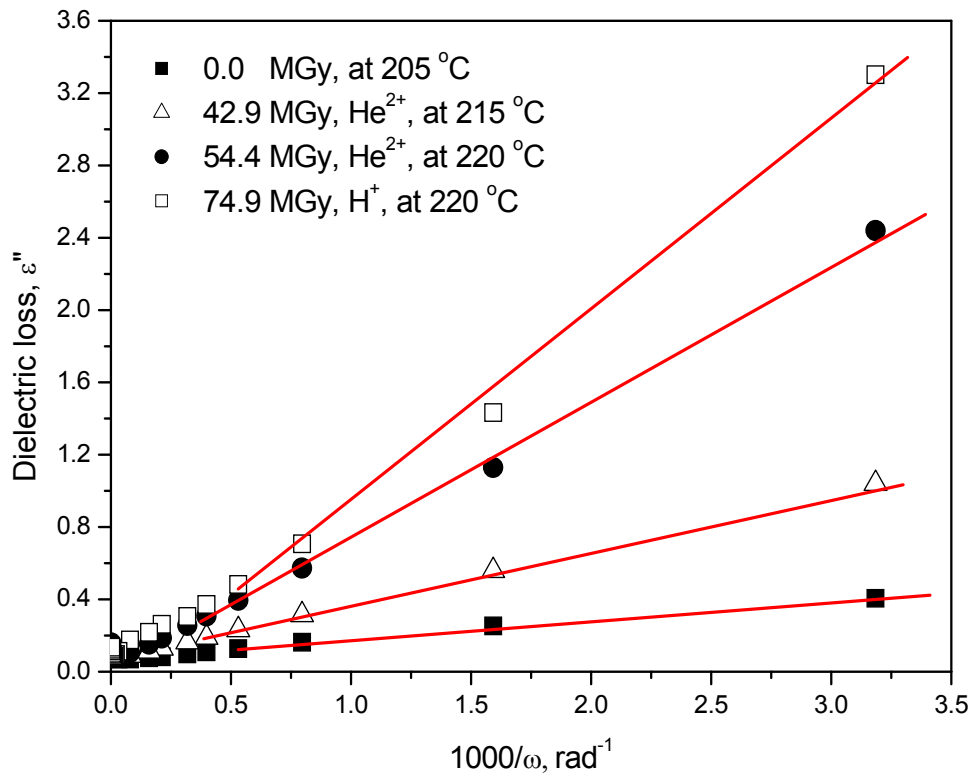
Figure 5.8: The ionic conductances of irradiated PEEK samples.

The increase in conductivity with temperature was similar in the irradiated samples to that observed for the amorphous sample, implying that cross linking had little effect on the ionic conductivity. The temperature dependence of the conductivity was first analyzed using the Arrhenius equation, see Figure 5.9 (a), such that,

$$\ln \sigma = \ln \sigma_o - \frac{\Delta H}{RT} \tag{5.19}$$

As can be seen from Table 5.5, the increase in both activation enthalpy and the pre-exponential factor with irradiation dose was only apparent at high doses reflecting the greatly reduced mobility of the cross linked matrix and the energetics of the migration of the ion.

Table 5.5: The Vogel-Fulcher parameters of the PEEK samples at $T > T_\alpha$.

Irradiation	Dose (MGy)	ΔE_f (kJ mol^{-1})	$-\ln\sigma_o$	$\Delta H_\sigma^{(*)} \pm 50$ (kJ mol^{-1})	$\sigma_o^{(*)}$ (S.m^{-1})
amorphous	0	6.6 ± 0.1	10.7 ± 0.1	190	2.2×10^{12}
Proton, H$^+$	50.5	7.1 ± 0.2	9.9 ± 0.3	190	1.1×10^{12}
	59.1	6.0 ± 0.1	10.4 ± 0.1	190	6.5×10^{13}
	74.9	7.0 ± 0.2	8.4 ± 0.1	205	2.6×10^{18}
Helium, He^{2+}	42.9	7.4 ± 0.2	8.9 ± 0.2	245	4.3×10^{15}
	54.4	7.2 ± 0.1	8.4 ± 0.1	225	8.6×10^{17}

$^{(*)}$ calculated using eq. (5.19)

However, it was observed that the temperature dependence was better described by a VFTH form, see Figure 5.9 (b), such that,

$$\ln\sigma = \ln\sigma_o - \frac{\Delta E_f}{R(T - T_o)} \qquad (5.20)$$

The results were obtained using the same T_o values reported in Table 5.4 and they are shown in Table 5.5. It is noteworthy that the values of activation energy determined from the conductivity analysis using the Arrhenius relationship are far less than those obtained for the dipole relaxations. This indicates that migration of the ions is independent of concerted segmental motion of the polymer chains as envisaged in the glass relaxation process.
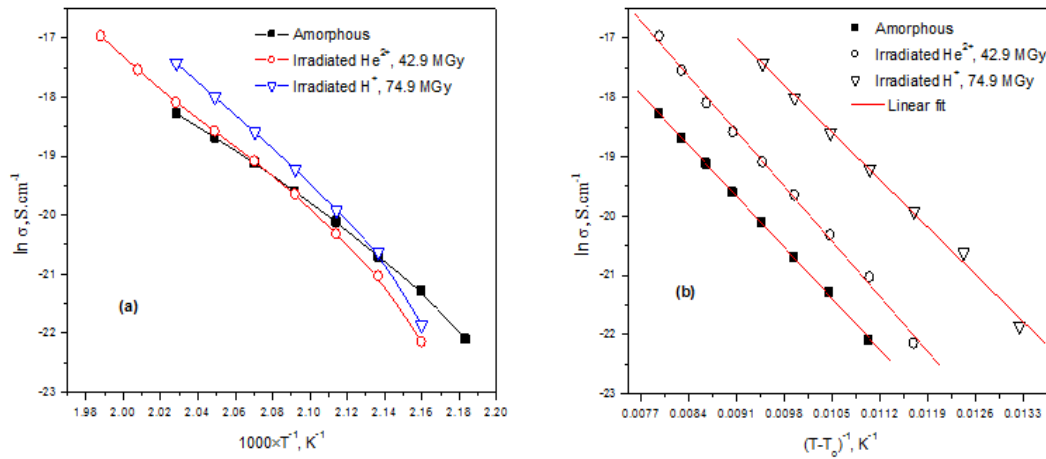
Figure 5.9: Effect of irradiation dose on conductivity, (a) Arrhenius dependence and (b) Vogel-Fulcher plots.

5.2.5 Details of the Effect of Irradiation on the α – Relaxation

The temperature dependence of the dielectric relaxation with time was also analysed using the Williams-Landel-Ferry (WLF) relationship, eq. (5.9). a_T was determined from isothermal plots of the dielectric constant, $\log \varepsilon'$, against temperature and a master curve determined at the designated temperature. An example is shown in Figure 5.10.
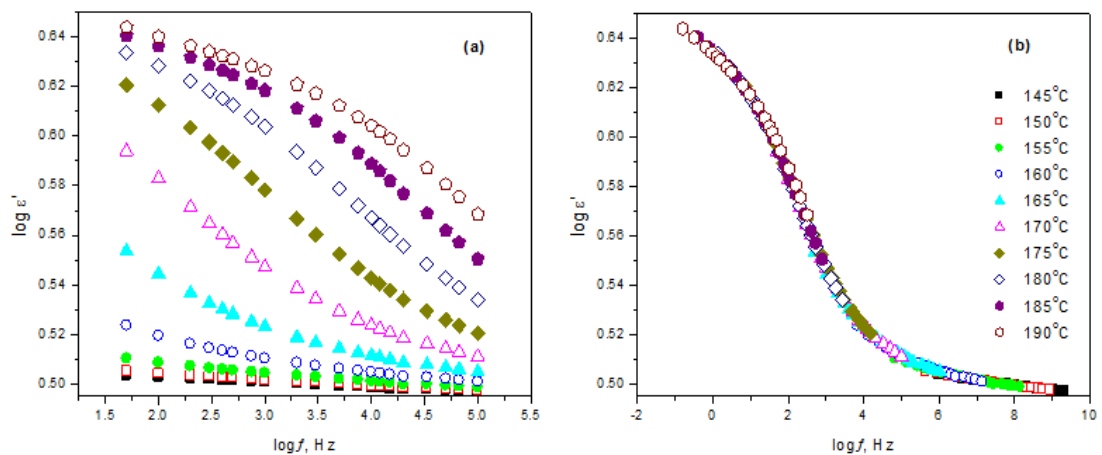
Figure 5.10: Time temperature superposition for PEEK sample irradiated with 42.9 MGy He^{2+} ions. (a) Dependence of the shift parameter on frequency and (b) Master curve at 170 $^{\circ}$C.

135

Different models have been suggested to analyse the dielectric dispersion curve of the $\alpha-$ relaxation process in polymers. For a broad relaxation process, the complex dielectric constant, $\varepsilon *$, is given by the Havriliak-Negami equation, eq. (5.4)

Plotting the dielectric loss against the dielectric constant for PEEK, see Figure 5.11, a skewed semi-circular arc was obtained and as shown the agreement between the experimental data and data calculated using the Cole-Cole and HN models is obtained for all samples indicating that both routines can be used to describe the dielectric response in this region. Subsequently α_{hn}, β_{hn} and β_{cc} were determined from eq. (5.4) for PEEK and irradiated PEEK as a function of irradiation dose and temperature. These are listed in Tables 5.6, 5.7 and 5.8.

Table 5.6: The Cole-Cole and Havrilak–Negami best fit parameters for amorphous PEEK.

Reference	Temp. (^{0}C)	Cole – Cole analysis			Havrilak–Negami analysis			
		$\Delta\varepsilon$	β_{cc} (±0.05)	$\tau\times10^{3}$ (s)	$\Delta\varepsilon$	β_{hn}	α_{hn}	$\tau\times10^{3}$ (s)
This work	154	1.98	0.45	2.90	1.66	0.60	0.48	6.90
	156	1.66	0.50	0.36	1.58	0.70	0.43	1.67
	158	1.44	0.59	0.11	1.42	0.76	0.41	0.62
Ref [162]	154	1.09	0.58	0.38	1.09	0.75	0.51	1.15
Ref [148]	154	1.24	0.64	0.126	1.25	0.84	0.44	0.44
	156	1.34	0.66	0.062	1.45	1.00	0.32	0.28
	158	1.37	0.63	0.022	1.54	0.86	0.36	0.10
Ref [160]	158	2.21	0.41	0.49	1.26	1.00	0.32	0.34
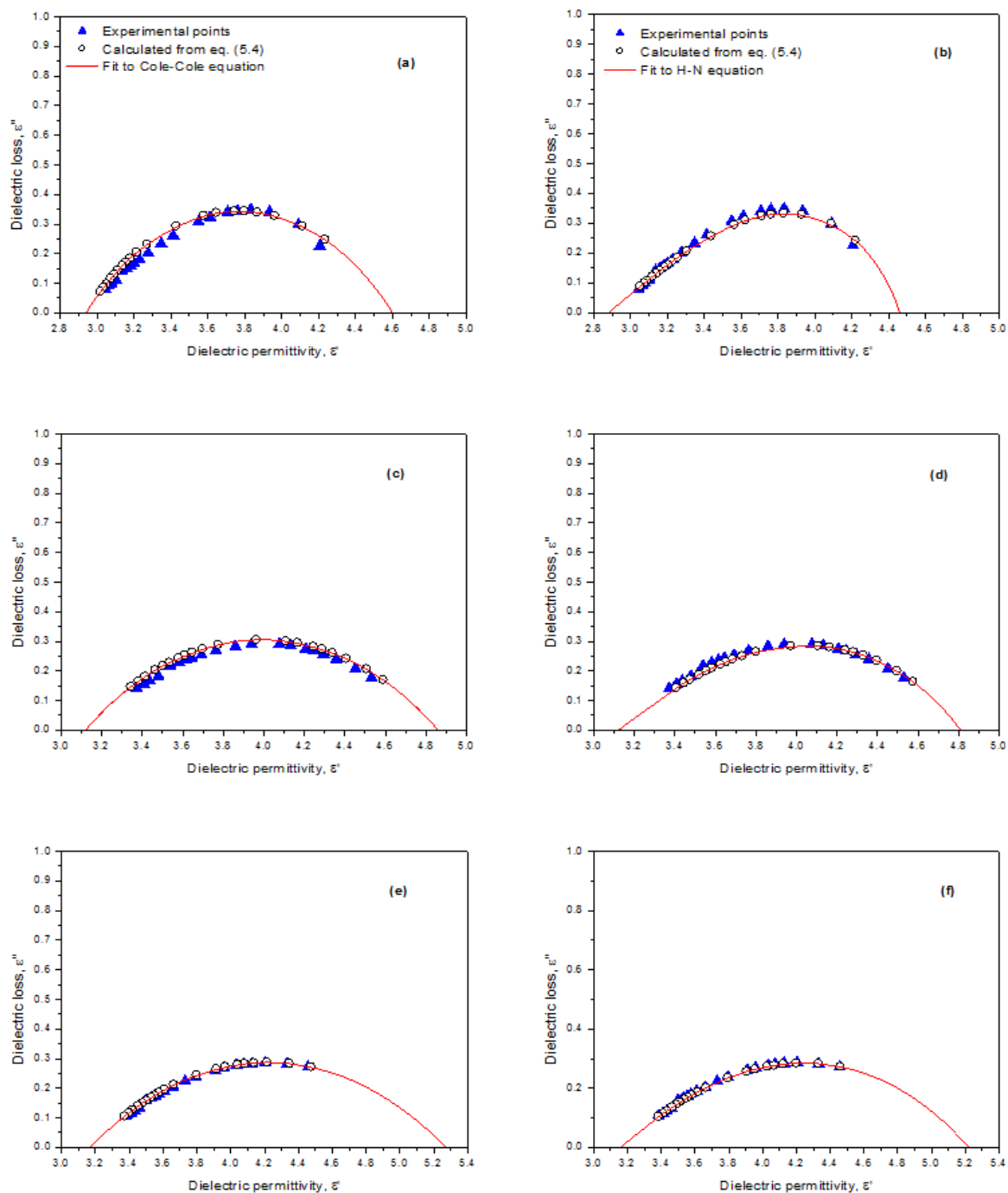
Figure 5.11: Best fit of the Cole-Cole and Havrilak–Negami relationship to the dielectric data of (a) Amorphous PEEK at 156°C, (b) 59.1 MGy proton irradiated PEEK at 175 $^{\circ}$C and (c) 54.4 MGy helium irradiated PEEK at 175 $^{\circ}$C.

Table 5.7 : Cole-Cole best fit parameters for irradiated PEEK.

Irradiation	Dose (MGy)	Temp. (°C)	$\Delta\varepsilon$	β_{cc} (±0.05)	$\tau \times 10^3$ (s)
Proton, H⁺	50.5	170	1.44	0.33	3.95
		175	1.35	0.37	0.82
		180	1.33	0.38	0.095
	59.1	170	1.87	0.39	0.097
		175	1.74	0.43	0.090
		180	1.68	0.43	0.015
	74.9	170	2.41	0.34	5.50
		175	2.03	0.39	0.23
		180	1.94	0.41	0.032
Helium, He²⁺	42.9	170	1.58	0.34	0.360
		175	1.43	0.38	0.022
		180	1.43	0.38	0.033
	54.4	170	2.31	0.32	17.5.0
		175	2.10	0.34	0.82
		180	1.99	0.37	0.095

For PEEK, the skewness of the relaxation as measured by the Cole-Cole β_{cc} value increased from 0.45±0.05 to 0.59±0.05 with temperature, implying that the relaxation was less skewed at higher temperatures but the values, observed at the same temperatures, compared favourably with reported values in the literature, see Table 5.6.

Table 5.8: Havrilak–Negami best fit parameters for irradiated PEEK.

Irradiation	Dose (MGy)	Temp. (°C)	$\Delta\varepsilon$	β_{hn}	α_{hn}	$\tau \times 10^3$ (s)
Proton, H^+	50.5	170	1.32	0.39	0.87	4.20
		175	1.31	0.40	0.76	0.67
		180	1.28	0.43	0.66	0.24
	59.1	170	1.81	0.42	0.85	1.62
		175	1.69	0.48	0.67	0.26
		180	1.65	0.55	0.59	0.10
	74.9	170	2.19	0.38	0.91	5.47
		175	1.92	0.45	0.70	0.72
		180	1.82	0.51	0.66	0.21
Helium, He^{2+}	42.9	170	1.51	0.39	0.76	6.54
		175	1.41	0.42	0.67	0.77
		180	1.32	0.50	0.53	0.16
	54.4	170	2.23	0.35	0.83	25.4
		175	2.06	0.37	0.78	1.92
		180	2.02	0.40	0.61	0.51

Figure 5.12(a) shows the dependence of the Cole-Cole broadening parameter on the cross link density at the normalised temperature, taken as $T=T_g+15$. Figure 5.12(b) show the dependence on the irradiation dose. It is evident that the deviation from the Debay behaviour increased with increasing cross link density and more complex systems are formed on

irradiation. The results also show that Cole-Cole formalism can be used to detect the LET effect as evident from Figure 5.12(b).
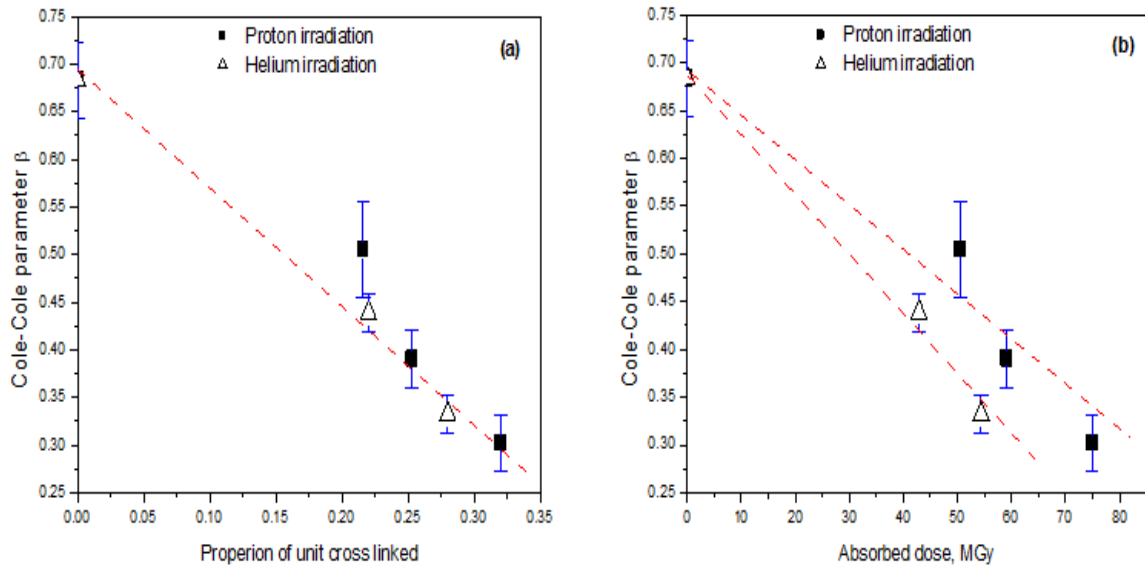
Figure 5.12: The dependence of the Cole-Cole broadening parameter at the normalised temperature on the portion of cross linking (a) and on the absorbed irradiation dose (b). Lines are guides for the eyes.

However, the H-N routine is more advantageous due to the possibility of relating the H-N parameters to molecular motion in polymers. According to Schlosser and Schönhals [163-165], two scaling parameters m and n are defined to relate the molecular motion of the polymer with the HN parameters [166]. The authors suggest that the mobility of the polymer chain segments at T_g is controlled by both intra- and intermolecular interactions. The parameter m describes the dielectric response in the low frequency region (i.e., $w\tau \ll 1$) that is related to the intermolecular correlation between chains and their segments. The parameter n describes the dielectric response in the high frequency region (i.e., $w\tau \gg 1$) that is related

to the local chain dynamics. These parameters are correlated with the HN parameters such that $n = \alpha_{hn} \times \beta_{hn}$ and $m = \beta_{hn}$.

Figure 5.13 (a) shows the dependence of both parameters m and n on the cross linking density at the normalised temperature. As can be seen the parameter n was nearly independent of cross link density suggesting that the local motions in amorphous PEEK were unaffected by irradiation. On the other hand, the parameter m decreased from 0.8 to 0.3 with increasing irradiation dose indicating that a slowing down of the long-range molecular motions is occurring with increasing cross linking density of the polymer. This results are in agreement with previous investigations in networks based on styrene-butyl acrylate divinylbenzene with a moderate degree of cross-linking in which n was not affected [167].

On the other hand, Figure 5.13(b) provide an evidence for the well know LET effect, and as observed earlier [57] helium ion was more effective in cross linking PEEK than proton ion at similar doses.

Similar conclusion was made from the analysis of the dielectric dispersion data using the Kohlrausch-Williams-Watts equation[*], KWW, eq. (5.6). Figure 5.14 summarizes the results of this analysis and shows the variation in β_{KWW} with temperature plotted for different amorphous and ion irradiated PEEK samples. All the irradiated samples had broader distributions and they also broadened with increasing temperatures. There was a general tendency for the value of β_{KWW} to decrease, and so the relaxation to broaden, with irradiation dose and temperature.

---

[*] The dielectric data were fitted to the KWW function using Relax software provided by Prof. J Matecki.
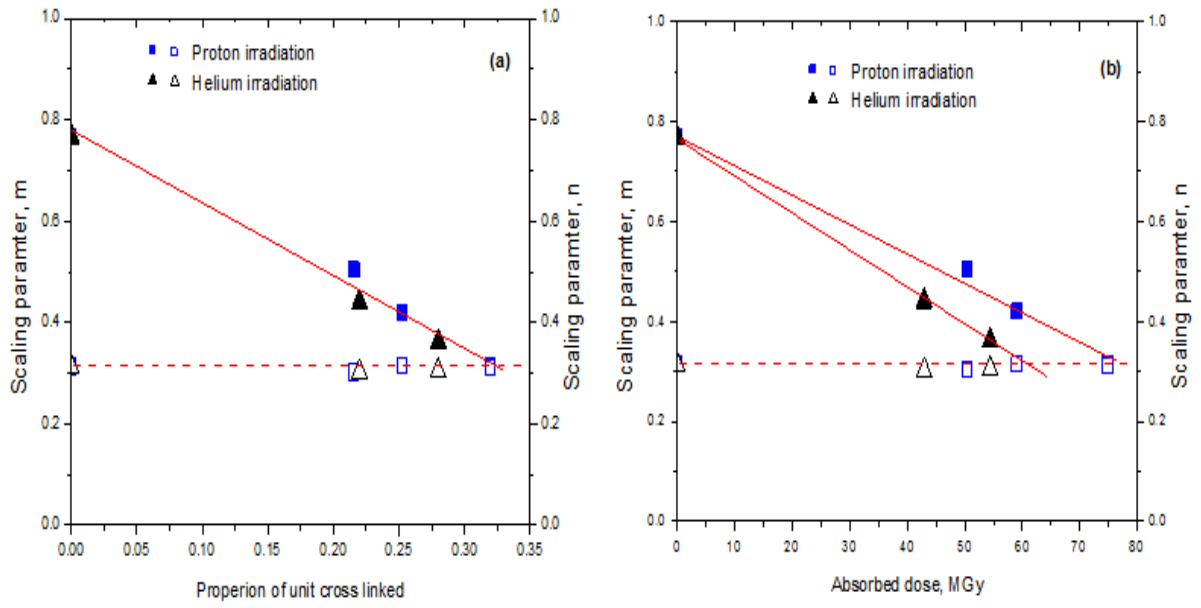
Figure 5.13: The scaling parameters *m* and *n* according to Schönhals and Schlosser, plotted at the normalised temperature as a function of cross linking (a) and absorbed dose (b). Lines are guides for the eyes.

The importance of network formation in lowering the observed β_{KWW} values can be seen from Figure 5.15(a) in which the effect of cross link density in broadening the distribution of life time can be seen to be independent of the irradiation ion used, although this was not the case with dose, as shown in Figure 5.15(b). Differences existed between the efficiencies of the two ions used in cross linking PEEK, in having different LET values.
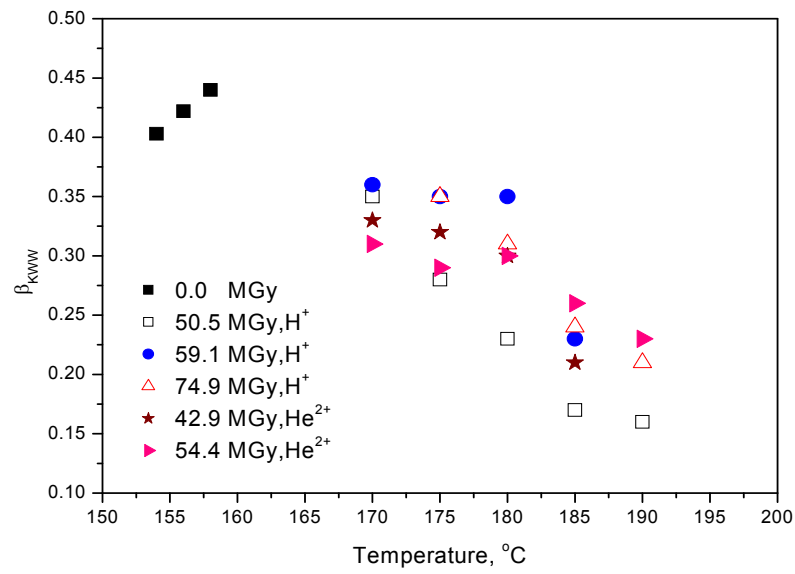
Figure 5.14: Temperature variation of the breadth, β_{KWW}, of the dielectric relaxation, (error is ±0.03).
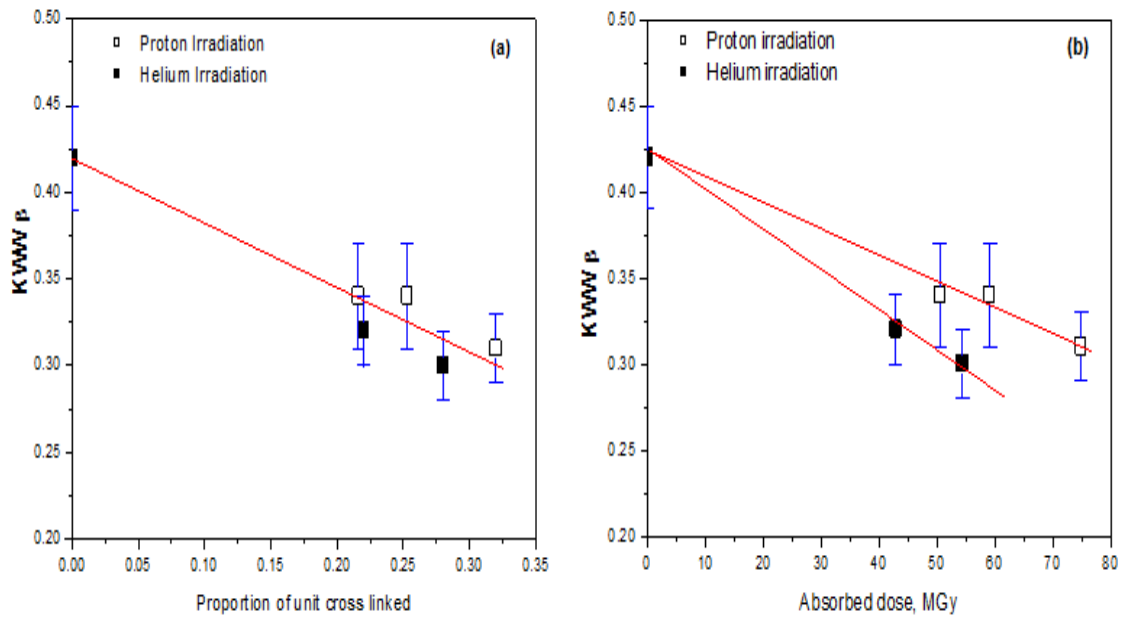
Figure 5.15: The effect of cross link density and absorbed dose on the breadth, β_{KWW}, of the dielectric relaxation.

According to the coupling model proposed by Ngai *et al.* the deviation from Debye behaviour is due to the intermolecular coupling of relaxing species with neighbouring non-bonded ones [168, 169]. The degree of coupling (cooperativity), n increased with decreasing the experimentally observed β_{KWW} value since $n = 1 - \beta_{KWW}$. This is the case with the irradiated samples studied, the observed decrease of β_{KWW} is the results of the increase of inter-chain coupling between the relaxing units caused by the additional constraints introduced by the cross-linking. These results are in accordance with previous investigations in networks based on a model heterocyclic polymer [170].

5.3 Conclusions

The specific influence of ion irradiation on the relaxations in poly(ether ether ketone) has been described by dielectric relaxation spectroscopy. The $\beta -$ transition appears to be sensitive to the amounts of water present and altered by oxidation. The measured activation enthalpy of 45 kJ mol^{-1} is consistent with molecular motions associated with onset of rotation of localised groups of the size of a chain link. This makes the overall relaxation insensitive to the development of the cross linked network produced on irradiation. By contrast the $\alpha -$ transition is extremely sensitive to the cross linking density and the glass transition temperature increases progressively with dose. However, the activation enthalpy of the relaxation is substantially reduced from about 950 to 450 -600 kJ mol^{-1}. By analogy to the activation enthalpy of the $\beta -$ transition, the large activation enthalpies associated with the $\alpha -$ transition is attributed to concerted rotational mobility of chain segments involving possibly 15 to 25 monomer units. The reduction in activation enthalpy on irradiation arises from the increased restrictions imposed by the progressive development of networks and to the onset of rotation of the smaller segments between cross links.

The results also showed that the Cole-Cole, Havriliak-Negami and the Kohlrausch-Williams-Watts formalisms could equally well describe the dielectric spectrum for both amorphous and irradiated PEEK in the frequency and temperature range studied.

With the H-N function, it was possible to describe the results in light of the Schönhals and Schlosser phenomenological model. It was found that the n parameter was nearly independent on the ion used or the cross link density, suggesting that the local motions of PEEK were uninhibited by the development of cross links. Furthermore, the analysis showed that the m parameter decreased with the progressive development of cross links indicating that a slowing down of the long-range molecular motions is occurring with increasing cross linking of the polymer.

With the KWW function, it was possible to describe the results in light of the coupling model. The observed decrease in the β_{KWW} parameter resulted from the increase of inter-chain coupling between the relaxing units caused by the growing hindrance with increasing degree of cross linking.

The analysis clearly indicated that the dielectric properties of polymers are influenced by the LET effect of the irradiated ion used.

Chapter 6

Synthesis and Characterization of Sulphonated PEEK

6.1 Introduction

Sulphonation is a powerful and versatile route to polymer modification that especially suits polymers containing an aromatic ring in their repeat unit. It is an electrophilic substitution reaction in which the more electronegative atoms of oxygen draw the electron density from the sulphur atom, which then becomes an electrophilic centre. This electrophilic centre can react with the delocalized π electron system of an aromatic ring at the position with the highest electron density, which is controlled by the position and type of other groups located around the aromatic ring.

Sulphonation reactions proceed easily in the presence of groups such as $-Cl$, $-NH_2$, $-OH$, $-SH$, etc., due to the increased electron density on the aromatic ring. On the other hand, sulphonation occurs slowly in the presence of substituents, which reduce the electron density on the aromatic ring, such as $=NR_2$, $>C=O$, etc.

Polymers are sulphonated to convert them into ionomers, which are able to conduct protons and therefore can be used in preparing proton exchange membranes, PEM. The sulphonation of these polymers is usually carried out by one of the following methods:

1) Direct sulphonation of the polymer backbone, e.g., the sulphonation of PEEK [44].

2) Radiation grafting of monomers onto the polymer backbone followed by sulphonation, e.g., PVDF-PS [171].

3) Chemical grafting of sulphonated monomers onto the polymer backbone, e.g., sulphonated polybenzimidazole PBI [172].

4) The polymer is built from monomeric units, which contain the sulphonic acid groups, e.g., sulphonated polyimide SPI [173].

Whatever method is used, the extent of sulphonation and the swelling properties of the PEM are extremely important, as they dictate the PEM performance by controlling proton conduction and mechanical properties.

6.2 Sulphonation Reaction

Scheme 6.1 shows the reactions involved in aromatic sulphonation using two sulphonating agents namely (a) SO_3 and (b) SO_3H^+.
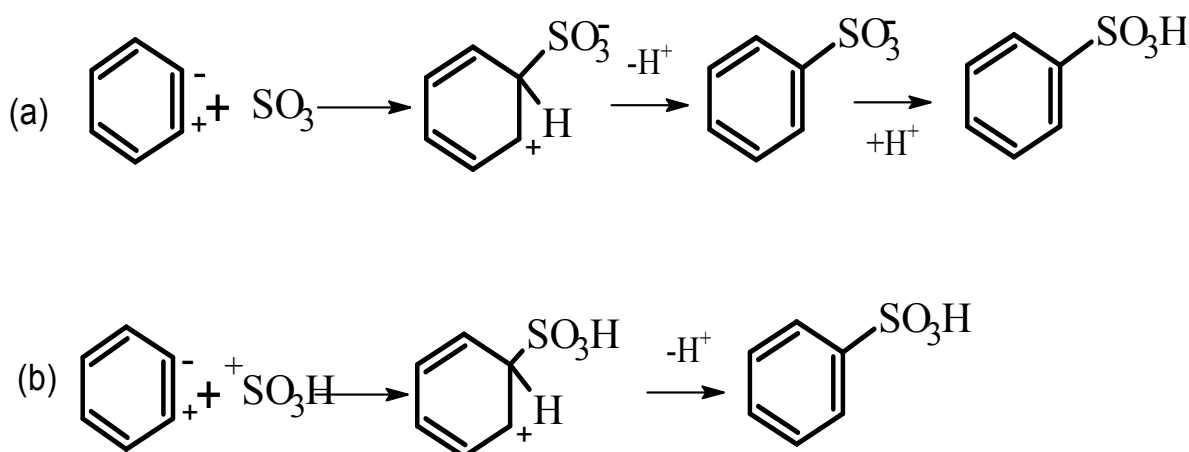
Scheme 6.1: Sulphonation of an aromatic system with (a) SO_3 and (b) SO_3H^+[174].

The kinetics of sulphonation is assumed to follow the general reactions of Scheme 6.2. Both reacting molecules determine the rate of sulphonation, and this electrophilic substitution can be considered to be a bimolecular reaction of the second order. This is in agreement with the proposed Scheme 6.2 and consistent with the results of kinetic studies [174-178]. In step 1, a fast reversible reaction occurs between an aromatic compound and an electrophilic agent, e.g., SO_3 and leads to the formation of a π-complex. No experimental evidence for the existence of the π-complex has been published, but it is assumed that the π-complex will be transformed slowly from π- to σ-complex (e.g., to the arenium ion) by the second reaction (step 2). This reaction then is the rate determining step. Although the σ-complex has been isolated, it is a highly reactive intermediate, which stabilizes itself by a further reaction step. At the end, (step 3), this electrophilic substitution is quickly terminated by the release of $X^{\oplus}$. If $X^{\oplus}$ is a proton, then a base B is necessary to ensure its removal[174].
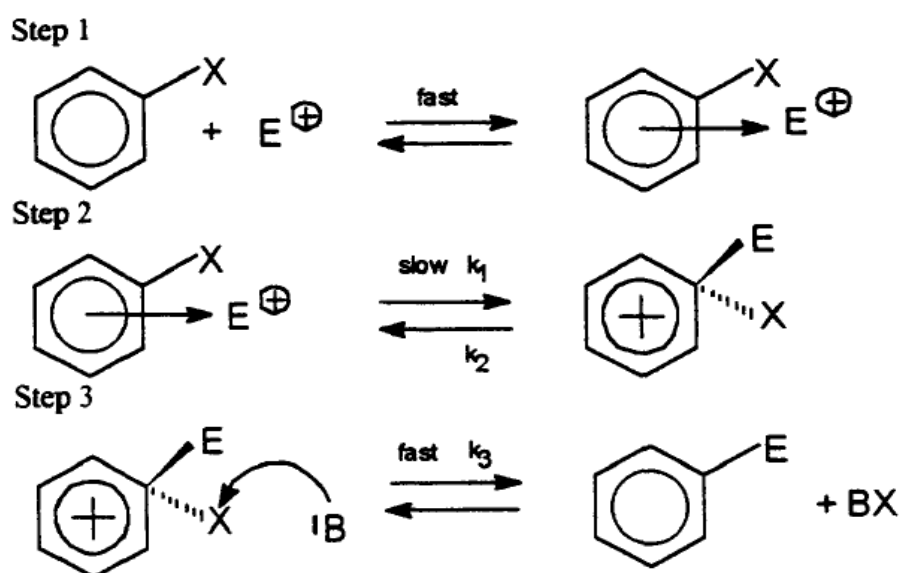
Scheme 6.2: General mechanism of the sulphonation reaction, showing three steps: formation of the π-complex (step 1), formation of the arenium ion or the σ-complex (step 2) and termination by the release of $X^{\oplus}$ (step 3) [174].

6.2.1 Desulphonation

The term desulphonation (or hydrolysis of $-SO_3H$ group) is used to describe the reverse reaction of sulphonation. Reaction conditions are such that the equilibrium between the sulphonation and desulphonation reactions is usually shifted toward sulphonation. The $-SO_3H$ groups can be removed from sulphonated compounds with dilute solutions of acids or with water, Scheme 6.3.

$$R - SO_3H + H_2O \rightarrow RH + H_2SO_4$$
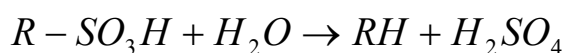
Scheme 6.3: Desulphonation reaction [174].

The hydrolysis is represented by the electrophilic release of the –SO$_3$H group by the participation of a proton in this reaction. In the presence of sulphuric or hydrochloric acid, hydrolysis runs simultaneously with the sulphonation because of high concentration of $H^{\oplus}$ ions. Reaction conditions determine the direction of the reaction. Sulphonation itself prefers high concentrations of sulphuric acid; however, partial desulphonation has been observed even in the presence of concentrated sulphuric acid [174].

There are several causes for desulphonation such that, (1) the $-SO_3H$ group is not conjugated with the benzene ring, (2) a strong, partially positive charge on the sulphur atom increases the electron density at the meta-position of the benzene ring and on the carbon atom of the C–S bond, (3) after the release of a proton, a negative charge located on the –SO$_3$H group can facilitate the hydrolysis of the $-SO_3H$ group; (4) substituents that support sulphonation can also promote hydrolysis of the $-SO_3H$ group, because of the increase of the electron density on the carbon atom of the C-S bond. When the formation of the sulphonic acid is easy, the hydrolysis also occurs readily [174].

6.2.2 Sulphone Formation

Because of the presence of relatively a highly reactive $-SO_3H$ groups, cross linking reactions can occur between the molecules of the sulphonated product, adding more complexity to the assumed reaction scheme. Very little information on this cross linking mechanism has been found. However, it seems that its rate increases with increasing temperature [174]. Cross links formed from sulphone formation are very stable and their decomposition can only be achieved on melting in the presence of alkaline hydroxides, Scheme 6.4.

$$\text{(a)} \quad 2R - SO_3H \rightarrow R - SO_2 - R + H_2SO_4$$

$$\text{(b)} \quad R - SO_2 - R + NaOH \rightarrow R - SO_3Na + RH$$
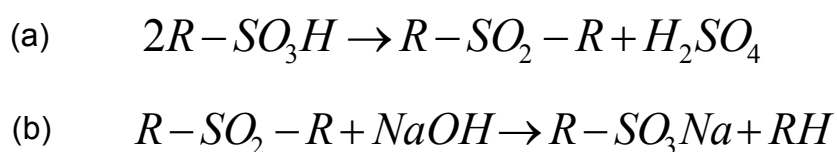
Scheme 6.4: Cross linking reaction (a) and sulphone decomposition (b) [174].

6.2.3 Factors Affecting the Sulphonation Reaction

The choice of reaction conditions for sulphonation is usually made from consideration of three factors; the first is the degree of sulphonation, the second is the type of products required and isomers produced, and the third is the yield of sulphonic acid.

The sulphonation reactions described in the literature were carried out over a wide range of temperatures, usually from -20°C to 300°C. Sulphonation gave a better yield at elevated temperatures, especially in the case of sulphonation to higher yields. However, sulphone formation is also increased by enhanced temperatures. In addition, the concentration of the sulphuric acid or oleum used as the sulphonating agent influences the course of sulphonation. Sulphonation prefers high concentrations of sulphonating agents, while water formed as a side product in the sulphonation reaction reduces the rate of sulphonation.

Only mercuric compounds (e.g., HgSO₄) have been found to catalyse the reaction but at concentrations above 1 wt%, they change the ratio and yield of isomers produced, when oleum was used as the sulphonating agent [174].

6.2.4 Sulphonating Agents

Sulphonating agents can be classified by the type of the reaction they produce. They react as three types of reagents, namely as electrophiles, nucleophiles and radicals [174]. The first group of sulphonating agents are used most frequently to sulphonate aromatic compounds and manufacture sulphonic acids. They are mainly reagents derived from sulphur trioxide, such as sulphuric acid, oleum, chlorosulphonic acid, free sulphur trioxide and complexes such as acetyl sulphate which can be prepared by the reaction in Scheme 6.5. The addition of acetic acid to the reaction reduces the risk of oxidation and cross linking of the substrate and acetyl sulphate is used as a mild sulphonating agent.

The second group contains nucleophilic agents such as sulphites and hydrogen sulphites, and sulphur dioxide, which react with halogen derivatives and unsaturated compounds containing multiple bonds.

The third group consists of radical initiators such as sulphurylchloride (SOCl₂) and blends of gases e.g., sulphur dioxide and chlorine (SO₂ + Cl₂), sulphur dioxide and oxygen (SO₂ + O₂).

$$2CH_3COOH + SO_3 \leftrightarrow CH_3COOSO_3H + CH_3COOH \leftrightarrow (CH_3CO)_2O + H_2SO_4$$
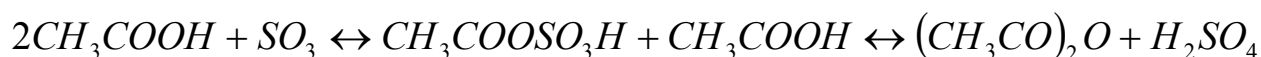
Scheme 6.5: Acetyl sulphate formation[174].

6.3 Sulphonation of Polymers

Generally, polymer sulphonation can be carried out as a heterogeneous reaction or as a homogeneous reaction in hydrocarbons or chlorinated solvents. The sulphonation of some polymers, namely PEEK, PEI, PS and PP are discussed below.

6.3.1 Sulphonation of PEEK

The sulphonation of commercially available PEEK (Victrex ICI, Gatone) using 96–98% sulphuric acid [44, 46, 179-185], mixtures of sulphuric acid and methane sulphonic acid [180], mixtures of concentrated sulphuric acid and fuming sulphuric acid [186-188] have been described in the literature. The kinetics of PEEK sulphonation in concentrated H_2SO_4 was investigated in the temperature range of 25–75°C and an activation energy around 82.8 kJ mol^{-1} has been reported [189, 190]. The sulphonation of cross linked PEEK has been recently described using chlorosulphonic acid as both swelling and sulphonating agent [58] as well as concentrated sulphuric acid [157]. The kinetics of cross linked PEEK sulphonation in concentrated sulphuric acid at room temperature has been shown to follow diffusion controlled mechanism [157].

Scheme 6.6 shows the chemical structure of the repeat unit of PEEK and the corresponding sulphonation reaction. Substitution takes place in one of the four equal positions on the aromatic ring between the ether bridges because the electron withdrawal nature of the neighbouring carbonyl group deactivates the other two aromatic rings [44]. At room temperature with the concentrated sulphuric acid used as the sulphonating agent, only one SO$_3$H group is attached to each repeat unit owing to the electron withdrawing nature of the acid sulphonic group introduced.
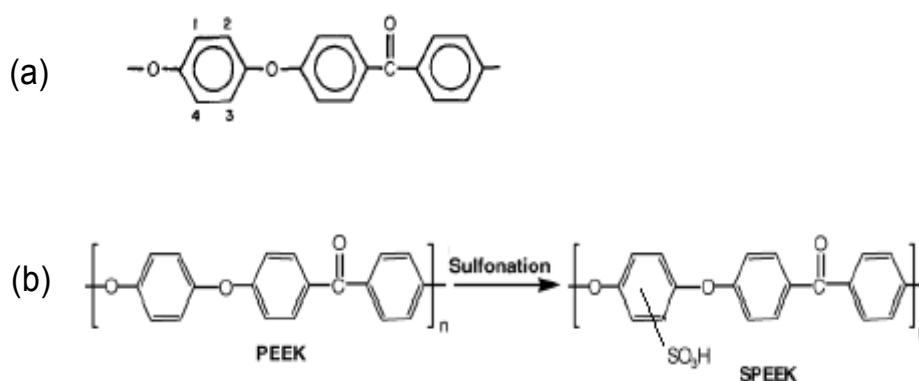
Scheme 6.6: The chemical structure of PEEK and possible sulphonation sites (a) and sulphonation reaction (b) [44].

The sulphonation of PEEK in concentrated H_2SO_4 is essentially free of degradation and cross linking reactions if the concentration of the acid is kept below 100%. It is believed that the presence of water decomposes the pyrosulphonate intermediates, which act as inter- and intra-molecular sulphone cross links [44]. Evidence of the chemical modification induced by sulphonation using concentrated sulphuric acid and of the degree of sulphonation has been obtained from infrared FTIR and NMR spectroscopies, elemental analysis and acid content titration. The extent of sulphonation can be controlled by changing reaction time, temperature and acid concentration and can produce a degree of sulphonation up to 100% mono-substitution of the repeat unit [44].

6.3.2 Sulphonation of other Polymers

6.3.2.1 Sulphonation of Poly Ether Imide, PEI

Polyimides are high-performance polymers that have been used in a wide variety of applications due to their excellent properties–price–processability balance. These polymers have excellent thermal stability, high mechanical strength, good film-forming ability, superior

radiation and chemical resistance, good adhesion properties and low dielectric constant [191, 192]. Poly(ether imide)s, PEI, are one of these polymer, the chemical structure of which is given in Scheme 6.7 along with that of sulphonated PEI, which are potential candidates for producing PEM.
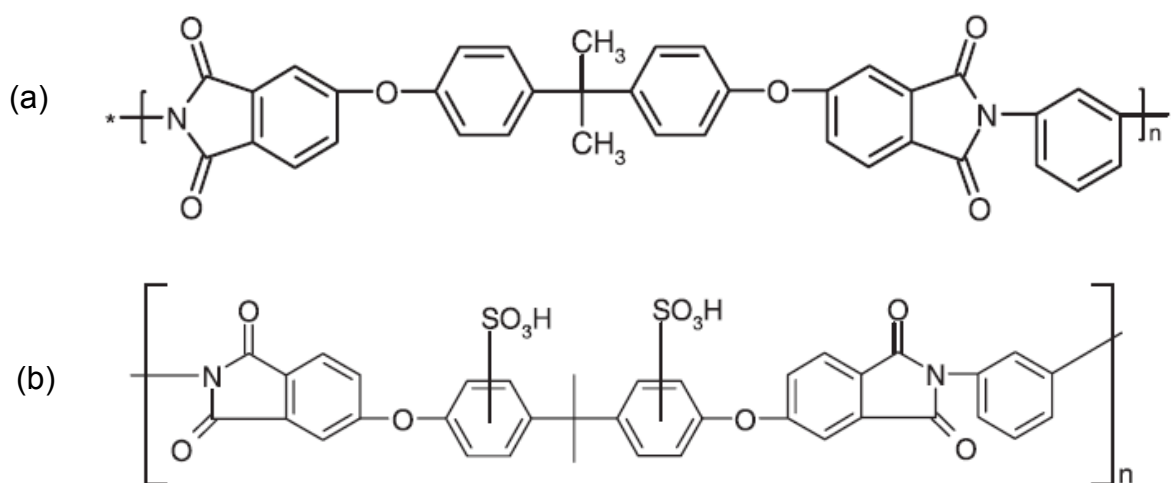
Scheme 6.7: Repeat unit of poly(ether imide) (Ultem®) (a) and sulphonated PEI (b) [193].

The modification of PEIs by sulphonation, with the aim of developing proton exchange membranes, PEM, has been achieved using different sulphonating agents such as acetylsulphate [193] and chlorosulphonic acid [194] .

The sulphonation of PEI is expected to take place on the electron-rich benzene rings of PEI, e.g., the bis-phenol-A segment. After introduction of one $-SO_3H$ group into the ring it is deactivated and further sulphonation on the same ring does not readily occur. Under mild sulphonating conditions (e.g., at low temperature) and depending on the duration of the reaction, one or two SO_3H groups are expected to be introduced per repeat unit. The extent of sulphonation can be determined by elemental analysis and determination of sulphur content.

The theoretical sulphur content if one sulphonic acid group is present per repeat unit is 4.76% and if two sulphonic acids are present then it is around 8.5% [193, 194].

6.3.2.2 Sulphonation of Polystyrene, PS

Polystyrene, PS, is an amorphous polymer with good mechanical and thermal stabilities. The first studies on the sulphonation of PS were published before World War II by Turbak who sulphonated polystyrene in a homogeneous phase reacting polystyrene with complexes of triethyl phosphate and sulphur trioxide as sulphonating agents in dichloroethane [174].

Makowski et al. also prepared lightly sulphonated polystyrene by using acetyl sulphate complexes as sulphonating reagent in a solution of dichloroethane. In this reaction, random ionic functionalities along the polymer chains are generated without significant degradation or cross linking of the reaction product [195]. Various methods of sulphonating polystyrene have been described in the literature [174, 196-198], see Scheme 6.8 as an example.
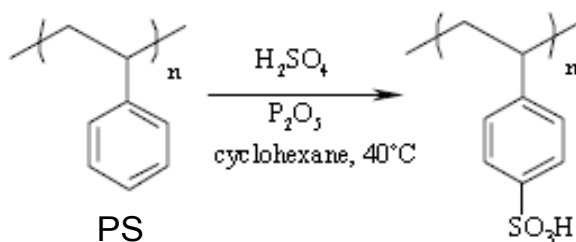
Scheme 6.8: Sulphonation of PS[198].

6.3.2.3 Sulphonation of Polypropylene, PP

Polypropylene, PP, has a highly crystalline structure, which gives it good rigidity, strength, and chemical resistance to organic solvents, acids, and alkalis. It is usually used as the

isotactic form in which the PP chains are attached in a head-to-tail fashion and all the methyl groups are aligned on the same side of the polymer chain. PP, a vinyl polymer, is structurally similar to polyethylene. One major difference is that PP has three different types of carbons, primary, secondary, and tertiary, in the repeating unit. It is known that these carbons show different reactivates in chemical reactions. It has been reported that the sulphonation of PP followed by slight oxidation and the formation of C=C bonds is enhanced with increasing reaction temperature and time [199]. The mechanism for the sulphonation of PP with fuming sulphuric acid has been outlined with consideration of the PP molecular structure [200].

6.4 Results and Discussions

6.4.1 Structural Analyses by FT-IR Spectroscopy

Figure 6.1(a) shows the FTIR spectra of PEEK and sulphonated PEEK, from which changes in the structure of PEEK on sulphonation was deduced. These corresponded with the appearance of new absorption bands and the splitting of others, consistent with the presence of $-SO_3H$ group on the 1.4-di-ether aromatic ring, see Scheme 6.6, and confirmed that the sulphonation reaction occurred in the absence of degradation or cross linking [44, 46, 67, 181].

New absorption bands at 3340, 1250 and 1078 cm^{-1} were assigned to the stretching of the O-H of the $-SO_3H$ group and to the asymmetric and symmetric stretching of the O=S=O group respectively. A single broad band between 860 and 840 cm^{-1} was characteristic of the out-of-plane C-H bending of two hydrogen atoms of 1, 4- di-substituted aromatic ether ring. This later band splits upon sulphonation into two, characteristic of an isolated hydrogen in a 1, 2, 4 tri-substituted aromatic ring.

The aromatic ring absorption bands at 1490 and 1414 cm^{-1} were split on sulphonation and new bands appeared at 1470 and 1402 cm^{-1} respectively. The intensity of the new band at 1470 cm^{-1} increased with increasing sulphonation time as well as the ratio of absorbances, A_{1470}/A_{1490}, as can be seen from Figure 6.1(b), thereby indicating that FTIR technique can be used for determination of the extent of sulphonation. These ratios were determined using OMNIC software by drawing a base line in the region 1430–1520 cm^{-1} and measuring the heights of these peaks. It has been reported [181] that the degree of sulphonation (calculated from elemental analyses and NMR spectroscopy) correlates linearly with the ratio of the absorbances of the bands at 1470 and 1490 cm^{-1}.

Analysis of the FTIR spectra also confirmed that sulphonation of the irradiated membranes, see Figure 6.2, had taken place and that the splitting of the band at 1490 cm^{-1} was not due to ion irradiation.
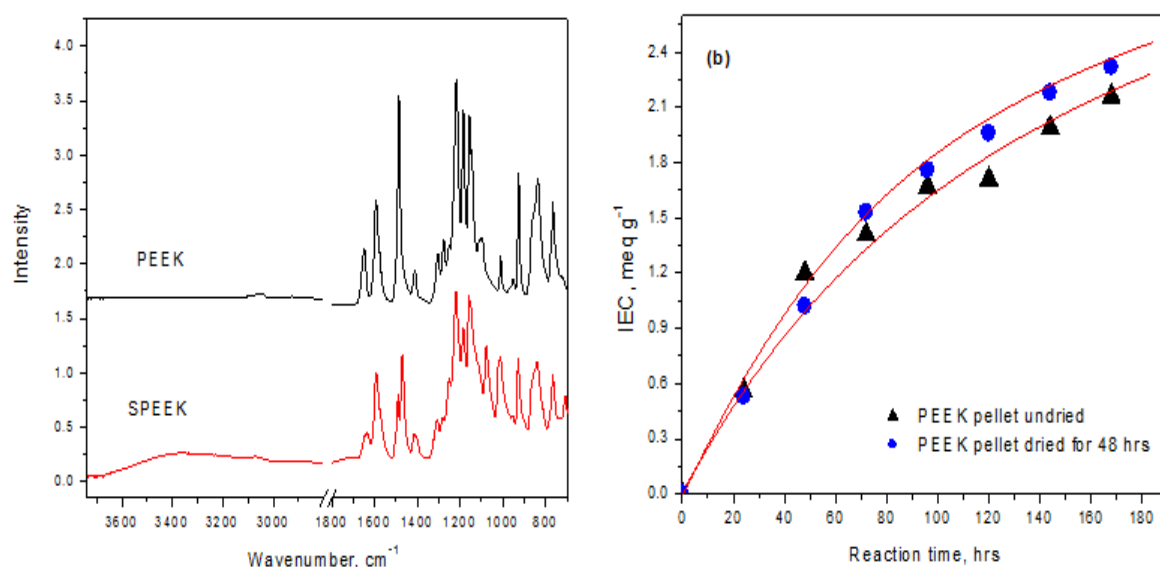
Figure 6.1: Changes to the FTIR spectrum on the sulphonation of PEEK, 450G: The spectrum of PEEK and sulphonated PEEK after reacting for 120 h (a) and variation of absorbance ratio (A_{1470}/A_{1490}) with reaction time (b).
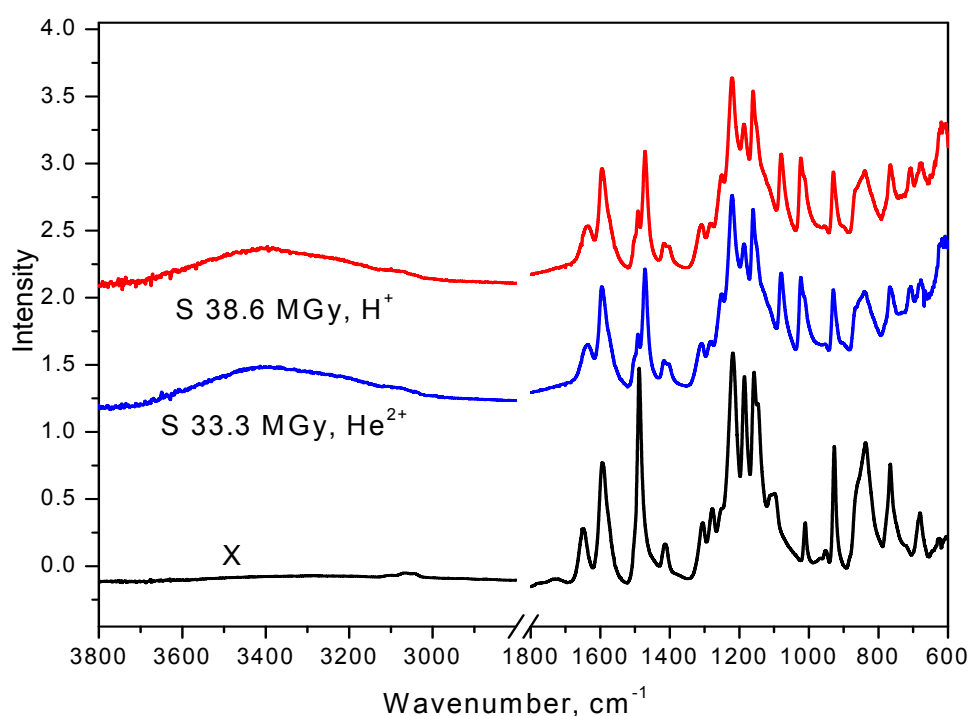
Figure 6.2: FTIR Spectra of cross linked PEEK (sample X) and sulphonated cross linked

PEEK after 76 h sulphonation (samples S).

6.4.2 Solubility of SPEEK

PEEK has excellent resistance to a wide range of chemical reagents. The strong

intercrystalline forces in PEEK make the polymer only soluble in concentrated strong acids,

such as sulphuric acid [201]. The sulphonation process makes the polymer soluble in many

other solvents such as dimethylsulphoxide, DMSO. It is noteworthy that the dissolution

properties of SPEEK are strongly dependent upon the degree of sulphonation, DS, such that

below 30% sulphonation the samples are insoluble, at least at moderate temperatures, in all

common solvents. Above 30% sulphonation the samples are soluble in hot DMF, DMAc and

DMSO; above 40 % in the same solvents at room temperature, above 70% in methanol and at

100% in hot water [44, 180]. The solubility of various sulphonated PEEK in the free acid form after different reaction time is quoted in Tables 6.1, 6.2 and 6.3.

The solubility test was carried out to find the most suitable solvent to cast SPEEK membranes. DMF and DMAc both were found to be the most suitable to prepare PEM. This was not the case however with the cross linked sulphonated membranes; these were not soluble and membranes were produced without casting. However, the solubility test was of prime importance as it provided information about the behaviour of the membranes in water and methanol. It was noted that the cross linked membranes only swelled in methanol and hot water and the extent of swelling depended on reaction time.

6.4.3 The Effect of Reaction Conditions on IEC and DS

The ion exchange capacity, IEC, of the PEM materials is an important material property since it determines proton conductivity, water uptake, and dimensional stability. Table 6.1 lists the IEC and the corresponding degree of sulphonation, DS, obtained by titration of the non cross linked sulphonated PEEK, 450G, with standard alkali. The correlation between these values and the ratio of the absorbances, A_{1470}/A_{1490} lead to the following relationship:

$$IEC = (\frac{A_{1470}}{A_{1490}} - 0.03)/0.874 \qquad (6.1)$$

FT-IR spectroscopy was used to determine the extent and follow the kinetics of the sulphonation reaction. As can be seen from Table 6.1, the degree of sulphonation as well as the IEC increased progressively in the initial stages of sulphonation and showed non linear time dependence in the final stages of the reaction. This has been explained as due to the negative effect of de-sulphonation of the product, SPEEK [189, 190] and the following rate expression has been shown to describe the sulphonation kinetics of PEEK in a large excess of

concentrated sulphuric acid, such that its concentration and the water content can be assumed to be constant through out the reaction, that is,

$$-\frac{dC}{dt} = \frac{k_1 C}{k_d (C_0 - C)}$$

(6.2)

Rearranging and integrating from the initial concentration of PEEK, C_0, to concentration, C, at time t gives the following equation,

$$-\frac{C_0 - C}{C_0} - \ln \frac{C}{C_0} = \frac{k_1}{k_d} \frac{1}{C_0} t$$

(6.3)

where k_1 is the rate constant of sulphonation, and k_d is the rate constant of the reaction, in which the product inhibits sulphonation. (C_0-C) is the concentration of product at time t.

It is more convenient to write the previous equations in term of the IEC, since the concentration of the substrate is defined as,

$$C = C_0 (2.8 - IEC) = C_0 \left(1 - \frac{IEC_t}{IEC_\infty} \right)$$

(6.4)

where IEC_t and IEC_∞ correspond to the ion exchange capacity at time t and at the end of the reaction when the sulphonation degree is 100%. The IEC_∞ was taken as 2.8 meq g^{-1}, assuming that only one sulphonic acid group is attached to each PEEK repeat unit [44], as outlined in Scheme 6.6.

Substitution eq. (6.4) in eq. (6.3) leads to the following rate expression,

$$-\frac{IEC_t}{IEC_\infty} - \ln(1 - \frac{IEC_t}{IEC_\infty}) = \frac{k_1}{k_d} \frac{1}{C_0} t$$

(6.5)

As can be seen from Table 6.1, the dried samples sulphonated to a higher degree than the un-dried and drying the polymer for a longer period lead to an increase in IEC. This is the case with samples 3, 8 and 12, which were dried for 0, 48 and 168 hours and were reacted using the same conditions. Water, present in the polymer, appeared to inhibit the reaction as the un-

dried sample sulphonated at a lower rate than the dried ones; rate constants, k_1 / k_d, are 2.8 ± 0.2 ×10^{-3} and 3.8 ± 0.1 × 10^{-3} respectively, see Figure 6.3.

Table 6.1: The IEC and DS values for sulphonated PEEK, 450 G.

Sample No.	Drying time (h)	Reaction time* (h)	IEC ± 0.04 (meq g^{-1})	DS ± 5.0 (%)	Solvents
1	Un-dried	48	1.21	38	DMAc, DMF
2		72	1.41	46	DMAc, DMF
3		96	1.67	56	DMAc, DMF
4		120	1.71	59	DMAc, DMF
5		144	1.99	68	Methanol
6		168	2.16	75	Methanol
7	48	72	1.53	50	DMAc, DMF
8		96	1.76	59	DMAc, DMF
9		120	1.96	67	DMAc, DMF
10		144	2.18	76	Methanol
11		168	2.32	82	Methanol
12	168	96	2.53	92	Hot water

* The time scale starts from the addition of PEEK to the sulphonation agent.

In addition, stirring plays an important role not only in obtaining homogeneous products but also in achieving higher IEC and sulphonation degree, see Table 6.2. The rate constant on stirring was found approximately 10 times higher than that without stirring. The rate constants are 3.2 ± 0.4 ×10^{-3} and 4.7 ± 0.1 × 10^{-4} respectively see Figure 6.4.
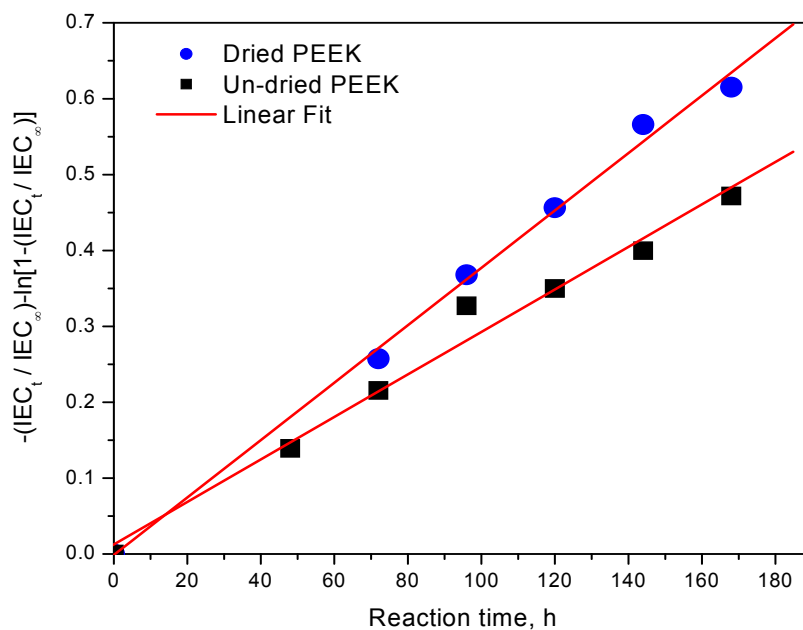
Figure 6.3: Sulphonation kinetics of PEEK pellets, G450, in concentrated sulphuric acid at room temperature; effect of drying.

Table 6.2: The IEC and DS values for sulphonated PEEK, P150.

Sample No.	Note	Reaction time* (h)	IEC ± 0.04 (meq g^{-1})	DS ± 5.0 (%)	Solvents
13	Without	48	0.36	11	Insoluble
14	stirring	72	0.78	25	DMF, DMAc
15		120	0.81	26	DMF, DMAc
16	With	24	0.81	25	DMF, DMAc
17	mechanical	48	1.31	47	DMF, DMAc
18	stirring	72	1.46	49	DMF, DMAc
19		96	1.79	61	DMF, DMAc
20		120	2.00	70	Methanol

* The time scale starts from the addition of PEEK to the sulphonation agent.
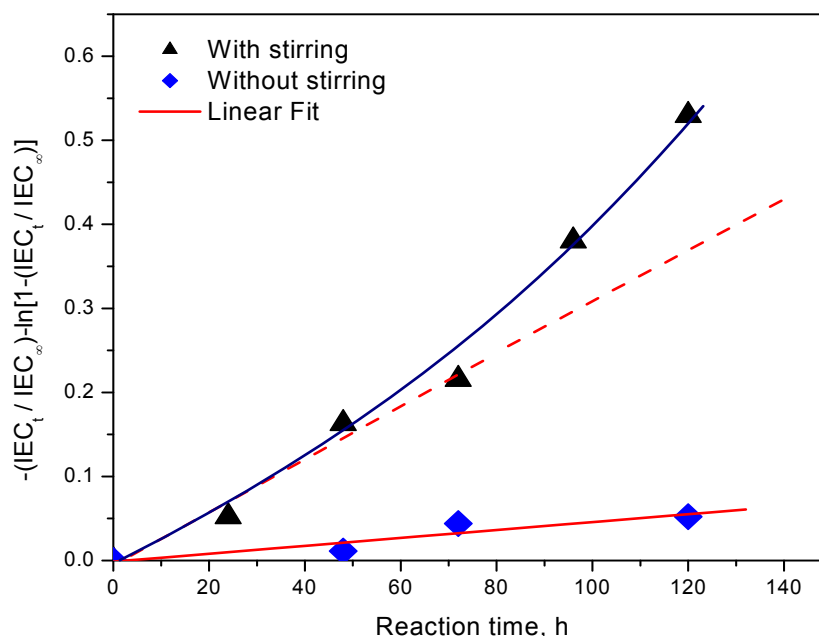
Figure 6.4: Sulphonation kinetics of PEEK powder, P150, in concentrated sulphuric acid at room temperature; effect of stirring.

It was also noted that the concentration of PEEK and its physical form became a significant factor to be considered when the reaction was carried out without stirring.

No effect of molecular weight was observed in the sulphonation reaction as both P150 and G450 (melt viscosities 0.135 and 0.468 respectively) have the same rate constant within experimental error.

The polymer physical state was noted to have an effect on the IEC and higher IEC values were obtained by sulphonating of PEEK powder and film, see Table 6.3. This may be due the difference in dissolution time of the polymer in sulphuric acid, since only 2 hours was taken to dissolve film or powder and more than 12 hours for the PEEK pellet at the same concentration. However, the polymer may be sulphonated to a small localised extent while it is dissolving.

Table 6.3: The IEC and DS values for sulphonated PEEK, 100 μ film.

Sample No.	Reaction time* (h)	IEC ± 0.04 (meq g^{-1})	DS ± 5.0 (%)	Solubility
21	24	1.40	46	DMF, DMAc
22	48	2.20	77	Methanol
23	72	2.46	87	Hot water
24	96	2.84	102	Hot water

* The time scale starts from the addition of PEEK to the sulphonation agent.

Increasing the reaction temperature has been reported to increase the IEC and DS significantly, and found to be independent of the initial PEEK concentration [189]. Dissolving PEEK in methane sulphuric acid, MSA, prior to sulphonation with H_2SO_4 has been shown to produce random SPEEK in the lower DS range (less than 20-30%) [45]. Sulphonation of other commercially available PEEK, Gatone from Garda Chemical Limited, has been reported to differ from that of Victrex PEEK in terms of the ease of sulphonation and product properties such as conductivity and water uptake [46].

6.4.4 The Effect of Cross Linking on IEC and DS

Cross linking was used to increase the mechanical strength and decrease the swelling properties of the resultant membranes. This has been carried out after sulphonation using thermal method [47, 48] and also using suitable cross linking agents such as amines [49], halides [50] and alcohols [51]. One of the drawbacks of this method is that conductivity is decreased since cross linking occurs through the coupling of sulphonic acid groups.

Cross linking the polymer can also be achieved prior to sulphonation. This solvent free procedure, however, leads to diffusion limiting the degree of sulphonation. The preparation of cross linked PEEK has been reported to occur via imine formation at carbonyl groups [53], and by a thermal method [54] but the sulphonation of the resultant polymers has not yet been investigated.

Cross linked PEEK was also prepared by irradiation using different radiation sources [55-58], and the interest of the following paragraphs is to discuss the effect of the cross links introduced by ions irradiation on the sulphonation reaction of PEEK as well as on the final degree of sulphonation, DS, achieved.

6.4.4.1 Mass Change Analyses

Figure 6.5 shows the change in mass of the irradiated film samples on immersing in sulphuric acid and sulphonation. There was a loss in mass consistent with the removal of soluble polymer but this became less with increasing dose as cross linking developed progressively and the polymer became less soluble.

The increase in mass with time is partly due to the increase of the polymer hydrophilicity on sulphonation and as a result to increasing amounts of ionically bound water in the polymer matrix, which did not evaporate under the drying conditions used in the present study. This was consistent with increasing the sulphonation degree of the films.
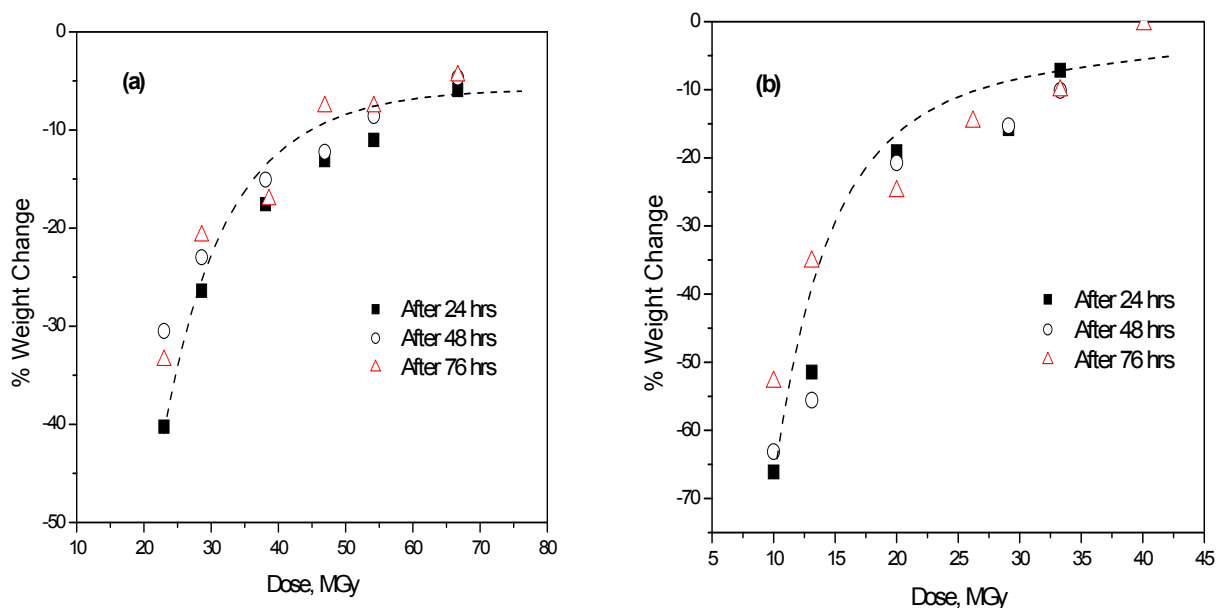
Figure 6.5: Mass changes for PEEK irradiated (a) with proton and (b) with helium ions, and sulphonated as indicated.

6.4.4.2 IEC vs Cross Link Density

Figure 6.6 shows the IEC of the cross linked films after various sulphonation times. At each sulphonation period the degree of sulphonation and the IEC decreased in proportion to the cross linking density [57] and increasing irradiation dose. However, the IEC for sample irradiated with He^{2+} ions were found to be higher than those obtained on irradiation with protons and in some cases those values were higher than that of the non cross linked samples.

This may be due to the higher probability of end-linking reaction on irradiation with helium, which produced hydroxyl group on the aromatic rings which in turn will increase the reactivity of the aromatic ring to sulphonation.
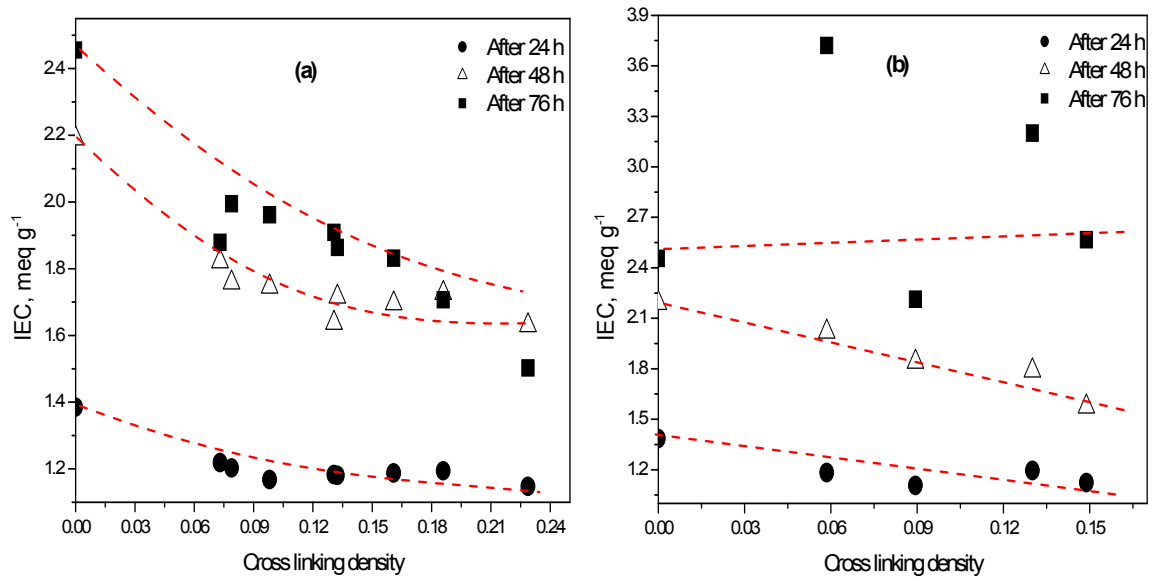
Figure 6.6: IEC vs cross linking density on sulphonation of irradiated PEEK (a) with protons and (b) with helium ions.

6.4.4.3 Diffusion Controlled Reaction

The sulphonation of PEEK has been widely studied and is a somewhat complicated reaction but the rate expression generally accepted is [189, 190]

$$-\frac{dC}{dt} = \frac{k_1 C}{k_d (C_0 - C)} \times \frac{a^2_{H_2SO_4}}{a_{H_2O}} \tag{6.6}$$

where k_1 and k_d are the reaction rate constants for sulphonation and de-activation by the product and C, and $(C_o - C)$ are the concentrations of PEEK, and sulphonated product, $a_{H_2SO_4}$ is the activity of sulphuric acid which is proportional to its concentration, C_s, in the system and a_{H_2O} is the activity of water which is proportional to its concentration in the system. The second order dependence on acid is attributed to a bimolecular reaction in which the sulphonating species is produced.

167

In a homogeneous solution and in the presence of excess concentrated acid, the quantities of sulphuric acid consumed and the water produced are both very small compared with their initial amounts, then the factor of $a^2_{H_2SO_4}/a_{H_2O}$ in eq. (6.6) can be treated as a constant and the rate equation simplifies to eq. (6.2).

However, this is not the case in the sulphonation of cross linked PEEK samples if diffusion of the sulphuric acid is the rate determining step and the local concentration of sulphonating species changes with time, t.

The reaction conditions adopted for sulphonating the cross linked films are consistent with diffusion of the sulphuric acid into the film, for which Fick's second law is appropriate [202]

$$\frac{\partial C_s}{\partial t} = D\frac{\partial^2 C_s}{\partial x^2} \qquad (6.7)$$

where C is concentration at distance x from the surface of the film at time t, and D is the diffusion coefficient. The boundary conditions for sulphuric acid is $C = C_{s,0}$ at the film surface, by ignoring film edge effects the cumulated concentration of sulphuric acid in the film of thickness l, at time t is $C_{s,t}$

$$C_{s,t} = 2C_{s,0}\sqrt{\frac{Dt}{\pi l^2}} \qquad (6.8)$$

From eq. (6.6) the sulphonation of PEEK is second order in sulphuric acid and first in PEEK repeating unit such that the rate of sulphonation in the presence of diffusion control is,

$$-\frac{dC}{dt} = \frac{4D}{\pi l^2}\frac{k_1 C}{k_d(C_0 - C)}C^2_{s,0}.t \qquad (6.9)$$

Since $C_{s,0}$ is constant and present in large excess and the equivalent of eq.(6.5) in the presence of diffusion is

$$-\frac{IEC_t}{IEC_\infty} - \ln(1 - \frac{IEC_t}{IEC_\infty}) = \frac{4D}{\pi l^2}\frac{k_1}{k_d C_0}.t \qquad (6.10)$$

Plots of $-(IEC_t/IEC_\infty) - \ln(1 - IEC_t/IEC_\infty)$ against t were linear (with regression coefficient larger than 0.975), see Figure 6.7, and the slope, $(4D/\pi l^2)(k_1/k_d C_0)$ is a relative measure of the diffusion coefficient, D. This decreased in proportion to the cross linking density and increasing irradiation dose. Cross linking limited the degree of swelling of the films and decreased the rate of diffusion of sulphuric acid into the films, see Figure 6.8.
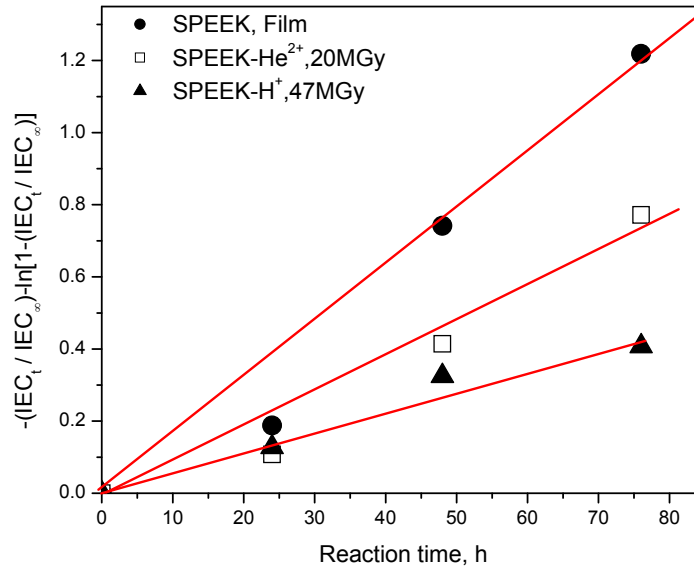
Figure 6.7: The sulphonation of cross linked PEEK films; kinetic treatments.

Moreover, the ratio of the intercept at zero cross linking density ($k_1/k_d C_0$) to values at other degree of cross linking is a measure of ($4D/\pi l^2$) from which D was evaluated and its dependence on cross link density is shown in Figure 6.9.
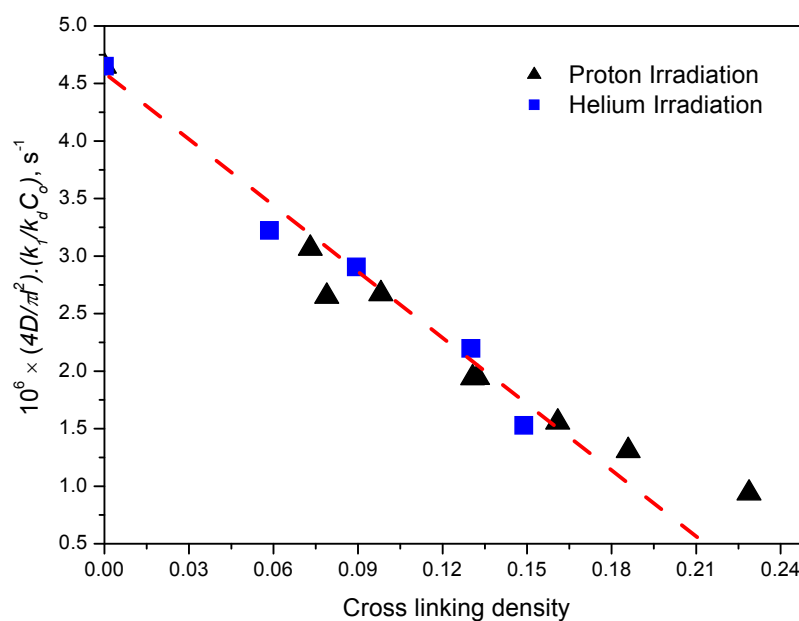
Figure 6.8: Diffusion controlled sulphonation of cross linked PEEK films; plot of slopes determined from eq. (6.10) as a function of cross linking density.
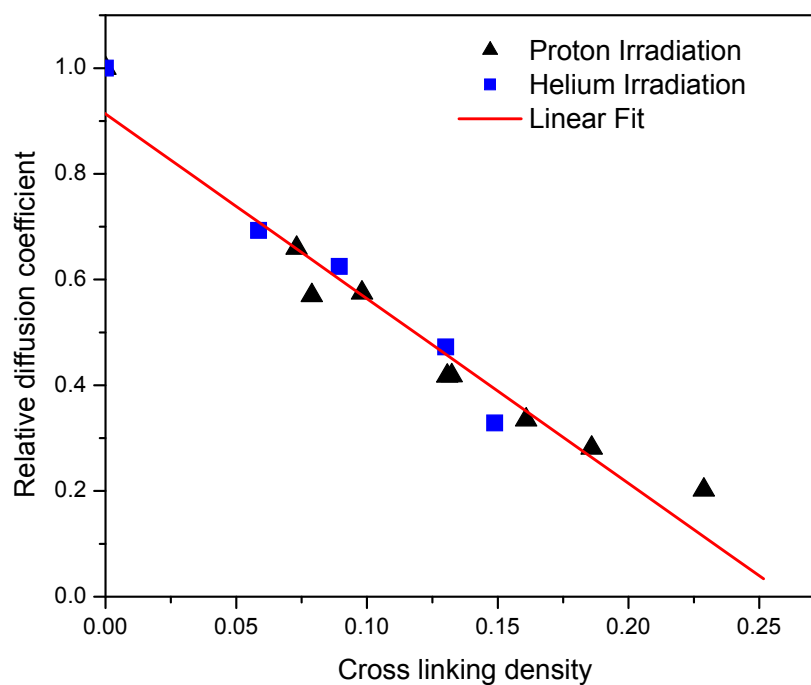
Figure 6.9: Relative diffusion coefficient of sulphuric acid into cross linked PEEK film as a function of cross link density.

6.5 Conclusions

The sulphonation of PEEK in concentrated sulphuric acid at room temperature was studied. The kinetics treatment indicated that both stirring and drying period play a role in determining the sulphonation degree. The sulphonation of cross linked membranes was also achieved by the use of concentrated sulphuric acid and this was confirmed by FTIR spectroscopy. The IEC of the cross linked membrane was shown to be dependent on the cross linking density and decreased with increasing irradiation dose.

The end groups such as hydroxyl introduced by irradiation increases the final ion exchange capacity of the cross linked membrane compared with the original materials. This effect was more pronounced in the case of the films irradiated with helium ions, confirming their higher efficiency in producing cross and end linking compared to proton ions.

The kinetics treatment using Fick's second law [202] was found to be a good model to describe the diffusion controlled feature of the sulphonation reaction of cross linked PEEK films. This model predicts a similar decrease in diffusion coefficient with increasing cross link density but this decrease was dependent on the irradiation ions used.

Chapter 7

Water Uptake, State of the Water and

Thermoporometry of Cross Linked PEM

7.1 Introduction

The main properties of the fuel cell membrane is to promote protonic conductivity and water transport, inhibit gas permeation as well as maintaining physical properties such as mechanical strength and dimensional stability. All of these properties are strongly dependent on the total water content as well as on the different types of water present in the membrane [2, 203].

7.2 The Effect of Water Uptake on PEM Properties

Water uptake itself strongly depends on the state of water used to equilibrate the membrane. It has been reported that a Nafion membrane has roughly a λ value (e.g., the number of water molecules per sulphonic acid group) of about 22 and 14 when equilibrated with liquid water and water vapour, respectively [204]. Moreover, water uptake from the liquid phase is dependent on the membranes pre-treatment in particular the drying temperature. It has been reported that water uptake after the Nafion membrane had been completely dried out at 105°C

is significantly smaller than if the membrane had been dried out at room temperature; $\lambda = 12$ to 16 depending on the temperature of rehydration for the membrane previously dried out at 105°C compared with $\lambda = 22$. It is also independent of the temperature of rehydration for the membrane previously dried at room temperature [205]. This was explained as due to changes in morphology occurring in the polymer at elevated temperatures [2].

7.2.1 Proton Conductivity

The protonic conductivity of Nafion membranes has been shown to be a strong function of water content and temperature. For a fully hydrated membrane, $\lambda = 22$, the protonic conductivity is about 0.1 S cm^{-1} at room temperature, and at $\lambda = 14$ (membrane equilibrated with water vapour) about 0.06 S cm^{-1}. Protonic conductivity dramatically increases with temperature and at 80 ºC reached a maximum of 0.18 S cm^{-1} for a membrane immersed in water [205].

The mechanism of proton conduction in Nafion has been extensively studied, and is reported to occur by a combination of proton hopping (the Grotthuss mechanism) and vehicular diffusion [206, 207]. It has been suggested that the Grotthuss mechanism is preferred in media which supports strong hydrogen bonding, e.g., in the centre of a water-swollen pore, while the vehicle mechanism is characteristic of species with weaker bonding. Consequently, the Grotthuss-type mechanism progressively gives way to vehicular diffusion with increasing temperature [208].

Moreover, the protonated clusters H_3O^+, $H_5O_2^+$, and $H_9O_4^+$ are considered mobile but short-lived, as shown by Kreuer [207] who estimated that hydrogen bond breaking and forming occurs at a rate of 10^{11} s^{-1}. As this rate decreases with increasing temperature, transport by the Grotthus mechanism is also believed to decrease. In addition, the Grotthus mechanism has

been shown to enhance proton transport because the transport of alkali metal cations through perfluorinated membranes, where the mechanism is absent, is much lower [209, 210] .

7.2.2 Mechanical Properties

On the other hand, excessive water uptake in a PEM leads to unacceptable mechanical properties, which could lead to weakness or dimensional mismatch when incorporated into a membrane electrode assembly, MEA [211-213]. The dimensional changes have been reported to be of the order of magnitude of 10% for Nafion membranes equilibrated under different conditions, e.g., 50% relative humidity, water at 23 ^{o}C and boiled in water at 100 ^{o}C, see Table 2.1 [2]. The mechanical strength of PEMs has also been related to their water uptake and swelling such that the hydration number, λ, after 1 h of full immersion in distilled water has been reported to be inversely proportional to the elastic modulus for various polymers of the S-PEEK family [213].

7.2.3 Water Transport

Water is carried into the fuel cell via the humidified gas streams entering gas diffusion electrodes. An additional source of water is the oxygen reduction reaction occurring at the cathode. The rate of water generation (in mole s^{-1}cm^{-2}) is [2]:

$$N_{H_2O, gen} = \frac{i}{2F} \tag{7.1}$$

where i is current density (A cm^{-2}), and F is Faraday's constant.

Water in the membrane is transported in two main ways: electro-osmotic drag of water by protons transported from anode to cathode and diffusion via concentration gradients that build up. The existence of concentration gradients across the membrane is visualized when one

considers that electro-osmotic drag and water production by the oxygen reduction reaction both tend to create an excess of water near the cathode. Back-diffusion of water from cathode to anode tends to oppose the build-up of water and normalise the water concentration profile across the membrane [2, 204].

The flux of water due to electro-osmotic drag (in mole $s^{-1}cm^{-2}$) is [2]:

$$N_{H_2O,drag} = \xi(\lambda)\frac{i}{F} \tag{7.2}$$

where ξ is the electro-osmotic drag coefficient. It is defined as the number of water molecules per proton and it is a function of membrane hydration λ.

Water generation and electro-osmotic drag creates a large concentration gradient across the membrane and because of this gradient, some water diffuses back from the cathode to the anode. The rate of water diffusion (in mole $s^{-1}cm^{-2}$) is [2]:

$$N_{H_2O,diff} = D(\lambda)\frac{\Delta c}{\Delta z} \tag{7.3}$$

where D is the water diffusion coefficient in an ionomer having a water content of λ and $\Delta c/\Delta z$ is a water concentration gradient along the z-direction (through the membrane).

In addition to diffusion, due to the concentration gradient, water may be hydraulically pushed from one side of the membrane to the other if there is a pressure difference between the cathode and the anode. The rate of hydraulic permeation (in mole $s^{-1}cm^{-2}$) is [2]:

$$N_{H_2O,hyd} = k_{hyd}(\lambda)\frac{\Delta P}{\Delta z} \tag{7.4}$$

where k_{hyd} is the hydraulic permeability coefficient of the membrane of water content λ, and $\Delta P/\Delta z$ is a pressure gradient along the z-direction (through the membrane).

For a thin membrane, water back diffusion may be sufficient to counteract the anode-drying effect due to the electro-osmotic drag. However, for a thicker membrane, drying may occur on

the anode side. Buchi and Scherer [214] created thick membranes by combining several layers of Nafion membranes and found that the membrane resistance is independent of current density for the membranes up to 120 μm, but it does increase for thicker membranes. The resistance of each layer was measured and only the layer next to the anode exhibited resistance increase with current density. This indicated that drying due to electro-osmotic drag occurred close to the anode, because back diffusion was not sufficient to counteract the electro-osmotic drag [2].

7.2.4 Gas Permeation

One requirement which a PEM should meet is to be impermeable to reactant species, in order to prevent their mixing before they have had a chance to participate in the electrochemical reaction. However, because of the porous structure of the membrane, its water content and the solubility of hydrogen and oxygen in water, some gas does permeate through the membrane. Permeability, P_m, is defined as the product of diffusivity, D, expressed in cm^2 s^{-1} and solubility, S, expressed in mole cm^{-3} Pa^{-1}, e.g.,

$$P_m = D \times S \tag{7.5}$$

It has been reported that permeability of both hydrogen and oxygen through wet Nafion is an order of magnitude higher than that through dry Nafion. It was also observed that the permeation through the wet membrane was lower than permeation through water, and permeation through dry Nafion was lower than permeation through Teflon [2].

7.3 Understanding the Effect of Water on PEM Properties

The transport properties and the swelling behaviour of Nafion and different sulphonated poly ether ketones have been related to differences in the microstructures and the acidity of the

sulphonic groups, see Figure 7.1. The less pronounced hydrophobic/hydrophilic separation of sulphonated poly ether ketones compared to Nafion results in narrower, less connected hydrophilic channels and larger separations between less acidic sulphonic acid functional groups. At high water contents, this is shown to reduce significantly the electro-osmotic drag and water permeation whilst maintaining high proton conductivity [215].

The state of water in a PEM has been reported to have more effect than the bulk water content on the electrochemical properties of a membrane [203]. The state of water in a PEM has been classified into three types: the first is non-freezing water, e.g., water that is strongly bound to the polymer chain and has a role in effective glass transition plasticization; the second is the freezable loosely bound water, e.g., water that is weakly bound to the polymer chain or interacts weakly with non-freezing water and displays a relatively broad melting point; the third is free water, e.g., water that is not intimately bound to the polymer chain and behaves like bulk water. It exhibits a sharp melting point at 0 °C [203, 216-218].

Using the state of water rather than the total water uptake makes the correlation between water content and other electrochemical and physical PEM properties more interpretable. It also helps to compare the properties of different membranes. It has been reported that the bound water leads to a depression of the glass transition temperature of the PEM. This depression affects the temperature of visco-elastic induced morphological relaxation and as an indirect result influences the proton conductivity and reduces the upper limit temperature of use for the PEMFCs. A larger amount of bound water leads to a lower electro-osmotic coefficient indicating that the concentration of loosely bound and free water plays a more important role in transport across the membrane than merely the total water uptake. Moreover, It has been suggested that an important reason for the higher methanol permeability for

Nafion is its higher fraction of freezable water compared to that of poly(arylene ether)-based copolymers [203].
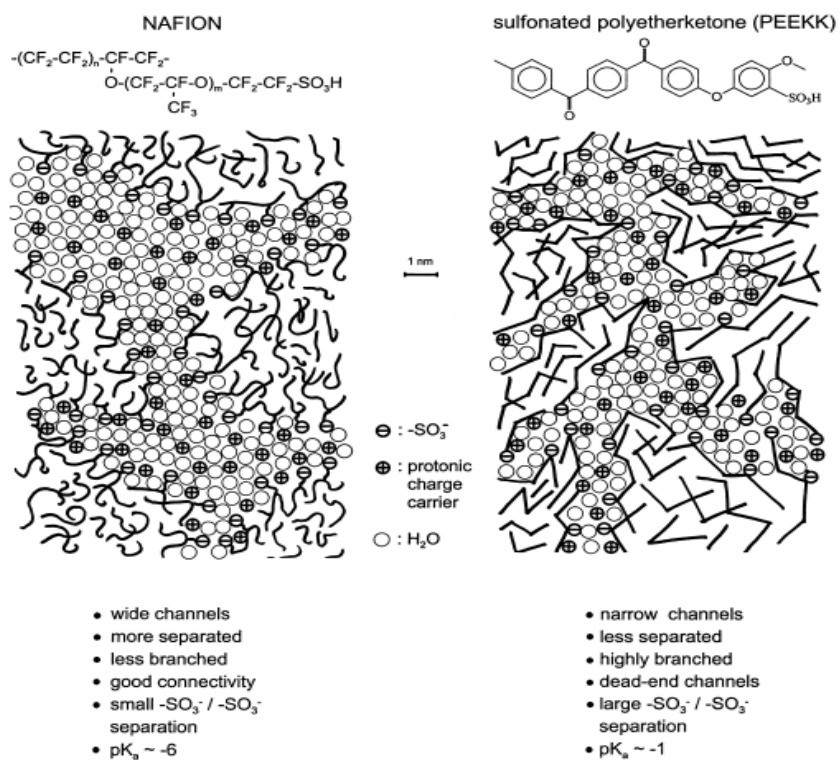
Figure 7.1: Schematic representation of the microstructures of Nafion and a sulphonated PEEKK (After Kreuer [215]).

7.4 Results and Discussions

7.4.1 Membranes Casting

Dimethylformamide (DMF, b.p. 153 ^{o}C), dimethylacetamide (DMAc, b.p. 165 ^{o}C) and N-methyl-2-pyrrolidone (NMP, b.p. 202 ^{o}C) were used as solvents from which the sulphonated aromatic polymers were cast into PEM.

It has been demonstrated that DMF enters into strong hydrogen bonding with sulphonic acid groups of SPEEK, reducing the number of protons available for charge transfer, and dramatically reducing the PEM conductivity, see Scheme 7.1 (a). It has also been shown that both DMF and DMAc solvents may react with residual sulphuric acid during drying, resulting in the formation of dimethylaminium sulphate and the corresponding carboxylic acid, see Scheme 7.1 (b). The immediate result of this interaction is a decrease in conductivity due to the decrease in sulphonic acid concentration [219, 220]. NMP was reported to be the least susceptible solvent to adverse interactions but it is more difficult to get rid of NMP residues as it has the highest boiling point.

All of the limitations associated with solvent casting were eliminated by the one step film preparation of membranes. The cross linked PEEK films did not dissolve and were not deformed while being sulphonated in sulphuric acid, so that the PEM was directly prepared by sulphonation, without using the membrane casting process.
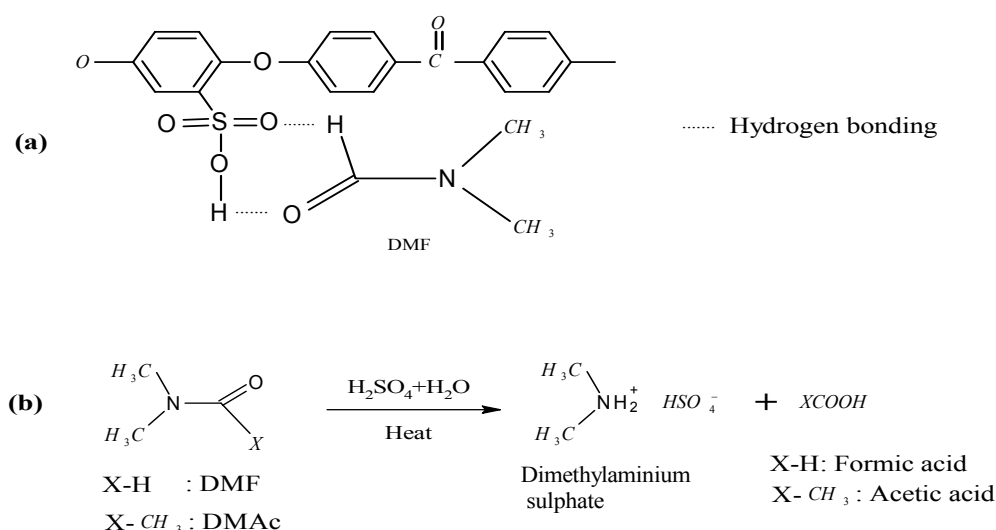
Scheme 7.1: A possible configuration of H-bonding between $-SO_3H$ groups of SPEEK and DMF molecules (a) and reaction of DMF or DMAc transformation in presence of sulphuric acid (b) [219, 220].

7.4.2 Irradiation Cost Consideration

The cost of a 100 μm thick PEEK film bought from Goodfellow Ltd., [221] was £ 251.0 for 0.6×2.0 m. Based on the most recent ion irradiation experiments, which were carried out on an area of 32×32 mm^2 using 12 MeV proton beam of current of 500 nA and a 30 MeV helium ion beam of current of 200 nA, it took approximately 90 minutes to achieve a cross linking density of 0.14 in the first PEEK layer. As 4-10 layers were irradiated and all of them could be used to prepare PEM so the cost of irradiation was about £ 300 divided by the total irradiated area, e.g., 40.9 and 102.3 cm^2 for irradiation with helium and proton respectively. This gave proton irradiation cost of 2.9 £ cm^{-2} compared to 7.3£ cm^{-2} for helium irradiation. The cost of helium irradiation was considerably higher due to the shorter projected range and only four films could be irradiated at one time.

It must be noted that using thinner membranes is desirable for fuel cells application and this would reduce the cost of irradiation. For example starting with PEEK film of 20 μm would result in irradiation cost of about 0.5 and 1.3£ cm^{-2} for irradiation with proton and helium ions respectively.

Further reduction of the cost could be achieved by increasing the energy of the incident beam, which should lead to an increase in the ion projected range, see Figure 7.2 and as a result increasing the total irradiated area. It should also be mentioned that increasing the radiation energy would result in a reduction in the LET effect, see Figure 7.2 and as consequence, the cross link density would be lowered. However, the later case was not covered in this study and it needs to be investigated in detail for an accurate estimation of the irradiation and final membrane cost.
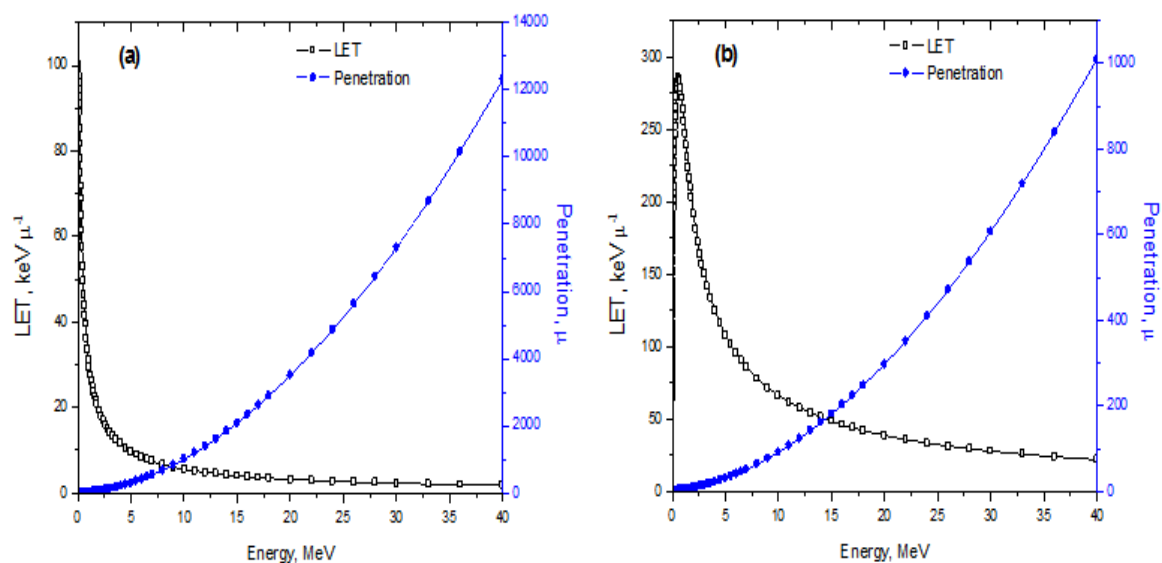
Figure 7.2: LET effect and penetration depth of (a) protons and (b) helium ions in amorphous PEEK, calculated by TRIM-89.

7.4.3 Alternative Approach to Preparing Cross Linked Sulphonated PEEK

It is well known that an alcohol can be formed by the reduction of a ketone. Many different reducing agents have been used, such as $LiAlH_4$ and $NaBH_4$, to do this. Sodium borohydride $NaBH_4$ is much less reactive than $LiAlH_4$ and due to its excellent solubility in water and methanol the later was used as a solvent for the reduction [175-178]. In general sodium borohydride ($NaBH_4$) is an excellent reagent for the reduction of ketones or aldehydes in the presence of esters, hydroxyl groups α to the carbonyl, a carbohydrate residue or a halogens in the α position. Aryl ketones or aldehydes are also easily reduced and the yields are commonly greater than 80% [175]. The possibility of cross linking sulphonated PEEK by forming ether cross links between the polymer chains was investigated by the reduction of the carbonyl groups followed by elimination of water, see Scheme 7.2.

Step 1: Protection of sulphone group
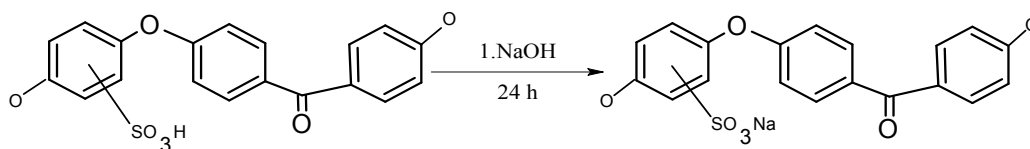
Step 2: The reduction of carbonyl group
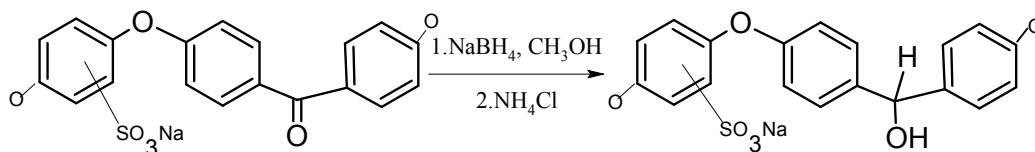
Step 3: The formation of cross Link
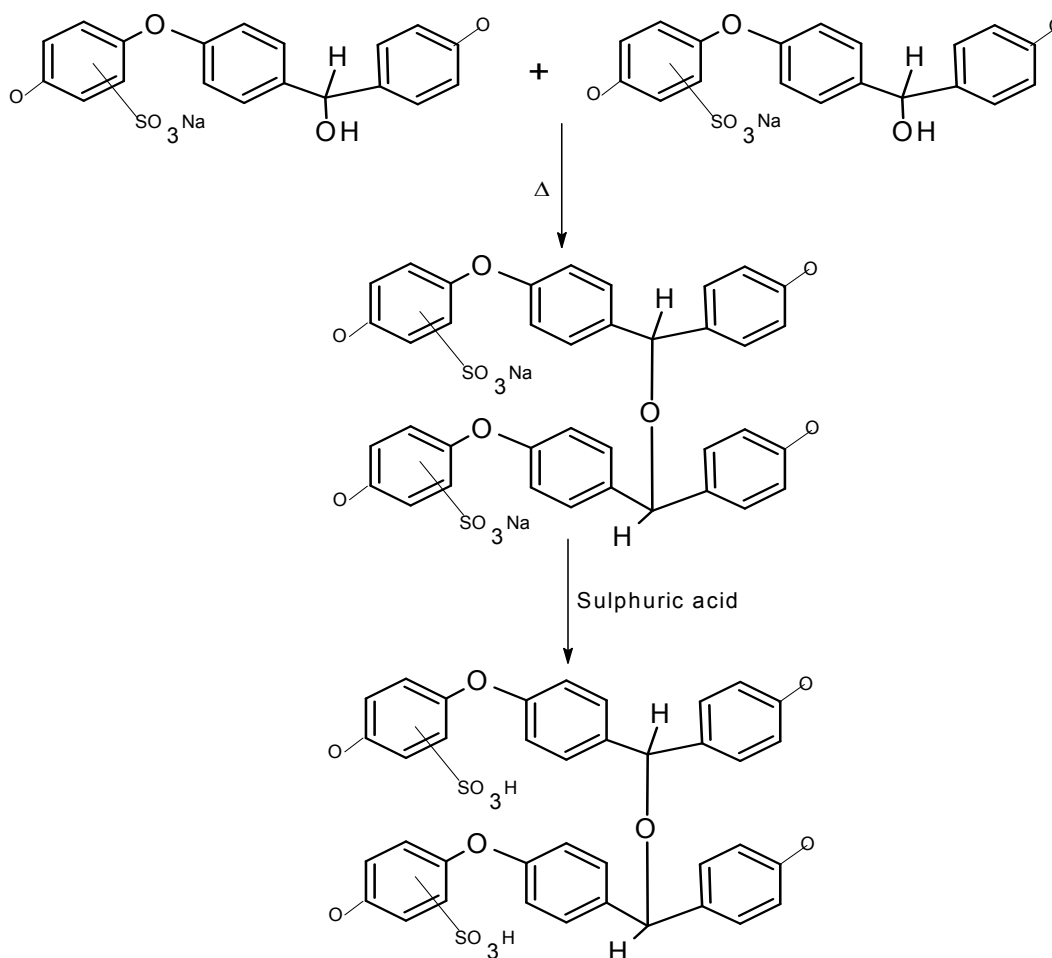
Scheme 7.2: Suggested chemical reaction for cross link formation in SPEEK.

To investigate the possibility of using this reaction scheme, different ratios of reducing agent were added to the methanol solutions of SPEEK samples having $IEC = 2.53$ meq g^{-1}. The solid product was characterized by FTIR spectroscopy and its spectrum is shown in Figure 7.3.

It was observed that the intensity of the carbonyl group at 1640 cm^{-1} reduced from 40% to 20% of the aromatic $C = C$ band at 1600 cm^{-1} taken as a reference, using a ratio of SPEEK:NaBH$_4$ 1:1. No absorbance was observed using a ratio of 1:5. However, the FTIR spectra indicated that other structural changes had taken place. The intensities of most of the absorption bands had increased on the reaction, which was interpreted as due to decrease in the reference peak, which in turn was indicative of reduction of the aromatic $C = C$. In addition, the peak at 920 cm^{-1} which was assigned to the diphenyl ether band, e.g., $Ph - O - Ph$, decreased on reduction and disappeared at a ratio of 1:5.
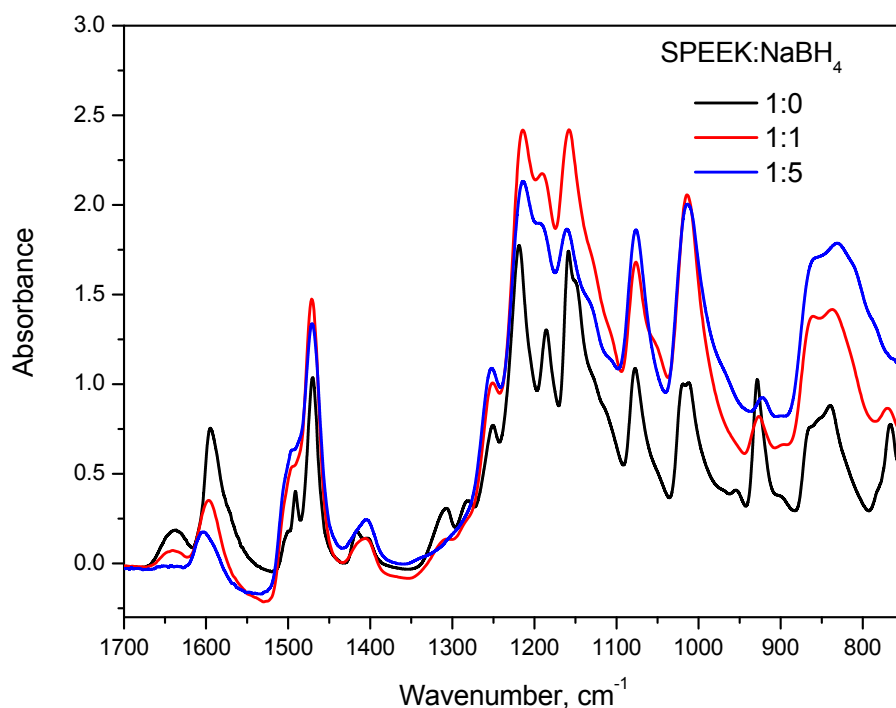
Figure 7.3: FTIR spectra of SPEEK samples before and after chemical modification.

Other experiments were carried out using SPEEK with $IEC = 2.2$ meq g^{-1}. A film was cast from DMAc and after the solvent had been evaporated at room temperature in a fume cupboard, it was washed with distilled water and finally dried in a vacuum oven at 160°C for 24 h. The film was washed with distilled water and immersed in NaOH for 24 h prior to the addition of a 10% solution of the reducing agent. The reaction was stopped after 2 h by washing the film in distilled water and immersing in a solution 0.5 M sulphuric acid for 24 h. Finally the film was left to dry at room temperature. A red coloured film was obtained.

Changes in the FTIR spectrum were detected only on drying at 120 ^{o}C, see Figure 7.4. These included a decrease in intensity of the two $-SO_2$ bands between 1000-1100 cm^{-1}, the appearance of a new band at 1350 cm^{-1} and the shift of the carbonyl band from 1640 to 1655 cm^{-1}. The reduction in intensity was assigned as due to the thermal condensation of the sulphonic acid groups of SPEEK [47], as shown in Scheme 7.3.
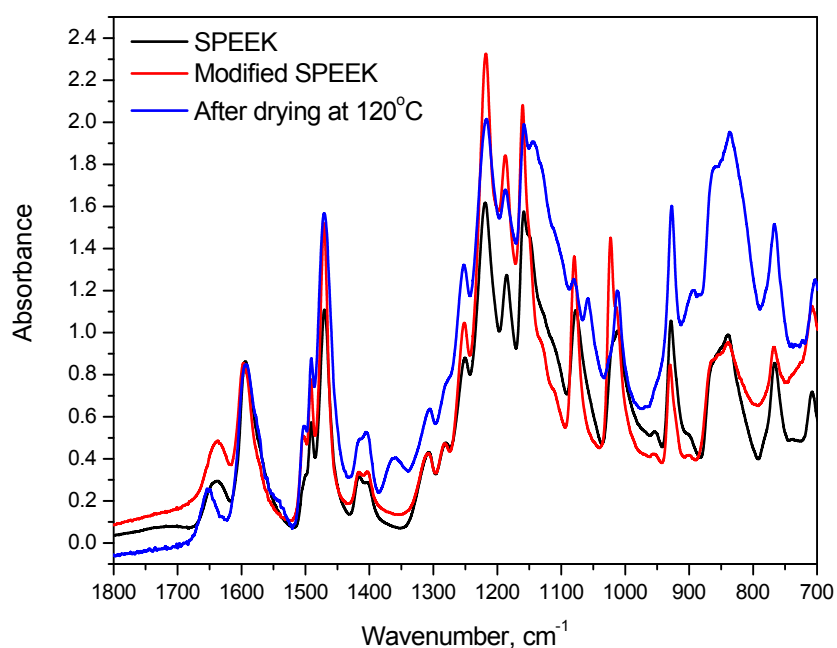
Figure 7.4: Chemical modification of SPEEK as characterized by FTIR spectroscopy.
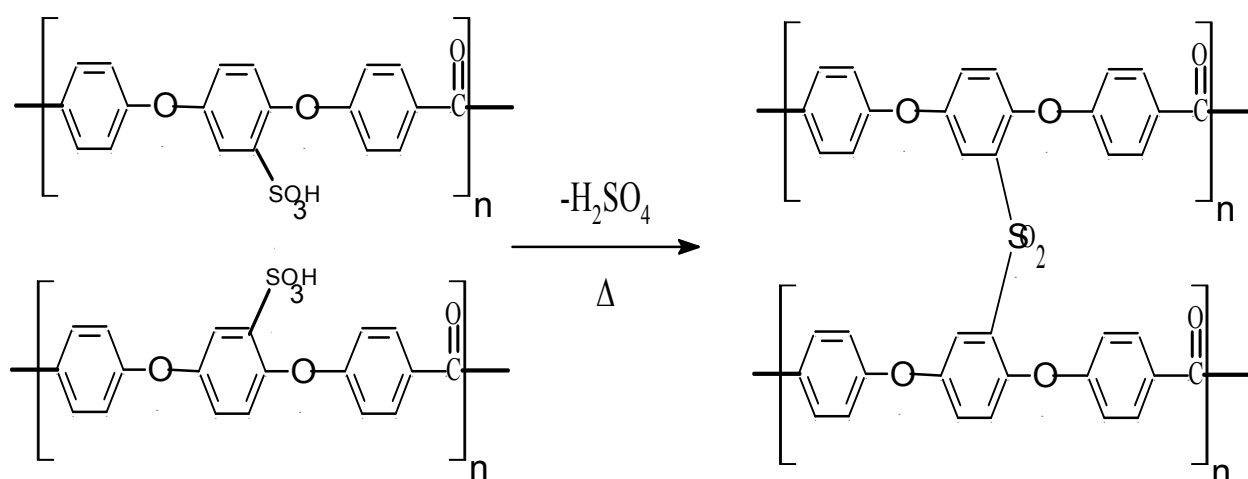
Scheme 7.3: Cross linking of SPEEK by heating at 120°C under vacuum [47].

Similarly, a reduction in intensity of the two $-SO_2$ bands between 1000-1100 cm^{-1} was observed when treating the SPEEK powder at 120 $^{\circ}$C, see Figure 7.5 (a). On the other hand, many attempts to cross link SPEEK film casted from DMF or DMAc by thermal treatments at 120, 130 and 160 $^{\circ}$C in a vacuum failed and the FTIR spectroscopy did not show any evidence of cross linking, see Figure 7.5 (b). Mikhailenko and co-workers [51] reported no cross linking occurred on thermal treatment in the temperature range 120-150 $^{\circ}$C in spite of Yen and co-workers [47] having already patented the formation of cross linking at 120 $^{\circ}$C.

It was concluded that the reducing agent (at low concentration) may have destroyed the bond between the solvent and SPEEK and enabled thermal condensation reaction to proceed. On the other hand, using high ratios of the reducing agent:SPEEK may have resulted in the reduction of other bonds such as the aromatic rings which was undesirable and further investigation of the effect of such reaction on the molecular structure of SPEEK is required to elucidate these effects.
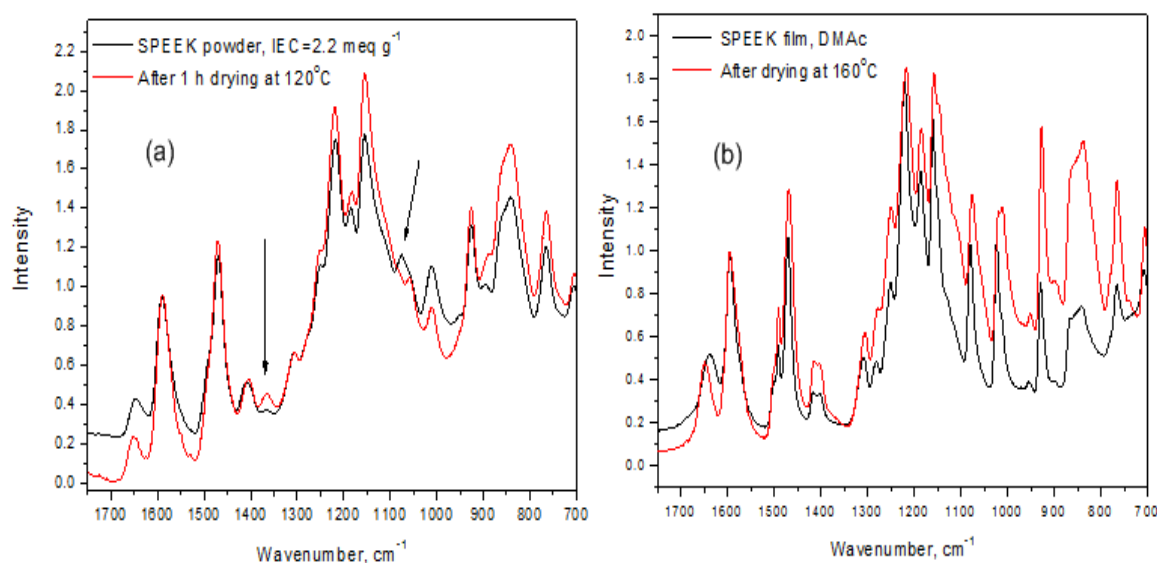
Figure 7.5: FT-IR spectra of SPEEK powder treated at 120 $^{\circ}$C in air (a) and SPEEK membrane from DMAc after thermal treatment at 160 $^{\circ}$C (b).

7.4.4 Characterization of the Cross Linked Membranes

7.4.4.1 Water Uptake Analysis

Figure 7.6 (a) shows typical kinetics of water uptake by cross linked sulphonated PEEK with different IEC at 22 $^{\circ}$C. The water uptake was expressed as λ, the number of water molecules per sulphonic acid group present per monomer unit and was normalized with respect to the thickness of the membranes in order to compare the data [222]. It was observed that λ increased rapidly with time and reached a stable value which was observed to increase on increasing the IEC of the membranes. Figure 7.6 (b) shows the water uptake results obtained at 50 $^{\circ}$C for membranes having similar IEC values of 1.84±0.04 meq g^{-1} but the cross linking density varied in the range 0.13 to 0.23. Cross link density acted in the opposite sense, and a significant decrease in the equilibrium water uptake was observed with increasing the cross link density at a constant IEC.
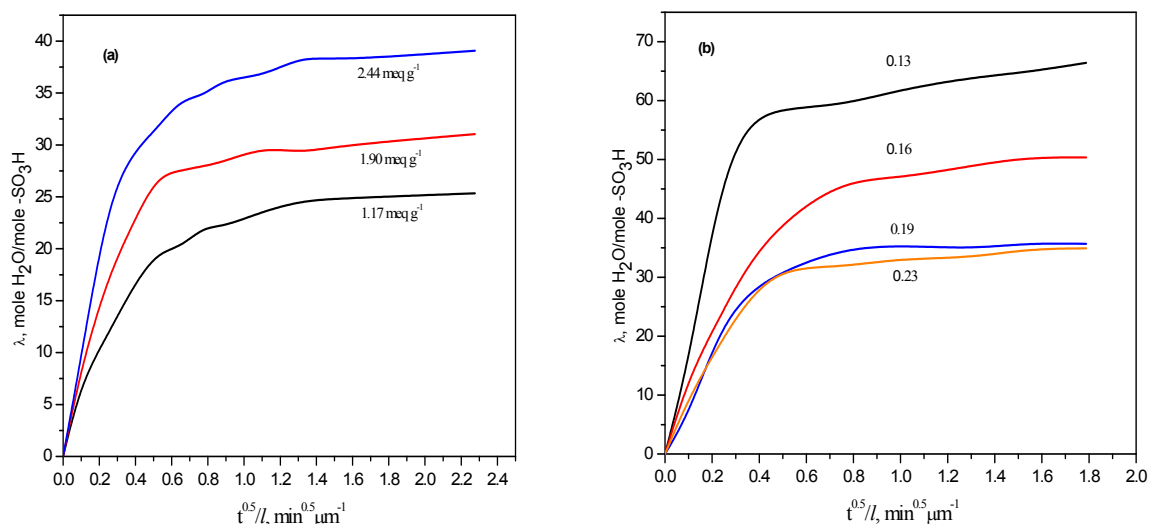
Figure 7.6: Water uptake kinetics of cross linked SPEEK membranes, (a) at 22 ^{o}C for a cross link density of 0.13 and different IEC values and (b) at 50 ^{o}C for IEC of 1.84±0.04 and different cross link densities.

Figures 7.7 (a) and (b) show the water uptake results at three different temperatures for membranes having similar IEC but different cross link densities. As can be seen, a significant improvement of the water uptake occurred on increasing the cross link density. It was interesting that all cross linked membranes did not dissolve even at higher water uptake. In comparison the un-cross linked PEMs broken up or dissolved with increasing temperature. The effect of cross linking was more apparent at higher temperature and with increasing cross link density from 0.13 to 0.23, the hydration number decreased from 150 to 50.

In conclusion, water sorption increased with increasing IEC and decreasing cross link density, but the later had less effect on the swelling by water. In comparison, the water uptake of SPEEK membranes equilibrated at room temperature over night have been reported to range from $\lambda = 5$ to 20 with increasing the IEC with a loss of their mechanical integrity. It reaches indeterminably large values with increasing temperature and equilibration time [223].
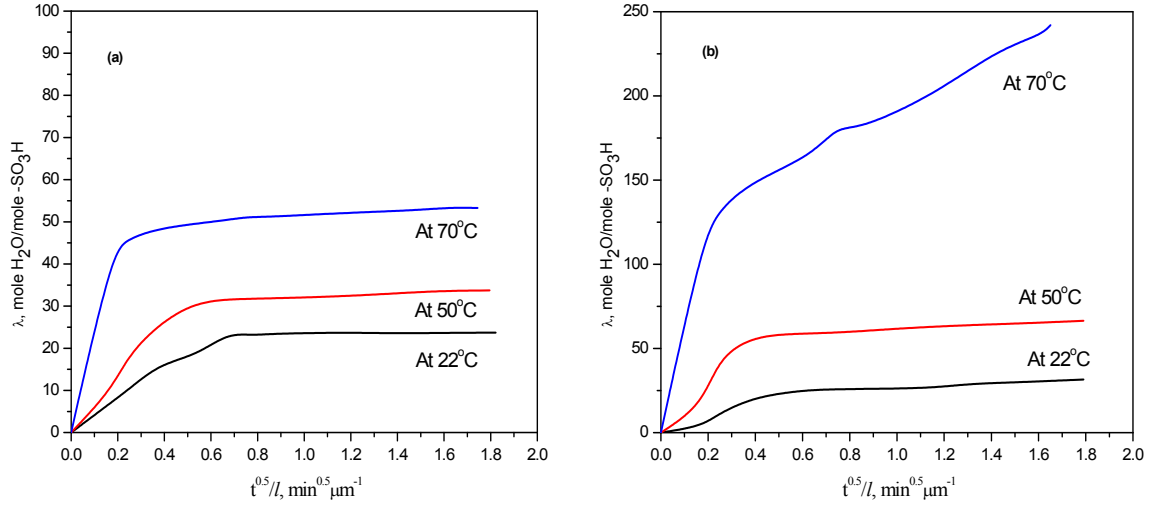
Figure 7.7: Water uptake kinetics by cross linked SPEEK membrane at different temperatures. Cross link densities were 0.23 and 0.13 for (a) and (b) respectively, the IEC values were similar at 1.84±0.04 meq g^{-1}.

7.4.4.1.1 Water Diffusion Coefficient

Chemical diffusion coefficients, *D*, of water in the cross linked polymer membranes were measured from the water sorption kinetics using an approximate solution of Fick's second law in which the chemical diffusion coefficient, D, is expressed by the following equation [202],

$$\frac{M_t}{M_\infty} = 1 - \frac{8}{\pi^2} \sum_{n=0}^{n=\infty} \frac{1}{(2n+1)^2} \times \exp\left[\frac{-\pi^2 D(2n+1)^2 t}{4l^2}\right] \tag{7.6}$$

where *l* is the thickness of the polymer film. For the earlier stages of water uptake eq. (7.6) simplifies to [213, 222],

$$\frac{M_t}{M_\infty} = 4\sqrt{\frac{D.t}{\pi.l^2}} \qquad \text{for} \qquad \frac{M_t}{M_\infty} < 0.5 \ or \ \frac{\sqrt{D.t}}{l} < 0.2 \tag{7.7}$$

The water diffusion coefficients were calculated from the initial slope, s, of the plots of M_t/M_∞ versus $\sqrt{t}$, using the relation,

$$D = \frac{\pi}{16}(sl)^2 \qquad (7.8)$$

The results of the previous analysis are reported in Figures 7.8 (a) and 7.9 (a) as a function of the ion exchange capacity and cross link density. As can be seen, the diffusion coefficient increased with increasing IEC values due to the increasing hydrophilicity of the membranes which in turn facilitates the water transport throughout the PEM.

In addition, cross link density had little effect on the diffusion of water due to the fact that water transports through the hydrophilic region of the membranes and this is controlled by the IEC.

Moreover, the diffusion coefficients increased with increasing temperature indicating a thermally activated process. The activation energy, ΔE, was calculated from an Arrhenius relationship between the diffusion coefficient, D, and temperature, T, such that,

$$D = D_o \exp\left(\frac{-\Delta E}{RT}\right) \qquad (7.9)$$

where ΔE is the activation energy of diffusion, R the ideal gas constant and D_o is the pre-exponential factor which is proportional to the number of molecules diffusing.

The results are plotted in Figures 7.8(b) and 7.9(b) as a function of IEC and X_c and were consistent with the values of the diffusion coefficients such that higher activation energies were observed for membranes with lower diffusion coefficient.
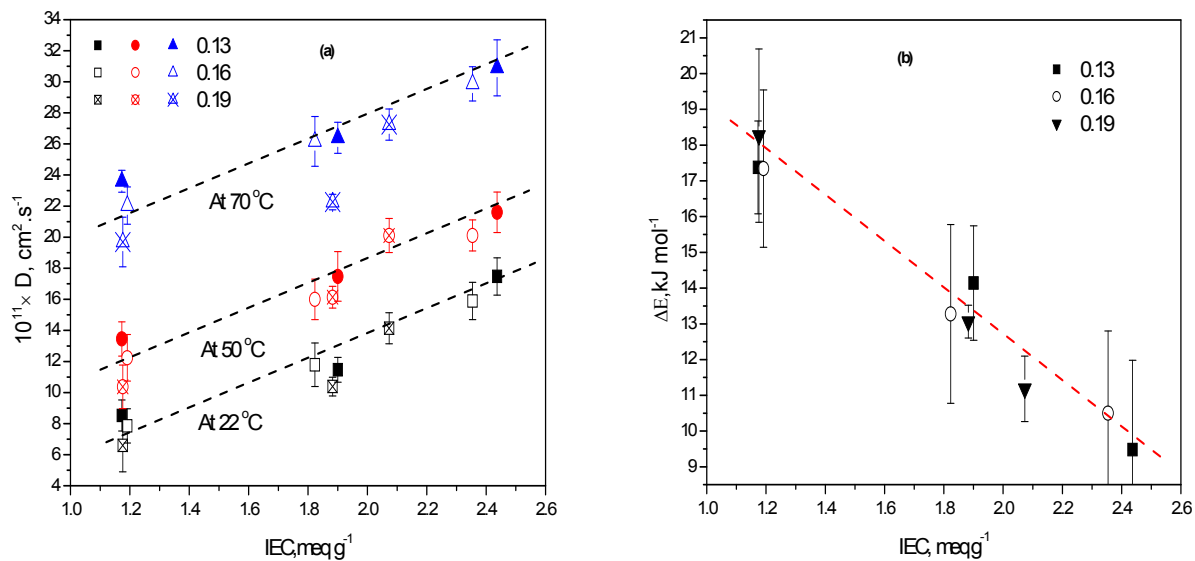
Figure 7.8: A plot of (a) the chemical diffusion coefficient at different temperatures and (b) the corresponding activation energy as a function of the ion exchange capacity for membranes having different cross link density as indicated.
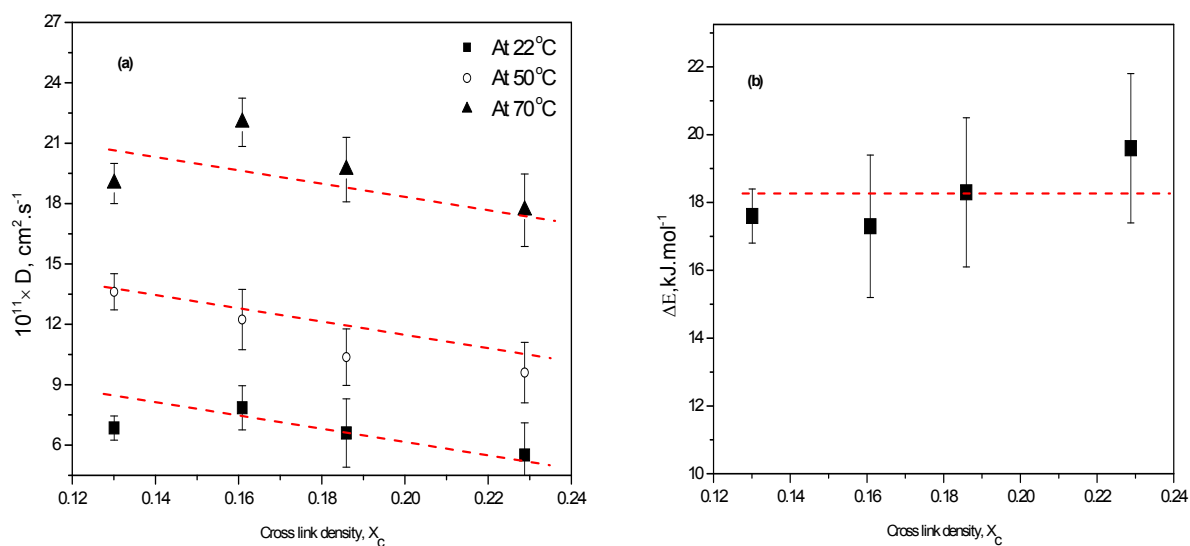
Figure 7.9 : A plot of (a) the chemical diffusion coefficient and (b) the corresponding activation energy as a function of the cross link density for membranes having similar IEC value of 1.2 meq g^{-1}.

It was concluded that cross linking did not alter the transport of water in the membranes but it did decrease the total water uptake. This was understood by the fact that cross links were formed before the sulphonation process and the formation of hydrophilic region in the membranes taking place. The cross linking process may have resulted in different distributions of different sizes of the channels through the membranes along which the water transports.

7.4.4.1.2 Detailed Effect of Cross Linking and IEC on Water Uptake

More detailed analysis of the water content in the cross linked PEM were carried out by considering the effect of water volume fraction, X_v, which is defined by the following equation [224, 225]:

$$X_v = \frac{V_{water}}{V_{wet\ membrane}}$$
(7.10)

It is related to the number of water molecules absorbed per $-SO_3H$ group, λ, by the equation:

$$X_v = \frac{\lambda}{\left(\overline{V}_M / \overline{V}_W\right) + \lambda}$$
(7.11)

where $\overline{V}_M \approx \dfrac{EW}{\rho_o}$ in which $EW = n.M_w$ is the equivalent weight in g mole^{-1} (taken as 368 for all cross linked samples assuming that only the repeat units with no cross link in it is sulphonated). ρ_o is the density of dry PEM in g cm^{-3} and $\overline{V}_W = 18.0\,cm^3.mole^{-1}$

It is also of interest to estimate the acid concentration, $[SO_3H]$, in the PEM at different water content. $[SO_3H]$ was determined from the following equation [218, 224, 225]:

$$[SO_3H] = \frac{moles\ of\ SO_3H}{V_{wet\ membrane}} = \frac{IEC \times W_1 \times d}{W_2 - W_1}.X_v$$
(7.12)

All data were measured after sufficient times to allow the PEMs to reach an equilibrium amount of water. Test times were varied from 400 to 900 hrs depending on the temperature of measurements. Figure 7.10 (a) shows the dependence of λ on X_v from which it was observed that λ values did not change significantly (20-40) over a narrow range of X_v from 0.5 to 0.7 at the three temperatures studied. It was also evident that higher values of both λ and X_v were achieved at higher temperatures.
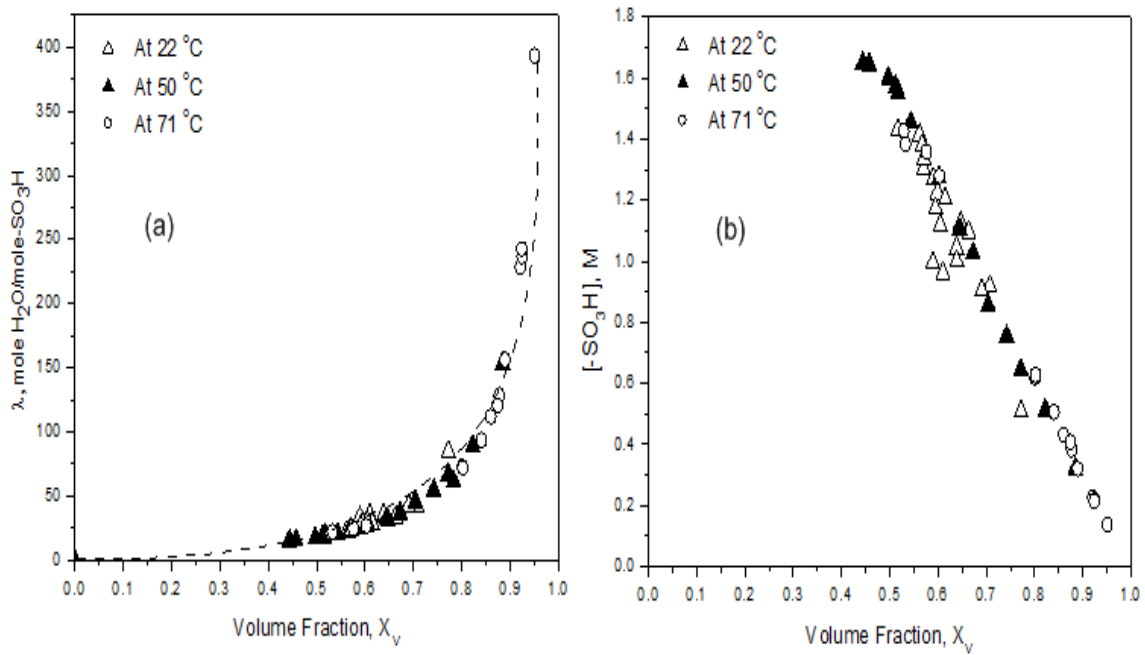
Figure 7.10: The hydration number, λ, as a function of X_v (a) and the estimated acid concentration Vs. X_v (b) for different cross linked sulphonated PEEK samples.

The dependence of acid concentration, $[SO_3H]$, on the volume fraction, X_v, is shown in Figure 7.10 (b). $[SO_3H]$ achieved a maximum at X_v=0.45 and then decreased progressively with increasing X_v. Similar conclusions were made by examining the relationship between $[SO_3H]$ vs. λ, see Figure 7.11. The high water content of the cross linked membranes may be due to their more porous structure. It was interesting that the cross linked membranes were able to

hold high water contents without completely losing mechanical integrity, and the sample returned to its original dimensions upon drying. This was attributed to the presence of cross links distributed through out the membranes.
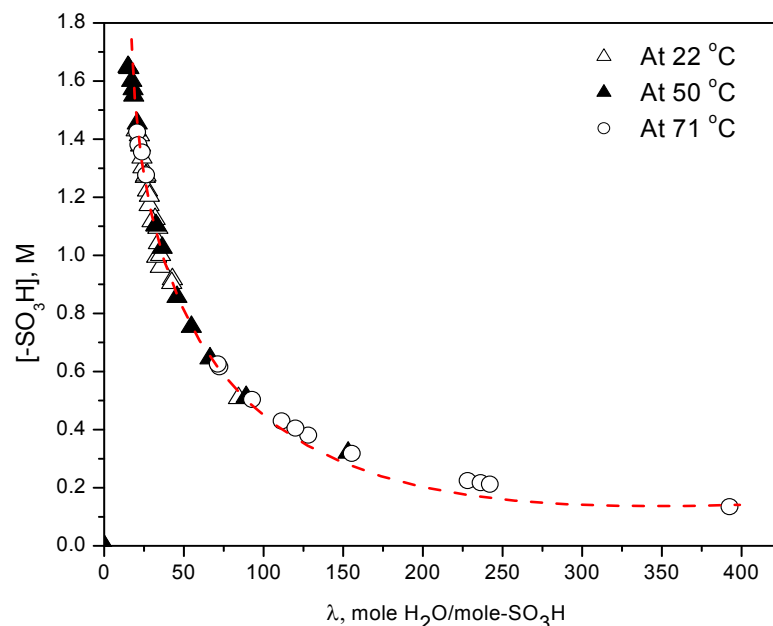
Figure 7.11: The estimated acid concentration vs. hydration number.

To a first approximation, $[SO_3H]$ would be expected to increase with higher IECs, since this implies that there are a greater number of sulphonic acid groups present. However, as can be seen in Figure 7.12 (a), $[SO_3H]$ actually decreases due to a disproportionate increase in water content with increasing IEC. The decrease was more apparent in a plot of $[SO_3H]$ against the normalized IEC, e.g., the ratio IEC/X_c, see Figure 7.12 (b). Although higher water contents enable greater dissociation of protons, and hence higher proton mobility, a significant increase in water content results in a dilution of the available sulphonic acid groups and thus a decrease in the observed values of $[SO_3H]$. In other words, the water content must achieve a level at which proton dissociation is high enough for good mobility, yet there must not be too much water because this leads to dilution of the available acid sites [225].
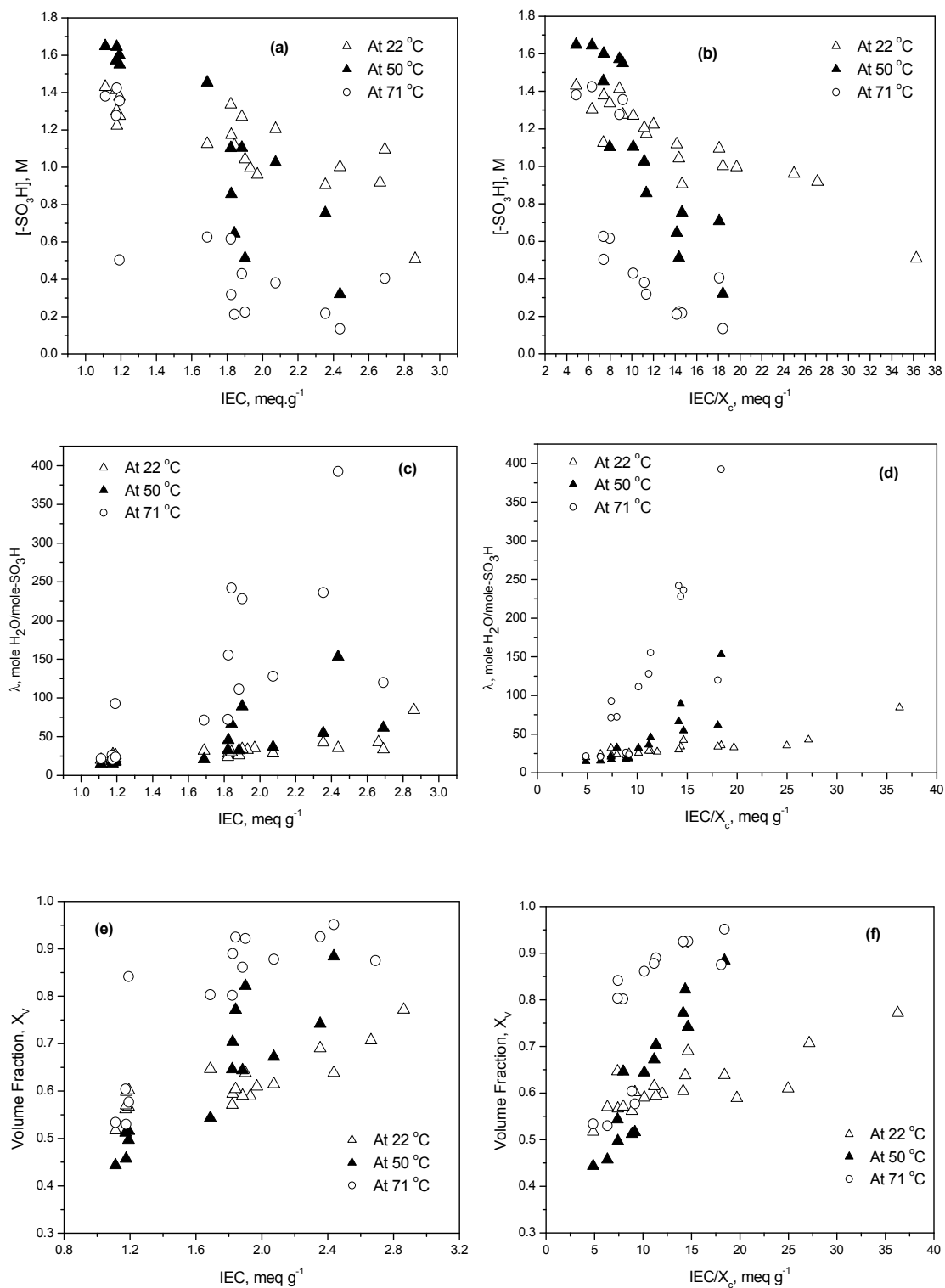
Figure 7.12: Detailed water uptake analysis; the dependence of $[SO_3H]$ (a) and (b), λ (c) and (d) and X_v (e) and (f) on the IEC and the normalised IEC/X_c.

Due to the hydrophilic nature of the $-SO_3H$ group, IEC can have a strong influence on the equilibrium water content; on both λ and X_V. The examination of such influence is presented in Figure 7.12 (c) and (e) and as can be seen there was a trend in which both λ and X_V increased with increasing IEC. It was also observed that at low cross link density the data was widely scattered and did not show any simple dependence of λ, X_V or $[SO_3H]$ on the normalised IEC/Xc. This may be due to the fact that crystallisation at low cross link density was sufficient to act as physical cross linking (crystalline regions do not absorb water) which caused the deviation presented in Figures 7.12 (b), (d) and (f).

7.4.4.1.3 State of Water in Cross Linked Membranes

DSC has been used for the quantitative determination of the amounts of freezing and non-freezing water present in membranes [203, 216-218]. Figures 7.13 (a) and (b) show the DSC profiles for hydrated to equilibrium cross linked SPEEK samples, while Table 7.1 summarizes the properties of these membranes.
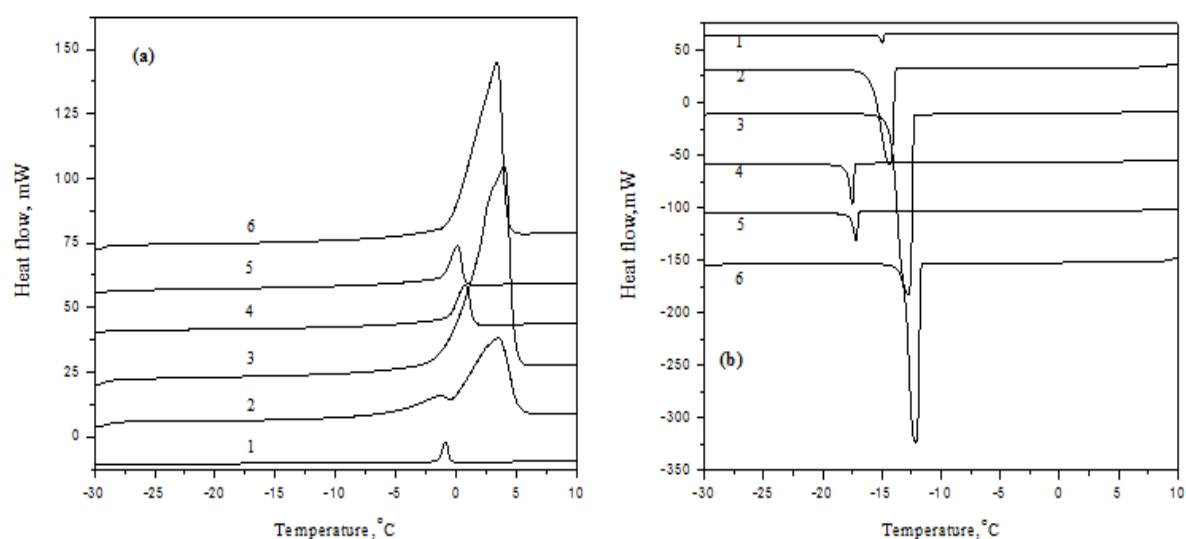
Figure 7.13: The heating (a) and cooling (b) DSC responses for hydrated membranes as listed in Table 7.1.

It is evident from Figure 7.13 and Table 7.1 that both cross link density and IEC have an effect on the state that water exists in the membranes. The water uptake decreased with increasing cross link density and increased with increasing IEC. Although the values were very high, the membranes did not break or dissolve unlike the un-cross linked SPEEK which gels and looses its shape or completely dissolved at such values of water uptake. These high values of water uptake were explained by the fact that the sulphonation reaction occurs at sulphonation tracks, through which the sulphuric acid can penetrate into the cross linked PEEK films. Therefore, a more distinct phase separation structure is possible to occur in the membranes, leading to the easy formation of water clusters in the membranes [58].

Table 7.1: Water absorption characteristics.

Curve ID	IEC±0.04 (meq g^{-1})	Cross link density, X_c (±0.005)	(%) Water uptake[a] (±5)	(%) Freezable water	λ (±2)
1	1.18	0.113	40	8	18
2	1.72	0.133	300	240	100
3	1.86	0.133	670	540	200
4	1.73	0.186	110	50	35
5	1.63	0.229	100	45	36
6	1.60	0.114	350	330	122
Nafion-112	0.90	-	35	30	21
Nafion-1135[b]	0.90	-	35	30	20
Nafion-117[c]	0.97	-	35	30	20

[a] water uptake at 50 $^{\circ}$C before DSC measurements [b] see Ref. [203] [c] see Ref. [218].

Figure 7.14 shows the dependence of both freezable and total water content expressed as λ on the IEC and cross link density. As can be seen, increasing the cross link density resulted in a decrease in free water, which was zero below $IEC/X_c = 9$, while increasing the IEC gave rise to more free water. This was consistent with reducing methanol permeability and electro-osmotic drag as well as improving mechanical stability as discussed in the introduction [203].
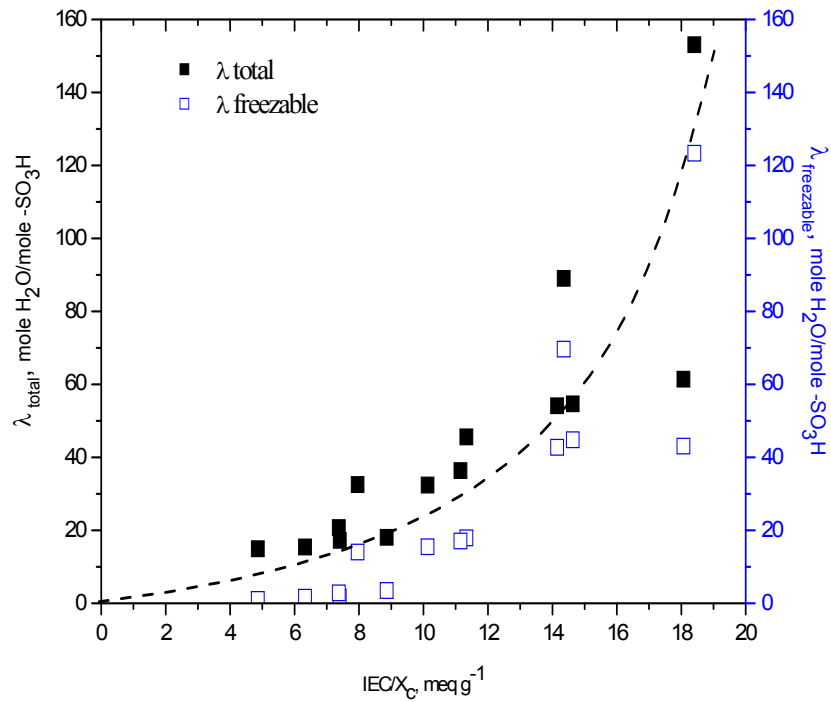
Figure 7.14: Freezable and equilibrium water uptake dependence on the IEC and cross link density.

7.4.4.1.4 Thermoporometry of Cross Linked Membranes

Thermoporometry is a widely used calorimetric method that measures pore size based on the melting or solidification point depression of a liquid, usually water, confined in a pore. The determination of the pore size distribution from the DSC thermogram depends on a number of

reasonable assumptions. These include that water present in the capillaries are considered to be freezable or non-freezable; the later water is formed from monolayers that lies along the inner pore surface. The analysis is also based on the assumption that the pores are fully saturated with liquid water [226-230].

According to Brun et al [226] the pore radius, R_p and differential pore volume, dV/dR_P can be calculated from the DSC thermogram by observing the melting point depression, ΔT, and changes in heat flow, q (W g^{-1}), such that,

$$R_P = A - \frac{B}{\Delta T} \tag{7.13}$$

$$\frac{dV}{dR_P} = k \frac{(\Delta T)^2 q}{\Delta H_a (T)} \tag{7.14}$$

for $0 > \Delta T > -40^o C$

where k is a 'calibration constant' given by $k = 1/(dT/dt)\rho B$ with dT/dt the heating or cooling rate, and ρ the density (taken to be as 1.000 g cm^{-3}) [227]. The apparent heat of fusion, $\Delta H_a(T)$, is temperature dependent and can be described by the formula [228-230]

$$\Delta H_a(T) = C\Delta T + D(\Delta T)^2 + \Delta H_f \tag{7.15}$$

where ΔH_f is the heat of fusion of the penetrant water under normal conditions (332 J g^{-1} for water). The numerical values of the constants A to D depend on the measurement conditions (heating or cooling), pore geometry and penetrant. In this study water was used as the penetrating liquid and a cylindrical pore shape was assumed for which Brun et al.[226] have reported the values shown in Table 7.2.

Table 7.2: Numerical values for constants in Eqs. (7.13) and (7.15)(after Brun et al[226]).

Constant	A (nm)	B (nm K)	C(J g^{-1}K^{-1})	D(J g^{-1}K^{-1})
Heating in cylindrical pores	0.68	32.33	11.39	0.0550
Cooling in cylindrical pores	0.57	64.67	7.43	0.0556

Figure 7.15 (a) shows the DSC profiles of some water equilibrated cross linked membranes heated at 5.0 K min^{-1}. The curve A represents a membrane with a small pore sizes, and water inside the pores and free water outside the membrane give separate peaks from which the pore size distribution could be calculated. In curves B and C, the data was fitted to separate the two components of the melting peak as shown in Figure 7.15 (b). A membrane having a broad pore size distribution exhibits thermogram D and water inside the pores could not be separated from that of free water.
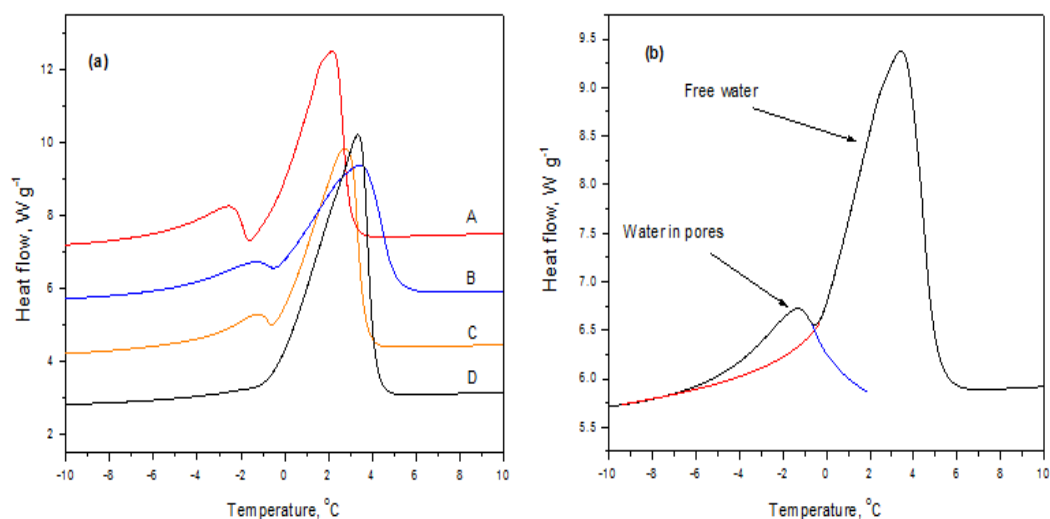
Figure 7.15: (a) Different melting DSC thermogram used to calculate pore size and (b) Fitting procedure showing two melting peaks corresponding to water in the pores and bulk water.

Only the melting process was used in the pore size analysis in this study; the pores corresponding to the maximum of the distribution curves $dV/dR_P = f(R_P)$ were considered as the average pore size present in the sample. Thermoporometry has been applied successfully for characterising the porosity in carbon/polymers composite electrodes [231], composite PEMs [232, 233] and it was applied to study the porosity in cross linked sulphonated PEEK membrane.

Figure 7.16 shows the pore size distribution determined for some of the cross linked membranes examined in this study. As can be seen the average pore sizes were very similar at 7±1 nm over a wide range of IEC values and cross link densities. However, the distribution broadened at the highest IEC values and the lowest cross link density, indicating that more than one distribution might be present in these membranes. This was confirmed in Figure 7.17, in which thermoporometry experiments showed evidence of the presence of two pore distributions as well as an important decrease in pore size with increasing cross link density. The full results of this analysis are shown in Table 7.3 along with the water content of the membranes before the DSC measurements were carried out.

It was concluded that both cross link density and the IEC had an effect on the pore size in the cross linked membranes, but the IEC had a more marked effect. This was consistent with the previous conclusion made by analysing the water uptake kinetics. Moreover, the presence of a nano-structure in the cross linked membranes was confirmed and the sizes of pore present were comparable to those reported in Nafion using NMR cryoporometry [234], e.g, 1-3 nm.
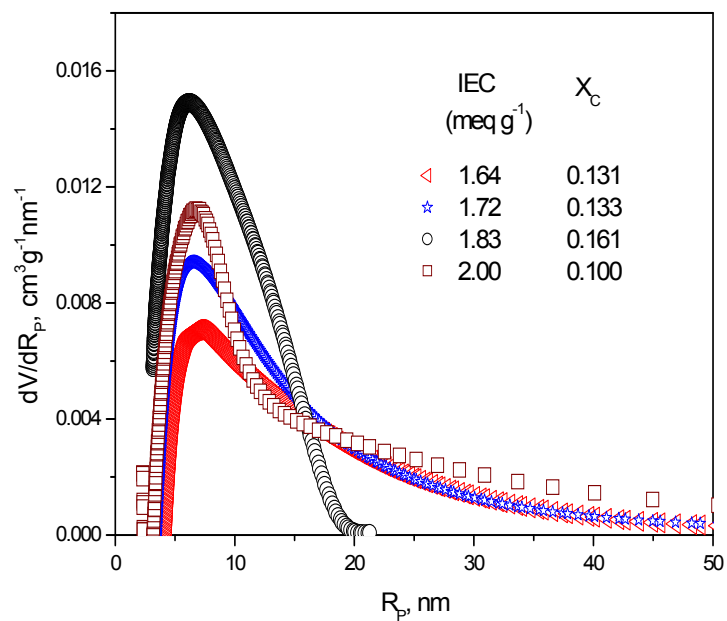
Figure 7.16: Pore size distribution curves for different cross linked sulphonated PEEK membranes, the effect of IEC and cross link density.
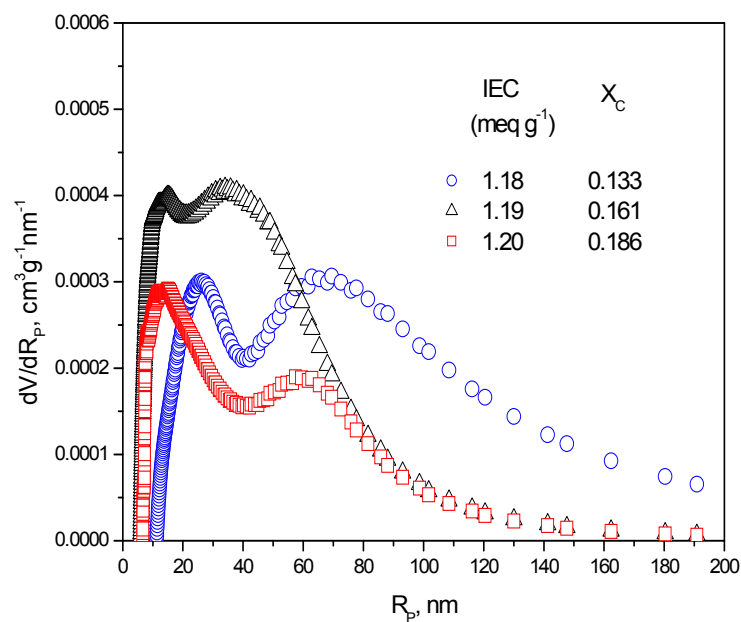
Figure 7.17: The effect of cross link density on pore size distribution for different cross linked sulphonated PEEK membranes.

Table 7.3: Properties of cross linked membranes and Thermoporometry analysis.

IEC±0.04 (meq g^{-1})	Xc	Pore size (nm)	EWC (%)	λ (moleH$_2$O/mole HSO$_3$H)
1.18	0.133	26-71	38	18
1.19	0.161	16-40	37	17
1.20	0.186	15-63	33	15
1.64	0.131	7	316	90
1.72	0.133	6.5	305	89
1.79	0.130	6-7	180	54
1.83	0.161	6	232	55
1.96	0.100	7	205	58
2.57	0.149	6-12	300	61

7.5 Conclusions

The materials properties of different cross linked SPEEK membranes have been investigated focusing on the extent and rate of water uptake and mechanical strength. The advantage of cross linking PEEK films by irradiation before sulphonation has been shown to be the one step preparation of the PEM and eliminating the drawbacks of using solvents to cast SPEEK

into film. On the other hand, this method has been shown to be very costly due to the high resistivity of PEEK to ion irradiation.

The chemical reduction of the carbonyl groups has been applied successfully as an alternative method of cross linking highly sulphonated PEEK but the structure of the resultant PEM has not been studied in detail. At the higher reduction agent ratios used a possible reduction of other chemical bond in the molecular structure of SPEEK was observed from analysis by FTIR spectroscopy, but by using lower ratios of the reduction agent it was possible to remove residual solvents and so allow the condensation reaction by which cross links were formed to proceed.

The main reason for cross linking the PEM was to reduce the extent of swelling in the presence of solvents and to attain high water content without loosing dimensional stability. The IEC values had a greater effect than the cross link density in controlling the water content and diffusion of water through the PEM, but cross linking enabled the PEMs to reach very high water content without loosing mechanical integrity.

It was concluded from DSC analysis that increasing cross link density resulted in more bound water present in the equilibrated membranes and increasing the IEC gave rise to more free water. The results indicated that the cross linked membranes have lower methanol permeability and electro-osmotic drag as well as improved mechanical stability.

Both cross link density and the IEC had an effect on the pore size in the cross linked membranes, but the IEC had a more marked effect. The presence of a nano-structure in the cross linked membranes was confirmed and the sizes of pore present were comparable to those reported for Nafion.

Chapter 8

Stability Testing of Cross Linked PEMs and Their

Performance in a Single PEM Fuel Cell

8.1 Stability of Polymer Electrolyte Membrane

A proper understanding of the mechanism of oxidative degradation in sulphonated PEEK is critical in order to improve the stability of the working proton exchange membrane in the fuel cell. It has been reported that early failures of the membranes (<1000 h) are usually due to oxidative decomposition and loss of structural integrity [235]. Many experimental procedures have been developed to assess the stability of PEMs, but thermal and oxidative stabilities have been used most frequently.

Good thermal stability is an important requirement for a PEM, especially when used at elevated operating temperatures. As a family, the poly(aryl ether) polymers have good thermal stability with decomposition temperatures in excess of 500 $^\circ$C, and with TG analysis exhibiting a single weight loss curve [57]. However, the introduction of sulphonic acid groups significantly reduces the thermal stability and multiple weight loss steps are generally observed [236].

In an active fuel cell, radical species such as $HO^\bullet$ and $HOO^\bullet$ are produced from reactant diffusion through the membrane from incomplete oxygen reduction. It is known that oxidative

attack by $HO^\bullet$ and $HOO^\bullet$ radicals occur mainly within the hydrophilic domains and results in the degradation of the polymer by chain scission. On the other hand, transition metal ions such as Fe^{2+}, Ti^{2+}, or Cu^{2+} released from the bipolar plates accelerate the membrane deterioration due to the formation of reactive oxygen radicals such as $HO^\bullet$ and $HOO^\bullet$, see Scheme 8.1 reactions (1) and (2). The $HO^\bullet$ radical can then attack an organic substrate or the membrane, RH, by H-abstraction, Scheme 8.1 reaction (3). The $R^\bullet$ radicals derived from the polymer combine with triplet oxygen to produce peroxy radicals and thus initiate a degradation cascade. Therefore, the useful lifetime of the fuel cell largely depends on the oxidative stability of the membrane [237].

$$(1)\quad Fe^{2+} + H_2O_2 \Rightarrow Fe^{3+} + HO^\bullet + HO^-$$

$$(2)\quad Fe^{3+} + H_2O_2 \Rightarrow Fe^{2+} + HOO^\bullet + H^+$$

$$(3)\quad HO^\bullet + RH \Rightarrow H_2O + R^\bullet$$
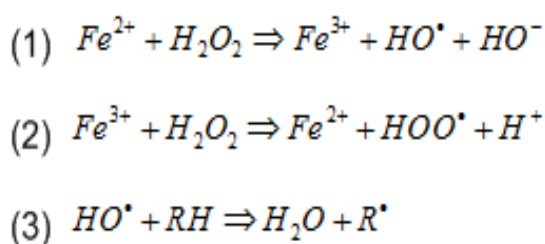
Scheme 8.1: Production of $HO^\bullet$ and $HOO^\bullet$ radicals in fuel cell and degradation of PEM[237].

The stability of the polymer electrolyte membrane in hydrogen peroxide (H_2O_2) solution has been used as an important indication of the lifetime of membranes [238-240]. The sulphuric groups in the Nafion structure can be cross linked under the influence of hydrogen peroxide and the breakdown of hydrogen bonding in the polymer decreases the proton conductivity of the membrane. It was also observed that the decomposition behaviour of the PEM by Fenton's reagent (solution containing H_2O_2 and transition metal ions) was similar to that of the PEMs in fuel cells. Thus, both chemical stability and structural stability of the membrane are critical for the long-term performance stability of the PEM fuel cells.

8.2 Hydrogen Fuel Cell Testing

The performance of fuel cell is characterised by several experimental protocols, but most importantly by its voltage-current density relationship, power density and efficiency. In order to understand the significance of each type of performance, the thermodynamics of the fuel cell reaction are discussed in the following paragraphs.

8.2.1 Open Circuit Voltage

One advantage of hydrogen is that it readily reacts electrochemically with oxygen under mild conditions, see Scheme 8.2. At the anode, hydrogen is oxidized liberating two electrons and two protons. The protons are conducted from the anode surface through the proton exchange membrane and the electrons travel through the external electronic circuit. At the cathode, oxygen is reduced, and the overall cell reaction is shown in Scheme 8.2.

$$H_2 \rightarrow 2H^+ + 2e^- \quad \text{At the anode}$$

$$\frac{1}{2}O_2 + 2H^+ + 2e^- \rightarrow H_2O \quad \text{At the cathode}$$

$$H_2 + \frac{1}{2}O_2 \rightarrow H_2O \quad \text{The overall cell reaction}$$
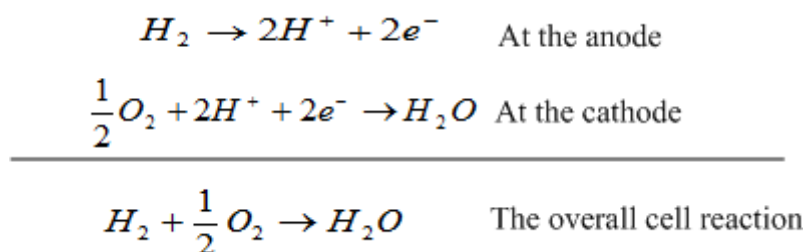
Scheme 8.2: Electrochemical reactions of a hydrogen fuel cell [2].

The standard electrochemical potential, E^o, for the H_2/O_2 cell reaction is defined by the change in Gibbs free energy, ΔG^o, of the cell reaction at unit activity of reactants and products by the relation,

$$E^o = -\frac{\Delta G^o}{n.F} = -\frac{\Delta H^o - T\Delta S^o}{nF} \tag{8.1}$$

where n is 2, the number of electrons involved in the cell reaction and F is Faraday constant (96485 coulombs equivalent^{-1}).

The change in Gibbs free energy is dependent on temperature and on the state of reactants and product. For the overall reaction in Scheme 8.2 at 25 ^{o}C, ΔG^o is -237.3 and -228.1 kJ mole^{-1} for liquid and vapour water respectively. Substitution in eq. (8.1) gives E^o values of 1.23 V when liquid water is produced and 1.18 V when water vapour is produced. The dependence of ΔG^o upon temperature is described by the equation,

$$\Delta G^o = -204.203 + 3.933.T.\ln(T) + 0.0069.T^2 - 1.54808 \times 10^{-6}.T^3 + 16.40.T \qquad (8.2)$$

with ΔG^o in J mol^{-1} and T in K and assuming that water vapour is produced. Equations (8.1) and (8.2) were used to calculate the theoretical cell voltage under unit activity conditions. However, in practice (using air and water vapour pressure) the activities of the reactant and products are less than unity.

The Nernst equation, used to calculate the reversible cell voltage, E, under non-standard conditions is,

$$E = E^o + \left(\frac{R.T}{n.F}\right)\ln\left(\frac{(P_{H_2})(P_{O_2})^{1/2}}{P_{H_2O}}\right) \qquad (8.3)$$

where R is the gas constant (8.314 J mol^{-1} K^{-1}), P is the partial pressure of H_2 and O_2. It is clear from eq. (8.3) that increasing the pressure, increases the concentration of reactants and will increases E. It also increases with temperature [1, 2, 4].

8.2.2 Voltage - Current Density Relationship, Polarization Curves

The current density is defined as the current of the electrochemical system divided by the active electrode area of the device. When a load is applied to the cell, non-equilibrium conditions are produced due to a net current flow across the cell. The cell voltage then becomes smaller as the net reaction rate increases and because of irreversible losses. These losses for a given fuel cell arises from its geometry, catalyst/electrode characteristics and membrane properties and operating conditions such as concentration, flow rate, pressure,

temperature and relative humidity. The losses are defined as kinetic or activation, ohmic and mass transfer resistances, see Figure 8.1 [1, 2].

8.2.2.1 Ohmic Resistance

Voltage loss due to resistance to ionic current in the electrolyte and electronic current in the electrodes is known as the ohmic polarization, η_{ohm}, and is related to the current by the equation,

$$\eta_{ohm} = i.R_{ohm} \tag{8.4}$$

where R_{ohm} is the ohmic resistance of the cell ($\Omega.cm^2$).

Electronic resistance arise from the cell electrodes, gas diffusion layers, current collectors and leads as well as contact resistances at junctions between these components. These types of resistances are usually much smaller than those associated with the resistance to ion, e.g., H^+, transport through the electrolyte, PEM, and across the catalyst layer. In practice, many techniques have been used to determine the ohmic resistance of the fuel cell, such as, the current interrupt method and impedance spectroscopy [1, 2, 4, 81].

8.2.2.2 Transport Limitations

This is also known as concentration polarization, η_{conc}, and occurs as a result of consumption of reactant at the surface of the electrode that causes a concentration gradient to develop between the bulk and the electrode surface. It is given by,

$$\eta_{conc} = 2.303 \frac{R.T}{n.F} \log\left(\frac{i_{lim}}{i_{lim} - i}\right) \tag{8.5}$$

where i_{lim} is the limiting current density (A cm^{-2}) and is defined as the reaction rate at which the surface concentration of reactant is zero. Concentration polarization is affected by the

concentration and the flow rate of the reactants fed to their respective electrodes, the cell temperature and the structure of the gas diffusion and catalyst layers.

The mass-transfer-limiting region of the current-voltage polarization curve is apparent at very high current density. In this region, increasing current density results in a depletion of reactant immediately adjacent to the electrode. When the current is increased to a point where the concentration at the surface falls to zero, a further increase in current is impossible. The current density corresponding to zero surface concentration is called the limiting current density, i_{lim} [1, 2].
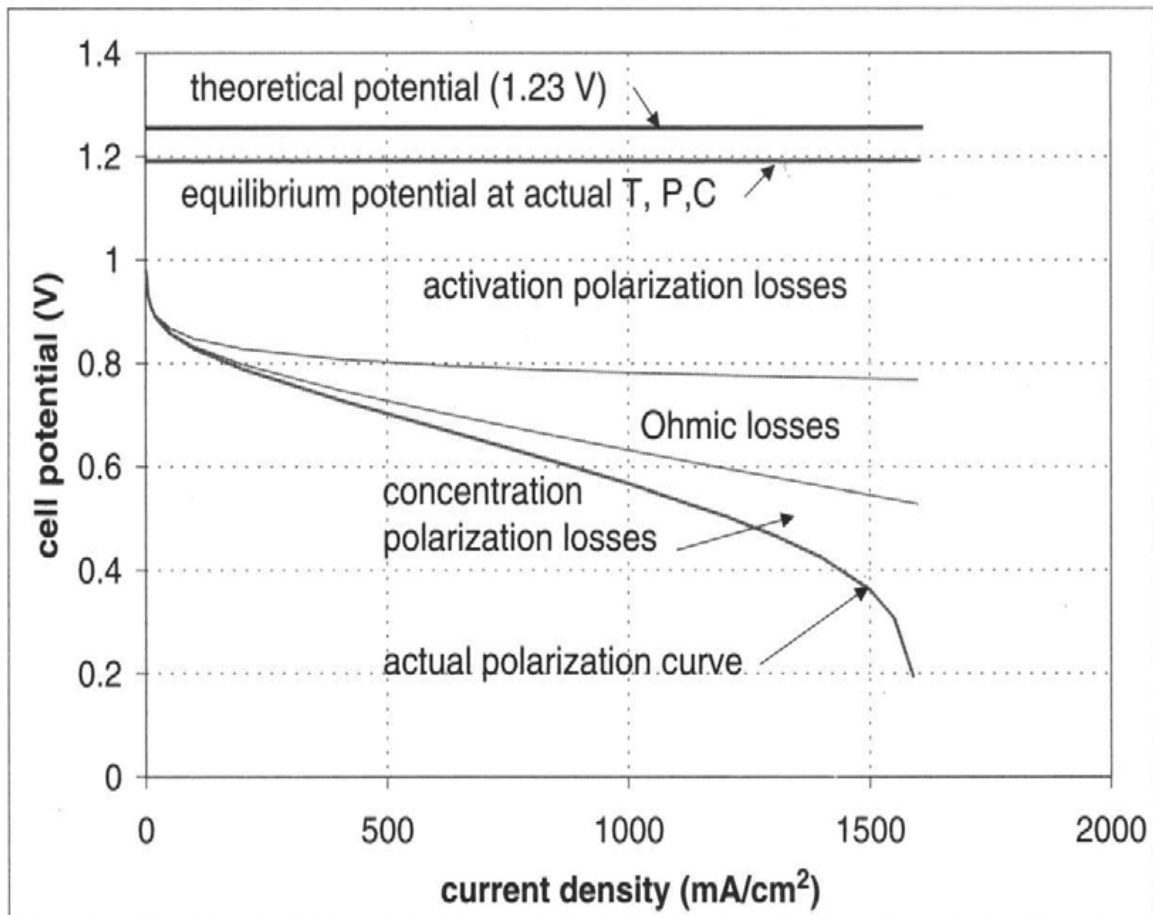
Figure 8.1: Voltage-current characteristic of a PEMFC [2].

8.2.2.3 Kinetic Resistance

This is also known as activation polarization, η_{act}, and is associated with overcoming the energy barrier of the electrode reaction. Temperature and other factor such as pressure, concentration and electrode properties all alter the activation polarization. Assuming that no other over voltage is present, which is the case if the current is small and therefore deviation from the equilibrium state is also small, then the following equation for the current-voltage relation, can be written,

$$i = i_o . \left(\exp\left(\frac{\alpha_a \eta F}{RT}\right) - \exp\left(\frac{-\alpha_c \eta F}{RT}\right) \right) \tag{8.6}$$

where i_o is the exchange current density and α is the anodic and cathodic transfer coefficient.

The exchange current density represents the rate at which the forward and backward reaction is equal. The transfer coefficient is an experimental parameter determined from the current-voltage relationship. It is equal to the inverse of the Tafel slope, b, expressed in units of $2.303 \, RT/F$. At low temperature, kinetic resistances dominate the low current density portion of the polarization curve of fuel cells, where deviations from equilibrium are relatively small. Under these conditions, reactants are plentiful (no mass transfer limitation) and the current density is so small that ohmic losses are negligible. The Tafel equation [2] then describes the current density-voltage polarization curve in this region,

$$\eta_{act} = b . \log|i| - a \tag{8.7}$$

where η_{act} is voltage loss due to activation polarization (V), a is kinetic parameter proportional to the $\log(i_o)$ (V) and b is the Tafel slope, (V dec^{-1}). Cathode dominated activation polarization is observed for PEM fuel cells because the oxygen reduction reaction on platinum is sluggish in comparison to the relatively facile hydrogen oxidation reaction.

The exchange current density for oxygen is 10^3 times less than for the hydrogen oxidation on platinum. The Tafel equation can be written in terms of the cathodic transfer coefficient α_c as,

$$i = i_o . \exp\left(\frac{-\alpha_c . n . \eta_{act,c} . F}{R.T}\right) \tag{8.8}$$

Rearranging gives,

$$\eta_{act,c} = -2.303 \frac{R.T}{\alpha_c . n . F} \log\left(\frac{i}{i_o}\right) \tag{8.9}$$

or,

$$\eta_{act,c} = b . \log\left(\frac{i}{i_o}\right) \tag{8.10}$$

where b is the Tafel slope in volt decade^{-1} of current density for the cathodic reaction. The Tafel slope is primarily a function of the reaction mechanism, electrode material, structure and surface condition, temperature and reaction environment (electrolyte), and can take a range of values. For oxygen reduction on Pt, for example, Tafel slope ranges from 0.04 to 0.12 V dec^{-1} [1, 2, 241].

8.2.2.4 Fuel Crossover and Internal Currents

Even when no current is drawn from a fuel cell, there is an irreversible voltage loss due to parasitic reactions. These produce energy losses due to crossover of fuel and electronic conduction, e.g., electronic short through the electrolyte, and oxidation of catalyst and electrode materials. The losses due to fuel crossover and electronic short are generally small. The combined effects of fuel crossover, internal short and parasitic oxidation, e.g., corrosion reactions occurring at the cathode are the source of the difference between the measured open circuit cell voltage and the theoretical cell potential [1, 2, 4].

The measurement of hydrogen crossover, in particular at open circuit voltage (OCV), at which the most severe crossover occurs, is of prime importance for the fundamental understanding

of fuel cell degradation and membrane failure. In a fuel cell, hydrogen crossover usually takes place from the anode side to the cathode side through the membrane. Hydrogen crossover can result in fuel efficiency reduction, cathode potential depression, and progressive peroxide radical formation. The hydrogen which crosses over can directly react with oxygen at the cathode surface, resulting in a lowering of the cathode potential. This direct reaction between H_2 and O_2 at the cathode can also produce peroxide radicals, which not only attack the catalyst layer but also the membrane, causing significant catalyst-layer and membrane degradation [242, 243].

The electrolyte membrane deteriorates during operation of the cell, in particular under low humidification [243]. It has also been reported that the degradation is more significant under open-circuit conditions, e.g., without net current [244]. That is because the rate of gas crossover is the highest under open-circuit conditions as no gases are consumed at the electrodes through the electrochemical fuel cell reactions.

8.2.3 Cell Voltage

The observed cell voltage at any given current density can be represented as the reversible voltage minus the activation, ohmic and concentration losses, such that,

$$V_{cell} = E - \left(\left| \eta_{act,c} \right| + \eta_{act,a} \right) - \eta_{ohm} - \left(\eta_{conc,c} + \eta_{conc,a} \right) \tag{8.11}$$

For H_2/O_2 cell with pure hydrogen as the fuel, the anode losses are generally much smaller than cathode losses and are frequently neglected. The dominant source of ohmic losses is due to the electrolyte membrane, and to ion transport. Further losses also occur at the electrode interface due to resistance to proton transport across these layers. Ohmic losses, due to contact resistance and electronic resistance within the electrodes and leads, are negligible in a well-

designed setup. Applying these assumptions and substituting the respective polarization relationships leads to a simplified equation that describes the complete cell voltage-current density relationship for the H_2/O_2 PEM fuel cell [1, 2, 4], such that

$$V_{cell} \cong E - |b.\log(i) - a| - i.R_{membrane} - 2.303 \frac{R.T}{n.F} \ln\left(\frac{i_{\lim}}{i_{\lim} - i}\right) \qquad (8.12)$$

8.2.4 Cell Efficiency

Fuel cell efficiency can be defined in several ways. Energy efficiency η_{energy} represents the amount of the input energy E_{input} which leaves the system, in the case of fuel cell, in the form of actually useful energy E_{useful}.

$$\eta_{energy} = \frac{E_{useful}}{E_{input}} = \frac{E_{electric}}{E_{hydrogen}} = \frac{\overline{V}.\overline{I}.t}{V_{H_2}.H_l} \qquad (8.13)$$

where V, I and t are the voltage (V), current (A) and time (s), V_{H2} is the consumed volume of hydrogen (m^3) and H_l is the heat produced. For hydrogen, this is 10.8×10^6 J m^{-3}.

To take account of the energy lost as heat $Q = T.\Delta S$, an ideal efficiency η_{id} is defined as the ratio of the free energy ΔG and the reaction enthalpy ΔH, such that,

$$\eta_{id} = \frac{\Delta G}{\Delta H} = \frac{\Delta H - T.\Delta S}{\Delta H} = 1 - \frac{T.\Delta S}{\Delta H} = 1 - \frac{298 \times (-162.985)}{-285840} \qquad (8.14)$$
$$\eta_{id} = 83\%$$

ΔS is the reaction entropy.

The faraday efficiency of the fuel cell is obtained from the equation:

$$\eta_{Faraday} = \frac{v_{H_2}(calculated)}{v_{H_2}(consumed)} \qquad (8.15)$$

Faraday First Law of Electrolysis relates the magnitude of the current flowing to the consumed volume of gas and so:

$$v_{H_2}(calculated) = \frac{R.\bar{I}.T.t}{F.P.Z} \qquad (8.16)$$

where: R is the universal gas constant, P is the ambient pressure (1.013 $\times 10^5$ Pa), F is Faraday's constant (96485 C mole^{-1}), T is the ambient temperature (K), I is the current (A), t is the time (s), and Z is the number of electrons released in the reaction, Z=2 [2, 74].

8.2.5 Power Density

The power density delivered by a fuel cell is the product of the cell voltage and the current density, e.g., power density (W cm^{-2}) $= i.V$. Power density is a non-linear function of current density and typically reaches a maximum at approximately 66% of the limiting current density [1, 4].

8.3 Results and Discussions

8.3.1 Thermal Stability

Figure 8.2 shows TG traces of % mass loss against temperature for both PEEK and SPEEK samples. It is evident that PEEK has a much higher thermal stability, significant mass loss for PEEK only occurring at about 510°C. This is a result of main chain decomposition of the polymer.
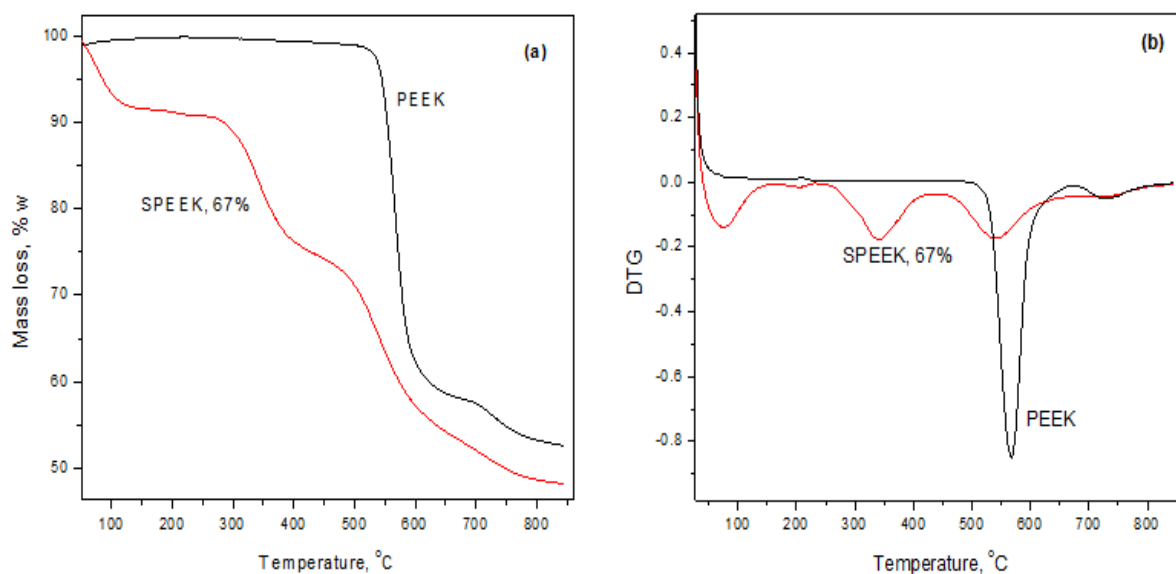
F**igure 8.2:** Example of TG (a) and DTG (b) curves for PEEK and SPEEK, 67%.

The introduction of SO_3H groups into PEEK decreased the thermal stability substantially, mostly due to an acid-catalyzed degradation [236]. Three-step mass loss was observed with SPEEK samples; see Table 8.1, up to 200, 200-450 and above 450°C. The mass loss from 60-200°C in SPEEK is due to the loss of physically and chemically bound water and to the unwashed free acid. The observed mass loss in the temperature range 200-450°C may be attributed to degradation of sulphonic acid groups and was noted to increase with increasing sulphonation degree [46, 181]. Similar to PEEK, breakdown of the polymer backbone takes place above 450°C in SPEEK samples.

The thermal degradation mechanism of sulphonated PEEK, SPEEK, with various degrees of sulphonation has been studied by pyrolysis-gas chromatography/mass spectrometry, Py-GC/MS, and thermogravimetry, TG [236]. It has been shown that both SPEEK and PEEK have quantitatively similar pyrograms (except for the SO_2 peak), but the pyrolyzate distribution of SPEEK depends strongly on the sulphonation degrees as well as the pyrolysis

215

temperature. Isothermal and dynamic TG data suggested a kinetic model based on random degradation of polymer chains. Two degradation processes were observed for SPEEK and were explained as due to degradation of the segments substituted by sulphonic acid groups (the first, lower degradation step) and, identical to that of PEEK, to random chain scission and transfer reactions (the second step) [236].

An attempt was made to correlate the mass loss in the region 200-450°C with the degree of sulphonation, DS, assuming that it represents the decomposition of $-SO_3H$ group only. A linear relationship was observed; see Figure 8.3, indicating that an increase in DS leads to an increase in mass loss in the region 200-450 $^{\circ}$C.

Table 8.1: Results of TG analysis of PEEK and SPEEK samples.

Sample	DS ± 5.0 (%)	%Mass loss (± 5.0)			% Char residue (± 5.0)
		60-200 $^{\circ}$C	200-450 $^{\circ}$C	Above 450 $^{\circ}$C	
PEEK	0	0	0	46.6	53
1	38	7.1	10.8	35.7	47
2	50	7.5	13.4	29.4	50
3	59	8.5	14.8	32.1	45
4	59	7.2	14.7	33.4	45
5	67	9.1	16.4	30.2	44
6	68	6.2	14.7	32.2	47
7	75	7.3	18.6	28.0	46
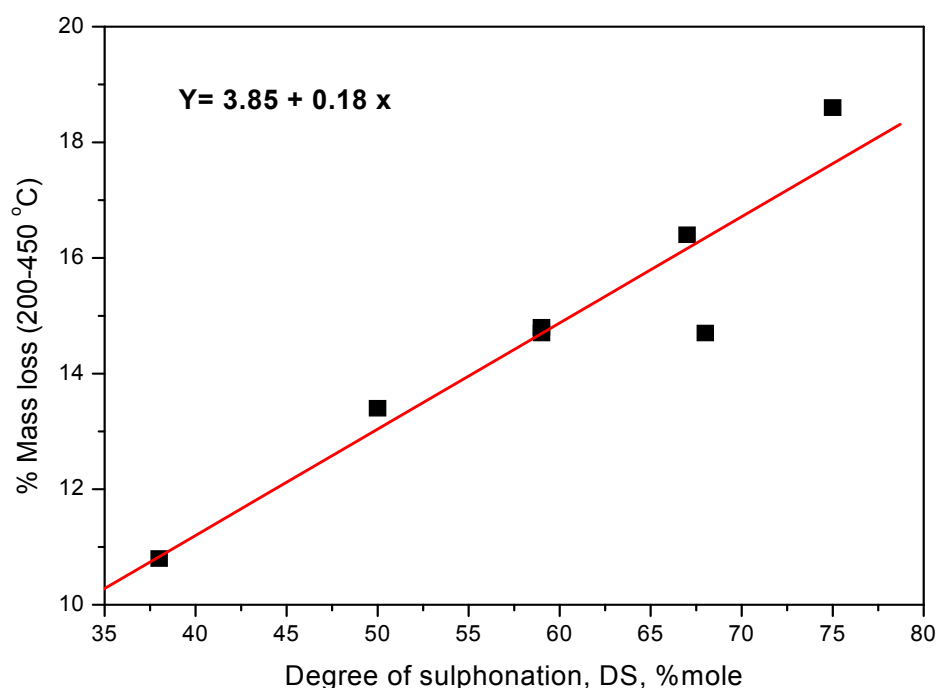
Figure 8.3: Mass loss % due to sulphonic acid as a function of DS, (calculated by titration).

In a sample with 100% DS the calculated mass loss due to SO_3 volatilization would be approximately 22%. However, if one calculates the theoretical mass loss based on the experimentally determined values of DS, the observed mass loss is slightly higher. This may be due to loss of phenol along with SO_3 group by a random chain scission catalyzed by the acid group [236].

The thermal stability of the cross linked PEEK was discussed in Chapter 3 and Figure 8.4 shows the TG traces of some cross linked sulphonated PEEK. The TG profiles of the cross linked membranes were similar to those of sulphonated PEEK but the char residual was observed to be higher and increased with increasing the degree of sulphonation. This could be attributed to the fact that no low molecular weight fractions, produced on irradiation as a result of chain scission, were present in the membranes after sulphonation reaction. The

increase in char with increasing degree of sulphonation must be due to the development of stable structures which did not decompose at the temperature range used in the present TG experiments.

The decomposition of Nafion membranes also involved three stages, the first one being water loss (moisture only) from 50 to 180°C, the second one from 310 to 380°C, due to sulphonic groups loss, and the last one from 420 to 590°C, due to the decomposition of the perfluorinated matrix [245]. As far as the PEM stability is concerned, it was concluded that both cross linked SPEEK and SPEEK samples were thermally stable when compared to Nafion within the temperature range for PEMFC application.
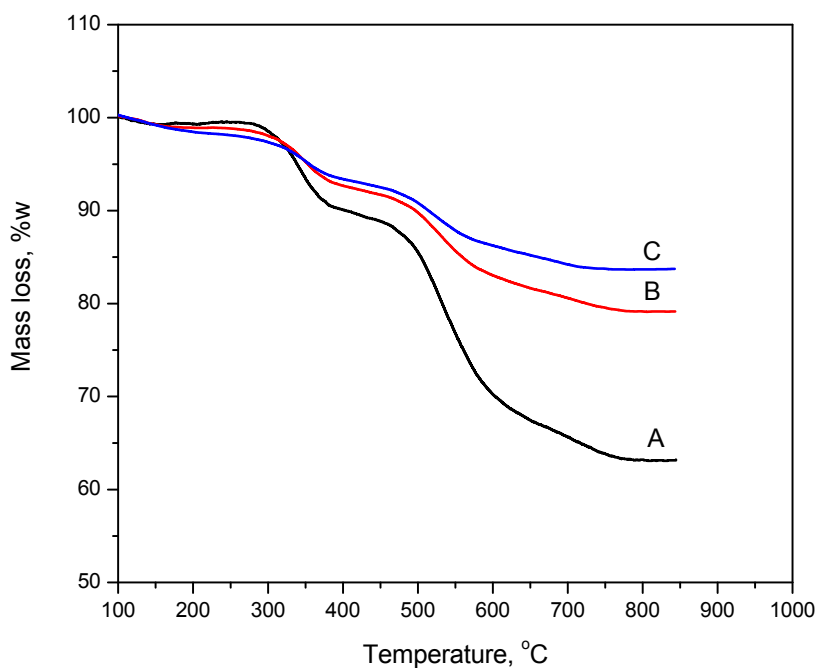
Figure 8.4: Thermal stability in nitrogen for membranes having the same cross link density of 0.15 and ion exchange capacity of A = 1.2, B=1.9 and C= 2.4 meq g^{-1}.

8.3.2 Oxidative Stability and Chemical Resistance

In this study the oxidative stability of the membranes was estimated at room temperature by measuring the time taken for the membranes to breakdown or dissolve in Fenton reagent (30% H_2O_2 and 15 ppm $FeSO_4$). It was observed that the stability of the membranes, in general, decreased with increasing IEC, but the cross linked membranes showed higher oxidative stability and this in turn was less dependent on the IEC content, compared to SPEEK having similar IEC. SPEEK membranes, having IEC in the range 0.8 to 2.4 meq g^{-1}, were observed to dissolve completely in Fenton reagent after 12 to 48 h. On the other hand, the breakdown of the cross linked sulphonated PEEK membranes having higher ratios of IEC/X_c occurred only after 72 h of treatment. Complete dissolution was not observed even after a one week test. This was attributed to the presence of an oxidative stable structure in the membranes produced by the cross linking process. Nafion membranes as well as other cross linked membranes, e.g., chemically cross linked sulphonated PEEK and irradiated membranes with lower ratio of IEC/X_c showed the highest oxidative stability and did not breakdown in the time scale of the experiment (one week).

While sulphonated PEEK dissolved in many aprotic polar solvents such as DMAc and DMF, the cross linked membranes were found to be insoluble in all organic solvents and to have very good chemical resistance. However, the test in methanol showed that only membranes with low IEC did not break down with increasing exposure time. It was observed that most of the irradiated membranes having IEC ≥ 2.0 meq g^{-1} absorbed up to 50% of their original weight during the first two hour of immersing in methanol and more than 100% after 20 h and were found to break up after one week. On the other hand, irradiated membranes with the highest cross linking density, e.g., $X_c = 0.23$ and $IEC = 1.68$ and 1.82 meq g^{-1} showed the

lowest equilibrium methanol uptake, e.g., 56 and 95% and did not break up during the experiment.

In addition, the chemically modified sulphonated PEEK was observed to dissolve in methanol on stirring overnight but after treating of the membranes at 120°C, they were insoluble in all solvents and absorbed up to 40% of methanol. This was attributed to the reduction of IEC due to the thermal condensation of the sulphonic acid groups as discussed earlier. It was concluded that the IEC values played a more important role than cross linking density in dictating the methanol permeability of the membranes.

8.3.3 Polarization Curve of PEM Using the Junior Basic Fuel Cell System

A polarization curve is the most important characteristic of a fuel cell and its performance. It can be used to investigate the effect of operating conditions on fuel cell output in addition to that other useful information about the fuel cell performance can be obtained from the potential-current data, e.g., power density is a product of potential and current density.

8.3.3.1 Effect of Membranes Thickness and IEC

Figures 8.5 (a) and (b) show the voltage-current and power curves for Nafion membranes with different thicknesses. The performance of the cell was improved by using a thinner membrane, and was consistent with the literature [246]. This has been explained as due to a lowering of the internal resistance of the cell and improving water management in the thinner membrane. For the same reason the performance of the cell improved with increasing IEC of the SPEEK membranes, as shown in Figures 8.5 (c) and (d) which represented the results obtained using sulphonated PEEK membranes having the same thickness, e.g., 60±5 μm, but they differed in IEC values.
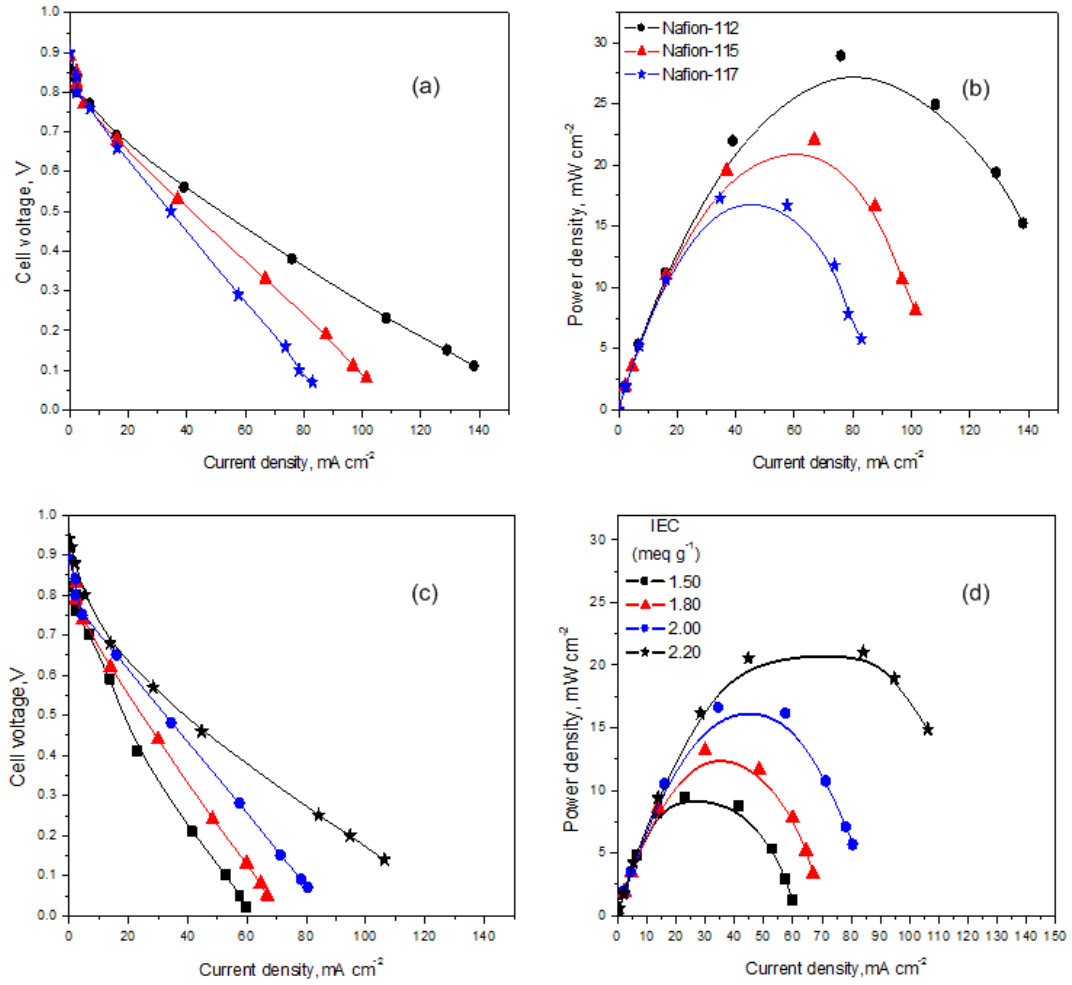
Figure 8.5: The voltage-current characteristic and the power curves for different membranes. The effect of Nafion thickness (a) and (b) and the effect of IEC of 60 ± 5 μm in sulphonated PEEK membranes (c) and (d).

8.3.3.2 Effect of Oxidant Partial Pressure and Electrode Materials

Generally, the operation of fuel cells at elevated pressures lead to a higher cell potential as evident from the Nernst equation eq. (8.3), and due to the increase in exchange current density because of increasing concentration of reactant gases at the electrodes. In the same way, elevated pressure increases the limiting current density by improving mass transfer of gaseous species [2].

221

Exchange current density, i_o, at pressure, P, different from ambient pressure, P_o, is given by the equation:

$$i_o = i_o^{ref} \left(\frac{P}{P_o} \right)^{\gamma}$$ (8.17)

The gain in cell potential, ΔV, at elevated pressure is given by the equation:

$$\Delta V = \frac{RT}{nF} \ln \left[\left(\frac{P_{H_2}}{P_o} \right) \left(\frac{P_{O_2}}{P_o} \right)^{0.5} \right] + \frac{RT}{\alpha F} \ln \left(\frac{P}{P_o} \right)$$ (8.18)

For given conditions, the gain resulting from a pressure increase from one atmosphere to 200 kPa is 34 mV, and from one atmosphere to 300 kPa is 55 mV. This gain applies at any current density, and results in an improved polarization curve at elevated pressures [2]. A similar performance improvement is observed using oxygen (100%) instead of air (21% O_2), see Figure 8.6 (a) to (d).

Further improvement to cell performance was observed when testing the MEA, using the same membrane, e.g., Nafion-112. This improved performance was related to conductivity enhancement by a well-designed MEA (improved water back diffusion by making the reaction occur at the surface of the membrane) as well as to the increase in catalyst loading on the cathode side (lowering the catalytic activity of Pt as the reaction proceeds) [246, 247].
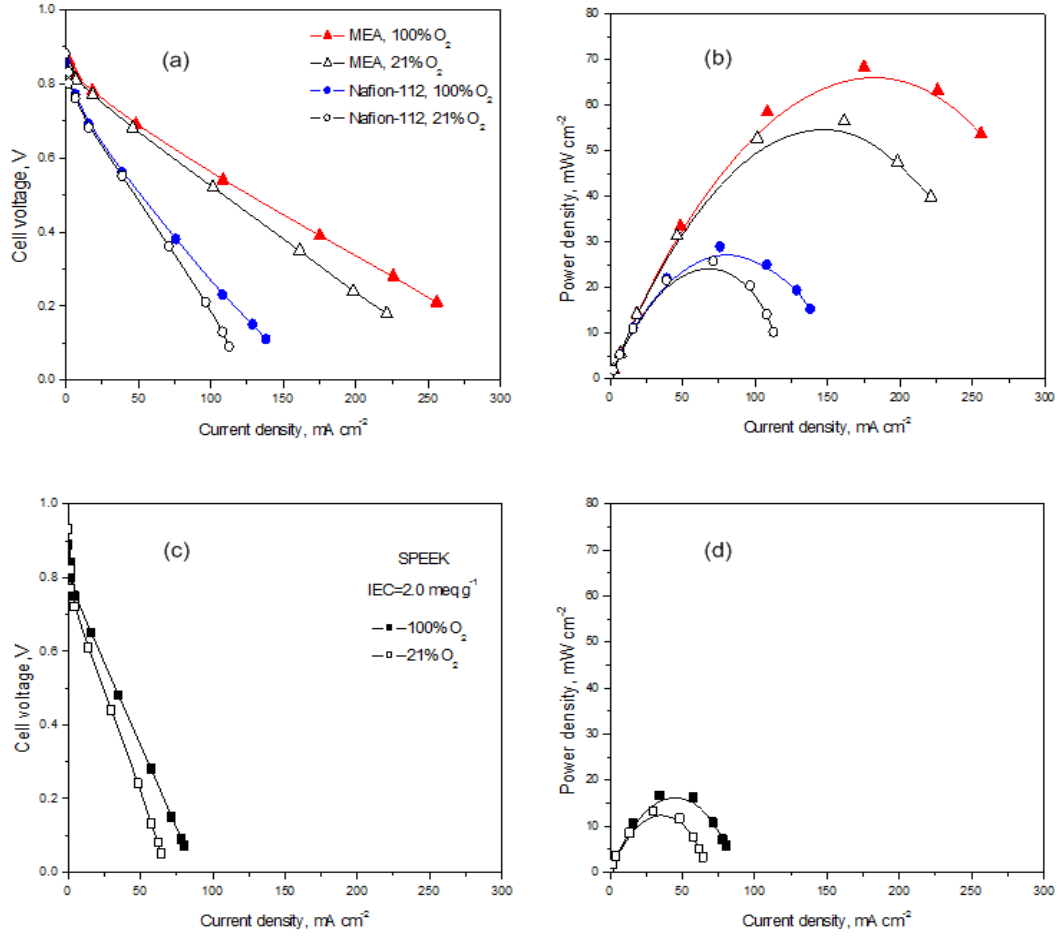
Figure 8.6: The voltage-current characteristic and the power curves for different membranes. The effect of catalyst loading and oxidant partial pressure on Nafion-112 (a) and (b) and effect of oxidant partial pressure on sulphonated PEEK membrane (c) and (d).

8.3.3.3 Effect of Operating Temperature

Generally, fuel cell performance has been reported to improve at elevated temperature. Although potential losses arise at higher temperatures due to: (i) the term $-\dfrac{T\Delta S^o}{nF}$ in eq. (8.1) and (ii) an increase in the Tafel slope [2]. On the other hand, increased temperature results in higher exchange current density and there is a significant improvement in mass transport properties [2, 4].
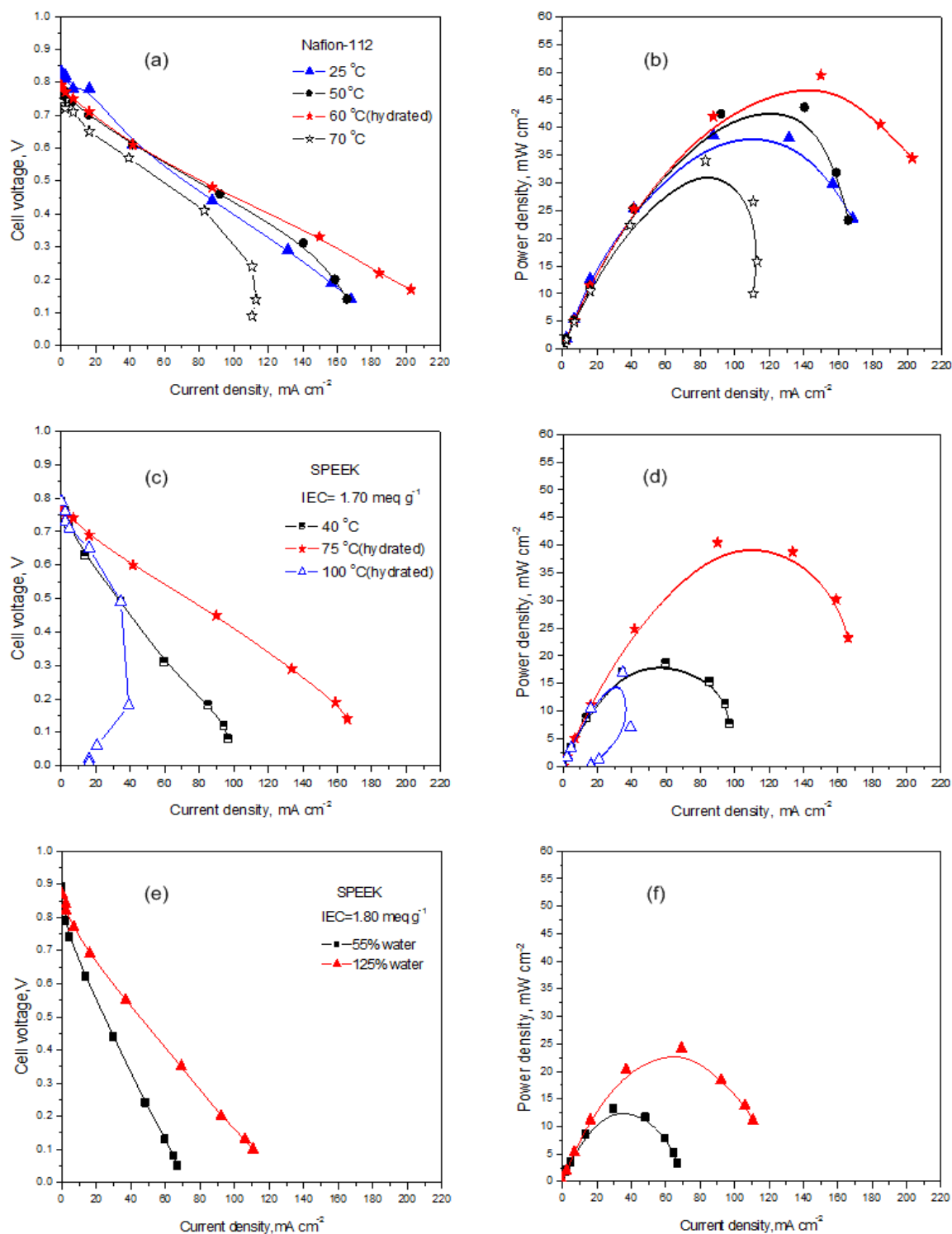
Figure 8.7: The voltage-current characteristic and the power curves for different membranes. The effect of operating temperature on Nafion-112 (a) and (b) and sulphonated PEEK (c) and (d) and the effect of water content on the performance of sulphonated PEEK membranes (e) and (f).

Figures 8.7 (a) and (c) show the results of an experiment carried out using Nafion-112 and SPEEK in which the cell temperature was increased from 25 to 100°C, and the resulting power curves clearly indicated output gain with increased temperature, see Figures 8.7 (b) and (d).

Although the open circuit voltage decreased, the cell output increased by approximately 30% by increasing the temperature to 60 ^{o}C. On the other hand, membrane dehydration occurred and was the reason for the cell performance collapsing at higher temperatures. Moreover, increasing the temperature to 100 ^{o}C resulted in the membrane breaking up and accounted for the dramatic decrease in performance at higher current density.

In addition, the water content of the membrane plays an important role in lowering the membrane resistance and improving the performance of the cell. This is shown in Figures 8.7 (e) and (f) which show the results obtained with SPEEK membranes equilibrated under different conditions prior to fuel cell testing, e.g., by immersing in distilled water at room temperature or in hot distilled water at 70°C for 3 hours.

8.3.3.4 The Performance of Cross Linked Membranes

The results obtained on operating the PEM fuel cells with two cross linked membranes are shown in Figures 8.8. Sample HX-10 was obtained by sulphonating a proton irradiated PEEK film for 50 h and sample HEX-3 was obtained by sulphonating a helium irradiated PEEK film for 76 h. Both membranes had the same cross link density of 0.30. As can be seen the performance was comparable to that of Nafion-117 and proved that cross linking before sulphonation was an effective route for preparing PEM.
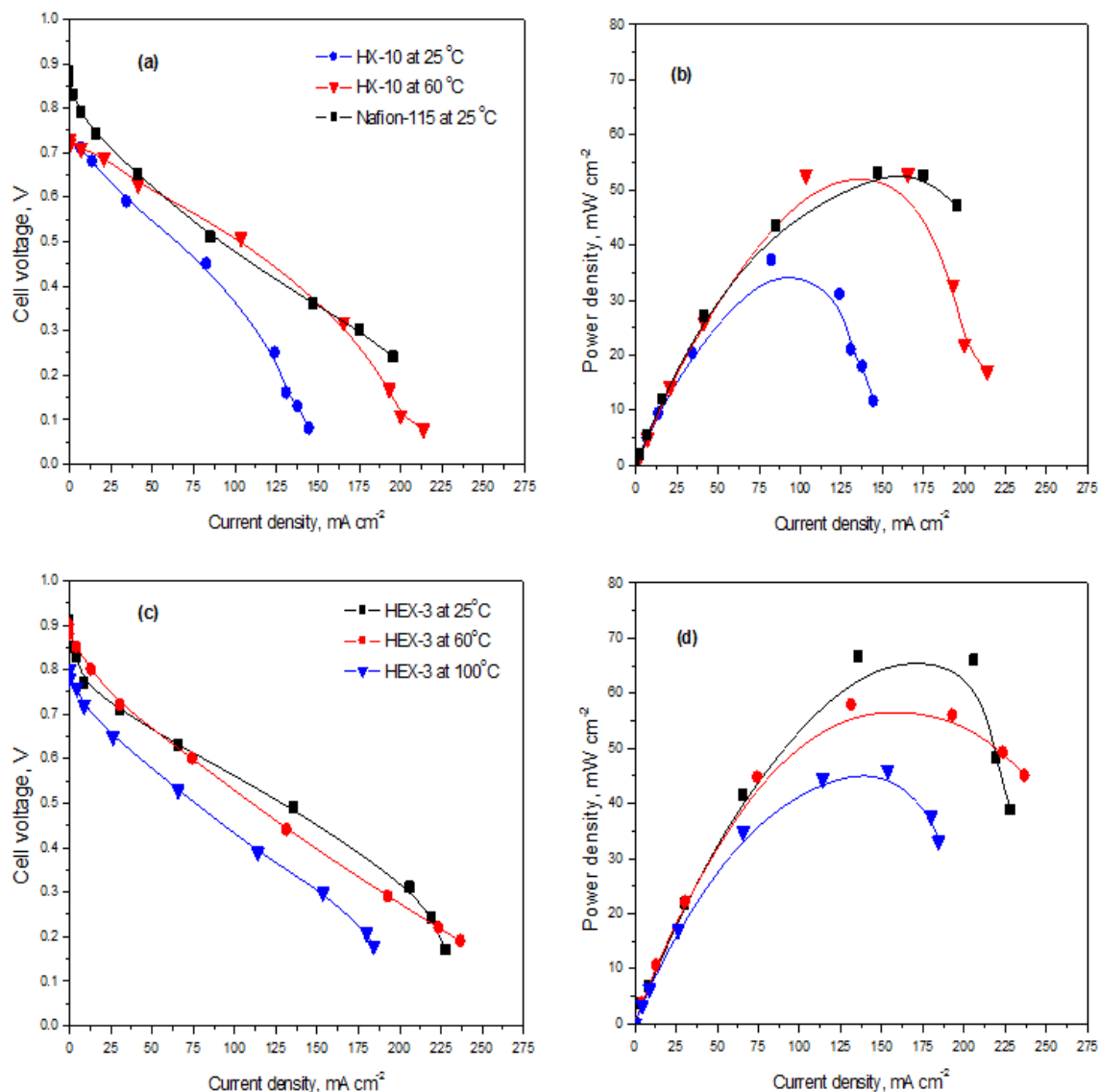
Figure 8.8: The voltage-current characteristic and the power curves at different temperature for different cross linked membranes. Both membranes HX-10 and HEX-3 had similar cross link densities of 0.30 and IEC of 1.8 and 2.2 meq g^{-1} respectively.

Two main conclusions can be drawn from these results. Firstly the cross linked membranes showed better performance (higher power output and current density) comparing to those of non cross linked solvent cast SPEEK membranes of similar IEC, see Figures 8.5 (c), (d) and

8.8 (c), (d). This was attributed to solvent effects as discussed in paragraph 7.4.1. Secondly, the effect of temperature on the effectiveness of the cross linked membranes was identical to that of the non cross linked membranes, e.g., increasing temperature led to an improvement in the cell performance which was observed to deteriorate after a limiting temperature due to drying of the membranes, see Figures 8.7 (c), (d) and 8.8 (a), (b).

8.3.4 Efficiency of a PEM Fuel cell

Figure 8.9 shows the relationship between the cell efficiency and power density for different membranes. For a fuel cell operated with Nafion, the maximum power was reached at an efficiency of 31%. This is significantly lower than the maximum theoretical fuel cell efficiency of 83%, calculated from eq. (8.17). A higher efficiency may be reached with the same fuel cell, but at significantly lower power densities. This means that for a required power output a fuel cell may be made larger (with a larger active area) and more efficient, or more compact but less efficient, by selecting the operating point anywhere on the polarization curve or on the efficiency-power density plot. Typically, a fuel cell rarely works anywhere close to the maximum power density [2].

More commonly, the operating point is selected at cell potential around 0.7 V. For the graph in Figure 8.9, this would result in power density of 33 mW cm^{-2} and efficiency of 43% for membrane HEX-3. For applications where a higher efficiency is required, a higher nominal cell potential may be selected (0.8 or higher), which would result in a 55% to 60% efficient fuel cell, but the power density would be less than 10 mW cm^{-2}. Similarly, for applications where fuel cell size is important, a lower nominal cell potential may be selected (around 0.6V), which would result in a higher power density, that is, a smaller fuel cell.

Although Figure 8.9 shows that fuel cell efficiencies above 60% are possible at very low current and power densities, at very low current densities hydrogen crossover and internal current losses, although very small, become important, and the efficiency-power dependence drops off [2].
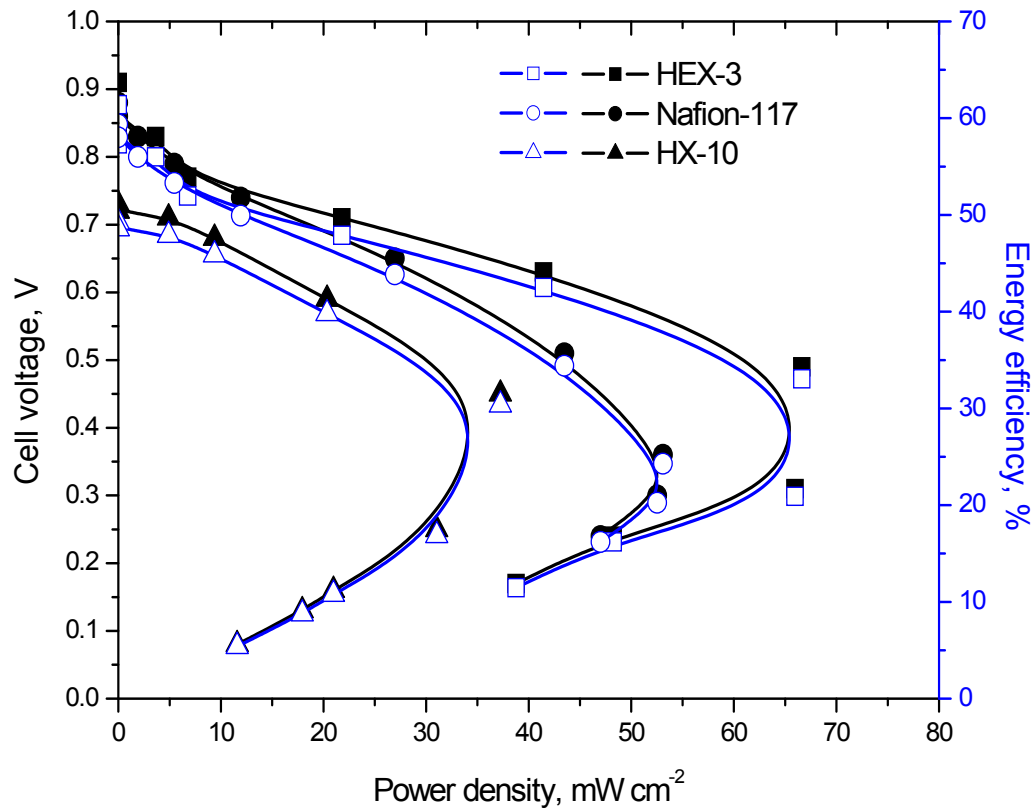
Figure 8.9: Energy efficiency and power output of PEM fuel cells operating with membranes as indicated.

8.4 Conclusions

The effects of cross linking and the extent of IEC on membrane stability in chemical, oxidative and thermal environments have been considered. Cross linking had little effect in improving both thermal and oxidative stabilities but its effect in improving the mechanical stability, in particular in methanol solution, was pronounced. This suggests that the lower methanol permeability of the cross linked membranes was consistent with the results on the form of water existing in the membranes, as reported in Chapter 7.

The polarisation curves indicate that thickness, IEC, cross link density, as well as temperature, alter the performance of the PEM fuel cell, but the IEC values had a greater effect than the cross link density. The performance of the cross linked membranes was very similar to that of non cross linked PEM suggesting that the same mechanism of proton transport is involved in both systems. The measurement of power output and energy efficiency suggests that the cross linked PEM produced in this work is a promising candidate to replace Nafion membranes but more information is required, in particular under fuel cell operating conditions, to understand the material property relationship in the cross linked membranes.

Chapter 9

Conclusions and Future Work

9.1 Summary

Ion irradiation has been employed as an effective means of cross linking PEEK in the preparation of long service thermally, mechanically and chemically stable PEMs.

Alterations produced in the molecular structure of amorphous PEEK by irradiation with 11.7 MeV H^+ and 25.6 MeV He^{2+} ions have been interpreted as due to chain scissions as well as the formation of cross links. The efficiency of the ions in inducing these changes was dependent on their relative linear energy transfer (LET) effects, but both ions altered the polymer's physical and thermal properties to a similar extent. The cross link densities were determined from sol-gel fraction analysis using the well known Charlesby–Pinner equation and were found to be 0.34 and 0.45% MGy^{-1} for irradiation with H^+ and He^{2+} ions respectively.

The chemical structure of the cross link units could not be established from the FT-IR spectra due to their relatively low concentration. However, there were little or no changes in the observed spectra on irradiation indicating that the molecular structure of PEEK is resistant to irradiation.

The measured T_g increases linearly with cross link density in accordance with the DiBenedetto equation from which the cross linking constants were found to be similar for both ion at 0.082. Since these two constants were very similar, the cross link structures produced by both ions must be very similar. The only difference between the two ions is their efficiency in cross linking in line with their LET effect.

The thermal decomposition of irradiated PEEK was similar to that of untreated PEEK and seems to be a random chain scission process. The thermal decomposition temperature and kinetic data for irradiated PEEK films quantitatively suggest that these films still have sufficient thermal stability for many long term applications.

Irradiation has a significant effect on the melting and crystallization behaviour of amorphous PEEK. The DSC results indicate that the cross links which accompanied irradiation retard the crystallization, but no changes were observed in the mechanism of crystallization.

The equilibrium melting point, T_m^o, decreased with increasing irradiation dose and this depression was analyzed using the Flory equation to calculate the concentration of non-crystallizable units in the molecular structure of irradiated PEEK. There was also a linear correlation between the amounts of these units and the increase in T_g which implies that these abnormal structures were cross links.

The depression in T_m^o alone was not sufficient to account for the overall retardation of the crystallization. In addition, the fold surface energy, σ_e, increased on irradiation. This increase resulted from the increasing amounts of cross link within the amorphous regions, which also depressed the melting points and reduced the rate of crystallization. The average length of the

repeating unit sequence between adjacent cross links determines the size of the lamellar thickness, and since this decreases with increasing cross link density, it directly accounts for the inhibition of crystallization and its eventual cessation at high radiation dose.

Cross linking by ion irradiation has a complex effect on the molecular relaxation of PEEK, and the $\alpha-$ and $\beta-$transitions are altered in different ways. The $\beta-$transition appeared to be sensitive to the amount of water present but unaltered by radiation dose; the measured activation enthalpy of 45 kJ mol^{-1} was consistent with molecular motions associated with onset of rotation of localised groups of the size of a chain link. This made the overall relaxation insensitive to the development of the cross linked network produced on irradiation. By contrast the $\alpha-$transition is extremely sensitive to the cross link density and the glass transition temperature increases progressively with dose. However, the activation enthalpy of the relaxation is substantially reduced from about 950 to 450 -600 kJ mol^{-1}. By analogy to the activation enthalpy of the $\beta-$transition, the large activation enthalpies associated with the $\alpha-$transition is attributed to concerted rotational mobility of chain segments involving possibly 15 to 25 monomer units. The reduction in activation enthalpy on irradiation arises from the increased restrictions imposed by the progressive development of networks and to the onset of rotation of the smaller segments between cross links.

The dielectric response at the glass transition has been interpreted by the KWW relationship in terms of a series of relaxations with a broad distribution of relaxation times, the breadth of the distribution being related to the reciprocal value of the exponent β_{KWW}. Irradiation decreased the value of β_{KWW} and increased the spread of the relaxation times of the processes involved due to the formation of the cross linked network.

SPEEK membranes with different degrees of sulphonation and cross linking were successfully prepared using sulphuric acid as the sulphonating agent. The formation of sulphonic acid group in SPEEK membranes was confirmed by FTIR spectroscopy. The kinetics of the sulphonation reaction indicated that both stirring and drying periods played a role in determining the sulphonation degree. The sulphonation of cross linked membranes was also achieved by the use of concentrated sulphuric acid and this was confirmed by FTIR spectroscopy. The ion exchange capacity (IEC) of the cross linked membrane was shown to be dependent on cross linking density and decreased with increasing irradiation dose.

Substitution of hydroxyl groups onto the chains by irradiation increases the final IEC of the cross linked membrane compared with the original materials. This effect was more pronounced in the case of films irradiated with helium ion, confirming its higher efficiency in producing cross links and functionality on the chain, compared to irradiation with protons.

The kinetic treatment using Fick's second law was found to be a good model to describe the diffusion controlled feature of the sulphonation reaction of cross linked PEEK films. This model predicts a similar decrease in diffusion coefficient with increasing cross link density but this decrease was dependent on the irradiation ions used.

Chemical reduction of the carbonyl groups was also successfully applied as an alternative method of cross linking highly sulphonated PEEK but the structure of the resultant PEM has not been studied in detail. At the higher reduction agent ratios used, a possible reduction of other chemical entities in the molecular structure of SPEEK was observed by FTIR spectroscopy, but at lower ratios it was possible to remove residual solvents and so allow the cross link forming condensation reaction to proceed.

The materials properties of different cross linked SPEEK membranes have been investigated focusing on water uptake and stability studies. The main reason for cross linking the PEM was to reduce the swelling in the presence of solvents and to attain high water content without losing dimensional stability. The IEC values had a greater effect than the cross link density in controlling the water content and diffusion of water through the PEM but cross linking enabled the PEMs to reach very much higher water content without losing mechanical integrity.

It was concluded from DSC analysis that increasing the cross link density resulted in more bound water present in the equilibrated membranes, and increasing the IEC gave rise to more free water. The results indicated that the cross linked membranes have lower methanol permeability and electro-osmotic drag, as well as improved mechanical stability.

It was shown that both cross link density and the IEC had an effect on the pore size in the cross linked membranes, but the IEC had a more pronounced effect. Moreover, the presence of a nano-structure in the cross linked membranes was confirmed and the sizes of pores present were comparable to those reported in Nafion using NMR cryoporometry, e.g, 1-3 nm.

The effects of cross linking and IEC on the membranes stability in chemical, oxidative and thermal environments have also been considered. Cross linking had little effect in improving both thermal and oxidative stabilities but its effect in improving the chemical stability in particular in methanol solution was pronounced.

The polarisation curves indicate that thickness, IEC, cross link density as well as temperature affect the performance of the PEM fuel cell, but the IEC values had a greater effect than the cross link density. The performance of the cross linked membranes was very similar to that of

the non cross linked PEM, suggesting the same mechanism of proton transport was involved in both systems. The cross linked membranes showed better performance (higher power output and current density) compared to that of the non cross linked solvent cast SPEEK membranes of similar IEC due to solvent effect. The effect of temperature on the performance of the cross linked membranes was identical to that of the non cross linked membranes, e.g., increasing temperature led to an improvement in the cell performance but led to deterioration after a limited time due to drying out of the membranes.

The measurement of power output and energy efficiency suggests that the cross linked PEM produced in this work is a promising candidate to replace Nafion membranes, but that more information is required in particular under fuel cell operating conditions to understand the material property relationship in the cross linked membranes.

9.2   Importance and Limitation of the Work

The advantage of cross linking PEEK films before sulphonation in preparing PEM in a simple step has been shown in that it eliminates the drawbacks of using solvents to cast films. It has also been shown that the cross linking process enabled high values of IEC to be attained with the result that the water content increased, meaning high conductivity. Cross linking after sulphonation significantly reduced the conductivity of the membranes. The higher water content was achieved due to sulphonation reaction, and may occur along tracks in the membrane through which the sulphuric acid would penetrate into the cross linked PEEK films. Therefore, more distinct phase separation occurs in the cross linked membranes, leading to the formation of water clusters in the membranes. This was confirmed by measurement of the pore size in the cross lined membranes, which confirmed the presence of nano-structures similar to these in Nafion. The cross linked membranes immersed in water

contained an increased water content but still retained mechanical strength and they did not dissolve or break up at these high water contents.

On the other hand, cross linking by ion irradiation has been shown to be very costly due to the high resistivity of PEEK to ion irradiation.

9.3 Future Work

There is still a great deal of information that needs to be ascertained in order to completely understand the structure-property relationships of the cross linked polymers and their effects on membrane properties, in particular under fuel cell operation conditions. Three major areas of future interest are outlined below.

- Preparation of cross linked polymers:

Recent work conducted in the School laboratory has shown that thermal treatment of PEEK at temperatures below its decomposition temperature, leads to the formation of cross links. This was confirmed by gel-sole analysis and DSC measurement. The evaluation of the cross link density and mechanism, as well as the comparison to ion irradiation, will be the next step before considering the use of cross linked polymers in the sulphonation process and in the production of PEMs. Extending these two methods (thermal and irradiation) to other polymeric system such as polyamides will be of considerable interest.

- Characterisation of cross linked PEM:

It is expected that the conductivity of the cross link PEM is similar to that of non cross linked PEEK and Nafion. However, the investigation of conductivity at high temperature

and low humidity would provide useful information to better understand the transport process in these cross linked membranes.

The determination of other PEM properties such as mechanical properties of the wet membranes, T_g as well as methanol and fuel permeability is another area worthy of study. This includes hydrolytic stability and loss of IEC on boiling the PEM in water.

- Fuel cell testing:

Although a great deal of time and effort has been spent in building the fuel cell test station it was not possible to test all the PEMs under all conditions of humidity and temperature. However, the irradiated PEMs should be tested in a commercial fuel cell test station such as a Scribner FC-850e over an extended period of time. The use of impedance spectroscopy to analyze fuel cell performance would be invaluable in considering the limitations and further development of new PEMs as well as other fuel cell components such as the membranes electrode assembly (MEA). Experiments including linear sweep voltammetry, cyclic voltammetry as well as durability testing would enable properties such as fuel crossover, active electrode area and lifetime of the MEA to be assessed quantitatively.

References:

[1] Larminie J, Dicks A. Fuel cell systems explained. john Wiley & Sons, New York, 2000.

[2] Barbir F. PEM fuel cells: Theory and practice. Elsevier Academic Press, London, 2005.

[3] McDougall A. Fuel cells. The Macmillan Press Ltd, London, 1976.

[4] Cooper KR, Ramani V, Fenton JM, Kunz HR. Experimental methods and data analyses for polymer electrolyte fuel cells. Scribner Associates, Inc. USA, 2005.

[5] http://www.tkk.fi/Units/AES/projects/renew/fuelcell/pem_index.html, 2009.

[6] Doyle M, Rajendran G. in Handbook of fuel cells, Vol. 3, W. Vielstichm, A. Lamm and H. A. Gasteiger (eds.). John Wiley & Sons, New York, 2003.

[7] Li Q, He R, Jensen JO, Bjerrum NJ. Approaches and recent development of polymer electrolyte membranes for fuel cells operating above 100 °C. Chemistry and Materials 2003:15:4896-4915.

[8] Sopian K, Daud WRW. Challenges and future developments in proton exchange membrane fuel cells. Renewable Energy 2006:31:719-727.

[9] Kreuer KD. On the development of protonic conducting materials for technological applications. Solid State Ionics 1997:97:1-15.

[10] Ise M, Kreuer KD, Maier J. Electro-osmotic drag in polymer electrolyte membranes: an electrophoretic NMR study. Solid State Ionics 1999:125:213-223.

[11] Ren X, Gottesfeld S. Electro-osmotic drag of water in poly(perfluorosulphonic acid) membranes. Journal of the Electrochemical Society 2001:148:A87-A93.

[12] Xiao G, Li Q, Hjuler HA, Bjerrum NJ. Hydrogen oxidation on gas diffusion electrodes for phosphoric acid fuel cells in the presence of carbon monoxide and oxygen. Journal of the Electrochemical Society 1995:142:2890-2893.

[13] Oetjen HF, Schmidt VM, Stimming U, Trila F. Performance data of a proton exchange membrane fuel cell using H_2/CO as fuel gas. Journal of the Electrochemical Society 1996:143:3838-3842.

[14] Thomas CE, Kuhn F, James BD, Lomax FD, Baum GN. Affordable hydrogen supply pathways for fuel cell vehicles. International Journal of Hydrogen Energy 1998:23:507-516.

[15] Peppley BA, Amphlett JC, Kearns LM, Mann RF. Methanol-steam reforming on Cu/ZnO/Al$_2$O$_3$. Part 1: The reaction network. Applied Catalysis: A General 1999:179:21-29.

[16] Peppley BA, Amphlett JC, Kearns LM, Mann RF. Methanol-steam reforming on Cu/ZnO/Al$_2$O$_3$. Part 2: A comprehensive kinetic model. Applied Catalysis: A General 1999:179:31-49.

[17] Schmidt TJ, Noeske M, Gasteiger HA, Behm RJ, Britz P, Bönnemann H. PtRu alloy colloids as precursors for fuel cell catalysts. Journal of the Electrochemical Society 1998:145:925-931.

[18] Wasmus S, Kuver A. Methanol oxidation and direct methanol fuel cells: A selective review. Journal of Electro-analytical Chemistry 1999:461:14-31.

[19] Heinzel A, Barragan VM. A review of the state-of-the-art of the methanol crossover in direct methanol fuel cells. Journal of Power Sources 1999:84:70-74.

[20] Lee JS, Quan ND, Hwang JM, Lee SD, Kim H, Lee H, H. S. Kim. Polymer electrolyte membranes for fuel cells. Journal of Industrial Engineering and Chemistry 2006:12:175-183.

[21] Li Q, He R, Gao J, Jensen JO, Bjerrum NJ. The CO poisoning effect in PEMFCs operational at temperatures up to 200°C. Journal of the Electrochemical Society 2003:150:A1599-A1605.

[22] Li Q, Hjuler HA, Hasiotis C, Kallitsis JK, Kontoyannis CG, N. J. Bjerrum. A quasi-direct methanol fuel cell system based on blend polymer membrane electrolytes. Electrochemical and Solid-State Letters 2002:5:A125 –A128.

[23] Savinell R, Yeager E, Tryk D, Landau U, Wainright J, Weng D, Lux K, Litt M, Rogers C. A polymer electrolyte for operation at temperatures up to 200$^\text{o}$C. Journal of the Electrochemical Society 1994:141:L46-L48.

[24] Malhotra S, Datta R. Membrane-supported nonvolatile acidic electrolytes allow higher temperature operation of proton-exchange membrane fuel cells. Journal of the Electrochemical Society 1997:144:L23-L26.

[25] Dhar H. Near ambient un-humidified solid polymer fuel cell, U.S. Patent 5,242,764. 1993.

[26] Watanabe M, Uchida H, Seki Y, Emori M, Stonehart P. Self-humidifying polymer electrolyte membranes for fuel cells. Journal of the Electrochemical Society 1996:143:3847-3852.

[27] Choi P, Jalani NH, Thampan TM, Datta R. Consideration of thermodynamic, transport, and mechanical properties in the design of polymer electrolyte membranes for higher

temperature fuel cell operation. Journal of Polymer Science: Part B: Polymer Physics 2006:44:2183–2200.

[28] Jannasch P. Recent developments in high-temperature proton conducting polymer electrolyte membranes. Current Opinion in Colloid and Interface Science 2003:8:96–102.

[29] Adjemian KT, Srinivasan S, Benziger J, Bocarsly AB. Investigation of PEMFC operation above 100 ^{o}C employing perfluorosulfonic acid silicon oxide composite membranes. Journal of Power Sources 2002:109:356-364.

[30] Zang H, Chen T-L, Yuan Y-G. Chinese Patent 85108751.

[31] Liou K, Zang H. Chinese Patent 85101721.

[32] Trotta F, Drioli E, Moraglio G, Poma EB. Sulphonation of poly(ether ether ketone) by chlorosulphuric acid. Journal of Applied Polymer Science 1998:70:477-482.

[33] Basile A, Paturzo L, Iulianelli A, Gatto I, Passalacqua E. Sulfonated PEEK-WC membranes for proton-exchange membrane fuel cell: Effect of the increasing level of sulfonation on electrochemical performances. Journal of Membrane Science 2006:281:377–385.

[34] Kobayashi T, Rikukawa M, Sanui K, Ogata N. Proton-conducting polymers derived from poly(ether-etherketone) and poly(4-phenoxybenzoyl-1,4-phenylene). Solid State Ionics 1998:106:219-225.

[35] Hübner G, Roduner E. Journal of Materials Chemistry 1999:9:409.

[36] Dobrovol'skii YA, Volkov EV, Pisareva AV, Fedotov YA, Likhachev DY, Rusanov AL. Proton-exchange membranes for hydrogen-air fuel cells. Russian Journal of General Chemistry 2007:77:95-104.

[37] Hasegawa S, Suzuki Y, Maekawa Y. Preparation of poly(ether ether ketone)-based polymer electrolytes for fuel cell membranes using grafting technique. Radiation Physics and Chemistry 2008:77:617-621.

[38] Patri M, Hande VR, Phadnis S, Somaiah B, Roychoudhury S, Deb PC. Synthesis and characterization of SPE membrane based on sulphonated FEP-g-acrylic acid by radiation induced graft copolymerization for PEM fuel cell. Polymer for Advanced Technologies 2004:15:270–274.

[39] Jones DJ, Roziére J. Recent advances in the functionalisation of polybenzimidazole and polyetherketone for fuel cell applications. Journal of Membrane Science 2001:185:41-58.

[40] Kerres JA. Development of ionomer membranes for fuel cells. Journal of Membrane Science 2001:185:3-27.

[41] Wainright JS, Wang JT, Weng D, Savinell RF, Litt M. Acid-doped polybenzimidazoles: A new polymer electrolyte. Journal of the Electrochemical Society 1995:142:L121-L123.

[42] Walker M, Baumgärtner KM, Kaiser M, Kerres J, Ullrich A, Räuchle E. Proton conducting polymers with reduced methanol permeation. Journal of Applied Polymer Science 1999:74:67-73.

[43] Alberti G, Casciola M, Massinelli L, B. Bauer. Polymeric proton conducting membranes for medium temperature fuel cells (110-160°C). Journal of Membrane Science 2001:185:73–81.

[44] Jin X, Bishop MT, Ellis TS, Karasz FE. A solphonated poly(aryl ether ketone). British Polymer Journal 1985:17:4-10.

[45] Bailly C, Williams DJ, Karasz FE, MacKnight WJ. The sodium salts of sulphonated poly (aryl ether ether ketone) (PEEK): Preparation and characterization. Polymer 1987:28: 1009 -1016.

[46] Lakshmi VV, Choudhary V, Varma IK. Sulphonated poly(ether ether ketone): synthesis and characterization. Macromolecules Symposia 2004:210:21-29.

[47] Yen SPS, Narayanan SR, Halpert G, Graham E, Yavrouian A. Polymer material for electrolytic membranes in fuel cells. 1998: US Patent 5,795,496.

[48] Mao SS, Hamrock SJ, Ylitalo DA. Cross linked ion conductive membranes. 2000: US Patent 6,090,895.

[49] Helmer-Metzmann F, Osan F, Schneller A, Ritter H, Ledjeff K, Nolte R, Thorwirth R. Polymer electrolyte membrane, and process for the production thereof. 1995: US Patent 5,438,082.

[50] Kerres J, Zhang W, Tang C-M, Haring T. Covalently cross-linked polymers and polymer membranes via sulphonate alkylation. 2003: US Patent Appl. No. 0032739

[51] Mikhailenko SD, Wang K, Kaliaguine S, Xing P, Robertson GP, Guiver MD. Proton conducting membranes based on cross linked sulphonated poly(ether ether ketone) (SPEEK). Journal of Membrane Science 2004:233:93-99.

[52] Sammas SR, Wasmus S, Savinell RF. Thermal stability of proton conducting acid doped polybenzimidazole in simulated fuel cell environments. Journal of the Electrochemical Society 1996:143:1225-1232.

[53] Thompson A, Farris RJ. A novel method for cross-linking poly(ether ether ketone). Journal of Applied Polymer Science 1988:36(5):1113-1120.

[54] Day M, Sally D, Wiles DM. Thermal degradation of poly(aryl-ether-ether-ketone): Experimental evaluation of crosslinking reaction. Journal of Applied Polymer Science 1990:40:1615-1625.

[55] EI-Sayed AH, Sasuga T, Seguchi T. Irradiation effects on aromatic polymers: 3. Changes in thermal properties by gamma irradiation. Polymer 1992:33:2911-2914.

[56] Al Lafi AG, Hay JN, Parker DJ. The effect of proton irradiation on the melting and isothermal crystallization of poly(ether ether ketone). Journal of Polymer Science Part B: Polymer Physics 2008:46:1094-1113.

[57] Al Lafi AG, Hay JN, Parker DJ. The effect of ion irradiation on the thermal properties of poly(ether ether ketone). Journal of Polymer Science Part B: Polymer Physics 2008:46:2212-2221.

[58] Chen J, Maekawa Y, Asano M, Yoshida M. Double crosslinked polyetheretherketone-based polymer electrolyte membranes prepared by radiation and thermal cross linking techniques. Polymer 2007:48:6002-6009.

[59] http://www.fuelcells.dupont.com. 2005.

[60] http://www.victrex.com. 2002.

[61] Sasuga T, Kudoh H. Ion irradiation effects on thermal and mechanical properties of poly (ether-ether-ketone) PEEK. Polymer 2000:41:185-194.

[62] International Atomic Energy Agency (IAEA) Charged particle cross section database for medical radioisotope production: monitor reactions 2009.
(a)http://www-ndsiaeaorg/medical/cup65zn0html
(b) http://www-ndsiaeaorg/medical/cua65zn0html

[63] Bishop MT, Karasz FE, Russet PS. Solubility and properties of a poly(aryl ether ketone) in strong acids. Macromolecules 1985:18:86-93.

[64] Paronen M, Sundholm F, Rauhala E, Lehtinen T, Hietala S. Effects of irradiation on sulphonation of poly (vinyl fluoride). Journal of Material Chemistry 1997:7(12):2401–2406.

[65] Roy A, Hickner MA, Yu X, Li Y, Glass TE, Mcgrath JE. Influence of chemical composition and sequence length on the transport properties of proton exchange membranes. Journal of Polymer Science: Part B: Polymer Physics 2006:2226-2239.

[66] Wang J, Yue Z, Economy J. Preparation of proton-conducting composite membranes from sulphonated poly(ether ether ketone) and polyacrylonitrile. Journal of Membrane Science 2007:291:210-219.

[67] Lambert JB, Shurvell HF, Lightner DA, Cooks RG. Organic structural spectroscopy. Prentice-Hall, Inc., New Jersey, 1998.

[68] Bellamy LJ. The infrared spectra of complex molecules, Vol:1. Chapman & Hall, London, 1975.

[69] Bellamy LJ. The infrared spectra of complex molecules, Vol: 2. Advances in infrared group frequencies. Chapman & Hall, London, 1980.

[70] Menczel JD, Judovits L, Prime RB, Bair HE, Reading M, Swier S. Differential scanning calorimetry (DSC), In Thermal analysis of polymers; fundamentals and applications, J. D. Menczel and R. B. Prime (edts). John Wiley & Sons, New York, 2009.

[71] Hay JN. Application of the modified Avrami equations to polymer crystallisation kinetics. British Polymer Journal 1971:3:74-82.

[72] Kim SJ, Park sJ, Kim SI. Synthesis and characteristics of interpenetrating polymer network hydrogels composed of poly(vinyl alcohol) and poly(N-isopropylamide). Reactive & Functional Polymers 2003:55:61-67.

[73] Prime RB, Bair HE, Vyazovkin S, Gallagher PK, Riga A. Thermogravimetric analysis (TGA), In Thermal analysis of polymers; fundamentals and applications, J. D. Menczel and R. B. Prime (edts). John Wiley & Sons, New York, 2009.

[74] http://www.h-tec.com. 2005.

[75] http://www.scientific-computing.com/scwjanfeb03fuelcell.html. 2006.

[76] Hurley P. Build your own fuel cell. Wheelock Mountain Publication, USA, 2005.

[77] Dova AV-, Kalogeras IM. Dielectric analysis (DEA), In Thermal analysis of polymers; fundamentals and applications, J. D. Menczel and R. B. Prime (edts). John Wiley & Sons, New York, 2009.

[78] Kao KC. Dielectric phenomena in solids with emphasis on physical concepts of electronic processes. Elsevier Academic Press, London, 2004.

[79] McCrum NG, Read BE, Williams G. An elastic and dielectric effects in polymeric solids. Dover Publication, New York, 1991.

[80] www.google.com/Triton Technology/ Lit. Ref. TTInf_DETA_1.pdf. 2009.

[81] Barsoukov E, Macdonald JR, editors. Impedance spectroscopy: Theory, experiment, and applications. John Wiley & Sons, New York, 2005.

[82] Marschall R, Bannat I, Caro Jr, Wark M. Proton conductivity of sulphonic acid functionalised mesoporous materials. Micro-porous and Mesoporous Materials 2007:99:190-196.

[83] Charlesby A. Atomic radiation and polymers. Pergamon Press, London, 1960.

[84] Chapiro A. Radiation chemistry of polymeric systems. John Wiley & Sons, New York, 1962.

[85] Cheng S, Kerluke DR. Radiation processing for modification of polymers. The 2003 Annual Technical Conference of the Society of Plastic Engineering (ANTEC), Nashville, USA, 2003.

[86] O'Donnell JH, Sangster DF. Principles of radiation chemistry. Edward Arnold (publishers), London, 1970.

[87] Wilson JE. Radiation chemistry of monomers, polymers and plastics. Marcel Dekker, New York, 1974.

[88] Dole M. The radiation chemistry of macromolecules, Vol: 1. Academic Press, London, 1972.

[89] Dole M. The radiation chemistry of macromolecules, Vol: 2. Academic Press, London, 1973.

[90] Mackova` A, Havranek V, Svorcik V, Djourelov N, Suzuki T. Degradation of PET, PEEK and PI induced by irradiation with 150 keV Ar^+ and 1.76 MeV He^+ ions. Nuclear Instruments and Methods in Physics Research B 2005:240:245-249.

[91] Sasuga T, Hagiwara M. Molecular motions of non-crystalline poly (aryl ether ether ketone) (PEEK) and influence of electron beam irradiation. Polymer 1985:26:501-505.

[92] Sasuga T, Hagiwara M. Mechanical relaxation of crystalline poly (aryl ether ether ketone) (PEEK) and influence of electron beam irradiation. Polymer 1986:27:821-826.

[93] Vaughan AS, Stevens GC. On crystallization, morphology and radiation effects in poly (ether ether ketone). Polymer 1995:36:1531-1540.

[94] Shinyama K, Baba M, Fujita S. Influence of heating on dielectric relaxation phenomena of electron beam irradiated PEEK. The 6th International Conference on Properties and Applications of Dielectric Materials 2000.

[95] EI-Sayed AH, Sasuga T, Nishii M, Seguchi T. Irradiation effects on aromatic polymers: 2. Gas evolution during electron-beam irradiation. Polymer 1992:33:2904-2910.

[96] Vaughan AS, Stevens GC. Irradiation and the glass transition in PEEK. Polymer Communication 2001:42:8891-8895.

[97] Vaughan AS, Sutton SG. On radiation effects in oriented poly (ether ether ketone). Polymer 1995:36:1549-1554.

[98] EI-Sayed AH, Sasuga T, Nishii M, Seguchi T. Irradiation effects on aromatic polymers: 1. Gas evolution by gamma irradiation. Polymer 1992:33:2897-2903.

[99] Saito O. Effect of impurity on molecular linking of irradiated polymer. Journal of the Japanese Physical Society 1959:14:798-806.

[100] Hill DJT, Lewis DA, O'Donnell JH, Whittaker AK. The crosslinking mechanism in gamma irradiation of polyarylsulfone: Evidence for Y-links. Polymers for Advanced Technologies 1998:9:45–51.

[101] Li J, Oshima A, Miura T, Washio M. Preparation of the crosslinked polyethersulfone films by high-temperature electron-beam irradiation. Polymer Degradation and Stability 2006:91:2867-2873.

[102] Nguyen HX, Ishida H. Molecular analysis of the melting behaviour of poly(aryl ether ether ketone). Polymer 1986:27:1400-1405.

[103] Alkan AAM, Hay JN. The crystallinity of PEEK composites. Polymer 1993:34:3529-3531.

[104] Cowie JMG. Polymers: Chemistry & physics of modern materials. Chapman & Hall, London, 1991.

[105] Stutz H, Illers K-H, Mertes J. A generized theory for the glass transition temperature of cross linked and uncross linked polymers. Journal of Polymer Science Part B: Polymer Physics 1990:28:1483-1498.

[106] Hay JN, Kemmish DJ. Thermal decomposition of PEEK and PEK. Polymer 1987:28:2047-2051.

[107] Huang M-R, Li X-G. Thermal degradation of cellulose and cellulose ester. Journal of Applied Polymer Science 1998:68:293-304.

[108] Chang WL. Decomposition behaviour of polyurethanes via mathematical simulation. Journal of Applied Polymer Science 1994:53:1759-1769.

[109] Day M, Cooney JD, Wiles DM. The thermal stability of poly(aryl-ether-ether-ketone) as assessed by thermogravimetry. Journal of Applied Polymer Science 1989:38:323-337.

[110] Li X-G, Huang M-R. Thermal decomposition kinetics of thermotropic poly(oxybenzonate-co-oxynaphthoate) vectra copolyster. Polymer Degradation and Stability 1999:64:81-90.

[111] Aoki Y, Kouchi N, Shibata H, Tagawa S, Tabata Y. Radiation effects of ion beams on polystyrene resist films. Nuclear Instruments and Methods in Physics Research B 1988:33:799-802.

[112] Licciardello A, Puglisi O, Calcagno L, Foti G. Cross-linking yield in particle beam irradiated polystyrene. Nuclear Instruments and Methods in Physics Research B 1990:46:338-341.

[113] Schnabel W, Klaumunzer S, Sotobayashi H, Asmussen F, Tabatas Y. Linear energy transfer effects in the radiolysis of polymers. 1. Main-chain degradation of poly(methyl methacrylate). Macromolecules 1984:17:2108-2111.

[114] Flory PJ. Principles of Polymer Chemistry. Cornell University Press, New York, 1953.

[115] Carlier V, Devaux J, Legras R, Blundell DJ. Extrapolation of short-chain oligomers melting temperatures at infinite molecular weight. Journal of Polymer Science: Part B: Polymer Physics 1998:36:2563-2571.

[116] Hoffman JD, Weeks JJ. Journal of Research, NBS, 1962:66A:13.

[117] Wunderlish B. Macromolecular physics, Vol:3 Crystal melting. Academic Press, London, 1980.

[118] Young RJ. Introduction to polymers. Chapman & Hall, London, 1981.

[119] Jenkins MJ. Crystallisation in miscible blends of PEEK and PEI. Polymer 2001:42:1981-1986.

[120] Wunderlich B. Macromolecular physics; Vol: 2, Crystal nucleation, growth, annealing Academic Press, London, 1976.

[121] Gibbs JW. The scientific papers of J. Williard Gibbs. Dover, New York, 1962.

[122] Cebe P, Hong S-D. Crystallisation behaviour of poly (ether-ether-ketone). Polymer 1986:27:1183-1192.

[123] Jenkins MJ, Hay JN, Terrill NJ. Structure evolution in melt crystallized PEEK. Polymer 2003:44:6781-6787.

[124] Hay JN, Kemmish DJ, Langford JI, Rae AIM. Structure of crystalline PEEK. Polymer Communication 1984:29:175-178.

[125] Avrami M. Kinetics of phase change. II Transformation-time relations for random distribution of nuclei. Journal of Chemical Physics 1940:8:212-224.

[126] Avrami M. Granulation, phase change, and microstructure kinetics of phase change. III. Journal of Chemical Physics 1941:9:177-184.

[127] Evans UR. The laws of expanding circles and spheres in relation to the lateral growth of surface films and the grain-size of metals. Transactions of the Faraday Society 1945:41:365 - 374.

[128] Blundell DJ, Osborn BN. The morphology of poly (aryl ether ether ketone). Polymer 1983:24:953-958.

[129] Lee Y, Porter R. Effects of thermal history on crystallization of Poly(ether ether ketone) (PEEK). Macromolecules 1988:21:2770.

[130] Lopez LC, Wilkes GL. Crystallization kinetics of poly(p-phenylene sulphide): effect of molecular weight. Polymer 1988:29:106-113.

[131] Booth A, Hay JN. The use of differential scanning calorimetry to study polymer crystallisation kinetics. Polymer 1969:10:95-104.

[132] Hay JN, Mills PJ. The use of differential scanning calorimetry to study polymer crystallization kinetics. Polymer 1982:23:1380-1384.

[133] Mandelkern L, Fatou JG, Howard C. The nucleation of long-chain molecules. The Journal of Physical Chemistry 1964:68:3368-3391.

[134] Beech PR, Booth C, Hillier ZH, Pickles CJ. The crystallization of poly(ethylne oxide) fractions: temperature dependence of growth rate. European Polymer Journal 1972:8:799-807.

[135] Kong Y, Hay JN. Miscibility and crystallization behaviour of poly (ethylene terephthalate)/polycarbonate blends. Polymer 2002:43:1805-1811.

[136] Chen M, Chen J-Y. Analysis of crystallization kinetics of poly (ether ether ketone). Journal of Polymer Science B: Polymer Physics 1998:36:1335–1348.

[137] Schönhals A. Dielectric spectroscopy on the dynamics of amorphous polymeric systems, Application Note Dielectrics 1. Novocontrol GmbH, 1998.

[138] Havriliak S, Negami S. A complex plane representation of dielectric and mechanical relaxation processes in some polymers. Polymer 1967:8:161-210.

[139] Havriliak S, Watts DG. Comparing graphical and statistical methods for analysing dielectric dispersions of polymers represented in the complex plane. Polymer 1986:27:1509-1512.

[140] Cole KS, Cole RH. Dispersion and absorption in dielectrics: I. Alternating current characteristics. Journal of Chemical Physics 1941:9:341-351.

[141] Cole KS, Cole RH. Dispersion and absorption in dielectrics: II. Direct current characteristics. Journal of Chemical Physics 1942:10:98-105.

[142] Williams G, Watts DC. Non-symmetrical dielectric relaxation behaviour arising from a simple empirical decay function. Transactions of the Faraday Society 1970:66: 80-85.

[143] Williams G, Watts DC, Dev SB, North AM. Further considerations of non symmetrical dielectric relaxation behaviour arising from a simple empirical decay function. Transactions of the Faraday Society 1971:67:1323-1335.

[144] Williams ML, Landel RF, Ferry JD. The temperature dependence of relaxation mechanisms in amorphous polymers and other glass-forming liquids. Journal of the American Chemical Society 1955:77:3701-3707.

[145] Vogel H. The law of the relation between the viscosity of liquids and the temperature. Physikalische Zeitschrift 1921:22: 645-646

[146] Fulcher GS. Analysis of recent measurements of the viscosity of glasses. Journal of the American Ceramic Society 1995:8:339-355.

[147] Tammann G, Hesse W. Z Anorg Allgem Chem 1926:156:245.

[148] Kalika DS, Krishnaswamy RK. Influence of crystallinity on the dielectric relaxation behavior of poly(ether ether ketone). Macromolecules 1993:26:4252-4261.

[149] Kalikal DS, Yoon DY. Dielectric relaxation studies of poly(4-hydroxybenzoic acid) and copolyesters based on 4-hydroxybenzoic acid and 6-hydroxy-2-naphthoic acid. Macromolecules 1991:24:3404-3412.

[150] Kang PH, Lee C, Kim KY. Radiation and thermal effects on the dielectric relaxation properties of PEEK. Journal of Industrial and Engineering Chemistry 2007:13:250-256.

[151] Shinyama K, Fujita S. Dielectric and thermal properties of irradiated poly(ether ether ketone). IEEE Transactions on Dielectrics and Electrical Insulation 2001:8:538-542.

[152] Fujita S, Shinyama K, Baba M. Dielectric properties of electron beam irradiated PEEK. Electrets, 1999 ISE 10 Proceedings 10th International Symposium on 1999:115-118.

[153] Jonas A, Legras R. Relation between PEEK semicrystalline Morphology and Its subglass relaxations and glass transition. Macromolecules 1993:26:813-824.

[154] Suljovrujic' E, Kostoski D, Kacˇarevic´-Popovic´ Z, Dojcˇilovic´ J. Effect of gamma irradiation on the dielectric relaxation of uniaxially oriented low density polyethylene. Polymer International 1999:48:1193-1196.

[155] Suljovrujic' E, KacĬarevic'-Popovic' Z, Kostoski D, DojcĬilovic' J. Effect of ageing on the dielectric relaxation of oriented and gamma irradiated LDPE. Polymer Degradation and Stability 2001:71:367-373.

[156] Suljovrujic' E. Dielectric studies of molecular β-relaxation in low density polyethylene: the influence of drawing and ionizing radiation. Polymer 2002:43:5969-5978.

[157] Al Lafi AG, Hay JN. Sulphonation of cross linked poly(ether ether ketone)- diffusion controlled kinetics. Journal of Polymer Science Part B: Polymer Physics 2009:47:775-783.

[158] Schartel S, Wendorff JH. Dielectric investigations of secondary relaxation of polyarylates: comparison of low molecular models and polymeric compounds. Polymer 1995:36:899-904.

[159] Nu´n˜ez L, Go´mez-Barreiro S, Gracia-Ferna´ndez CA, Nu´n˜ez MR. Use of the dielectric analysis to complement previous thermoanalytical studies on the system diglycidyl ether of bisphenol A/1,2 diamine cyclohexane. Polymer 2004:45:1167–1175.

[160] Huo P, Cebe P. Temperature-dependent relaxation of the crystal-amorphous interphase in poly(ether ether ketone). Macromolecules 1992:25:902-909.

[161] Ferry JD. Viscoelastic properties of polymers, 3rd ed.; John Wiley & Sons: New York, 1980, pp.287-291.

[162] Goodwin AA, Simon GP. On the analysis of dielectric relaxation data of poly(ether ether ketone). Macromolecules 1995:28:7022-7025.

[163] Schlosser E, Schönhals A. Recent development in dielectric relaxation spectroscopy of polymers. Colloid Polymer Science 1989:267:963-969.

[164] Schlosser E, Schönhals A. Dielectric relaxation in polymer solids Part 2: Application of the new model to polyurethane systems Colloid Polymer Science 1989:267:133-138.

[165] Schönhals A, Schlosser E. Dielectric relaxation in polymeric solids Part 1. A new model for the interpretation of the shape of the dielectric relaxation function. Colloid Polymer Science 1989:267:125-132.

[166] Schönhals A, Kremer F, Schlosser E. Scaling of the α relaxation in low molecular weight glass forming liquids and polymers. Physical Review Letters 1991:67:999-1002.

[167] Glatz-Reichenbach JKW, Sorriero LJ, Fitzgerald JJ. Influence of cross-linking on the molecular relaxation of an amorphous copolymer near its glass-transition temperature. Macromolecules 1994:27:1338-1343.

[168] Ngai KL, White CT. Frequency dependence of dielectric loss in condensed matter. Physical Review B 1979:20:2475-2486.

[169] Ngai KL, Rajagopal AK, Teitler S. Slowing down of relaxation in a complex system by constraint dynamics. Journal of Chemical Physics 1988:88:5086-5094.

[170] Kramarenko VY, Ezquerra TA, Sˇics I, Balta´-Calleja FJ. Influence of cross-linking on the segmental dynamics in model polymer networks. Journal of Chemical Physics 2000:113:447-452.

[171] Lehtinen T, Sundholm G, Sundholm F. Effect of crosslinking on the physicochemical properties of proton conducting PVDF-g-PSSA membranes. Journal of Applied Electrochemistry 1999:29:677-683.

[172] Gieselman MB, Reynolds JR. Water soluble polybenzimidazole based polyelectrolytes. Macromolecules 1992:25:4832-4834.

[173] Gebel G, Aldebert P, Pineri M. Swelling study of perflurosulphonated ionomer membranes. Polymer 1993:34:333-339.

[174] Kucˇera F, Jancaˇrˇ J. Homogeneous and heterogeneous sulphonation of polymers: A review. Polymer Engineering and Science 1998:38:783-792.

[175] Smith MB. Organic synthesis. McGraw-Hill, London, 1994.

[176] Schmid GH. Organic chemistry. Mosby-Year Book, St. Louis MO, 1996.

[177] McMurry J. Fundamentals of organic chemistry. Wadsworth, California, 1990.

[178] McMurry J. Organic chemistry, 3[ed]. Wadsworth, California, 1992.

[179] Jiang R, Kunz HR, Fenton JM. Investigation of membrane property and fuel cell behavior with sulfonated poly(ether ether ketone) electrolyte: Temperature and relative humidity effects. Journal of Power Sources 2005:150:120–128.

[180] Bailly C, Williams DJ, Karasz FE, MacKnight WJ. The sodium salts of sulphonated poly (aryl- ether-ether-ketone) (PEEK): Preparation and characterization. Polymer 1987:28:1009-1016.

[181] S. MLRT, Choudhary V, Varma IK. Sulphonated poly(ether ether ketone): Synthesis and characterization. Journal of Materials Science 2005:40:629-636.

[182] Marrony M, Rozie̍re J, Jones DJ, Lindheimer A. Multilayers sulphonated polyaromatic PEMFC membranes. Fuel Cells 2005:5(3):412-418.

[183] Xing P, Robertson GP, Guiver MD, Mikhailenko SD, Wang K, Kaliaguine S. Synthesis and characterization of sulfonated poly(ether ether ketone) for proton exchange membranes. Journal of Membrane Science 2004:229:95–106.

[184] Zaidi SMJ, Mikhailenko SD, Robertson GP, Guiver MD, Kaliaguine S. Proton conducting composite membranes from polyether ether ketone and heteropolyacids for fuel cell applications. Journal of Membrane Science 2000:173 17–34.

[185] Othman MHD, Ismail AF, Mustafa A. Proton conducting composite membrane from sulfonated poly (ether ether ketone) and boron orthophosphate for direct methanol fuel cell application. Journal of Membrane Science 2007:299:156–165.

[186] Gasa JV, Weiss RA, Shaw MT. Influence of Blend Miscibility on the Proton Conductivity and Methanol Permeability of Polymer Electrolyte Blends. Journal of Polymer Science: Part B: Polymer Physics 2006:44:2253–2266.

[187] Swier S, Ramani V, Fenton JM, Kunz HR, Shaw MT, Weiss RA. Polymer blends based on sulfonated poly(ether ketone ketone) and poly(ether sulfone) as proton exchange membranes for fuel cells. Journal of Membrane Science 2005:256 122–133.

[188] Swier S, Shaw MT, Weiss RA. Morphology control of sulfonated poly(ether ketone ketone) poly(ether imide) blends and their use in proton-exchange membranes. Journal of Membrane Science 2006:270 22–31.

[189] Shibuya N, porter RS. Kinetics of PEEK sulphonation in concentrated sulphuric acid. Macromolecules 1992:25:6495-6499.

[190] Shibuya N, Porter RS. A reconsideration of kinetics of aromatic sulphonation by sulphuric acid. Macromolecules 1994:27:6267-6271.

[191] Mark HF, Bikales NM, Overberger CG, Menges G, Kroschwitz JI. Encyclopaedia of polymer science and engineering. John Wiley & Sons, New York, 1988.

[192] Kricheldorf HR. Hand book of polymer synthesis. Marcel Dekker, New York, 1992.

[193] Pinto BP, Maria LCdS, Sena ME. Sulphonated poly(ether imide): A versatile route to prepare functionalized polymers by homogenous sulphonation. Material Letters 2007:61:2540-2543.

[194] Lakshmi RTSM, Bhattacharya S, Varma IK. Effect of sulphonation on thermal properties of poly(ether imide). High Performance Polymers 2006:18:115-126.

[195] Makowski HN, Londberg RD, Singhal GH. US. Patent 3,870,841, 1975.

[196] Martins CR, Ruggeri G, Paoli M-AD. Synthesis in pilot plant scale and physical properties of sulphonated polystyrene. Journal of Brazilian Chemical Society 2003:14(5):797-802.

[197] Baigl D, Seery TAP, Williams CE. Preparation and characterization of hydrosoluble, partially charged poly(styrenesulfonate)s of various controlled charge fractions and chain lengths. Macromolecules 2002:35:2318-2326.

[198] Bozkurt A. Anhydrous proton conductive polystyrene sulphonic acid membranes. Turkish Journal of Chemistry 2005:29:117-123.

[199] Tada H, Ito S. Conformational change restricted selectivity in the surface sulphonation of polypropylene with sulphuric acid. Langmuir 1997:13(15):3982-3989.

[200] Kaneko M, Sato H. Sulfonation of Poly(propylene) Films with Fuming Sulphuric Acid. Macromolecular Chemistry and Physics 2005:206:456–463.

[201] Bishop MT, Karasz FE, Russet PS. Solubility and Properties of a Poly(ary*l* ether ketone) in Strong Acids. Macromolecules 1985:18:86-93.

[202] Crank J. The mathematics of diffusion. Oxford University Press, New York, 1975.

[203] Kim YS, Dong L, Hickner MA, Glass TE, Webb V, McGrath JE. State of water in disulphonated poly(arylene ether sulphone) copolymers and a perfluorosulphonic acid copolymer (Nafion) and Its effect on physical and electrochemical properties. Macromolecules 2003:36:6281-6285.

[204] Zawodzinski TA, Derouin C, Radzinski S, Sherman RJ, Smith VT, Springer TE, Gottesfeld S. Water uptake by and transport through Nation-117 membranes. Journal of the Electrochemical Society 1993:140:1041−1047.

[205] Zawodzinski TA, Springer TE, Davey J, Jestel R, Lopez C, Valerio J, Gottesfeld S. A comparative study of water uptake by and transport through ionomeric fuel cell membranes. Journal of the Electrochemical Society 1993:140:1981−1985.

[206] Eikerling M, Kornyshev AA, Kuznetsov AM, Ulstrup J, Walbran S. Mechanisms of proton conductance in polymer electrolyte membranes. Journal of Physical Chemistry B 2001:105:3646−3662.

[207] Kreuer KD. Fast proton conductivity: A phenomenon between the solid and the liquid state. Solid State Ionics 1997:94:55-62.

[208] Paddison SJ, Paul R. The nature of proton transport in fully hydrated Nafion. Physical Chemistry Chemical Physics 2002:4:1158−1163.

[209] Okada T, Satou H, Okuno M, Yuasa M. Ion and water transport characteristics of perfluorosulfonated ionomer membranes with H^+ and alkali metal cations. Journal of Physical Chemistry B 2002:106:1267−1273.

[210] Okada T, Nakamura N, Yuasa M, Sekine I. Ion and water transport characteristics in membranes for polymer electrolyte fuel cells containing H^+ and Ca^{2+} cations. Journal of the Electrochemical Society 1997:144:2744−2750.

[211] Kim YS, Dong L, Hickner MA, Glass TE, webb V, McGrath JE. State of water in disulphonated poly(arylene ether sulphone) copolymers and a perfluorosulphonic acid copolymer (Nafion) and its effect on physical and electrochemical properties. macromolecules Symposia 2006:36:6281-6285.

[212] Siu A, Pivovar B, Horsfall J, Lovell KV, Holdcroft S. Dependence of methanol permeability on the nature of water and the morphology of graft copolymer proton exchange membranes. Journal of Polymer Science: Part B: Polymer Physics 2006:2240-2252.

[213] Vona MLD, Sgreccia E, Licoccia S, Khadhraoui M, Denoyel R, Knauth P. Composite proton-conducting hybrid polymers: Water sorption isotherms and mechanical properties of blends of sulphonated PEEK and substituted PPSU. Chemistry and Materials 2008:20:4327–4334.

[214] Buchi FN, Scherer GG. Investigation of the transversal water profile in Nafion membranes in polymer electrolyte fuel cells. Journal of the Electrochemical Society 2000:148:A181-A188.

[215] Kreuer KD. On the development of proton conducting polymer membranes for hydrogen and methanol fuel cells. Journal of Membrane Science 2001:185:29–39.

[216] Elomaa M, Hietala S, Paronen M, Walsby N, Jokela K, Serimaa R, Torkkeli M, Lehtinen T, Sundholmc G, Sundholm F. The state of water and the nature of ion clusters in cross linked proton conducting membranes of styrene grafted and sulphonated poly(vinylidene fluoride). Journal of Materials Chemistry 2000:10:2678-2684.

[217] Karlsson LE, Wesslen B, Jannasch P. Water absorption and proton conductivity of sulphonated acrylamide copolymers. Electrochemica Acta 2002:47:3269-3275.

[218] Siu A, Schmeisser J, Holdcroft S. Effect of water on the low temperature conductivity of polymer electrolytes. Journal of Physical Chemistry B 2006:110:6072-6080.

[219] Robertson GP, Mikhailenko SD, Wang KP, Xing P, Guiver MD, Kaliaguine S. Casting solvent interactions with sulphonated poly(ether ether ketone) during proton exchange membrane fabrication. Journal of Membrane Science 2003:219:113-121.

[220] Kaliaguine S, Mikhailenko SD, Wang KP, Xing P, Robertson G, Guver M. Properties of SPEEK based PEMs for fuel cell application. Catalyst Today 2003:82:213-222.

[221] http://www.goodfellow.com. 2009.

[222] Vona MLD, Marani D, D'Epifanio A, Licoccia S, Beurroies I, Denoyel R, Knauth P. Hybrid materials for polymer electrolyte membrane fuel cells: Water uptake, mechanical and transport properties. Journal of Membrane Science 2007:304:76–81.

[223] Kopitzke RW, Linkous CA, Anderson HR, Nelson GL. Conductivity and water uptake of aromatic-based proton exchange membrane electrolytes. Journal of the Electrochemical Society 2000:147:1677-1681.

[224] Thampan T, Malhotra S, Zhang J, Datta R. PEM fuel cell as a membrane reactor. Catalyst Today 2001:67:15–32.

[225] Peckham TJ, Schmeisser J, Rodgers M, Holdcroft S. Main-chain, statistically sulphonated proton exchange membranes: the relationships of acid concentration and proton mobility to water content and their effect upon proton conductivity. Journal of Materials Chemistry 2007:17:3255–3268.

[226] Brun M, Lallemand A, Quinson J, Eyraud C. A new method for the simultaneous determination of the size and the shape of pores: The Thermoporometry. Thermochimica Acta 1977:21:59-88.

[227] Price DM, Bashir Z. A study of the porosity of water-plasticised polyacrylonitrile films by thermal analysis and microscopy. Thermochimca Acta 1995:249:351-366.

[228] Hay JN, Laity PR. Observations of water migration during thermoporometry studies of cellulose films. Polymer 2000:41:6171–6180.

[229] Kim KJ, Fane AG, Aim RB, Liu MG, Jonsson G, Tessaro IC, Broek AP, Bargeman D. A comparative study of techniques used for porous membrane characterization: Pore characterization. Journal of Membrane Science 1994:81:35-46.

[230] Nakao S. Determination of pore size and pore size distribution 3. Filtration membranes. Journal of Membrane Science 1994:96:131-165.

[231] Escribano S, Aldebert P, Pineri M. Volumic electrodes of fuel cells with polymer electrolyte membranes: electrochemical performances and structural analysis by thermoporometry. Electrochimica Acta 1998:43:2195-2202.

[232] Lim TH, Tham MP, Liu Z, Hong L, Guo B. Nano-structured proton exchange membranes molded by polymerizing bi continuous microemulsion. Journal of Membrane Science 2007:290:146–152.

[233] Chow PY, Chew CH, Ong CL, Wang J, Xu G, Gan LM. Ion-containing membranes from microemulsion polymerization. Langmuir 1999:15:3202-3205.

[234] Jeon JD, Kwak SY. Ionic cluster size distributions of swollen Nafion/sulfated â-cyclodextrin membranes characterized by nuclear magnetic resonance cryoporometry. Journal of Physical Chemistry B 2007:111:9437-9443.

[235] Tang H, Peikang S, Jiang SP, Wang F, Pana M. A degradation study of Nafion proton exchange membrane of PEM fuel cells. Journal of Power Sources 2007:170:85–92.

[236] Luo Y, Hue R, Jin X, Karasz FE. Thermal degradation of sulphonated poly(aryl ether ether ketone). Journal of Analytical and Applied Pyrolysis 1995:34:229-242.

[237] Bosnjakovic A, Schlick S. Nafion perfluorinated membranes treated in Fenton media: Radical species detected by ESR spectroscopy. Journal of Physical Chemistry B 2004:108:4332-4337.

[238] Lee JK, Kerres J. Synthesis and characterization of sulphonated poly(arylene thioether)s and their blends with polybenzimidazole for proton exchange membranes. Journal of Membrane Science 2007:294:75–83.

[239] Xing D, Kerres J. Improved performance of sulphonated polyarylene ethers for proton exchange membrane fuel cells. Polymer for Advanced Technologies 2006:17:1-7.

[240] Kerres J, Xing D, Schuonberger F. Comparative investigation of novel PBI blend ionomer membranes from nonfluorinated and partially fluorinated polyarylene ethers. Journal of Polymer Science Part B: Polymer Physics 2006:44:2311–2326.

[241] Kunz HR, Gruver GA. The catalyst activity of platinuim supported on carbon for electrochemical oxygen reduction in phosphoric acid. Journal of the Electrochemical Society 1975:122:1279-1287.

[242] Cheng X, Zhang J, Tang Y, Song C, Shen J, Song D, Zhang J. Hydrogen crossover in high-temperature PEM fuel cells. Journal of Power Sources 2007:167:25–31.

[243] Inaba M, Kinumoto T, Kiriake M, Umebayashi R, Tasaka A, Ogumi Z. Gas crossover and membrane degradation in polymer electrolyte fuel cells. Electrochimica Acta 2006:51:5746–5753.

[244] Cleghorn S, Kolde J, Liu W. in Handbook of fuel cells, Vol. 3, W. Vielstichm, A. Lamm and H. A. Gasteiger (eds.). John Wiley & Sons, New York, 2003. P566.

[245] Lage LG, Delgado PG, Kawano Y. Thermal stability and decomposition of Nafion membranes with different cations using high-resolution thermogravimetry. Journal of Thermal Analysis and Calorimetry 2004:75:521–530.

[246] Passos RR, Paganin VA, Ticianelli EA. Studies of the performance of PEM fuel cell cathodes with the catalyst layer directly applied on Nafion membranes. Electrochemica Acta 2006:51:5239–5245.

[247] Gasteiger HA, Panels JE, Yan SG. Dependence of PEM fuel cell performance on catalyst loading. Journal of Power Sources 2004:127:162–171.

Supporting Publications

1. **Abdul G. Al Lafi**, James N. Hay and David J. Parker*; The effect of proton irradiation on the melting and isothermal crystallization of poly (ether-ether-ketone):* Journal of Polymer Science Part B Polymer Physics, 2008, 46, 1094-1103.

2. **Abdul G. Al Lafi**, James N. Hay and David J. Parker*; The effect of ions irradiation on the thermal properties of poly (ether-ether-ketone):* Journal of Polymer Science Part B Polymer Physics, 2008, 46, 2212-2221.

3. **Abdul G. Al Lafi** and James N. Hay*; The sulphonation of cross linked PEEK; diffusion controlled kinetics:* Journal of Polymer Science Part B Polymer Physics, 2009, 47, 775-783.